# METAMATERIALS AND THEIR APPLICATIONS IN IMAGING

by

Suresh Venkatesh

A dissertation submitted to the faculty of
The University of Utah
in partial fulfillment of the requirements for the degree of

Doctor of Philosophy

Department of Electrical and Computer Engineering

The University of Utah

May 2017

**The University of Utah Graduate School**

**STATEMENT OF DISSERTATION APPROVAL**

The dissertation of **Suresh Venkatesh**
has been approved by the following supervisory committee members:

| | | |
|---|---|---|
| **David Schurig** , | Chair(s) | **26 Oct 2016** Date Approved |
| **Gianluca Lazzi** , | Member | **26 Oct 2016** Date Approved |
| **Ajay Nahata** , | Member | **26 Oct 2016** Date Approved |
| **Cynthia Furse** , | Member | **26 Oct 2016** Date Approved |
| **Mathieu Francoeur** , | Member | **26 Oct 2016** Date Approved |

by **Gianluca Lazzi** , Chair/Dean of
the Department/College/School of **Electrical and Computer Engineering**
and by **David B. Kieda** , Dean of The Graduate School.

# ABSTRACT

Microwave/millimeter-wave imaging systems have become ubiquitous and have found applications in areas like astronomy, bio-medical diagnostics, remote sensing, and security surveillance. These areas have so far relied on conventional imaging devices (employing Nyquist principles) which at best can provide diffraction-limited images. With the advent of metamaterials, unique and extraordinary electromagnetic responses can be achieved which can potentially revolutionize imaging devices. Such extraordinary responses include: negative refraction, strong anisotropy, gradient-index response, perfect absorption, magneto-electric effects (chirality), and many more. When adopted into imaging devices, these response characteristics could potentially: beat diffraction-limits, improve imaging performance, or lead to unprecedented control over light propagation. Along with metamaterials, mathematical tools like transformation optics or torsion optics (which leverages Riemannian geometry under the geometrical optics limit) facilitate the design and development of systems with exclusive effects such as invisibility cloaking, perfect and/or aberration-free lensing, near-field magnification, and total control of the polarization field. When metamaterial devices are combined with computational imaging techniques, the resulting systems can exploit apriori information to reach previously unattainable trade-off positions in the space of: image quality, size, weight, power, and cost. In this dissertation we present and discuss metamaterial-based imaging devices, and associated principles and techniques that achieve such enhanced imaging performance.

Dedicated to my parents, sister, and my advisor David Schurig.

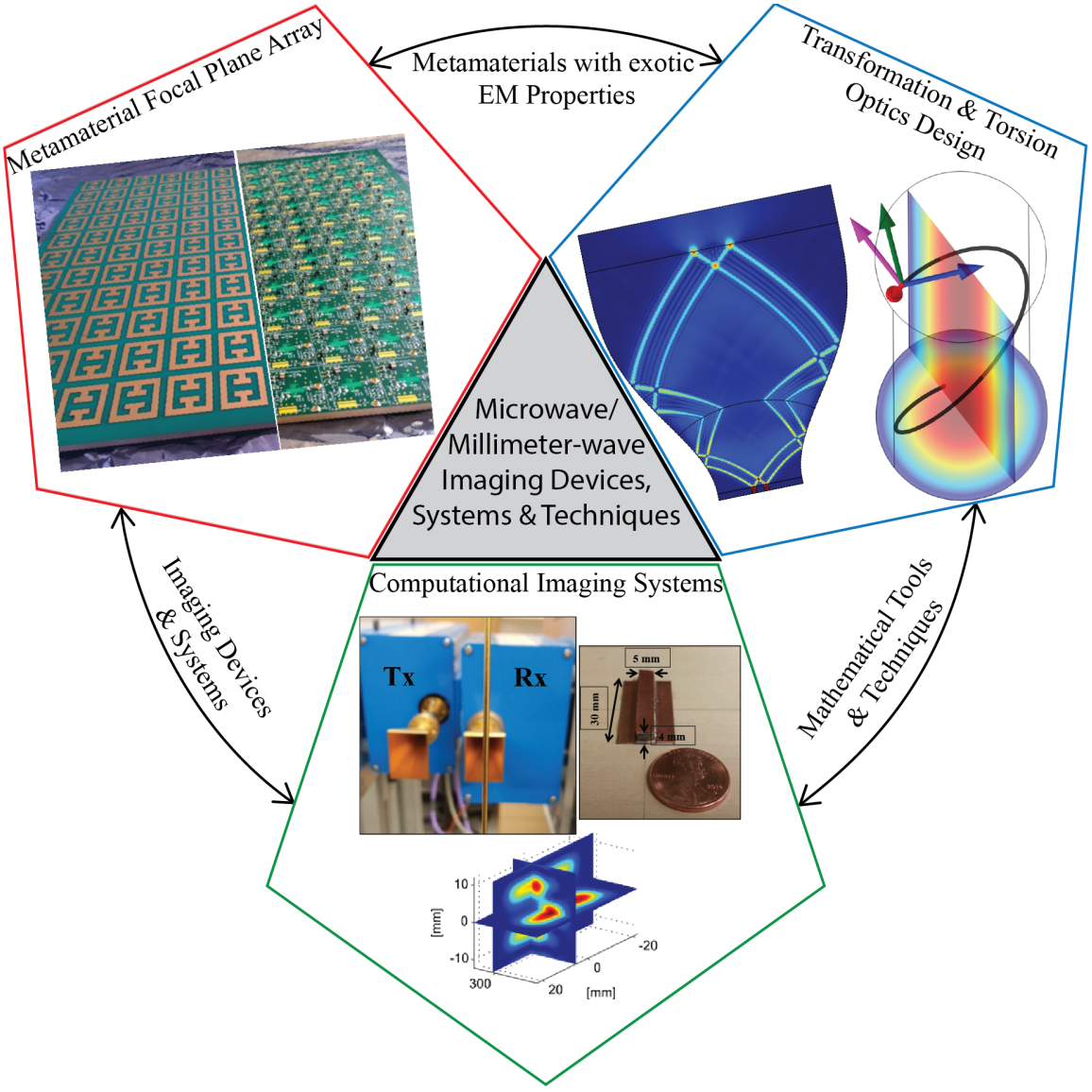


Summary of the dissertation.

# CONTENTS

# LIST OF TABLES

# PREFACE

In Chapters 1 and 2, we present a novel "medium-as-device" approach to experimentally demonstrate a metamaterial, perfect-absorber-based focal plane array. The microwave focal plane array was demonstrated both as an intensity detector and as a vector signal detector. The former setup was used to perform interferometric direction finding of RF emitters.

In Chapter 3, we present a transformation optics designed near-field magnifier, for subwavelength imaging. We discuss and present various design parameters and tradeoffs associated with such magnifiers. We adopt grid relaxation techniques that result in material properties that are more amenable to implementation. In Chapter 4, we present a novel "Torsion Optics" design method, leveraging Riemannian geometric concepts, that facilitates the design of devices with gradient chiral material properties, giving an unprecedented control over the polarization field.

In Chapter 5, we demonstrate a prototype W-band (75 -110 GHz) sparse, synthetic-aperture, computational imaging system that leverages intrinsic frequency diversity in the sparse aperture. We also formulate an information-based metric to evaluate the performance of a given image transfer matrix for noise-limited, computational imaging systems. In Chapter 6, we describe a computationally fast approach for propagation of vector electromagnetic fields through an axi-symmetric medium (such as a lens) using cylindrical harmonic decomposition techniques. The motivating application is to computational imaging systems, where the forward propagation model must be computed quickly, for real time results. This approach was also applied in the near-field magnifier design and analysis.

In Chapter 7, as a part of future directions, we exploit all of the above approaches to propose a multi-functional RF system leveraging commercial off-the-shelf integrated circuits. We propose to investigate, in particular, the synergies that result when a single hardware platform can support: focusing-optic-free computational imaging, satellite links on mobile platforms, and electronic targeting of nonlethal force.

Each chapter of this thesis has been or will be submitted for journal publication as listed below:

- **S. Venkatesh**, D. Schurig, "Transformation optics design of a planar near field magnifier for sub-diffraction imaging," to be submitted.
- **S. Venkatesh**, D. Schurig, "Computational imaging with low cost Ku-band sat-com hardware," to be submitted.
- **S. Venkatesh**, N. Korevaar, D. Schurig, "Controlling the twisting of light," submitted to *Physical Review X*.
- **S. Venkatesh**, D. Schurig, "Computationally fast propagation of arbitrary electromagnetic fields through an axially symmetric medium," *Optics Express*, vol. 24, no. 25, pp. 29246-29268, 2016.
- **S. Venkatesh**, N. Viswanathan, D. Schurig, "W-band sparse synthetic aperture for computational imaging," *Optics Express*, vol. 24, no. 8, pp. 8317-8331, 2016.
- **S. Venkatesh**, D. Shrekenhamer, W. Xu, S. Sonkusale, W. Padilla, D. Schurig, "Interferometric direction finding with a metamaterial detector," *Applied Physics Letters*, vol. 103, no. 25, 2013.
- D. Shrekenhamer, W. Xu, **S. Venkatesh**, D. Schurig, S. Sonkusale, W. J. Padilla, "Experimental realization of a metamaterial detector focal plane array," *Physical Review Letters*, vol. 109, p. 177401, Oct. 2012.

I would like to thank my advisor David Schurig for all his support and encouragement during my graduate program. He always has, and continues, to motivate me to work on challenging and interesting research problems. My parents and my sister, Soumya, have always been the essential support of my life. I thank my collaborators, namely Willie Padilla (Duke University, formerly Boston College), David Smith (Duke University), Sameer Sonkusale (Tufts University), Nicholas Korevaar (Math Dept., University of Utah), and the rest of my committee members for their help and support. I would like to thank Ramesh Balasubramanyam and Sharath for the great times at Raman Research Institute, Bangalore. I thank Aadhithya, Arunesh, Mihir, and all my friends/roommates for the fun times at NC State University, Raleigh. I thank my dissertation committee members for their support. Lastly, I thank all my friends and labmates at the University of Utah, Salt Lake City.

# CHAPTER 1

# EXPERIMENTAL REALIZATION OF A METAMATERIAL DETECTOR FOCAL PLANE ARRAY

This chapter, in full, has been published in Physical Review Letters, **109**, 177401 (2012), with authors David Shrekenhamer, Wangren Xu, Suresh Venkatesh, David Schurig, Sameer Sonkusale, and Willie Padilla. (reprinted with permission)

## 1.1 Abstract

We present a metamaterial absorber (MMA) detector array that enables room-temperature, narrow-band detection of gigahertz (GHz) radiation in the S-band (2-4 GHz). The system is implemented with a commercial printed circuit board process and we characterize the detector sensitivity and angular dependence. A modified MMA geometry allows for each unit cell to act as an isolated detector pixel and to collectively form a focal plane array (FPA). Each pixel can have a dedicated microwave receiver chain and functions together as a hybrid device tuned to maximize the efficiency of detected power. The demonstrated sub-wavelength pixel shows detected sensitivity of -77 dBm, corresponding to a radiation power density of 27 $nW/m^2$, with pixel to pixel coupling interference below -14 dB at 2.5 GHz.

## 1.2 Letter

Engineered artificial materials consisting of sub-wavelength, periodic metallic inclusions, can exhibit exotic electromagnetic properties not readily available in nature. Over the past decade, interest of the scientific and engineering communities for developing such metamaterial structures has been continuous and increasing. Experimental realizations of negative index of refraction [1,2], invisibility cloaks [3], and perfect lensing [4] all served to ignite the field. As metamaterial research continues to mature, demonstrations of practical

devices will become increasingly important for continued growth. Metamaterial based sources, detectors and modulators that could be used in communication systems, or for imaging and sensing applications, would go far to validate the initial promise of the technology. Thus far several modulator designs have been experimentally demonstrated [5–7], but the development of metamaterial based sources and detectors is lacking [8, 9].

Microwave imaging systems working between 8-30 GHz have been used for decades in remote sensing and radio astronomy [10, 11]. Common designs are often notably massive and bulky, employing mechanical positioning stages (to raster scan a single pixel across an image plane to build up an image), or using an array of efficient but very substantial elements, such as horn antennas [12]. Though the greatest gains in performance come from increasing the aperture, if compactness, mobility or inconspicuousness are desirable, one would like to have an imaging system that maximizes the performance and minimizes the weight and bulk at a given aperture size. With pixel spacing on the order of the diffraction limited spot size $a \sim \lambda_0/2\pi$ (where $\lambda_0$ is the wavelength of the radiation at the imaging frequency), the focal plane can be adequately sampled and all available information acquired. However, such dense spacing is at odds with pixel channel independence. Minimizing cross-talk between detector pixels can require spacings that result in poor resolution and sparse spatial sampling of the image [13–15]. Achieving a high detected-to-incident power efficiency is another key aspect to consider in order to improve the sensitivity. Ideally, one would like to transfer all power to the detector that is incident within the boundaries of a pixel. In all examples to-date there are trade-offs between power efficiency and pixel independence [16, 17]. We believe that resonators developed in the metamaterial community can offer different and potentially superior options for pixel density, channel independence and power efficiency.

In this letter, we present a metamaterial absorber (MMA) that operates as a detector of microwave radiation. Each MMA unit cell functions as an individual antenna coupled detector and, collectively, as a focal plane array (FPA). The metamaterial unit cell converts the incident microwave radiation into electric currents, which are guided to a dedicated receiver chain and finally detected with a power detector to produce DC voltage linearly proportional to the signal. All metamaterial elements and receiver system components can be integrated into a single printed circuit board (PCB).

The ability of metamaterial unit cells to completely absorb incident electromagnetic energy – with effectively zero reflected signal – has been demonstrated across much of the electromagnetic spectrum [18–20], and have shown great potential for use in applications ranging from thermal emitters [21] to energy harvesting [22]. One key design feature afforded by metamaterials is the ability to engineer materials for matching the impedance of the MMA to that of free space. The resonant nature of the MMA structures generates high electric fields in the gap, completely dissipating the incident energy into a combination of dielectric and ohmic losses [23, 24]. However, here we modify the MMA design in order to instead transfer the incident energy into a detector circuit. We have utilized the highly absorbing capability of the MMA to fashion a focal plane array by letting each individual unit cell serve as an array elements.

The microwave FPA presented here consists of metamaterial unit cells arranged on a square lattice of 11 by 11 elements. The entire detector system architecture – all contained within the footprint of each unit cell – consists of the metamaterial absorber followed by a balun, impedance matching circuit, low noise amplifier (LNA) and a microwave power detector. The FPA has been implemented in a twelve layer commercial PCB process fabricated and assembled by Hughes circuits, including four metal layers and *vias*, see Fig. 1.1. The device is constructed from a 30.5 $\mu$m copper layer which constitutes the electrically coupled LC (ELC) resonators [25, 26], followed by a patterned ground plane, power routing plane, and the circuit layer – where the ELC and ground plane are separated by Rogers 4003 dielectric with a 4.88 mm thickness. Microwave radiation received by the metamaterial perfect absorber is transferred by the 0.5 mm diameter *vias* to the circuit layer where a balun is used to transform the balanced signal to an unbalanced signal. The signal is then fed into the impedance matching circuit which not only maximizes the signal power, but also serves to compensate for variances in the MPA resonance frequency – due to imperfections in the fabrication process. Finally the signal is amplified by the LNA before being converted to a DC signal by the microwave power detector.

We simulate the design of the entire detector array using commercial 3D electromagnetic simulation software CST's Microwave Studio 2011. The ports, (shown schematically in Fig. 1.1), are used to investigate the transfer of electromagnetic energy in the device and consist of waveguide ports (port 1 and 2), and a discrete port (port 3). The discrete port is

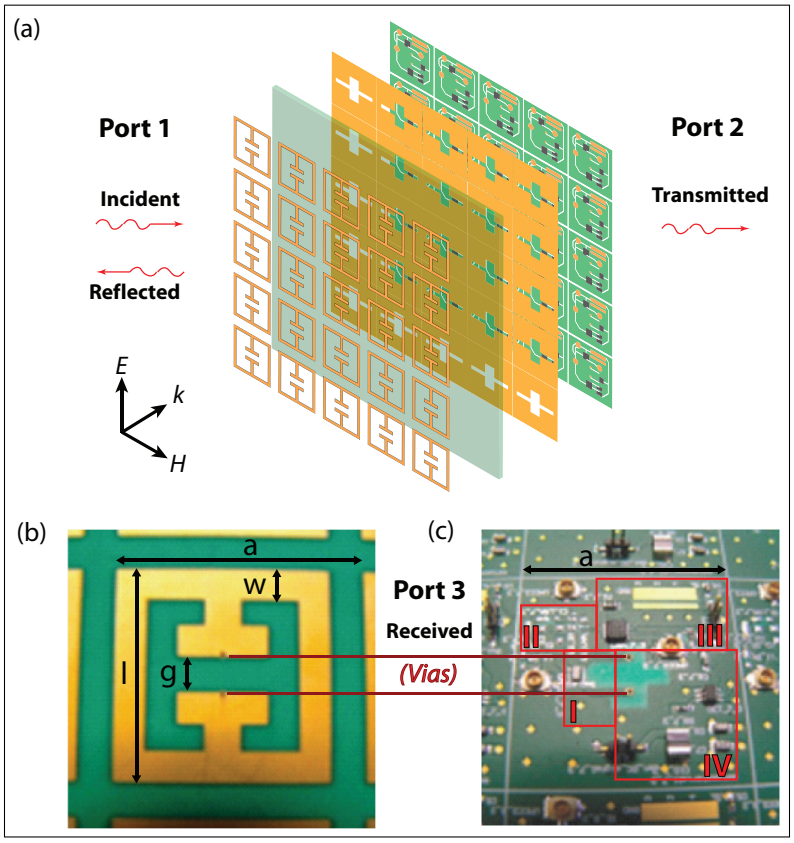


**Figure 1.1**: (Color online) System architecture of our metamaterial microwave power detector array. (a) Radiation is incident from port 1 with electric field polarization as depicted. A schematic of the full device is shown (exploded view) and the layers shown from top to bottom are: the ELC, Rogers dielectric spacer, patterned ground plane, and microwave power receiver circuit. (b) Photo of an individual pixel, i.e. an ELC unit cell with dimensions of $a$ = 27.3, $l$ = 24, $w$ = 3.5, and $g$ = 4; all in millimeters. (c) Photo of the circuit layer with *vias* indicated. The *vias* transport the received signal (port 3) to the microwave power receiver circuit underneath each unit cell where the different highlighted regions are: (I) balun, (II) impedance matching circuit, (III) low noise amplifier, and IV) microwave power detector.

a lumped circuit element that connects the *vias* to one another with a defined impedance set equal to 100 Ohms ($\Omega$), which is equivalent to the input impedance of the balun. The metamaterial was configured to maximize the transfer of energy into port 3, i.e. $S_{31}$, while at the same time minimize both the free space reflection coefficient ($S_{11}$) and reflection coefficient ($S_{33}$) at 2.0 GHz. In order to achieve this goal we tuned the dimensions of the MMA; consisting of the ELC geometry, thickness of the Rogers 4003 ($\tilde{\varepsilon} = \varepsilon_1 + i\varepsilon_2 = 3.38 + i0.007$) dielectric spacer, and the opening in the ground plane. The final dimensions

of the ELC resonator are shown in Fig. 1.1(b) with parameters as labeled. The dimensions of the cross shaped opening in the ground plane, (Fig. 1.1(c)), were optimized to minimize the coupling between the *vias* and ground plane, as well as tune the MMA's effective magnetic response. The ground plane also helps to shield any undesirable coupling effects between the circuit components and the electromagnetic metamaterial performance.

The simulated scattering parameters are shown in Fig. 1.2(a) and demonstrates that a maximum in transmission corresponds with the minima of both reflection coefficients $S_{11}$ and $S_{33}$ at 2.0 GHz. As mentioned, the MMA design typically utilizes the dielectric and ohmic losses within the constituent components in order to achieve a minimum in $S_{11}$. In contrast, the design presented here achieves $S_{31}$= 0.986, indicating that over 97% of the incident intensity is transmitted into the detector circuit. In Fig. 1.2(b) we plot the surface current density at resonance and find that our MMA achieves a response similar to prior designs [25]. Figure 1.2(c) shows the magnitude of the electric field and, as can be observed, the electric field is focused into the ELC split gap (right panel) and the *vias* are sufficiently decoupled from the ground plane.

Although simulations presented above indicate that a high performance MMA unit cell may be used as a detector of incident radiation, tolerances in both the component values and the geometry can occur in the fabrication process and may thus alter the ideal electromagnetic response. Characterization of $S_{11}$ is not possible with our experimental setup. However, simulations presented in Fig. 1.2(a) indicate that $S_{33}$ is a reasonable approximation of $S_{11}$. Thus we measure $S_{33}$ in order to investigate the resonant properties of the fabricated MMA, shown as the red curve in Fig. 1.3(a). We observe a high reflection coefficient across the range investigated but notably minima occur at 2.5 and 3.15 GHz, with values of -33 dB and -29 dB, respectively. The simulated minimum in $S_{33}$ occurring at 2.0 GHz has shifted to 2.5 GHz, which we attribute to the variation in the fabrication from the simulated design (see the Supplemental Material [27] for more details).

Free space measurements of the center pixel were performed within an anechoic chamber (see the Supplemental Material [27] for more details). We use a HP 8510B vector network analyzer (VNA) with a double ridge guide horn antenna (700 MHz - 18 GHz range) as a transmitter. The horn was connected to a port of the VNA which provided a power level of -3 dBm. Another port of the VNA was directly connected following the

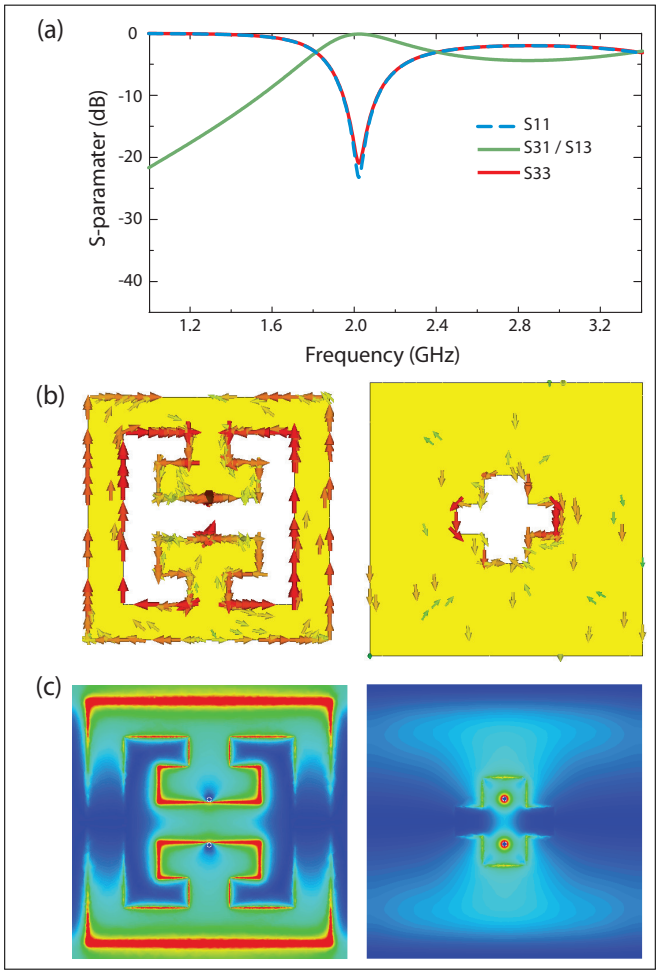


**Figure 1.2**: (Color online) Numerical simulations of metamaterial absorber. (a) Simulated results of the free space reflection ($S_{11}$ dashed blue curve), transmission ($S_{31}$ green curve), and reflection coefficient ($S_{33}$ red curve). Simulated current densities (b) and electric field magnitude (c) shown directly underneath the ELC (left) and above the ground plane (right) at the simulated design frequency of 2.0 GHz.

unbalanced signal output of the balun on the center single pixel of the MMA / FPA. The resulting S-parameters measured were for only this center pixel with all neighboring unit cells having 50 Ω terminations following their respective balun output connections. The MMA / FPA was placed 1.75 m away from the horn antenna to be in the far field of the horn's radiating field pattern. In Fig. 1.3(a), the green $S_{31}$ curve shows a peak about 2.5 GHz overlapping with the minimum observed in $S_{33}$.

The gold curve in Fig. 1.3(b) displays the measured mutual coupling (MC) between neighboring unit cells parallel to the electric field direction. At 2.5 GHz the MC was

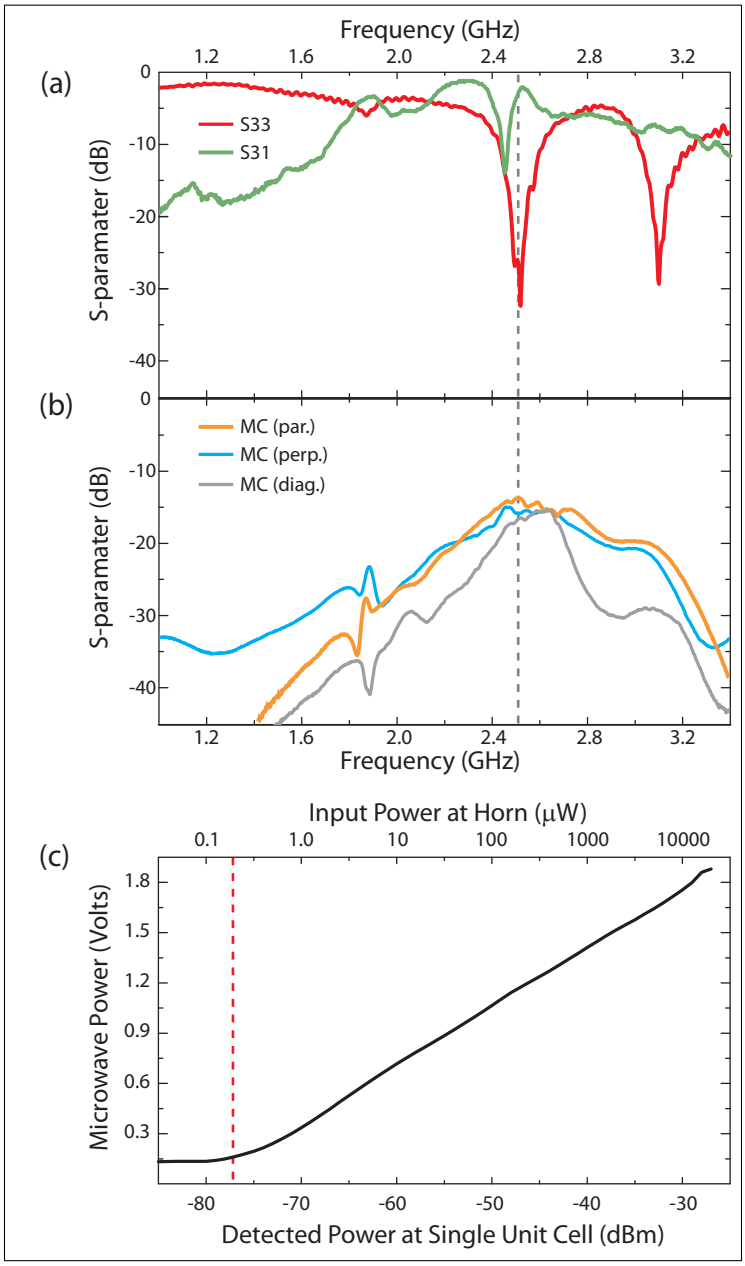


**Figure 1.3**: (Color online) Experimental measurements in anechoic chamber for the center pixel on the MMA / FPA. (a) S- parameter data shows the reflection coefficient ($S_{33}$ red curve) and the transmission ($S_{31}$ green curve) with the dashed grey line at 2.5 GHz the frequency for sensitivity and off-angle measurements. (b) Mutual coupling (MC) between neighboring metamaterial pixels located parallel (gold curve), perpendicular (blue curve), and diagonal (grey curve) with respect to the electric field polarization. (c) Sensitivity characterization with the output of microwave power detector of single pixel as function of incident power, and is sensitive as indicated by dashed red line down to -77 dBm at 2.5 GHz.

measured to be below -14 dB. We have also measured the MC in the perpendicular and diagonal neighboring cells and values below -15 dB were found. Values of MC are significantly low, especially considering the proximity of nearest neighbors at a lattice spacing of $\lambda/4.4$ (27.3 mm) and with edge separation of $\lambda/40$ (3.0 mm). In addition to the clear benefit toward imaging, [13–15] reducing MC is of particular importance for multiple input multiple output (MIMO) communication systems that suffer reduction in channel capacity due to these affects [28, 29].

We now turn toward characterization of the sensitivity and angular dependence of the MMA / FPA. A microwave source was fixed to operate at 2.5 GHz and fed to the horn antenna. The DC voltage output from the MMA / FPA was recorded as the horn power was swept from -50 dBm to +20 dBm as shown in Fig. 1.3(c). We determine an ultimate pixel sensitivity of -77 dBm, corresponding to a radiation power density of 27 $nW/m^2$, after calibrating for cable and free space losses. Figure 1.4 shows the resulting off-angle performance characterization of the MMA / FPA at 2.5 GHz for both transverse electric (TE) and transverse magnetic (TM) polarizations. However it should be noted that our metamaterial does not posses 90° rotational symmetry and thus we characterized TE and TM for both the "correct" polarization – as shown in Fig. 1.1(a) – the cross polarization to this. The measurement results demonstrate that the MMA / FPA operates as a wide angle antenna. This is consistent with the off-angle absorption performance typical to MMAs [23]. Both TE and TM cross-polarized angular dependent measurements are at minimum of 20dB lower that the co-polarized measurements. Thus the presented MMA / FPA may be used for polarization discrimination imaging.

The characterization of our metamaterial absorber focal plane array was demonstrated to operate at 2.5 GHz and have high pixel sensitivity of -77 dBm, with low pixel to pixel coupling interference below -14 dB, good frequency selectivity and wide angular performance. We note that the FPA is not restricted to the frequency applied in this work but could prove useful at higher frequency operation from microwave to millimeter wave. Even more generally, the MMA due to its ability to capture nearly all of the incident electromagnetic energy at design frequencies across the entire electromagnetic spectrum could serve as an excellent candidate to act as detector pixels when implemented into bolometric or semiconducting configurations. The sub-wavelength unit cell and narrow resonant

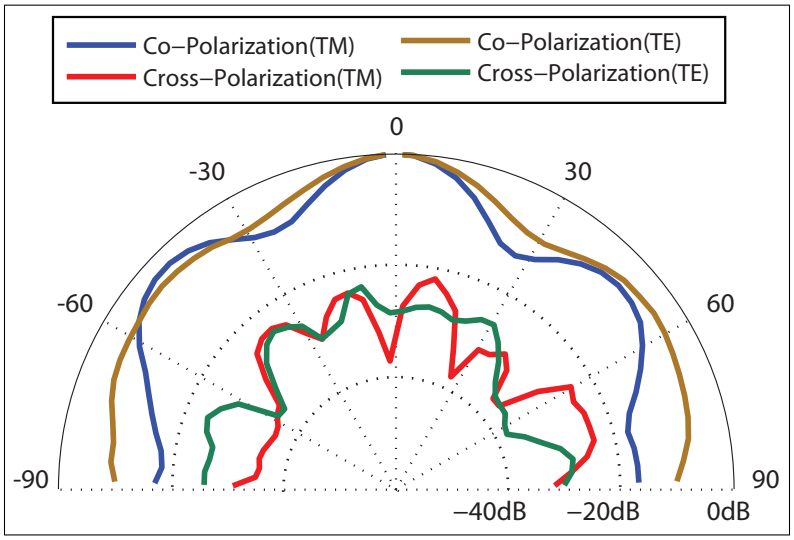


**Figure 1.4**: (Color online) Off-angle performance characterization of the MMA / FPA at 2.5 GHz for both the electric field vector perpendicular (TE) and parallel (TM) to the floor of the chamber. The ELC resonator's are rotated between the correct polarization (E-field perpendicular the split gap) and the cross polarization (E-field parallel to the gap).

spectral bandwidth can also be expanded to enable multi-color and co- and cross-polarized pixels.

## 1.3 Supplementary Material: Fabrication and Characterization

Fabrication: Our metamaterial focal plane array exhibited several undesirable deviations from the designed values during commercial fabrication. We characterized various parameters of our device and found errors that include: layer thickness, *via* dimensions, layer alignment (registration), balun impedance, and dielectric values. These variances result in a reduction of ideal electromagnetic performance which leads to an impedance mismatch between the metamaterial unit cell and the 50 Ω input circuit modules. Overall, this results in diminished reception of electromagnetic energy due to increased reflection between the metamaterial and detector circuit. We anticipated various fabricational errors and therefore, in the design process, preemptively added a reconfigurable element to tune the impedance of the circuit layer after the metamaterial unit cell. Thus an impedance matching circuit directly following the balun compensates for MMA variances and tunes the strength and frequency of the resonance at the selected operating frequency. Due to the hardware and component limitations we decided to operate at 2.5 GHz, as opposed to

the simulated 2.0 GHz operational frequency.

Characterization: We used a separate board to implement the impedance matching circuit and low-noise amplifier (LNA) (Board 2) and another board (Board 3) for the microwave power detector. We connected the output of Port 3 with a UMCC connector to Board 2 as shown schematically in Fig. 1.5. After the signal propagates through the impedance matching network and LNA, it passes through a SMA connector, which we call Port 4. We use the ADL5523 LNA made by Analog Device which provides a gain of approximately 15 dB at 2.5 GHz. In Fig. 1.6, the gold $S_{41}$ curve shows over a 15 dB improvement of $S_{31}$ at 2.5 GHz as a result of having an impedance matching circuit followed by the LNA. The microwave power detector converts the microwave output signal from port 4 into a DC voltage and is implemented using a monolithic LT5534 made by Linear Technology. The LT5534 has a 50MHz to 3GHz detected bandwidth and is capable of measuring microwave signals with over a 60dB dynamic range with a linear DC output with respect to signal amplitude in decibel scale.

## 1.4 Acknowledgments

We acknowledge support from the Office of Naval Research under U.S. Navy Contract No. N00014-07-1-0819, the Department of Energy under Grant No. DE-SC0005240, and the National Science Foundation under Grant No. ECCS-1002340.

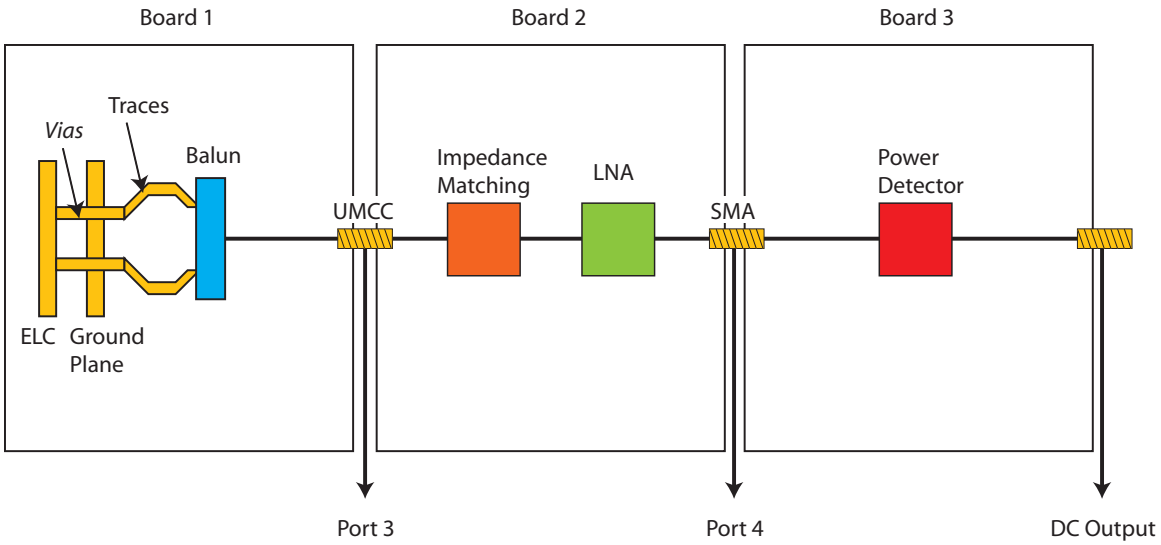


**Figure 1.5**: (Color online) System architecture consists of three boards with board 1 which containing the metamaterial connecting through the *vias*, traces and balun out through a ultraminiature coax connector (UMCC) designated as port 3. The UMCC cable connects to board 2 containing both the impedance matching circuit and low noise amplifier (LNA) with output labeled as port 4. The third board consists of only the microwave power detector providing a DC voltage output signal.

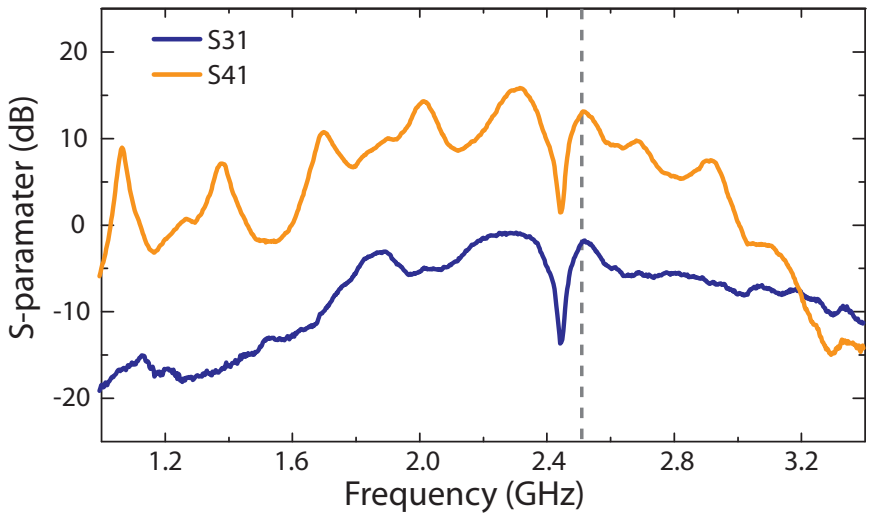


**Figure 1.6**: (Color online) S-parameter data shows the transmission without ($S_{31}$ blue curve) and with ($S_{41}$ gold curve) the addition of the impedance matching and low noise amplifier (LNA) with the dashed grey line at 2.5 GHz the frequency for sensitivity and off-angle measurements.

## 1.5 References


[1] R. A. Shelby, D. R. Smith, and S. Schultz, "Experimental verification of a negative index of refraction," *Science*, vol. 292, no. 5514, pp. 77–79, 2001.

[2] D. R. Smith, W. J. Padilla, D. C. Vier, S. C. Nemat-Nasser, and S. Schultz, "Composite medium with simultaneously negative permeability and permittivity," *Phys. Rev. Lett.*, vol. 84, pp. 4184–4187, May 2000.

[3] D. Schurig, J. J. Mock, B. J. Justice, S. A. Cummer, J. B. Pendry, A. F. Starr, and D. R. Smith, "Metamaterial electromagnetic cloak at microwave frequencies," *Science*, vol. 314, no. 5801, pp. 977–980, 2006.

[4] J. B. Pendry, "Negative refraction makes a perfect lens," *Physical review letters*, vol. 85, no. 18, p. 3966, 2000.

[5] H.-T. Chen, S. Palit, T. Tyler, C. M. Bingham, J. M. O. Zide, J. F. OHara, D. R. Smith, A. C. Gossard, R. D. Averitt, W. J. Padilla, N. M. Jokerst, and A. J. Taylor, "Hybrid metamaterials enable fast electrical modulation of freely propagating terahertz waves," *Applied Physics Letters*, vol. 93, no. 9, 2008.

[6] H.-T. Chen, W. J. Padilla, M. J. Cich, A. K. Azad, R. D. Averitt, and A. J. Taylor, "A metamaterial solid-state terahertz phase modulator," *Nature Photonics*, vol. 3, no. 3, pp. 148–151, 2009.

[7] D. Shrekenhamer, S. Rout, A. C. Strikwerda, C. Bingham, R. D. Averitt, S. Sonkusale, and W. J. Padilla, "High speed terahertz modulation from metamaterials with embedded high electron mobility transistors," *Optics express*, vol. 19, no. 10, pp. 9968–9975, 2011.

[8] H. Tao, E. A. Kadlec, A. C. Strikwerda, K. Fan, W. J. Padilla, R. D. Averitt, E. A. Shaner, and X. Zhang, "Microwave and terahertz wave sensing with metamaterials," *Optics express*, vol. 19, no. 22, pp. 21 620–21 626, 2011.

[9] F. B. Niesler, J. K. Gansel, S. Fischbach, and M. Wegener, "Metamaterial metal-based bolometers," *Applied Physics Letters*, vol. 100, no. 20, p. 203508, 2012.

[10] http://www.skatelescope.org.

[11] C. Carilli and S. Rawlings, "Science with the square kilometer array: motivation, key science projects, standards and assumptions," *arXiv preprint astro-ph/0409274*, 2004.

[12] R. Appleby and R. N. Anderton, "Millimeter-wave and submillimeter-wave imaging for security and surveillance," *Proceedings of the IEEE*, vol. 95, no. 8, pp. 1683–1690, 2007.

[13] J. P. Weem and Z. Popovic, "A method for determining noise coupling in a phased array antenna," in *Microwave Symposium Digest, 2001 IEEE MTT-S International*, vol. 1. IEEE, 2001, pp. 271–274.

[14] C. Craeye, B. Parvais, and X. Dardenne, "Mom simulation of signal-to-noise patterns in infinite and finite receiving antenna arrays," *IEEE transactions on antennas and propagation*, vol. 52, no. 12, pp. 3245–3256, 2004.

[15] K. F. Warnick and M. A. Jensen, "Effects of mutual coupling on interference mitigation with a focal plane array," *IEEE transactions on antennas and propagation*, vol. 53, no. 8, pp. 2490–2498, 2005.

[16] M. V. Ivashina, M. N. M. Kehn, P.-S. Kildal, and R. Maaskant, "Decoupling efficiency of a wideband vivaldi focal plane array feeding a reflector antenna," *IEEE Transactions on Antennas and Propagation*, vol. 57, no. 2, pp. 373–382, 2009.

[17] M. N. M. Kehn, M. V. Ivashina, P.-S. Kildal, and R. Maaskant, "Definition of unifying decoupling efficiency of different array antennascase study of dense focal plane array feed for parabolic reflector," *AEU-International Journal of Electronics and Communications*, vol. 64, no. 5, pp. 403–412, 2010.

[18] N. Landy, S. Sajuyigbe, J. Mock, D. Smith, and W. Padilla, "Perfect metamaterial absorber," *Physical review letters*, vol. 100, no. 20, p. 207402, 2008.

[19] H. Tao, N. I. Landy, C. M. Bingham, X. Zhang, R. D. Averitt, and W. J. Padilla, "A metamaterial absorber for the terahertz regime: Design, fabrication and characterization," *Optics express*, vol. 16, no. 10, pp. 7181–7188, 2008.

[20] J. Hao, J. Wang, X. Liu, W. J. Padilla, L. Zhou, and M. Qiu, "High performance optical absorber based on a plasmonic metamaterial," *Applied Physics Letters*, vol. 96, no. 25, p. 251104, 2010.

[21] X. Liu, T. Tyler, T. Starr, A. F. Starr, N. M. Jokerst, and W. J. Padilla, "Taming the blackbody with infrared metamaterials as selective thermal emitters," *Physical review letters*, vol. 107, no. 4, p. 045901, 2011.

[22] K. Aydin, V. E. Ferry, R. M. Briggs, and H. A. Atwater, "Broadband polarization-independent resonant light absorption using ultrathin plasmonic super absorbers," *Nature communications*, vol. 2, p. 517, 2011.

[23] H. Tao, C. Bingham, A. Strikwerda, D. Pilon, D. Shrekenhamer, N. Landy, K. Fan, X. Zhang, W. Padilla, and R. Averitt, "Highly flexible wide angle of incidence terahertz metamaterial absorber: Design, fabrication, and characterization," *physical review B*, vol. 78, no. 24, p. 241103, 2008.

[24] X. Liu, T. Starr, A. F. Starr, and W. J. Padilla, "Infrared spatial and frequency selective metamaterial with near-unity absorbance," *Physical review letters*, vol. 104, no. 20, p. 207403, 2010.

[25] D. Schurig, J. Mock, and D. Smith, "Electric-field-coupled resonators for negative permittivity metamaterials," *Applied Physics Letters*, vol. 88, no. 4, p. 041109, 2006.

[26] W. Padilla, M. Aronsson, C. Highstrete, M. Lee, A. Taylor, and R. Averitt, "Electrically resonant terahertz metamaterials: Theoretical and experimental investigations," *Physical Review B*, vol. 75, no. 4, p. 041102, 2007.

[27] See Supplemental Material for a detailed description of the materials and methods of fabrication, experiment, and numerical simulations.

[28] M. A. Jensen and J. W. Wallace, "A review of antennas and propagation for mimo wireless communications," *IEEE Transactions on Antennas and Propagation*, vol. 52, no. 11, pp. 2810–2824, 2004.

[29] C.-Y. Chiu, C.-H. Cheng, R. D. Murch, and C. R. Rowell, "Reduction of mutual coupling between closely-packed antenna elements," *IEEE Transactions on Antennas and Propagation*, vol. 55, no. 6, pp. 1732–1738, 2007.

# CHAPTER 2

# INTERFEROMETRIC DIRECTION FINDING WITH A METAMATERIAL DETECTOR

This chapter, in full, has been published in Applied Physics Letters, **103**, 254103 (2013), with authors Suresh Venkatesh, David Shrekenhamer, Wangren Xu, Sameer Sonkusale, Willie Padilla, and David Schurig. (reprinted with permission)

## 2.1 Abstract

We present measurements and analysis demonstrating useful direction finding of sources in the S band (2-4 GHz) using a metamaterial detector. An augmented metamaterial absorber that supports magnitude and phase measurement of the incident electric field, within each unit cell, is described. The metamaterial is implemented in a commercial printed circuit board process with off-board back-end electronics. We also discuss on-board back-end implementation strategies. Direction finding performance is analyzed for the fabricated metamaterial detector using simulated data and the standard algorithm, MUtiple SIgnal Classification (MUSIC). The performance of this complete system is characterized by its angular resolution as a function of radiation density at the detector. Sources with power outputs typical of mobile communication devices can be resolved at kilometer distances with sub-degree resolution and high frame rates.

## 2.2 Letter

The metamaterial concept enables the implementation of structures with desired material properties through the design of the elemental units that comprise them [1]. The collection of elemental units, or unit cells, exhibit an average behavior which can be understood through effective medium theory [2]. A very powerful feature of this concept is the wide range of length scales at which one can design the unit cells, within the requirement that the simplest (and most useful) average behavior will arise when they are small compared

to the operational wavelength [3, 4]. At gigahertz frequencies, where the unit cells can be on the millimeter scale, one can bring to bear the arsenal of micro-electronics within the unit cell itself. One can then design a medium with desired material properties, but with the added ability to sense, excite or tune the individual unit cells in an addressable manner. In a traditional material, such microscopically local interactivity is generally not practical. This convenience of scale opens up a unique design methodology wherein the medium is the device. One can always implement the desired functionality with a more traditional design strategy, but the "medium-as-device" approach will usually lead to a different implementation with different and possibly preferred performance trade-offs.

There have been several applications of this methodology in the literature, including metamaterials that provide gain [5], non-linear phenomena [6], beam steering [7], and recently, focal plane array imaging [8]. In this article we describe additional functionality for a device previously used as a focal plane array. We have replaced the power detecting back end with a vector measurement. The resulting vector array can perform useful sensing tasks without the use of a focusing element. A sensing task of interest in the gigahertz range is source direction finding.

For both amplitude and phase sensing mediums, a desirable base is the perfect absorber, i.e. a thin or two dimensional medium that is perfectly matched to free space, resulting in minimal reflection over a range of incidence angles. Reflection minimization helps maximize the detected power and minimize the device's observability at operational frequencies. To incorporate sensing into the medium, the unit cells are adapted so that the power absorbed by the medium is dissipated in the input resistance of a low noise amplifier mounted within the unit cell area. Additional electronics implement either an intensity or vector measurement.

In this article we describe direction finding measurements performed with our existing device medium, where the vector measurements are performed off-board with a lock-in amplifier, and unit-cell (pixel) addressing is achieved by manually connecting coaxial cables to ports on the unit-cell back-side. We also discuss the performance of an integrated device, with in-unit-cell mixing. This avoids the routing of high frequency signals from the detector to the off board back-end electronics, as these high frequency signals are more prone to amplitude and phase distortions. Here, performance measures are determined

using the existing mediums geometry and matching capability, together with proposed integrated measurement electronics, and with signals processed using the well known MUSIC algorithm.

The detector consists of 11 x 11 electrically coupled LC resonators (ELC) arranged in a square lattice. These ELCs form the front end elements and are designed to have a surface impedance that matches free space, thus acting as a perfect absorber [9, 10]. Instead of absorbing the incident RF radiation and dissipating it in the metamaterial structure, one can tap electromagnetic energy through vias and process it with conventional electronics as described later in the article. The array of ELCs were patterned on Rogers 4003 substrate; Fig. 2.1 shows one of the pixels and its corresponding back-end electronics. Free space measurements of the center pixel were carried out in an anechoic chamber to measure reflection (S33) and transmission (S31) coefficients. We used an HP8510B 2-port vector network analyzer (VNA) with one port connected to a double ridge horn antenna (port1) and the other connected to the unbalanced signal output of balun on the pixel (port3, see Fig. 2.1(b,c)) to measure the S-parameters. Neighboring pixels in the array were terminated with a 50 ohm impedance at their respective balun end. The array was placed in the far field of the radiating horn, about $\sim$1.75 m away. The S33 showed a clear dip around 2.5 GHz (-33 dB) with a noticeable peak in S31 (-2 dB) at the same frequency. Characterization of S11 was not possible with the our experimental setup, but simulations indicate that S33 is a reasonable approximation of S11. Mutual coupling between the adjacent pixels was found to be less than -14 dB. Maintaining low inter pixel coupling is necessary especially in a densely packed array as it can hamper the interferometric or beam-forming measurements. A detailed discussion on the unit cell design, fabrication and characterization has been presented in our earlier article [8].

The correlative interferometry configuration consists of a dual channel receiver that simultaneously processes signals from any two pixels in the array. The RF signals from the two pixels are directly tapped after the balun and fed to the receiver. The primary channel (blue) in the receiver always acts as a phase reference. The signal from the center pixel was chosen for this purpose. Only the signal from the primary/phase reference channel is amplified with a high gain low noise RF amplifier. Later, both the signals are directly down converted to baseband (DC - 100 kHz) using passive RF mixers with a common local

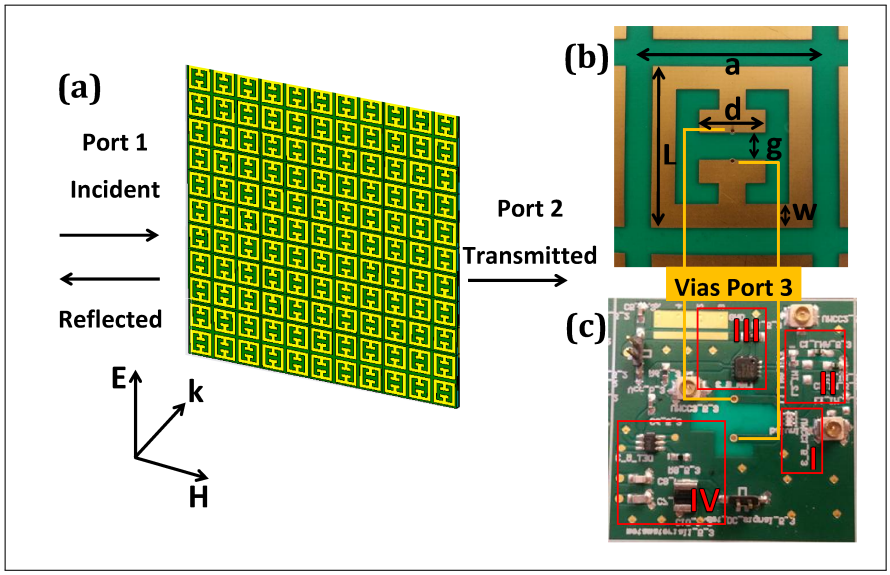


**Figure 2.1**: (a) 11 × 11 ELC resonator array which form the metamaterial detector. (b) one of the ELCs in the fabricated array with a = 27.3, L = 24, w = 3.5, d = 10, and g = 4 (units in mm). (c) back plane of the fabricated pcb showing (I) balun, (II) impedance matching circuit, (III) low noise amplifier and (IV) microwave log power detector. The rest of the circuitry after balun was bypassed through a microSMA to an off-board back-end for this experiment.

oscillator (LO). (A common LO is essential in order to maintain coherence between the two signals). These down converted signals are then filtered with low pass filters (LPF) and fed to the lock-in amplifier which acts as an analog correlator. Correlation coefficients with the center pixel and other test pixels are recorded by manually connecting the secondary channel (red) to the respective test pixel. Figure 2.2(a) shows the dual channel receiver.

For a demonstration of direction finding, the detector was tilted with respect to the horn antenna, so that the horn appeared to be a source at an angle of 45° to the detector normal. By this approach a uniform phase gradient was established along the detector in the horizontal direction. Using the interferometric receiver described in the previous paragraph, correlations of the central horizontal strip of pixels with the phase reference pixel were manually recorded. Figure 2.2(b) shows the measured phase variation by making eight correlation measurements along with the linear regression fit to the measured data. The measurements of the edge pixels were justifiably removed from the data, and did not match the slope of the remaining points. This deviation is likely due to diffraction effects at the edges and the absence of a complete set of nearest neighbors [11]. For the plane

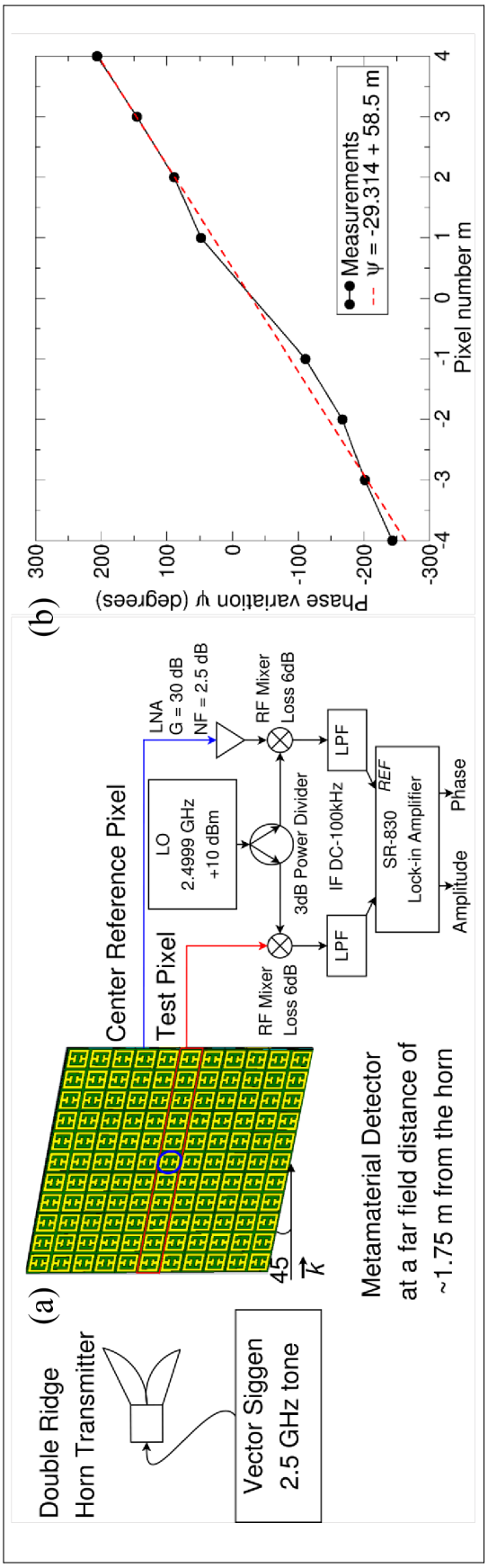


**Figure 2.2**: a) system architecture of correlative interferometry dual channel receiver. b) measured phase variation across the central horizontal line of pixels with respect to the reference pixel for incident wavefronts at 45°(black dotted) and linear regression fit to the measured data (red dashed).

wave $\mathbf{E} = \mathbf{E}_0\, e^{i\,\mathbf{k}\cdot\mathbf{r}} = \mathbf{E}_0\, e^{i\,\psi}$, the phase variation $\psi$ and the direction of arrival (DOA) of the wavefront $\phi$ are related by,

$$\psi\,(\mathbf{r}) = \mathbf{k}\cdot\mathbf{r} + \psi_0 \tag{2.1}$$

$$\psi_m = \sin\,(\phi)\;\; k\,a\,m + \psi_0 \tag{2.2}$$

$$\Delta\psi = \psi_{m+1} - \psi_m = \sin\,(\phi)\;\; k\,a \tag{2.3}$$

where $\mathbf{k}$ is the wave vector with $k$ = $2\pi/\lambda$, $\lambda$ is the operating wavelength = 0.12 m, $m$ is the pixel number on the detector, and $a$ is the unit-cell dimension = 27.3 mm. From linear regression, the phase interval $\Delta\psi$ is $58.5^\circ \pm 1.1^\circ$, and the predicted source direction is $45.6^\circ \pm 1.1^\circ$, in agreement with the experimentally configured angle. The uncertainty in the DOA $\Delta\phi$, depends inversely on the signal to noise ratio (SNR), the square root of number of correlations and the effective area of the detector.

The MUSIC algorithm is a DOA estimation technique first proposed by Schmidt [12]. The algorithm provides an unbiased estimate of the number of signals, their DOA and their strength, by exploiting the noise subspace of the input covariance matrix [12]. Conventional interferometry is a special case of MUSIC [12, 13]. The mathematical model of the 2D MUSIC algorithm is explained below.

Consider an N×N planar array in the $zy$ plane, where $x = r\sin\,(\theta)\cos\,(\phi), y = r\sin\,(\theta)\sin\,(\phi)$, $z = r\cos\,(\theta)$ and $(r, \theta, \phi)$ denotes the usual spherical coordinate system with $r \geq 0$, $0^\circ \leq \theta \leq 180^\circ$ and $-180^\circ \leq \phi \leq 180^\circ$. Let K signals $[S_1\,(t)\,, S_2\,(t)\,, ....,\, S_K\,(t)]$ be incident on the array at angles $[(\phi_1, \theta_1)\,;\,(\phi_2, \theta_2)\,;\,....;\,(\phi_K, \theta_K)]$ where $(\phi_k, \theta_k)$ is the azimuth and elevation angle of the $k^{th}$ signal. Let $S_k\,(t) = Re\left[e^{i\,2\pi f_c t}\right]$, where each $S_k\,(t)$ contains at least $2f_c\tau = P$ independent samples, $f_c$ is the frequency of the signal, and $\tau$ is the system integration time.

The received signal at the $m^{th}$ pixel, at time = $t$ can be written as,

$$X_m\,(t) = \sum_{k=1}^{K} A_m\,(\phi_k, \theta_k)\,S_k\,(t) + \nu\,(t) \tag{2.4}$$

$$\mathbf{X} = [X_1\,(n)\,, X_2\,(n)\,, ....,\, X_{N^2}\,(n)]^T \tag{2.5}$$

where, $A_m\,(\phi_k, \theta_k)$ is the time delay or phase factor for a signal incident at an angle $(\phi_k, \theta_k)$ on the $m^{th}$ pixel, $\nu\,(t)$ is the noise function with zero mean and variance = $\sigma^2$, $n = [0, 1, ..., P-1]$

is the discrete time index, and $\mathbf{X}$ is a data matrix of size $N^2 \times P$.

The input covariance matrix $\mathbf{R}$ can be constructed as,

$$\mathbf{R} = \mathbf{X}\,\mathbf{X}^{\dagger} \tag{2.6}$$

where, $\mathbf{R}$ is a square matrix of size $N^2 \times N^2$. Eigen value decomposition of $\mathbf{R}$ leads to,

$$\mathbf{R} = \mathbf{E}_s \mathbf{\Lambda}_s \mathbf{E}_s^{\dagger} + \mathbf{E}_n \mathbf{\Lambda}_n \mathbf{E}_n^{\dagger} \tag{2.7}$$

where, $\mathbf{E}_s = \begin{bmatrix} e_1 & e_2 & .... & e_K \end{bmatrix}$ is the eigen signal space, $\mathbf{E}_n = \begin{bmatrix} e_{K+1} & e_{K+2} & .... & e_{N^2} \end{bmatrix}$ is the eigen noise space and $\mathbf{\Lambda} = \begin{bmatrix} \Lambda_1 & \Lambda_2 & .... & \Lambda_{N^2} \end{bmatrix}$ are the eigenvalues. The full rank of the matrix $\mathbf{R}$ is K, where K is the number of eigenvalues that fall above certain threshold (K is also the number of incident signals at the array). These are called the signal eigenvalues, and the remaining eigenvalues are called the noise eigenvalues. One needs to note that in case of incident signals that are coherent, the rank of the matrix $\mathbf{R} = 1 < K$, leading to the deteriorated performance of the MUSIC algorithm. One can overcome this problem by non-uniformly sampling at each pixel [14] or by spatial smoothing techniques [15].

The MUSIC pseudospectrum is calculated as,

$$P_M(\phi, \theta) = \frac{1}{|\mathbf{A}(\phi, \theta)^{\dagger}\ \mathbf{E}_n \mathbf{E}_n^{\dagger}\ \mathbf{A}(\phi, \theta)|} \tag{2.8}$$

where, $\mathbf{A}(\phi, \theta)$ is the array factor for any given $(\phi, \theta)$ and any significant peaks in the pseudospectrum denote the DOA of incident signals.

We demonstrate the working of this algorithm for the current metamaterial detector properties: $N = 11$ with uniform pixel weighting, pixel spacing of 27.3 mm and frequency of operation $f_c = 2.5$ GHz. Figure 2.3(a) shows the pseudospectrum of MUSIC algorithm for eight signals with arbitrarily chosen directions of incidence. The '+' markers in the figure show the actual DOA of eight signals. Each signal has an input SNR = 0 dB and is sampled at the Nyquist rate ($f_s = 2f_c$) with P = 512 samples. The noticeable peaks of the pseudospectrum coincide with the markers, demonstrating the working of this algorithm for the current detector parameters.

Figure 2.3(b) shows the performance of conventional beam-forming method for the same input parameters as above. In beam-forming, one constructs a primary narrow beam from individual pixels of the array operating in interferometric mode. This single

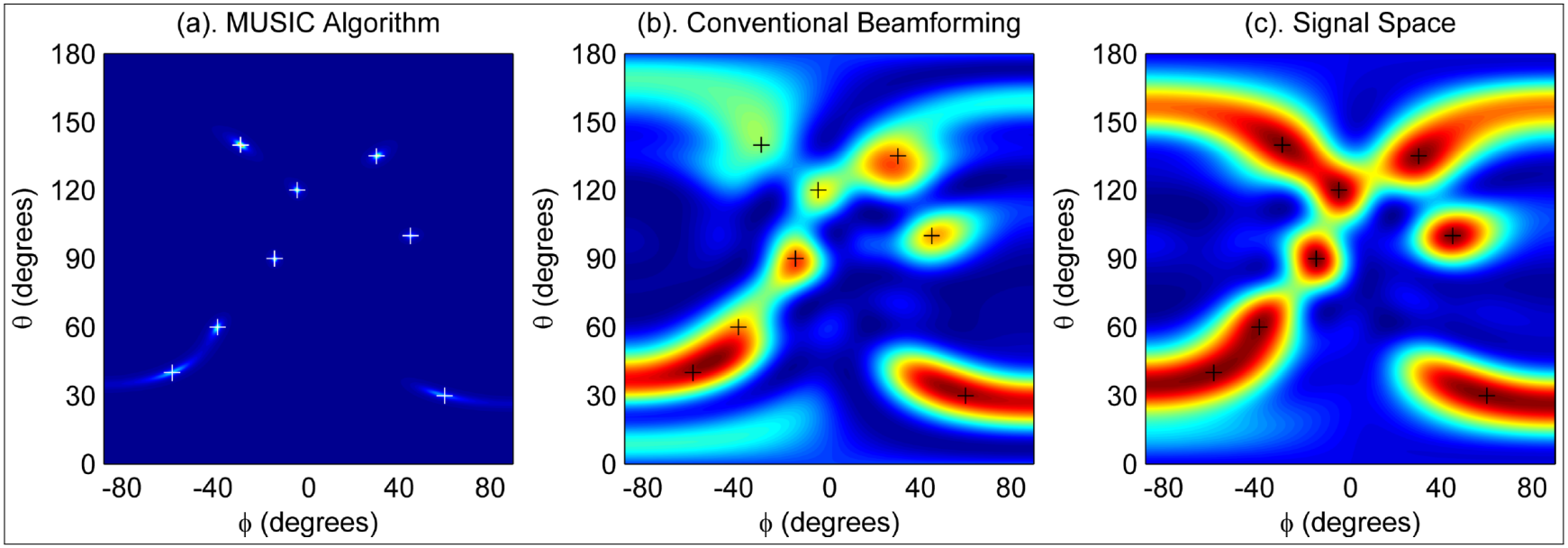


**Figure 2.3**: Direction finding using MUSIC algorithm. a) shows the normalized MUSIC pseudospectrum. b) & c) show the conventional beam-forming method and signal space method on the same incident signals. (8 incident signals with the following (azimuth, elevation) angles (-60°, 40°), (-40°, 60°), (-30°, 140°), (-15°, 90°), (-5°, 120°), (30°, 135°), (45°, 100°), (60°, 30°). Each signal SNR = 0 dB, P= 512 samples).

narrow beam can be spatially scanned (weighting each pixel with appropriate delay and summing) to measure the power received from each direction. The direction at which the received power is maximum is the DOA estimate. The received power pattern can be calculated as,

$$P_B(\phi,\theta) = |\mathbf{A}(\phi,\theta)^{\dagger}\ \mathbf{R}\,\mathbf{A}(\phi,\theta)| \tag{2.9}$$

where, $\mathbf{R}$ is the input covariance matrix in (2.6). The primary -3 dB beamwidth using this technique is $\sim \lambda/D$ which is the conventional Abbe's limit, where $\lambda$ is the operating wavelength and $D$ is the largest baseline. The beam-forming method has substandard performance when compared with the MUSIC algorithm.

Instead of constructing the pseudospectrum based on the noise space, one can do the inverse by constructing the pseudospectrum based on the signal space. The pseudospectrum based on the signal space is given by,

$$P_S(\phi,\theta) = |\mathbf{A}(\phi,\theta)^{\dagger}\ \mathbf{E}_s\mathbf{E}_s^{\dagger}\,\mathbf{A}(\phi,\theta)| \tag{2.10}$$

The MUSIC algorithm based on the noise space again performs better in terms of the resolving power as compared with the signal space method shown in Fig. 2.3(c).

To implement DOA estimation using MUSIC with the current metamaterial detector configuration, requires discretized time domain samples from each pixel. These samples should be of high fidelity and also have high SNR. Figure 2.4(a) shows a system level architecture for the back-end. The back-end electronics consist of on-board down converting stage for each pixel and an off-board sampling stage, comprised of commercial off-the-shelf components. The on-board system consists of a matching stage and a heterodyne stage. The heterodyne stage has a high-gain-low noise S-band amplifier whose output is filtered by a narrow bandpass surface acoustic wave filter. Then the filtered RF signal is down converted by an active mixer to baseband (DC - 8 MHz). Footprints of all these components are small enough to be mounted on the back plane within each pixel. The down converted signal is then sampled by an off-board sampling stage which consists of an LPF and an analog to digital converter (ADC). The ADC is chosen to have a sampling rate of 16 Msamples/second and an integration time of 1 ms, therefore collecting 16k samples from each pixel. The sampling of each pixel output happens in a time division multiplexed (TDM) fashion in order to reduce the complexity. The digital data from each

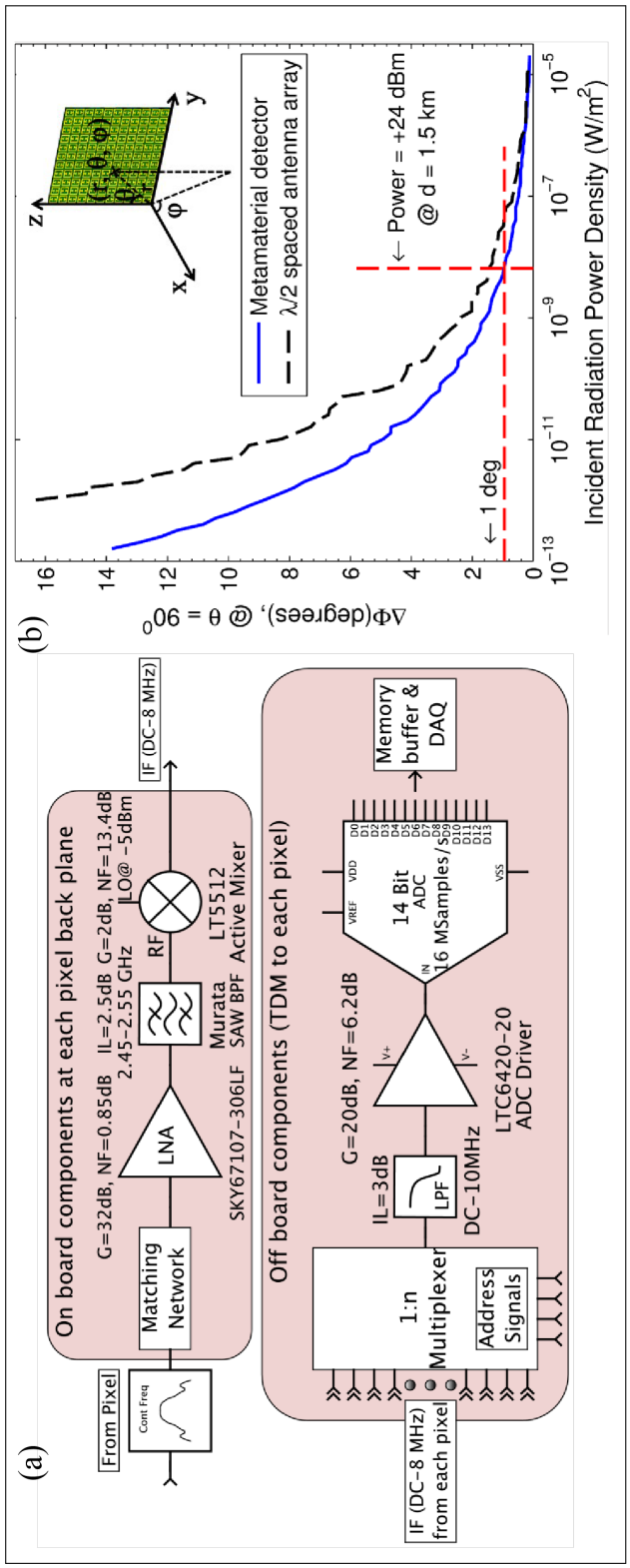


**Figure 2.4**: a) proposed system architecture for implementation of MUSIC. b) angular resolution versus incident radiation power density with the proposed back-end architecture.

pixel should be phase adjusted for the multiplexing time delay and processed to form the MUSIC pseudospectrum. For this configuration the pseudospectrum can be generated at frame rates of $\sim$100 ms. The calculated overall noise figure of this receiver chain is about 2.5 dB.

The device's resolving power with the proposed back-end architecture was analyzed. The azimuthal separation between two sources (of equal amplitude and near normal incidence $\theta = 90^{\circ}$) was decreased until no local minimum of the MUSIC psuedospectrum was observed between them. Figure 2.4(b) shows the angular resolution for a given incident radiation density at the device (blue curve). Sources with power outputs typical of mobile/wireless devices (about +24 dBm) can potentially be resolved at a kilometer distance away with sub-degree resolution. This metric was also analyzed for a traditional $\lambda/2$ spaced antenna array with the same aperture area (Fig. 2.4(b) black dashed curve). The metamaterial detector out performs the traditional array at low SNRs. Such RF direction finders can find potential applications in detecting RF interference sources in radio astronomy, remote sensing, radio monitoring and imaging applications.

## 2.3 Supplementary Material: Edge Diffraction Effects

Simulations were performed to understand the effects of edge diffraction and the absence of a complete set of nearest neighbors. Figure 2.5 shows this effect and the change in S31 phase is $\sim$20 degrees at the designed frequency.

## 2.4 Acknowledgments

Suresh Venkatesh would like to acknowledge Prof. Ajay Nahata, Prof. Cynthia Furse and Prof. Neal Patwari for lending some of the measurement instruments used in the experiment and Prof. John Mathews for helpful conversations about the MUSIC algorithm. Suresh Venkatesh would also like to acknowledge Alex Orange for fabricating a mount for the detector. This research was supported in part by the Army Research Office through Multidisciplinary University Research Initiative under Grant No. W911NF-09-1-0539, the Office of Naval Research under U.S. Navy Contract No. N00014-07-1-0819, the Department of Energy under Grant No. DESC0005240, and the National Science Foundation under Grant No. ECCS-1002340.

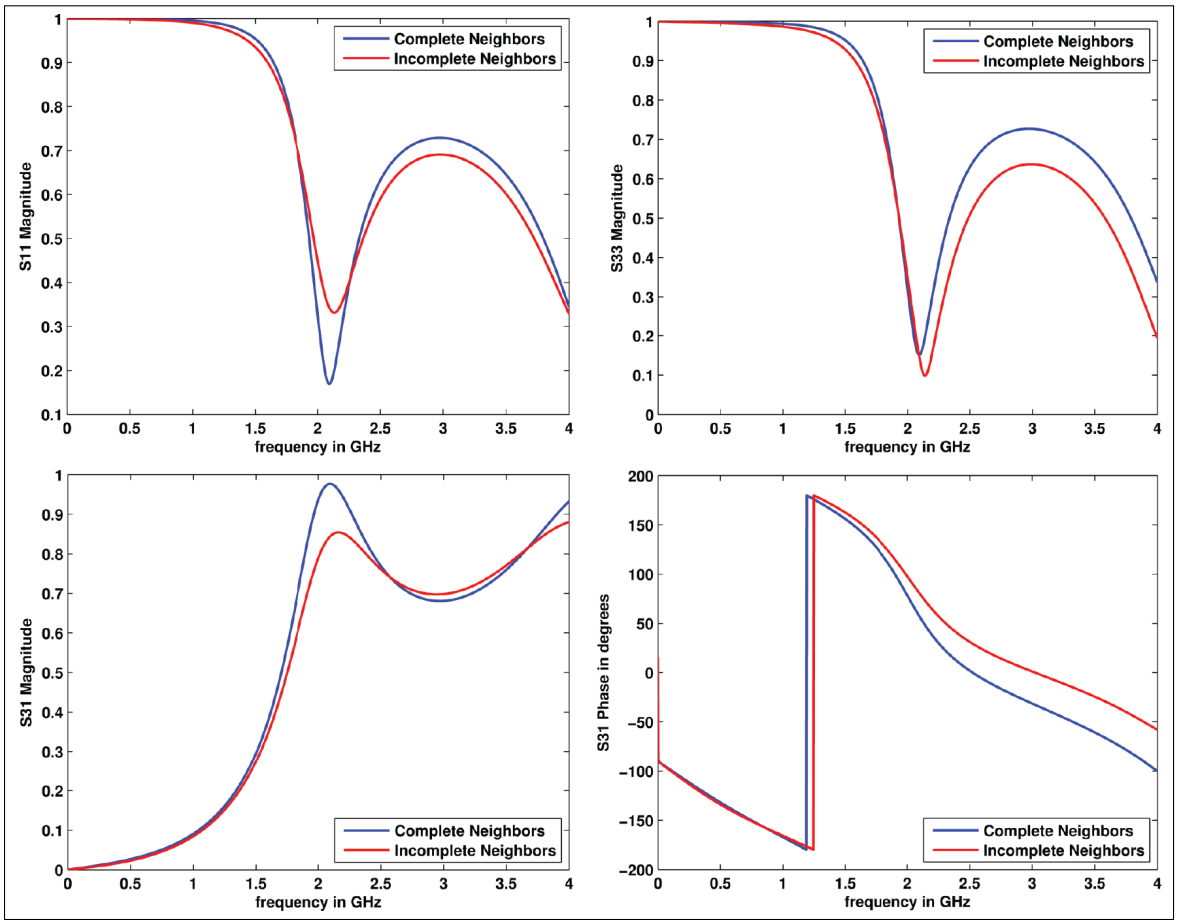


**Figure 2.5**: Simulations showing the effect of edge diffraction and the absence of a complete set of neighbors.

## 2.5 References

[1] D. R. Smith, J. B. Pendry, and M. C. K. Wiltshire, "Metamaterials and negative refractive index," *Science*, vol. 305, no. 5685, pp. 788–792, 2004.

[2] D. R. Smith, S. Schultz, P. Markoš, and C. M. Soukoulis, "Determination of effective permittivity and permeability of metamaterials from reflection and transmission coefficients," *Phys. Rev. B*, vol. 65, p. 195104, Apr 2002.

[3] V. M. Shalaev, W. Cai, U. K. Chettiar, H.-K. Yuan, A. K. Sarychev, V. P. Drachev, and A. V. Kildishev, "Negative index of refraction in optical metamaterials," *Opt. Lett.*, vol. 30, no. 24, pp. 3356–3358, Dec 2005.

[4] M. C. K. Wiltshire, "Radio frequency (rf) metamaterials," *physica status solidi (b)*, vol. 244, no. 4, pp. 1227–1236, 2007.

[5] B.-I. Popa and S. A. Cummer, "An architecture for active metamaterial particles and experimental validation at rf," *Microwave and Optical Technology Letters*, vol. 49, no. 10, pp. 2574–2577, 2007.

[6] A. Rose, D. Huang, and D. R. Smith, "Controlling the second harmonic in a phase-matched negative-index metamaterial," *Phys. Rev. Lett.*, vol. 107, p. 063902, Aug 2011.

[7] J. Hunt, N. Kundtz, B. Sun, and D. R. Smith, "Transformation optics compressed rotman lens implemented with complementary metamaterials," pp. 80 210–80 210–7, 2011.

[8] D. Shrekenhamer, W. Xu, S. Venkatesh, D. Schurig, S. Sonkusale, and W. J. Padilla, "Experimental realization of a metamaterial detector focal plane array," *Phys. Rev. Lett.*, vol. 109, p. 177401, Oct 2012.

[9] D. Schurig, J. J. Mock, and D. R. Smith, "Electric-field-coupled resonators for negative permittivity metamaterials," *Applied Physics Letters*, vol. 88, no. 4, 2006.

[10] N. I. Landy, S. Sajuyigbe, J. J. Mock, D. R. Smith, and W. J. Padilla, "Perfect metamaterial absorber," *Phys. Rev. Lett.*, vol. 100, p. 207402, May 2008.

[11] See supplementary material for the simulation on unit cells with and without neighboring pixels.

[12] R. Schmidt, "Multiple emitter location and signal parameter estimation," *IEEE Transactions on Antennas and Propagation*, vol. 34, no. 3, pp. 276–280, Mar 1986.

[13] G. Hislop and C. Craeye, "On the mathematical link between the music algorithm and interferometric imaging," *IEEE Transactions on Antennas and Propagation*, vol. 59, no. 4, pp. 1412–1414, April 2011.

[14] A. Li and S. Wang, "Performance of nonuniform sampled signal with music algorithm," in *Intelligent Control and Automation, 2008. WCICA 2008. 7th World Congress on*. IEEE, 2008, pp. 3560–3563.

[15] W. Du and R. L. Kirlin, "Improved spatial smoothing techniques for doa estimation of coherent signals," *IEEE Trans. Signal Process.*, vol. 39, no. 5, pp. 1208–1210, May 1991.

# CHAPTER 3

# TRANSFORMATION OPTICS DESIGN OF A PLANAR NEAR FIELD MAGNIFIER FOR SUBDIFFRACTION IMAGING

This chapter, in full, will be submitted for publication, with authors Suresh Venkatesh and David Schurig.

## 3.1 Abstract

It is well known that imaging systems with either isotropic negative index or hyperbolic (indefinite) media under certain conditions can achieve super-resolution. However, achieving subdiffraction limited imaging along with uniform aberration-free magnification can be challenging. In this article, we design, simulate, and evaluate the performance of planar near-field magnifier lenses capable of achieving super-resolution based on transformation optics design principles. Specifically, we use a grid-relaxed transformation that results in material properties that are more amenable to implementation. We discuss the possible design choices in terms of material properties, adverse effect of loss tangent on such magnifier, the effect of magnification factor, and other design constraints that are associated with such magnifying super-resolution lenses. We also present a complete 3D simulation of a planar near-field magnifier (with magnification = $3\times$) based on cylindrical harmonic decomposition and 2.5D technique and evaluate its imaging performance with a standard resolution target. We investigate and propose a potential path to achieve higher magnification factors using transformation optics design.

## 3.2 Introduction

Near-field magnifiers (NFM), also known as hyper-lenses, are imaging elements or devices that preserve subdiffraction-limit image detail while simultaneously providing image magnification. In so doing, these devices allow image spatial information that

lies well below the length scale of the operational wavelength, to be projected into the far-field, where traditional cameras and capture methods can then be employed. Though the functionality is probably not as compelling, one can also operate in reduction mode to generate subdiffraction-limit illumination patterns from masks, or other pattern generators that do not possess sub-wavelength features. Thus, near-field magnification is one method by which the diffraction limit, Abbe limit, or Rayleigh criterion may be circumvented. Another family of such methods are the near-field scanning methods. The primary advantage of the NFM is that, combined with a traditional camera (with a standard resolution image sensor), parallel acquisition of image pixel data may be achieved without the need for mechanical motion control, whereas with scanning methods, image pixels are acquired sequentially (at least to some degree). Both methods can be combined with a perfect lens element (or its variants) to provide a limited amount of free-space (or free-medium) working distance, though such facility will not be discussed here. The primary disadvantages of near-field magnification, as compared to scanning methods, are bandwidth limitations, and design and implementation complexity. The bandwidth limitations are intrinsic to the negative material properties required for preservation of sub-diffraction image information. Such materials are necessarily frequency dispersive for quite fundamental reasons. However, design and implementation complexity are probably the limiting factors for current development work. In this article we address the design of material specifications for near-field magnifiers that would be of practical use, that is, providing: useful levels of magnification, planar image and object planes, and aberration-free images. The implementation of such material specifications requires metamaterial design sophistication that is possible, though still rarely seen. Another performance factor we discuss is insertion loss of the device. Here we analyze device performance with realistically achievable material loss tangents. Low insertion loss may be important for some applications, and is probably useful in comparing near-field magnification devices to each other, however, it is not a significant disadvantage as compared to scanning methods, where illumination throughput can be quite low.

The most popular design variant of magnifying optical hyper-lens involves alternating layers of positive and negative index medium (Ag and $Al_2O_3$ layers) on a half cylindrical cavity [1]. One disadvantage in such a curved cavity design is that the image plane is

curved and the magnification factor is nonuniform on this curved surface [1–5]. Curved image plane hyper-lenses are extremely hard to interface with flat focal plane arrays or detectors. Different strategies have been discussed in the literature to achieve planar image plane [6,7]. However, these designs again lead to nonuniform magnifications on the planar surface along with higher order aberrations. Apart from electromagnetic implementations, there have been designs and demonstrations of similar curved image plane acoustic counterparts [8, 9]. In this article we propose a hyperlens design with planar object and image plane based on transformation design. The design we propose is aberration free and provides uniform magnification along the image plane. We also propose strategies to achieve higher magnification factors.

## 3.3 Isotropic Negative Index versus Hyperbolic Anisotropic Bilayer

A symmetric perfect lens slab of thickness d, first conceptualized by Pendry [10], consists of a vacuum layer of thickness d/2 and an isotropic negative index (antivacuum) layer of thickness d/2. Such a medium behaves as a *perfect lens* by transporting both the propagating and nonpropagating (evanescent modes) spatial Fourier components from the object plane to the image plane, if and only if the losses in the layers are minimal. The nonpropagating modes in a vacuum are converted into exponentially growing waves inside the negative index layer which help in restoring these modes effectively at the image plane. However, transmission characteristics, and in turn the perfect lensing property of an isotropic negative refractive index lens, degrades dramatically with the introduction of finite losses in the material [11]. This has led to the investigation of other kinds of media specifically for sub-diffraction imaging. One such is a hyperbolic medium.

Hyperbolic or indefinite bilayer slab consists of anisotropic materials whose principal diagonal components of permittivity and permeability tensors do not have the same sign. One simple example of a hyperbolic bilayer of thickness d = $z_1 + z_2$ comprises of one layer of thickness $z_1$ with material properties $\epsilon_1 = \mu_1$, followed by another layer of thickness $z_2$ with properties $\epsilon_2 = \mu_2$, where $\epsilon_1, \mu_1, \epsilon_2, \mu_2$ are of the form;

$$\epsilon_1 = \mu_1 = \begin{bmatrix} + & 0 & 0 \\ 0 & + & 0 \\ 0 & 0 & - \end{bmatrix}, \quad \epsilon_2 = \mu_2 = \begin{bmatrix} - & 0 & 0 \\ 0 & - & 0 \\ 0 & 0 & + \end{bmatrix} \tag{3.1}$$

Such anisotropic materials have an unique never cut-off dispersion relation, $k_z = \pm\sqrt{k_0^2 + k_x^2}$, for a plane wave $\mathbf{E} = \hat{\mathbf{y}} e^{[i(k_x x + k_z z - \omega t)]}$ which is hyperbolic in nature, as shown in Fig. 3.1. Such a medium supports propagating waves for all transverse wave vectors. Hyperbolic bilayers, unlike the perfect lens configuration, is less susceptible to losses [12, 13]. Hence they are viable and attractive candidates for unconventional lenses that perform sub-diffraction imaging. However, one major disadvantage of such hyperbolic material configurations is the absence of free space working distance which is inherently present in a perfect lens.

The effect of losses in such configurations can be analyzed using a transfer matrix approach. The general transfer matrix $\mathbf{M}$, for an S-polarized plane wave $\mathbf{E} = \hat{\mathbf{y}} e^{[i(k_x x + k_z z - \omega t)]}$ incident on a 2D slab of thickness $z_0$ with permittivity $\epsilon$ and permeability $\mu$ tensors (in Cartesian coordinates) is given by,

$$\mathbf{M} = \begin{bmatrix} \alpha - \beta\zeta_+ & -\beta\zeta_- \\ \beta\zeta_- & \alpha + \beta\zeta_+ \end{bmatrix} \tag{3.2}$$

where,

$$\epsilon = \begin{bmatrix} \epsilon_x & 0 & 0 \\ 0 & \epsilon_y & 0 \\ 0 & 0 & \epsilon_z \end{bmatrix}, \; \mu = \begin{bmatrix} \mu_x & 0 & 0 \\ 0 & \mu_y & 0 \\ 0 & 0 & \mu_z \end{bmatrix}$$

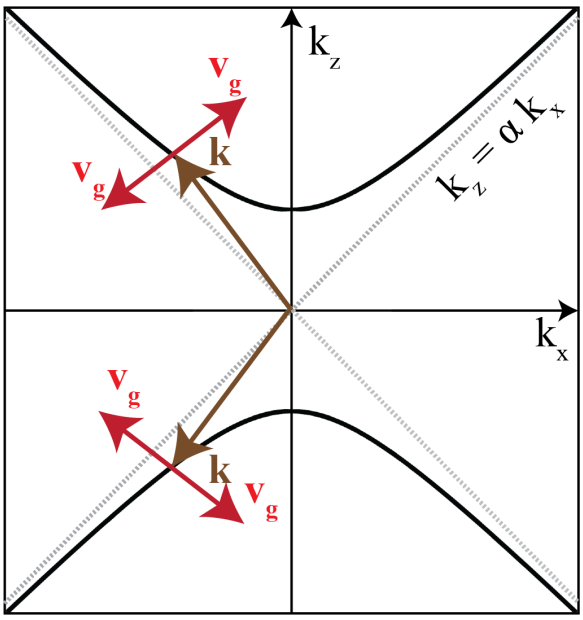


**Figure 3.1**: The hyperbolic dispersion curve of anisotropic hyperbolic media. Two possible $k_z$ components are shown for the same $k_x$ component. The z components of $\mathbf{k}$ and $\mathbf{v}_g$ can be of the same or opposite sign.

$$\alpha = \cos(p_z z_0), \;\; \beta = i\sin(p_z z_0),$$
$$\zeta_{\pm} = \frac{1}{2}\left(\frac{p_z}{\mu_x k_z} \pm \frac{\mu_x k_z}{p_z}\right)$$

and the z-components of wave vectors are given by,

$$k_z = \pm\sqrt{k_0^2 - k_x^2}\,, \;\; k_0 = \omega/c$$
$$p_z = \pm\sqrt{\epsilon_y \mu_x k_0^2 - \frac{\mu_x}{\mu_z}k_x^2}$$

From a given transfer matrix $\mathbf{M}$ one can derive the transmission ($\tau$) and reflection coefficient ($\rho$) as,

$$\tau = \frac{1}{M_{11}} \;\text{ and }\; \rho = \frac{M_{21}}{M_{11}} \tag{3.3}$$

For a bilayer, the overall transfer matrix is the matrix product of individual transfer matrices $\mathbf{M}_1$ and $\mathbf{M}_2$ corresponding to each layer,

$$\mathbf{M} = \mathbf{M}_1\mathbf{M}_2 \tag{3.4}$$

From [12] , the transmission coefficient for a general bilayer with material tensors $(\epsilon_1, \mu_1)$ for layer 1 of thickness $d_1$ and $(\epsilon_2, \mu_2)$ for layer 2 of thickness $d_2$, with overall thickness $d = d_1 + d_2$ is given by,

$$\tau = 8\left[\begin{array}{l} e^{i(\phi+\psi)}(1-Z_0)(1+Z_1)(1-Z_2) + e^{i(\phi-\psi)}(1-Z_0)(1-Z_1)(1+Z_2) + \\ e^{-i(\phi-\psi)}(1+Z_0)(1-Z_1)(1-Z_2) + e^{-i(\phi+\psi)}(1+Z_0)(1+Z_1)(1+Z_2) \end{array}\right]^{-1} \tag{3.5}$$

where the z-components of wave vectors in the individual layer are similar to (3.3), given by,

$$p_z = \pm\sqrt{\epsilon_{1y}\mu_{1x}k_0^2 - \frac{\mu_{1x}}{\mu_{1z}}k_x^2}\,, \;\; q_z = \pm\sqrt{\epsilon_{2y}\mu_{2x}k_0^2 - \frac{\mu_{2x}}{\mu_{2z}}k_x^2}$$

the effective relative impedances are given by,

$$Z_0 = \frac{p_z}{\mu_{1x}k_z},\; Z_1 = \frac{\mu_{1x}q_z}{\mu_{2x}p_z},\; Z_2 = \frac{\mu_{2x}k_z}{q_z}$$

and individual layer phase advances are given by,

$$\phi = p_z d_1\,, \;\; \psi = q_z d_2$$

### 3.3.1 Case 1: Isotropic Free Space Compensated Bilayer

The material property tensors for this case are $\epsilon_1 = \mu_1 \Rightarrow \epsilon_{1x} = \epsilon_{1y} = \epsilon_{1z} = (1 + i\delta)$ for layer one and $\epsilon_2 = \mu_2 \Rightarrow \epsilon_{2x} = \epsilon_{2y} = \epsilon_{2z} = (-1 + i\delta)$ for layer two with $d_1 = d_2 = d/2$,

where $\delta$ is the loss tangent of the material. The transmission coefficient for this example can be found by plugging in the material property values in (3.5). The transfer matrix for this case can be denoted as,

$$\mathbf{M}_{[+++][---]} = \mathbf{M}_{1[+++]}\mathbf{M}_{2[---]} \tag{3.6}$$

where the subscript shows the sign of the diagonal components of the material property tensor (real part) for each individual layer.

### 3.3.2 Case 2: Anisotropic Hyperbolic Never Cut-off Bilayer

An example of material property tensors for this case are $\epsilon_1 = \mu_1 \Rightarrow \epsilon_{1x} = \epsilon_{1y} = (1 + i\delta), \epsilon_{1z} = (-1 + i\delta)$ for layer one and $\epsilon_2 = \mu_2 \Rightarrow \epsilon_{2x} = \epsilon_{2y} = (-1 + i\delta), \epsilon_{2z} = (1 + i\delta)$ for layer two with $d_1 = d_2 = d/2$, where $\delta$ is the loss tangent of the material. The transmission coefficient for this example can be found by plugging in the material property values in (3.5). The transfer matrix for this case can be denoted as,

$$\mathbf{M}_{[++-][--+]} = \mathbf{M}_{1[++-]}\mathbf{M}_{2[--+]} \tag{3.7}$$

where the subscript shows the sign of the diagonal components of material property tensor (real part) for each individual layer.

### 3.3.3 Case 3: Isotropic Free Space Compensated Multilayer

Suppose we consider a multilayer stack of alternating positive and negative refractive index, then the transfer matrix is just the matrix product of individual bilayer transfer matrices which are equal to one another. The transfer matrix of a single bilayer can be found from Case 1. If the multilayer comprises of N isotropic bilayers, such that each bilayer is of thickness $\Delta$, then the overall thickness $d = N\Delta$. The transfer matrix for this case can be written as,

$$\begin{aligned} \mathbf{M}_{multilayer} &= \mathbf{M}_{1[+++][---]}\mathbf{M}_{2[+++][---]}\cdots \\ &\cdots \mathbf{M}_{i[+++][---]}\cdots\mathbf{M}_{N[+++][---]} \\ &= \left[\mathbf{M}_{1[+++][---]}\right]^N \end{aligned} \tag{3.8}$$

Considering the interesting limiting case when $\Delta \to 0$ (which imples $N \to \infty$ as $N = d/\Delta$), (3.8) becomes,

$$\begin{aligned} \mathbf{M}_{multilayer} &= \lim_{\Delta \to 0} \left[ \mathbf{M}_{1[+++][---]} \right]^{d/\Delta} \\ &\equiv \mathbf{M}_{[++-][--+]} \end{aligned} \tag{3.9}$$

The above (3.9) implies that under the limiting condition, the multilayer isotropic case behaves exactly like a homogeneous anisotropic bilayer medium of equivalent total thickness d and having a loss tangent factor $\delta$.

The effect of loss tangent was studied comparatively for the above three cases. The loss tangent has a severe adverse effect on transmission magnitude of transverse spatial Fourier components when $k_x/k_0 > 1$ for Case 1 as compared to Case 2. However, the transmission magnitude improves drastically with the stacking of thin isotropic bilayers and approaches the anisotropic case under the limiting condition. This improved transmission is traded-off with the free space working distance. The transmission magnitude as a function of transverse wave vector is plotted for different cases in Fig. 3.2(f). Full-wave simulations were also performed for the three cases. The electric field norms for each case along with their respective configurations are shown in Fig. 3.2(a)-(e). In all these cases, a loss tangent of $\delta = 0.001$ is assumed. The anisotropic bilayer has a unique energy transport mechanism as shown in Fig. 3.2(d), which is due to the hyperbolic dispersion relationship. When $|k_x| \gg |k_0|$, $k_z \sim \pm k_x$; then the wave vector $\mathbf{k} = k_x\hat{\mathbf{x}} \pm k_z\hat{\mathbf{z}}$ can be written as $\mathbf{k} \sim k_x(\hat{\mathbf{x}} \pm \hat{\mathbf{z}})$. This is the reason for the waves emerging along sharp $\pm 45^\circ$ lines.

## 3.4 Design of Near Field-Magnifier

Transformation optics (TO) design is a concept based on a mathematical idea of coordinate transformations, which transforms an original space with certain material property tensors to a distorted space with new material property tensors [14]. As established in the previous section, an anisotropic hyperbolic bilayer performs better compared to a free space compensated bilayer for a given loss tangent. Hence, for a planar NFM, we start off from a simple rectangular anisotropic hyperbolic bilayer which is distorted appropriately to magnify the object at the image plane. The magnification factor M is achieved by stretching the image plane in the original undistorted space appropriately by a factor M. This magnification also increases the space-bandwidth product at the output plane by a factor of M, which could mean that some of the nonpropagating transverse vector components from the object plane can not only be magnified but can also be projected to

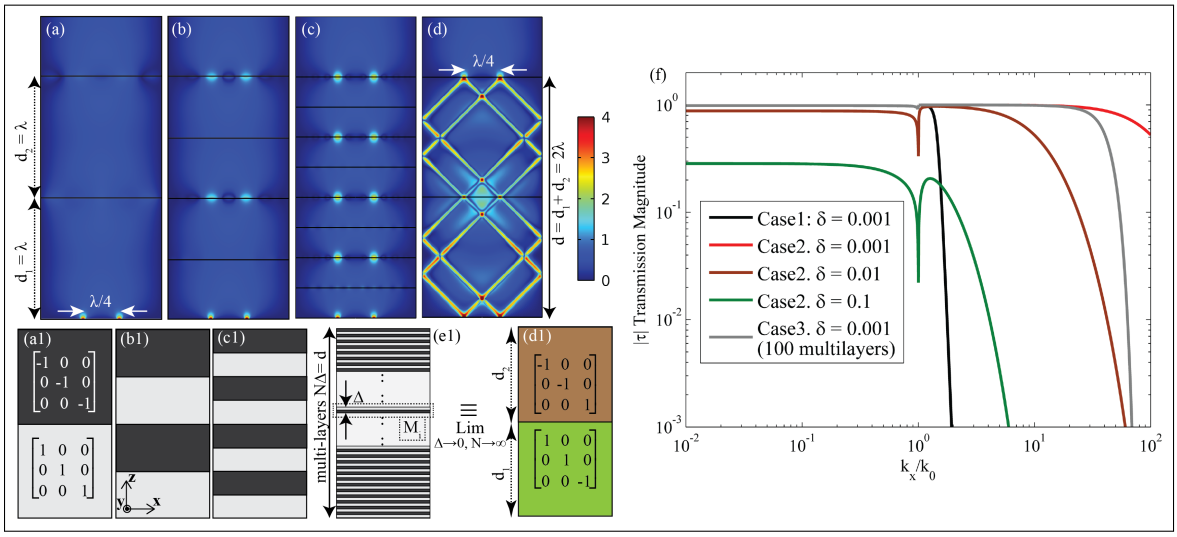


**Figure 3.2**: Shows the electric field norm for different configurations. (a & a1) shows the case of an isotropic free space compensated bilayer. (b & b1; c & c1) shows the case of isotropic free space compensated multilayer (4 and 8 respectively). The transmission magnitude increases with multilayering. (d & d1) shows the case of an anisotropic bilayer configuration and its equivalent limiting case of a multilayer configuration is shown in (e1). All these cases are simulated with two point sources separated by $\lambda/4$, with a loss tangent of $\delta = 0.001$ and an overall thickness $d = 2\lambda$. (f) shows the transmission magnitude $|\tau|$ as a function of transverse vector $k_x$ for different cases along with varying loss tangent. All the cases have an overall thickness of $d = 2\lambda$. Note: The transmission for Case 3 limiting condition exactly coincides with Case 2 plots for a given $\delta$. Hence they are not shown explicitly.

the far-field effectively using a conventional lens system. Thus an NFM plays a dual role in an imaging system.

Grid relaxation is a technique to generate conformal maps. Conformal maps are angle-preserving maps which change lengths in a transformed space but not the angles [15]. In other words, they preserve the grid cell aspect ratio in the transformed space. Such mappings are essential to generate more amenable material property tensors in the new distorted space [16]. In order to generate a relaxed grid for the magnifier, we start from a known nonorthogonal grid with a magnification factor M and the fixing of four boundary conditions in the transformed domain. We impose Neumann-Dirichlet or a slipping boundary on the right (which is shown in brown in Fig. 3.3) which satisfies the following orthogonality condition.

$$\frac{\partial \rho'}{\partial \rho}\frac{\partial \rho'}{\partial z} + \frac{\partial z'}{\partial \rho}\frac{\partial z'}{\partial z} = 0 \tag{3.10}$$

The choice of the boundary on the right (brown curve) affects the conformality of the

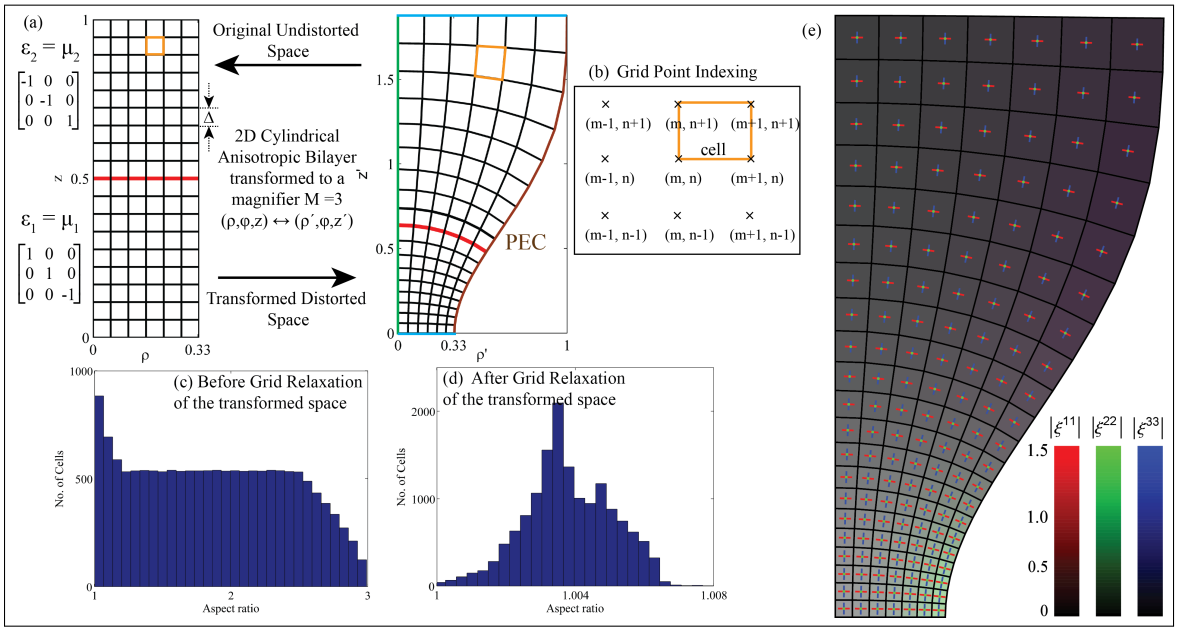


**Figure 3.3**: The overall harmonic grid relaxation procedure is shown. (a) shows the 2D cylindrical coordinate transformation $(\rho, \phi, z) \Rightarrow (\rho', \phi, z')$ of an anisotropic bilayer to a magnifier with a magnification factor of M = 3. The red line demarcates between the two layers which have different material propery tensor. The brown curve in the transformed space is the Neumann-Dirichlet boundary (slipping boundary). Blue and green lines indicate the Dirichlet boundaries. (b) shows a highlighted cell along with a central grid point and its nearest neighbors which are used in grid relaxation approach. An example grid cell is shown in orange box. (c) & (d) show the aspect ratio distributions of cells before and after grid relaxation of the transformed space. (e) shows the absolute principle components of the material property tensors represented in three color channels, namely: *red*, *green* and *blue*. The absolute principle values lie between 0.33 to 1.4 in the transformed domain. Different levels of gray indicate that the three absolute principle values are equal to one another and deviation from gray scale indicates that the *green* component has deviated from *red* and *blue* components. The principle directions are overlayed in the same figure. The *green* channel direction is out of plane and represents the $\phi$-component which is untransformed.

relaxed grid. We choose a smooth continuous function of the form,

$$\rho'_{m_{max},n} = \frac{1}{2M}\left[(M+1) + (M-1)\cos\left(\pi\left(1 - \frac{\tau_m}{h_0}\right)^{3/2}\right)\right] \tag{3.11}$$

$$z'_{m_{max},n} = \tau_m \tag{3.12}$$

where (m,n) are the grid point indexing numbers, $\tau_m$ is a relaxing parameter which maximizes the orthogonality condition at the slipping boundary, $h_0$ is the overall height of the magnifier, and M is the magnification factor. Dirichlet boundary conditions are also applied on top and bottom grid points ($\rho'_{m,0}$ and $\rho'_{m,n_{max}}$ are uniformly spaced along the

index $m$ and $z'_{m,0} = 0$ and $z'_{m,n_{max}} = h_0$), without which it could lead to image distortion. This boundary in Fig. 3.3(a) is shown in light blue color. At the left hand side, Dirichlet boundary conditions are applied only on $\rho'_{0,n}$ grid points and are set to zero. This boundary in Fig. 3.3(a) is shown in green color. We employ a trajectory method to generate an orthogonal grid using marching process as follows. On each relaxation iteration pass, the following operations are performed on each interior grid point [$\rho'_{m,n}$ , $z'_{m,n}$], namely (see Fig. 3.3 (a) and (b)),

$$\begin{aligned} \rho'_{m,n} &= \frac{1}{4}\left(\rho'_{m+1,n} + \rho'_{m-1,n} + \rho'_{m,n+1} + \rho'_{m,n-1}\right) \\ z'_{m,n} &= \frac{1}{4}\left(z'_{m+1,n} + z'_{m-1,n} + z'_{m,n+1} + z'_{m,n-1}\right) \end{aligned} \tag{3.13}$$

until convergence. The convergence criterion is based on the maximum difference between grid coordinates of consecutive iterations, $\kappa^{[\alpha]}$,

$$\kappa^{[\alpha]} = \max\left(|\rho'^{[\alpha]}_{m,n} - \rho'^{[\alpha-1]}_{m,n}|, |z'^{[\alpha]}_{m,n} - z'^{[\alpha-1]}_{m,n}|\right) \tag{3.14}$$

where the superscript $[\alpha]$ refers to the iteration number. The choice of $h_0$ affects the conformality of the relaxed grid and the height of NFM is approximately proportional to $\sqrt{\mathrm{M}}$. $h_0$ can also be optimized and relaxed on each convergence run based on the distribution characteristics of the aspect ratios of the grid cells. Aspect ratio is defined as the ratio between the longest side to the shortest side in a given cell. This can also determine the convergence of the relaxed grid and thereby its conformality. The convergence is achieved when all the cells have an aspect ratio close to 1. Aspect ratios greater than one lead to strong anisotropic material tensors (extreme mismatch of the absolute eigenvalues of the material property tensor) for the case of anisotropic bilayers and larger off-diagonal material property tensors in case the starting material property tensor is isotropic. (When the starting material property is anisotropic, no amount of optimization or grid relaxation will lead to nonzero off-diagonal components as rotation of a cell leads to off-diagonal components.) The distribution of the aspect ratios before and after grid relaxation of the transformed space are shown in Fig. 3.3(c) and (d) respectively.

Once we have a relaxed grid, we can assign the electric permittivity $\epsilon$ or the magnetic permeability $\mu$ for the new transformed space using the following relationship (Einstein's Notation) [17],

$$\epsilon^{p'q'} = \det\left(\Lambda^{p'}_{p}\right)^{-1} \Lambda^{p'}_{p} \Lambda^{q'}_{q} \epsilon^{pq} \tag{3.15}$$

where $\Lambda_p^{p'} = \dfrac{\partial x^{p'}}{\partial x^p}$ is the transformation operator with $p$ and $p'$ being the coordinate bases. The functions $x^{p'}$ and $x^p$ are related through the coordinate transformation $x^{p'} = x^{p'}(x^p)$. It is convenient to express the transformation operator in terms of unit bases. Since our coordinate transformation involves transforming $(\rho, \phi, z)$ to $(\rho', \phi, z')$, the transformation operator in cylindrical unit basis can be written as follows,

$$\Lambda_{\hat{p}}^{\hat{p}'} = \Lambda_{\hat{p}'}^{\hat{p}'} \Lambda_p^{p'} \Lambda_{\hat{p}}^{p} \tag{3.16}$$

$$= \begin{bmatrix} 1 & 0 & 0 \\ 0 & \rho' & 0 \\ 0 & 0 & 1 \end{bmatrix} \begin{bmatrix} \dfrac{\partial \rho'}{\partial \rho} & 0 & \dfrac{\partial \rho'}{\partial z} \\ 0 & 1 & 0 \\ \dfrac{\partial z'}{\partial \rho} & 0 & \dfrac{\partial z'}{\partial z} \end{bmatrix} \begin{bmatrix} 1 & 0 & 0 \\ 0 & \dfrac{1}{\rho} & 0 \\ 0 & 0 & 1 \end{bmatrix} \tag{3.17}$$

where the hat on the indices denotes a unit basis vector.

Equation (3.15) is evaluated discretely at each grid point and the material property tensor is assigned to it. The absolute principle components of the material property tensor ($\epsilon = \mu$) and their three principle directions for the transformed anisotropic bilayer are shown in Fig. 3.3(e). The different levels of gray regions in this figure indicate that the absolute principle values are close to one another. The principle directions are shown in three color channels, namely red, green, and blue. The *green* channel direction is out of the plane and represents the $\phi$-component, which is untransformed. When a grid cell is rotated in a plane about the $\phi$ axis, this leads to the deviation of green components from red and blue even though an aspect ratio of 1 is maintained. This is the reason why the combination of three of the principle channel values on the right-hand side of the relaxed grid is slightly green or magenta while the left-hand side unrotated/less rotated grid cells are mostly different levels of gray. The individual nonzero material tensor components in the original coordinate bases $(\rho, z)$ for an anisotropic bilayer, isotropic bilayer, and isotropic multilayer are shown in the supplementary material. The grid relaxations and the material property tensors are only calculated for the right half plane ($\phi = 0^\circ$) while the other half plane ($\phi = 180^\circ$) is a mirror image of the right half-plane. This helps to speed up the grid relaxation process. The transformed relaxed grid is quantified based on two metrics (figure of merits). The first metric we define is the *anisotropy metric*. This metric describes the quality of the grid based on the degree of anisotropy in the material property tensor. The lower the anisotropy metric, the more amenable are the material property tensors

for implementation. It is highly desirable to have no or very little variation between the absolute principle components in the material tensor. The anisotropy metric, AM, is defined as,

$$\mathrm{AM} = \frac{\max\left[|\xi_{11}-\xi_{22}|, |\xi_{11}-\xi_{33}|, |\xi_{22}-\xi_{33}|\right]}{\mathrm{mean}(\xi_{11}, \xi_{22}, \xi_{33})} \tag{3.18}$$

where $\xi_{11}, \xi_{22}$, and $\xi_{33}$ are the absolute eigenvalues of the material property tensor in the transformed space.

The second metric is the *orthogonality metric* which describes the quality of the relaxed grid based on the conformality and aspect ratio of the individual grid cell. The lower the orthogonality metric, the more conformal is the grid. The orthogonality metric, OM, is defined as,

$$\mathrm{OM} = 2\left|\frac{|n-0.5|^{2/3}\, Re\left[(w_{12}-w_{21})Im\left[w_{12}-w_{21}\right]+(w_{11}-w_{22})Im\left[w_{11}-w_{22}\right]\right]}{|Im\left[w_{11}-w_{22}\right]Re\left[w_{12}-w_{21}\right]+Im\left[w_{21}-w_{12}\right]Re\left[w_{11}-w_{22}\right]Re\left[w_{11}+w_{22}+w_{12}+w_{21}\right]|^{2/3}}\right| \tag{3.19}$$

where $w_{11} = \rho'_{m,n} + i\, z'_{m,n}$, $w_{22} = \rho'_{m+1,n+1} + i\, z'_{m+1,n+1}$, $w_{12} = \rho'_{m+1,n} + i\, z'_{m+1,n}$, and $w_{21} = \rho'_{m,n+1} + i\, z'_{m,n+1}$. $m$ and $n$ are the grid point indexing numbers. $Re$ and $Im$ stand for the real part and imaginary part of the expression. The detailed derivation regarding OM can be found in the supplementary material. Suppose the starting material property tensor is isotropic, OM should be as close to zero as possible. If not, it could lead to off-diagonal components in the material tensor. However, if the starting material tensor is anisotropic, a simple rotation of a grid cell could lead to off-diagonal components. It is important to maintain OM close to zero even for this case. If not, AM will drift away from zero. Hence both these metrics should be as low as possible irrespective of the starting material property tensor in the undistorted space in order to obtain more amenable material tensors in the transformed space. In Figs. 3.4 and 3.5, we show the anisotropy and orthogonality metrics before and after grid relaxation of the transformed space. Grid relaxation helps to reduce anisotropy by a factor of $\sim$3 and orthogonality metric by a factor of $\sim$100.

## 3.5 NFM Full-wave Simulation Results

### 3.5.1 2D NFM Simulations

After relaxing the grid and calculating the material property in the transformed space, we perform 2D full-wave simulations using COMSOL 5.1 RF Module. We chose a nominal magnification factor M = 3. The object plane field of view was chosen to be $1\lambda$ which

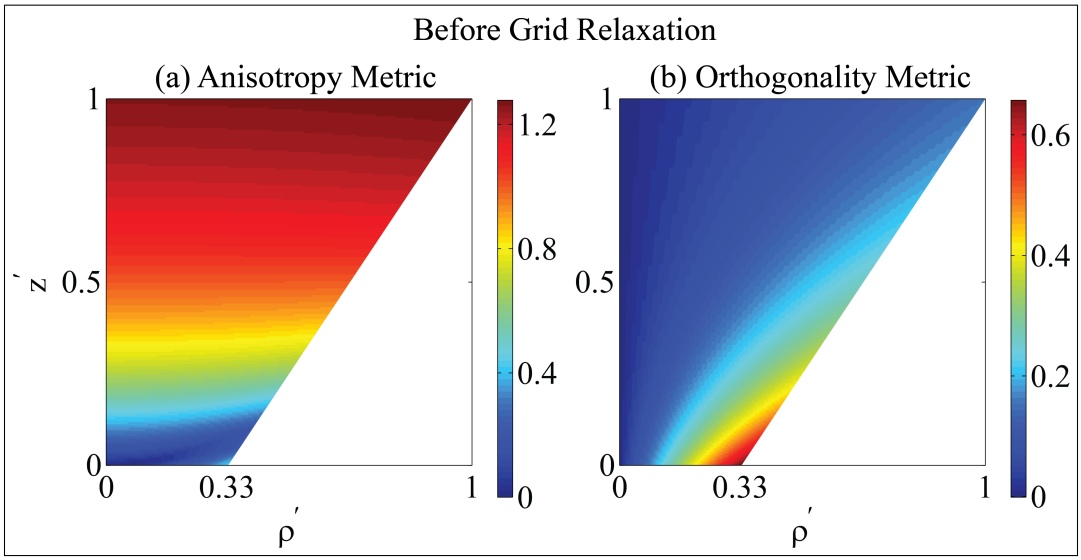


**Figure 3.4**: The anisotropy and orthogonality metric distribution (a & b respectively)in the transformed space before grid relaxation for a magnification factor of M = 3.

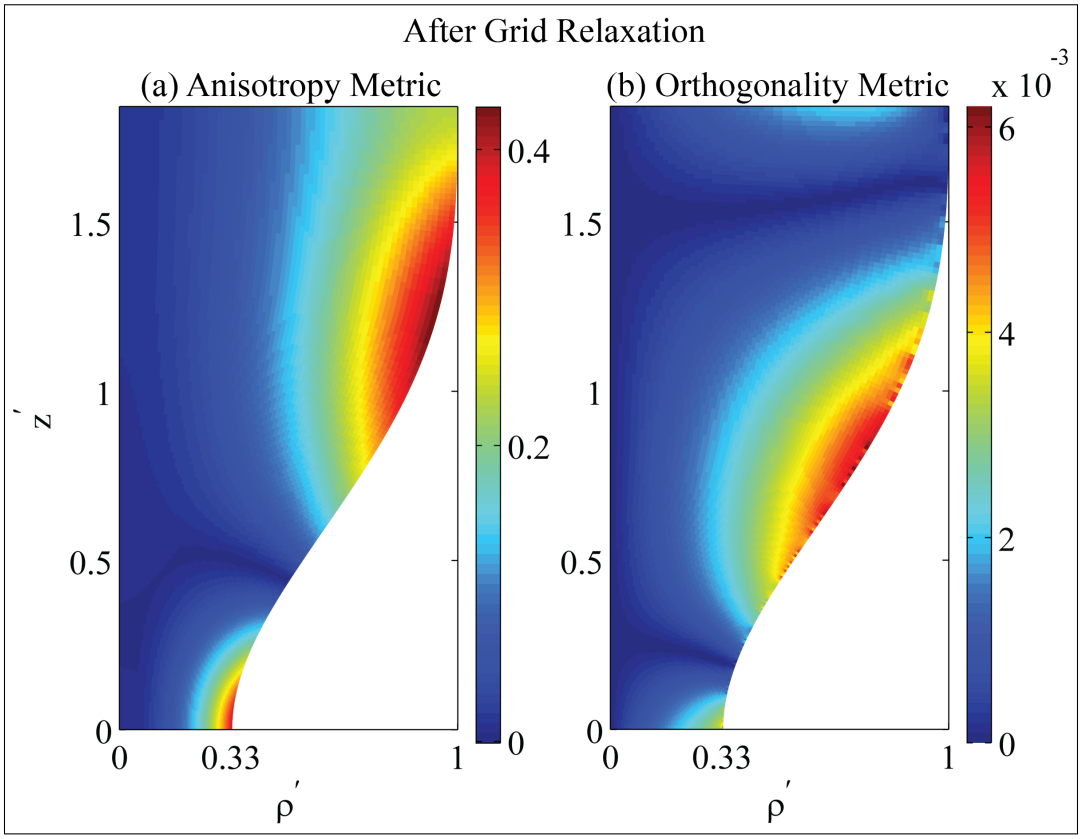


**Figure 3.5**: The anisotropy and orthogonality metric distribution (a & b respectively)in the transformed space after grid relaxation for a magnification factor of M = 3.

automatically sets the size of the image plane to be $3\lambda$. We performed NFM simulations for three different cases. The full-wave simulation results are shown in Fig. 3.6. The first case had the starting material property tensors as an anisotropic bilayer. The results for this case are shown in Fig. 3.6(a). The second case had an isotropic bilayer and the corresponding field norm distribution is shown in Fig. 3.6(b). The last case was an isotropic multilayer with alternating positive and negative indices (200 layers). The simulation result for this case is shown in Fig. 3.6(c). In all of these cases, we chose 2 point sources separated by $\lambda/4$ at the object plane. The excited point sources are TE polarized with electric field vector pointing out of the $(\rho, z)$ plane. All the cases had a loss tangent factor $\delta = 0.01$. The anisotropic bilayer performed the best by resolving and magnifying the subwavelength point sources at the image plane. The multilayer case barely resolved the point sources whereas the isotropic bilayer did not resolve the point sources. As explained in section 3.3, this is due to the transfer function characteristics of the anisotropic/isotropic bilayers and multilayer. One important characteristic of this design is that the output image plane is aberration free and provides uniform magnification across the complete field of view. This feature of NFM can be mainly attributed to the relaxed grid top and bottom boundary conditions and to the planar nature of the object and image plane. (Such distortion results when the magnification factor is a function of the distance away from the optical axis.) The magnification factor also increases the space-bandwidth product at the image plane by a factor of M. This means that some of the nonpropagating components in the object plane can now be converted to propagating components and projected to the far-field without much loss in resolution. The image plane cut line showing the electric field norm is shown in Fig. 3.6(d) and their corresponding normalized far field cut line plots are shown in Fig. 3.6(e). It is important to note that anisotropic bilayer NFM case could potentially resolve and magnify objects that are separated by further smaller distances (up to $\sim \lambda/10$ with $\sim \delta = 0.05$). The effect varying loss tangent factor on anisotropic bilayer NFM resolution was studied. The results are shown in Fig. 3.7. The NFM with up to loss tangent factor of $\delta = 0.05$ magnifies and resolves point sources that are $\lambda/10$ apart.

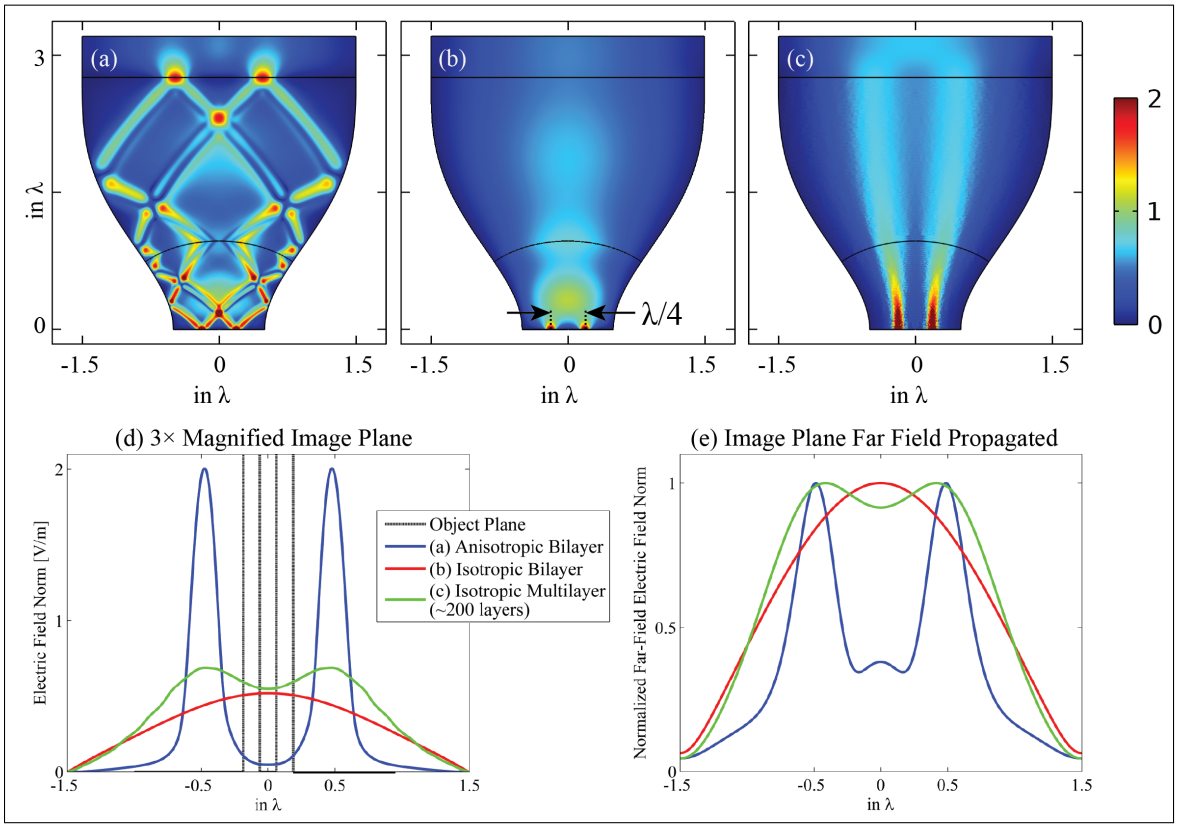


**Figure 3.6**: The electric field norm distribution for the three simulated 2D NFM cases with a magnification factor M = 3. The three simulated cases are when the starting material property tensors in the undistorted space are: (a) Anisotropic Bilayer (b) Isotropic Bilayer (c) Isotropic Multilayer (∼200 layer stack of alternating positive and negative index). All of the above cases ((a), (b) & (c)), the object plane consists of two point sources separated by $\lambda/4$ and have a loss tangent factor $\delta = 0.01$. (d) Shows the 1D plot of electric field norm at the magnified image plane of the NFM. (e) Shows the normalized far field norm when the image plane is far field propagated.

### 3.5.2 3D NFM Simulations

The main advantage of transforming space in cylindrical coordinates (i.e, $(\rho, \phi, z)$ to $(\rho', \phi, z')$) is that the material property tensors will be axially symmetric. One can exploit this fact to simulate and analyze a 3D NFM with extended planar targets apart from simple point sources as discussed previously. This helps to truly demonstrate the uniform, aberration-free magnification feature of NFM. We first decompose the planar resolution target in the object plane (shown in both Fig. 3.8(b) and Fig. 3.9(a)) into its harmonic components using a cylindrical harmonic decomposition technique. Then each of the cylindrical harmonic components (both TE & TM components) are propagated through the

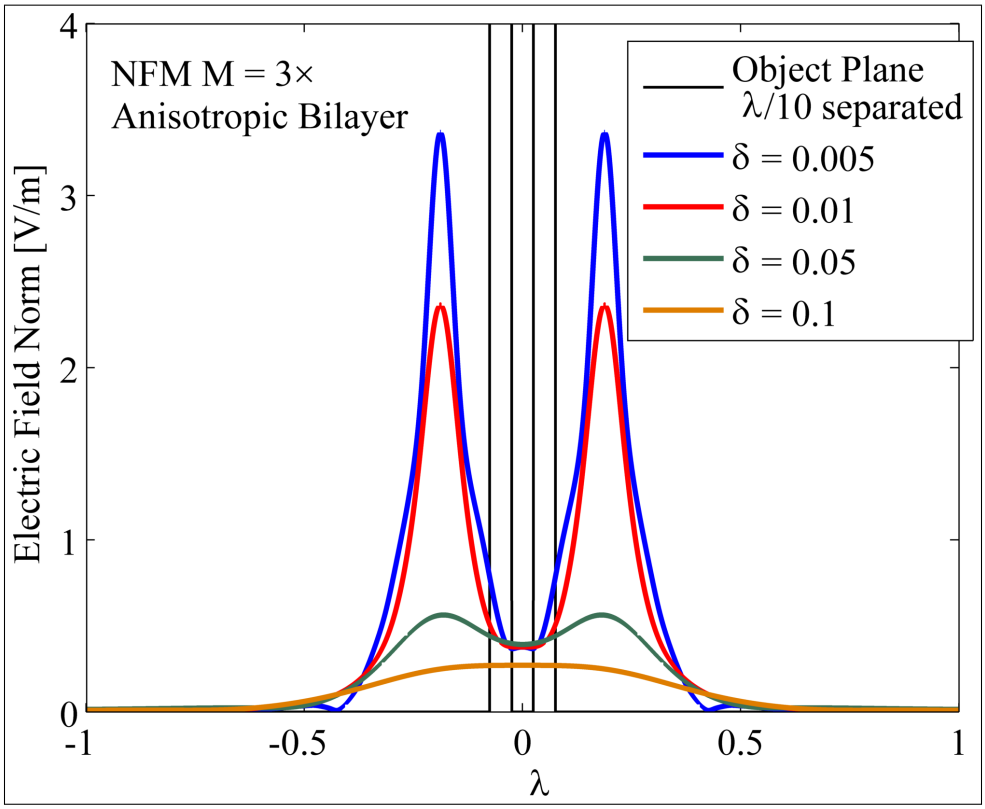


**Figure 3.7**: The effect of varying loss tangent factor $\delta$ on the image plane electric field norm. The effect of loss tangent is shown for the anisotropic bilayer NFM with M = 3. The point sources are separated by $\lambda/10$.

2D NFM medium. The propagated field components are then revolved and recomposed appropriately at the image plane to get a complete 3D vector solution. This technique is known as 2.5 D technique. This approach can be used only when the inhomogeneous medium is axially symmetric ($\phi$ independent). In such cases, a cylindrical harmonic mode of a given azimuthal mode number $\tilde{m}$, couples only to modes of the same mode number $\tilde{m}$. In such a structure, the electric field in cylindrical basis varies with azimuthal mode $\tilde{m}$ as, $\mathbf{E}(\rho,\phi,z) = \tilde{\mathbf{E}}(\rho,z)\ \exp(-j\,\tilde{m}\phi)$. However, this approach does not impose any restriction on the excitation or object plane fields. This approach helps in reducing the computational resource requirement significantly and is also advantageous in analyzing each mode behavior inside NFM. The details regarding cylindrical harmonic decomposition and the 2.5 D technique are published elsewhere [18].

The setup for the 2.5 D technique is shown in Fig. 3.8. The simulated domain is the $\phi = 0°$, 2D plane. NFM with transformed anisotropic bilayer material properties was

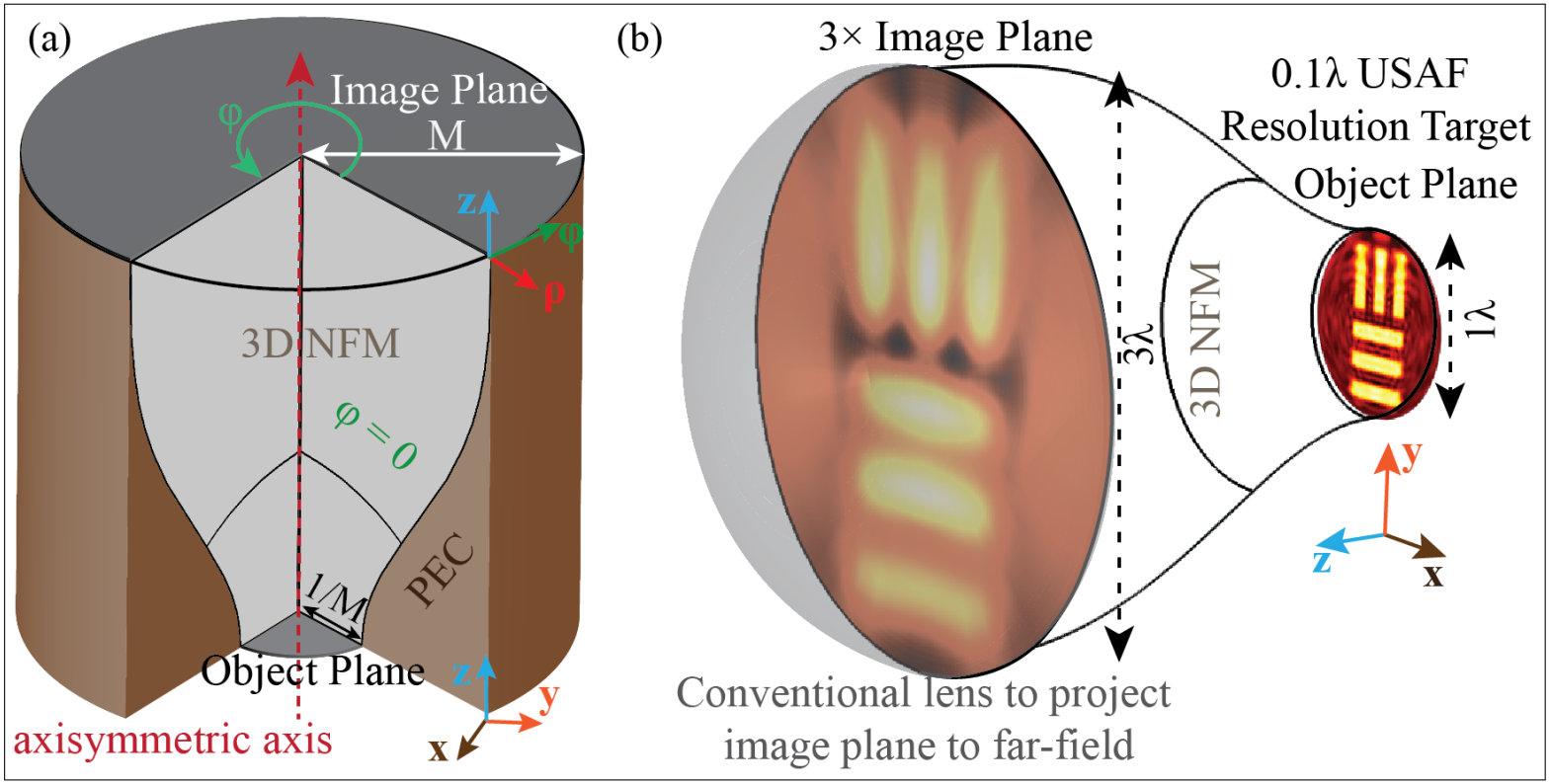


**Figure 3.8**: Setup for the 2.5 D simulation technique is shown. (a) shows the perspective section view of a 3D NFM, which is the axial revolution of a 2D planar NFM in $(\rho', \phi = 0, z')$ plane. The axisymmetric axis is shown as a dotted red line. The material property tensors correspond to that of the anisotropic bilayer. (b) shows the object plane transverse electric field norm and $3\times$ magnified image plane transverse electric field norm. A 0.1 $\lambda$ USAF resolution target was chosen for this demonstration.

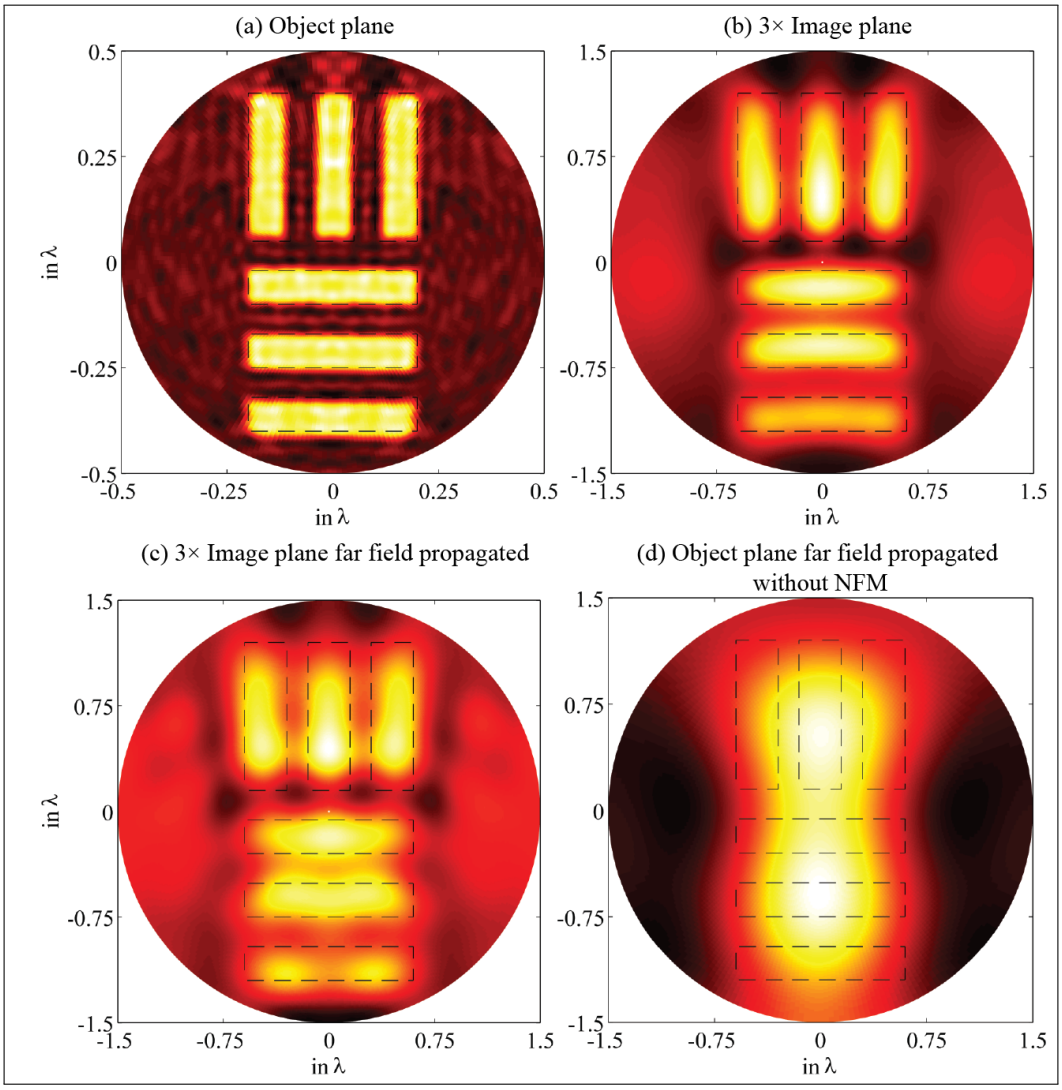


**Figure 3.9**: 3D NFM object and image planes are shown. (a) shows the $0.1\lambda$ resolution target at the object plane. (b) shows the $3\times$ magnified resolution target at the image plane of the 3D NFM. (c) shows the image plane far field propagated. (d) shows the object plane far field propagated without NFM.

chosen. The magnification factor was M = 3 and the loss tangent factor was $\delta = 0.01$. The object plane aperture area was $\pi\lambda^2/4$ which automatically sets the image plane aperture area to be $9\pi\lambda^2/4$. A $0.1\lambda$ resolution target shown in Fig. 3.9(a) was chosen for analyzing the complete 3D NFM. The $3\times$ magnified image plane is shown in Fig. 3.9(b). The 3D NFM magnifies and resolves the target. The far field propagated image plane is shown in Fig. 3.9(c). For comparison, we also show the case without NFM in Fig. 3.9(d).

## 3.6 Effect of Magnification

The overall magnification factor, M, of the NFM imposes several design constraints. As explained in the previous sections, higher magnification factors are desirable as the output plane space-bandwidth product increases by a factor of M. In terms of grid design, the relaxed grid height, $h_0$, is directly proportional to the square root of M. The appropriate increase in $h_0$ also helps in improving the relaxed grid anisotropy metric, AM, but the overall transmission decreases when losses are present in the transformed space. AM reduces by a factor of $\sim$ 2 with an increase in $h_0$ by a factor $\sim$ 2 when the magnification increases from M = 3 to M = 9. Another inevitable consequence due to increase in magnification factor is the overall energy density reduction at the image plane. The energy density at the output plane reduces by a factor of $\sim 1/\mathrm{M}^2$. Higher magnification factors may be undesirable when the signal to noise ratio of the detection system at the image plane is low. Full-wave simulations were performed on transformed anisotropic bilayers with different magnification factors, namely M = 3, 5, and 9. The electric field norm for these cases are shown in Fig. 3.10. The corresponding anisotropy metric of the transformed relaxed grid is shown in Fig. 3.11. However, the orthogonality metric, OM, for these cases remained consistently below $6 \times 10^{-3}$ (not plotted).

### 3.6.1 Cascaded NFM

The material property tensor closer to the output plane reduces with the magnification factor (space is being expanded) and index values decrease as $1/\mathrm{M}$. This is undesirable as implementing extremely small and accurate $\epsilon$ and $\mu$ values could be challenging which restrains larger magnification factors. However, this particular problem can be addressed by cascading NFMs. Suppose one requires an NFM with magnification factor $\mathrm{M}_2$, this can be achieved by cascading 'k' NFM stages each having a magnification factor $\mathrm{M}_1$ such that the overall magnification of these cascaded stages is $\mathrm{M}_2 = \mathrm{M}_1^k$ (Note: $\mathrm{M}_2 \geq \mathrm{M}_1$ & $\mathrm{k} \in \mathbb{Z}^+$). The $k^{th}$ stage is just a physically scaled version of $(k-1)^{th}$ stage with exactly the same material property tensors as the $(k-1)^{th}$ stage, providing a magnification factor of $\mathrm{M}_1$. Hence the minimum material property tensor at the output plane will be close to $(1/\mathrm{M}_1) \geq (1/\mathrm{M}_2)$. The overall relaxed height of such a cascaded NFM will be approximately equal to:

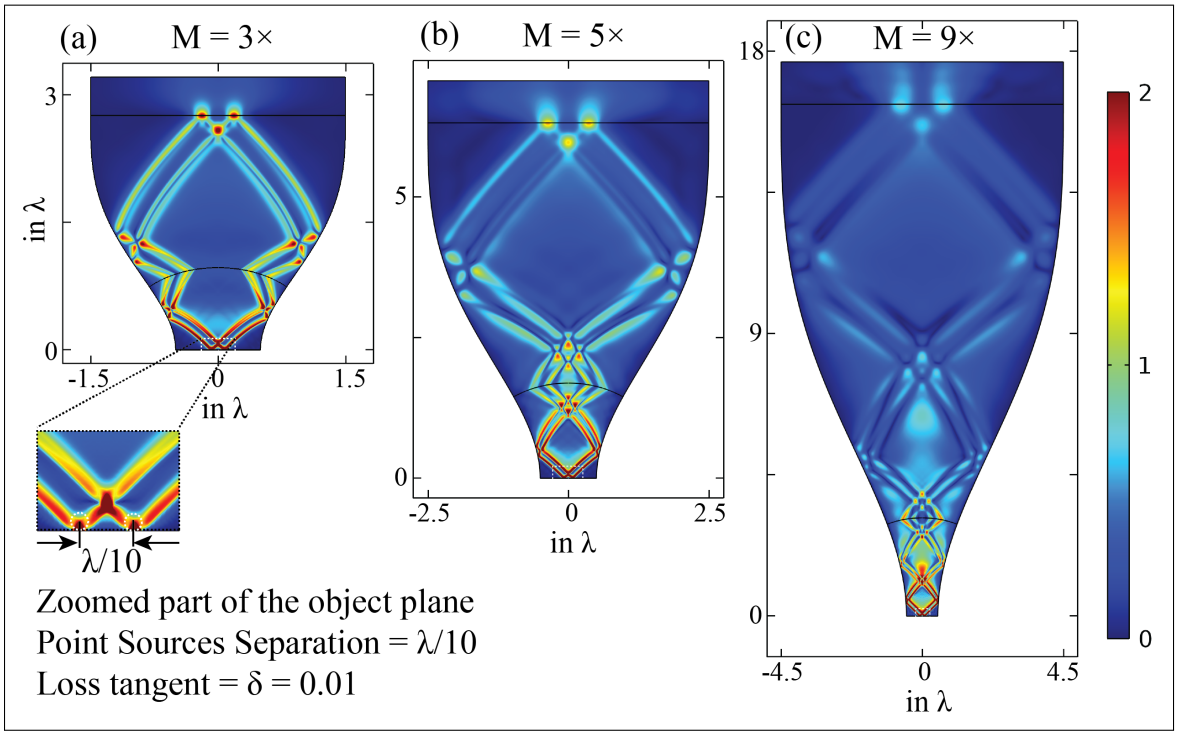


**Figure 3.10**: The electric field norm distribution for the simulated 2D NFM with different magnification factors. Namely, (a) M = 3×, (b) 5×, and (c) 9×. The two point sources in the object plane are separated by $\lambda/10$. All of the above three cases have a loss tangent factor $\delta = 0.01$.

$$h_0 \sim \frac{1}{M_2} \sum_{n=1}^{n=k} M_1^{n+0.5} \tag{3.20}$$

which can be lesser than $h_0 \sim \sqrt{M_2}$, when a single stage achieves a magnification factor of $M_2$. Due to the reduction in height, $h_0$, for a given loss tangent factor $\delta$, a cascaded NFM can have a higher throughput compared to a single stage with magnification $M_2$. One concern in such cascaded stages could be the mismatch reflections at the boundaries of any two cascaded stages. This can be minimized by implementing stages whose relative impedances, $Z_0$, at the boundaries are close to 1. This approach could be a potential path to achieve higher magnification factors.

As an example, we design and simulate such a cascaded NFM system with two stages (k = 2) each having a magnification factor of $M_1 = 3$ such that the overall magnification $M_2 = M_1^2 = 9$. Stage 1 provides a magnification factor of 3 and magnifies the $\lambda/10$ separated source plane. Now the image plane of Stage 1 acts as the source plane to Stage 2, which is just a physically scaled version of Stage 1 with exactly the same material property

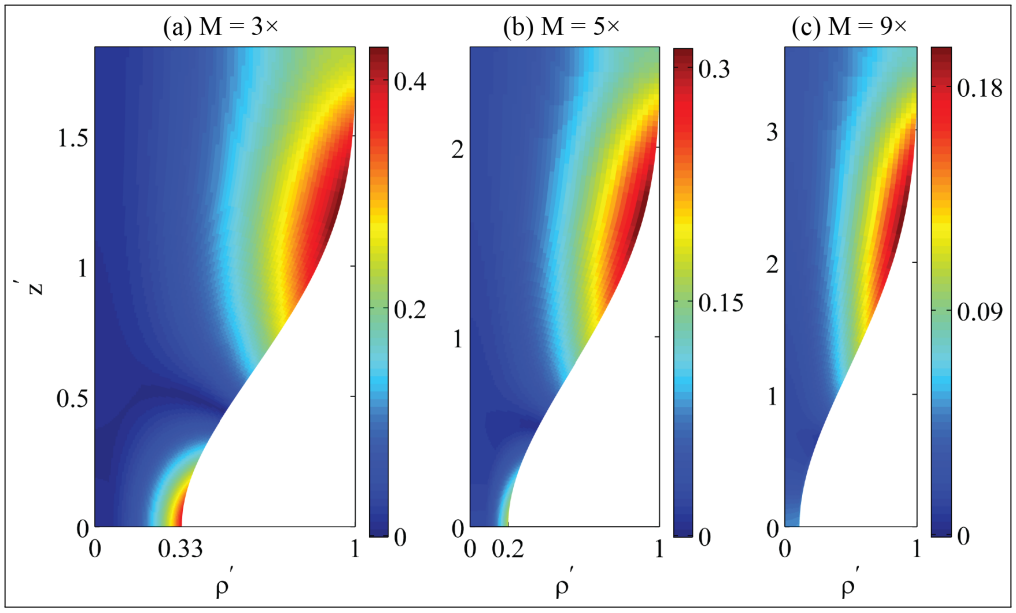


**Figure 3.11**: The effect of magnification on the anisotropy metric of the relaxed transformed grid.

spatial gradient as Stage 1. Stage 2 magnifies the fields again by a factor of 3 and an overall magnification of 9 is achieved at the final image plane. The full-wave simulation of a 2-stage cascaded NFM is shown in Fig. 3.12(a). We also compare the cascaded NFM image cut line results with single stage NFM (see Fig. 3.10 (c)) providing same magnification. As expected, the cascaded stages outperform the single stage in terms of transmission throughput. The different cut-line results are shown in Fig. 3.12(b).

## 3.7 Conclusion

In this article we provide a comprehensive design perspective for planar aberration-free near field magnifier involving transformation optics design principles. We discuss the effect of material choices, loss tangent and magnification factors on NFMs. We provide full wave simulations of near field magnifiers to demonstrate sub-diffraction imaging capability. We also propose a strategy to achieve higher magnification factors. With the advent of infra-red and optical metamaterials with anisotropic and gradient index material properties, such magnifiers will play a key role in sub-diffraction/ super-resolution imaging systems.

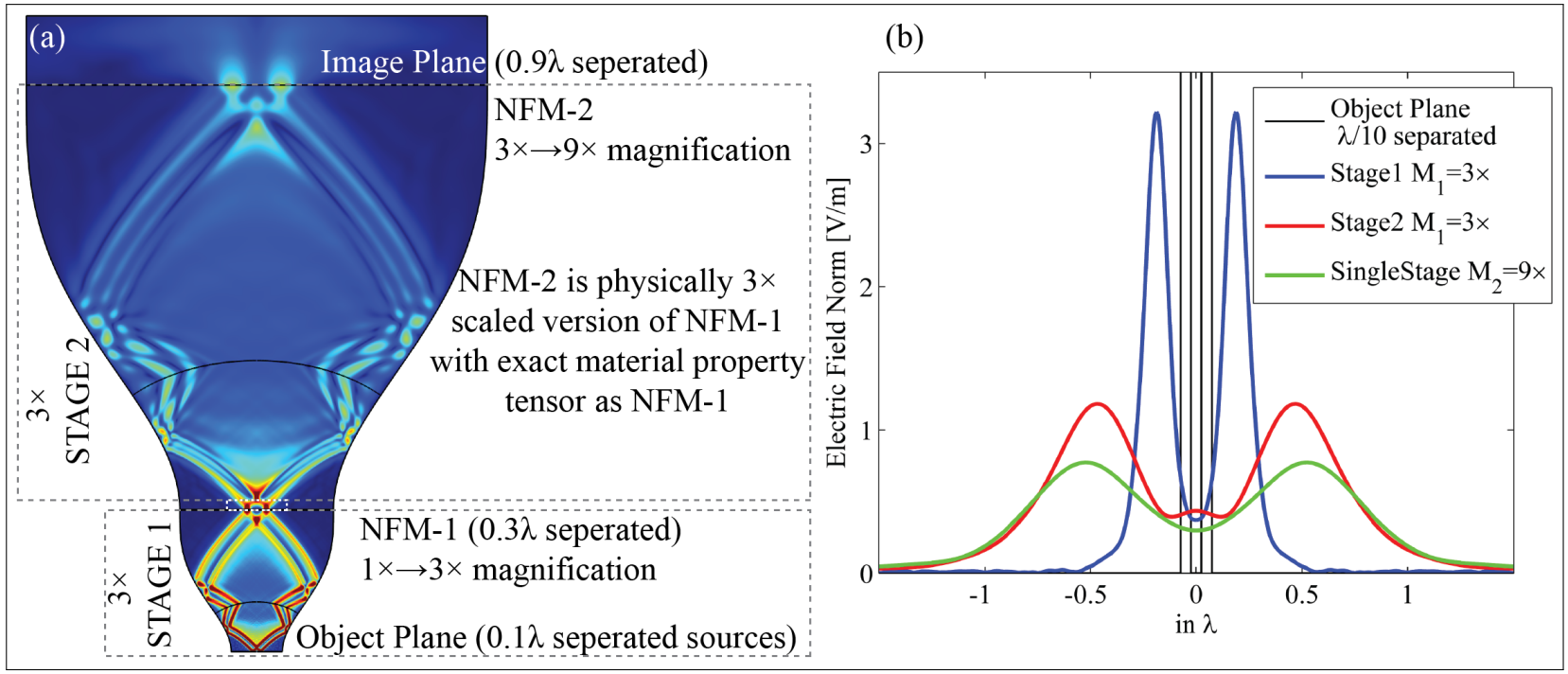


**Figure 3.12**: Cascaded NFM strategy to achieve higher magnification factor is shown. (a) shows the electric field norm distribution for a 2-stage cascaded NFM. Each stage provides a 3× magnification with an overall magnification of 9×. Stage 2 is a 3× scaled version of Stage 1 with exact material property spatial gradient(loss tangent factor for both stages is $\delta = 0.01$). (b) shows the electric field norm at different cut lines of cascaded Stage 1 image plane, cascaded Stage 2 image plane, and single stage M = 9 image plane.

## 3.8 Supplementary Material

### 3.8.1 Orthogonality Metric

Rewriting the cylindrical coordinate transformation with simple variables representing the transformation derivatives, the transformation operator becomes,

$$\Lambda_{\hat{p}}^{\hat{p}'} = \begin{bmatrix} 1 & 0 & 0 \\ 0 & \rho' & 0 \\ 0 & 0 & 1 \end{bmatrix} \begin{bmatrix} a & 0 & b \\ 0 & 1 & 0 \\ c & 0 & d \end{bmatrix} \begin{bmatrix} 1 & 0 & 0 \\ 0 & \frac{1}{\rho} & 0 \\ 0 & 0 & 1 \end{bmatrix} = \begin{bmatrix} a & 0 & b \\ 0 & \frac{\rho'}{\rho} & 0 \\ c & 0 & d \end{bmatrix} \tag{3.21}$$

If the original medium in the undistorted space is diagonal, the new medium is not diagonal. Let the original medium in general be,

$$\epsilon_{\text{orig}} = \mu_{\text{orig}} = \begin{bmatrix} \Gamma & 0 & 0 \\ 0 & \Upsilon & 0 \\ 0 & 0 & \Psi \end{bmatrix} \tag{3.22}$$

The new medium is given by,

$$\epsilon_{\text{new}} = \mu_{\text{new}} = \begin{bmatrix} \frac{(a^2\Gamma + b^2\Psi)\rho}{(ad-bc)\rho'} & 0 & \frac{(ac\Gamma + bd\Psi)\rho}{(ad-bc)\rho'} \\ 0 & \frac{\Upsilon\rho'}{(ad-bc)\rho} & 0 \\ \frac{(ac\Gamma + bd\Psi)\rho}{(ad-bc)\rho'} & 0 & \frac{(c^2\Gamma + d^2\Psi)\rho}{(ad-bc)\rho'} \end{bmatrix} \tag{3.23}$$

The derivatives for a grid cell are the average of two edge derivatives. The original radial coordinate is given, assuming the index begins with one. The transformed radial coordinate is the average radial coordinate of all four corners. Then,

$$a = \frac{1}{2}\left(\frac{Re[w_{21} - w_{11}]}{\Delta} + \frac{Re[w_{22} - w_{12}]}{\Delta}\right), \quad b = \frac{1}{2}\left(\frac{Re[w_{12} - w_{11}]}{\Delta} + \frac{Re[w_{22} - w_{21}]}{\Delta}\right)$$

$$c = \frac{1}{2}\left(\frac{Im[w_{21} - w_{11}]}{\Delta} + \frac{Im[w_{22} - w_{12}]}{\Delta}\right), \quad d = \frac{1}{2}\left(\frac{Im[w_{12} - w_{11}]}{\Delta} + \frac{Im[w_{22} - w_{21}]}{\Delta}\right)$$

$$\rho = (m - 0.5)\Delta, \quad \rho' = \frac{1}{4}Re[w_{11} + w_{12} + w_{21} + w_{22}]$$

where, $\Delta$ is the incremental grid length in the undistorted space and $m$ is the grid point indexing number.

Suppose the grid in the transformed space is orthogonal (the aspect ratio of every grid cell tends to 1), then $a, b, c$, and $d \neq 0$ as a grid cell could be rotated with respect to the original coordinate basis. In such a case, if the cell has an aspect ratio $\to 1$, then $d \to a$ and

$c \to -b$. The factor $\dfrac{ac+bd}{ad-bc} \to 0$. The quality of the transformed relaxed grid based on its conformality is described by the orthogonality metric, OM, as:

$$OM = \left| \frac{1}{\det(\epsilon_{\text{new}})^{1/3}} \frac{(ac+bd)\rho}{(ad-bc)\rho'} \right| \tag{3.24}$$

The above equation takes in to account the normalizing factor, which is $\det(\epsilon_{new})^{1/3}$, and when expanded (3.24) is similar to (3.19) (assuming $\Gamma = \Psi$). It is important to note that the off-diagonal material tensor element in (3.23) tends to 0, when $\Gamma = \Psi$ (i.e., isotropic case). However, no orthogonal grid will lead to zero off-diagonal element in the material tensor when $\Gamma = -\Psi$ (i.e., anisotropic case).

### 3.8.2 Material Property Tensor Maps

The following material property tensor maps in Figures 3.13, 3.14, and 3.15 are shown for different cases.

- **Anisotropic Bilayer NFM Material Tensors**

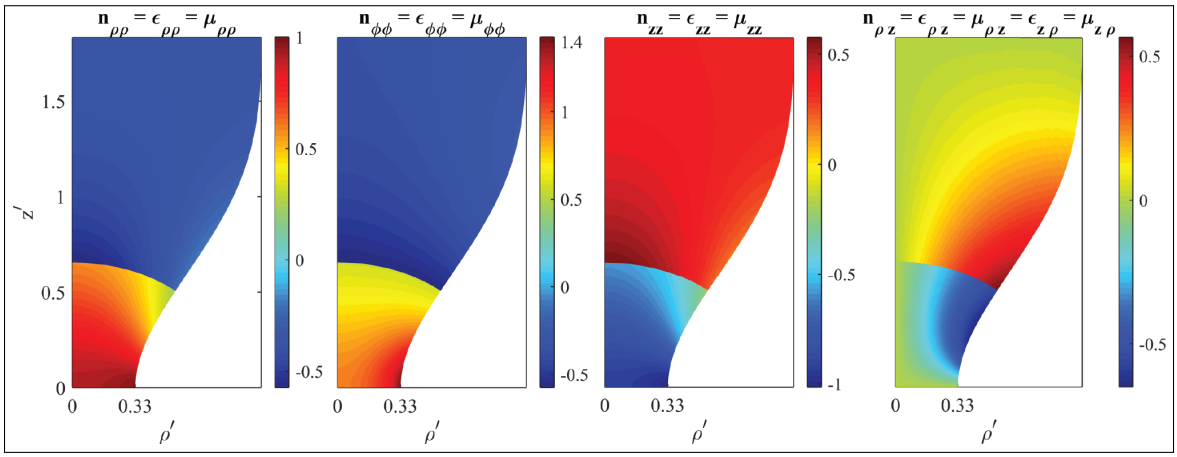


**Figure 3.13**: The individual components of the nonzero material property tensor in the transformed space with a magnification factor M = 3 when the starting material property tensors correspond to the anisotropic bilayer.

- **Isotropic Bilayer NFM Material Tensors**

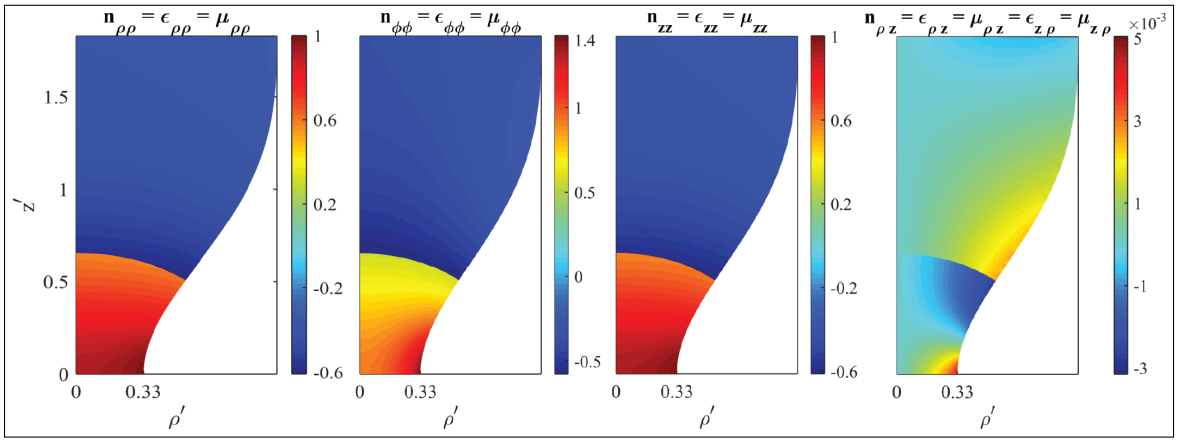


**Figure 3.14**: The individual components of the nonzero material property tensor in the transformed space with a magnification factor M = 3 when the starting material property tensors correspond to the isotropic bilayer. The off-diagonal $\rho z$ and $z\rho$ components can be neglected as they are extremely small due to the orthogonal nature of the transformed grid.

- **Isotropic Multilayer NFM Material Tensors**

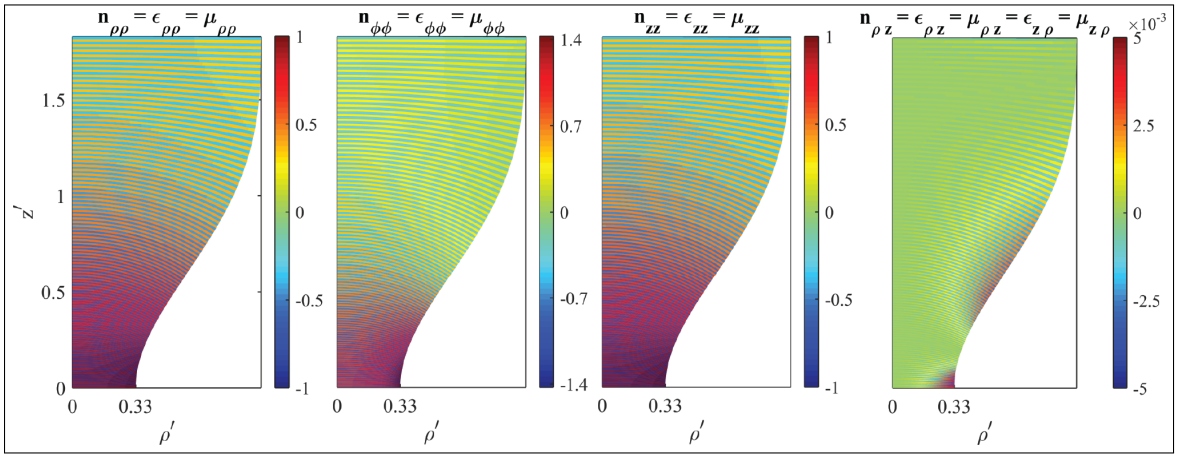


**Figure 3.15**: The individual components of the nonzero material property tensor in the transformed space with a magnification factor M = 3 when the starting material property tensors correspond to the isotropic multilayer. The off-diagonal $\rho z$ and $z\rho$ components can be neglected as they are extremely small due to the orthogonal nature of the transformed grid.

## 3.9 Acknowledgments

This research was supported by the Army Research Office through Multidisciplinary University Research Initiative under Grant No. W911NF-09-1-0539.

## 3.10 References

[1] Z. Liu, H. Lee, Y. Xiong, C. Sun, and X. Zhang, "Far-field optical hyperlens magnifying sub-diffraction-limited objects," *Science*, vol. 315, no. 5819, pp. 1686–1686, 2007.

[2] A. V. Kildishev and E. E. Narimanov, "Impedance-matched hyperlens," *Optics letters*, vol. 32, no. 23, pp. 3432–3434, 2007.

[3] V. A. Podolskiy and E. E. Narimanov, "Near-sighted superlens," *Optics letters*, vol. 30, no. 1, pp. 75–77, 2005.

[4] Z. Jacob, L. V. Alekseyev, and E. Narimanov, "Optical hyperlens: far-field imaging beyond the diffraction limit," *Optics Express*, vol. 14, no. 18, pp. 8247–8256, 2006.

[5] A. V. Kildishev and V. M. Shalaev, "Engineering space for light via transformation optics," *Optics letters*, vol. 33, no. 1, pp. 43–45, 2008.

[6] Y. Xiong, Z. Liu, and X. Zhang, "A simple design of flat hyperlens for lithography and imaging with half-pitch resolution down to 20 nm," *Applied Physics Letters*, vol. 94, no. 20, p. 203108, 2009.

[7] W. Wang, et al., "Far-field imaging device: Planar hyperlens with magnification using multi-layer metamaterial," *Optics Express*, vol. 16, no. 25, pp. 21 142–21 148, 2008.

[8] J. Li, L. Fok, X. Yin, G. Bartal, and X. Zhang, "Experimental demonstration of an acoustic magnifying hyperlens," *Nature materials*, vol. 8, no. 12, pp. 931–934, 2009.

[9] X. Ao and C. Chan, "Far-field image magnification for acoustic waves using anisotropic acoustic metamaterials," *Physical Review E*, vol. 77, no. 2, p. 025601, 2008.

[10] J. B. Pendry, "Negative refraction makes a perfect lens," *Physical Review Letters*, vol. 85, no. 18, p. 3966, 2000.

[11] D. R. Smith, D. Schurig, M. Rosenbluth, S. Schultz, S. A. Ramakrishna, and J. B. Pendry, "Limitations on subdiffraction imaging with a negative refractive index slab," *Applied Physics Letters*, vol. 82, no. 10, pp. 1506–1508, 2003.

[12] D. Schurig and D. Smith, "Sub-diffraction imaging with compensating bilayers," *New Journal of Physics*, vol. 7, no. 1, p. 162, 2005.

[13] V. P. Drachev, V. A. Podolskiy, and A. V. Kildishev, "Hyperbolic metamaterials: New physics behind a classical problem," *Optics Express*, vol. 21, no. 12, pp. 15 048–15 064, 2013.

[14] J. B. Pendry, D. Schurig, and D. R. Smith, "Controlling electromagnetic fields," *Science*, vol. 312, no. 5781, pp. 1780–1782, 2006.

[15] J. F. Thompson, B. K. Soni, and N. P. Weatherill, *Handbook of Grid Generation*. CRC press, 1998.

[16] N. I. Landy and W. J. Padilla, "Guiding light with conformal transformations," *Optics Express*, vol. 17, no. 17, pp. 14 872–14 879, 2009.

[17] D. Schurig, "An aberration-free lens with zero f-number," *New Journal of Physics*, vol. 10, no. 11, p. 115034, 2008.

[18] S. Venkatesh and D. Schurig, "Computationally fast EM field propagation through axi-symmetric media using cylindrical harmonic decomposition," *Optics Express*, vol. 24, no. 25, pp. 29246–29268, 2016.

# CHAPTER 4

# CONTROLLING THE TWISTING OF LIGHT

This chapter, in full, has been submitted for publication, with authors Suresh Venkatesh, Nicholas Korevaar, and David Schurig.

## 4.1 Abstract

In analogy to transformation optics, which exploits the inherent equivalence between coordinate transformation geometry and material properties in Maxwell's equations, torsion optics exploits the equivalence of geometric torsion and chirality, as a design tool for polarization controlling devices in the geometric optical limit. We define a geometric quantity called the scalar torsion function that intuitively describes the additional twisting of vector fields along geodesics (not inherent to the geodesic itself). Fundamental mathematical aspects of this torsion function are described in the context of connections, and the relationship to polarization evolution in the geometric limit of optics is given. The relation describing the functional equivalence of this torsion function and the chirality of the material is presented. Elucidating examples, that are validated with full-wave simulations, are presented, including a skew aberration reducing Luneburg lens and a vortex beam creating device.

## 4.2 Introduction

The transformation design method exploits a connection between coordinate transformation geometry and material properties inherent in Maxwell's equations. The method enjoyed a surge of attention beginning in 2006, when it was applied to the design of electromagnetic invisibility cloaks [1, 2]. Cloaks for different wave phenomena, with different topologies, approaches for nonmagnetic implementation and increased bandwidth further fueled the interest [3–7]. Since then the method has been applied to field rotation [8, 9], celestial modeling [10–12], field concentration [13–15], wave-guide bends [16], antennas

[17], hyper-lenses [18–22], and other optical operations [10, 23–29].

However, until very recently, polarization control in the transformation optics literature has been restricted to field manipulations that can be described locally as "rigid body" rotations. Associated with a single axis of rotation, such manipulations necessarily couple global field-pattern rotation (and an associated displacement) to the desired polarization control. These rotations are the most general possible when invoking a geometry representable by a coordinate transform. Abandoning the use of coordinate transformations, and employing geometries with curvature, does little to improve the polarization control capability. A device that performs a simple, finite, uniform polarization rotation (without global field-pattern rotation), requires nearby trajectories to acquire finite and incompatible rotations (see Fig. 4.1).

Horsley [30] was the first to discuss the relationship between (a particular extension of) Riemannian geometry, and a chiral medium in the geometrical-limit of optics. Horsley

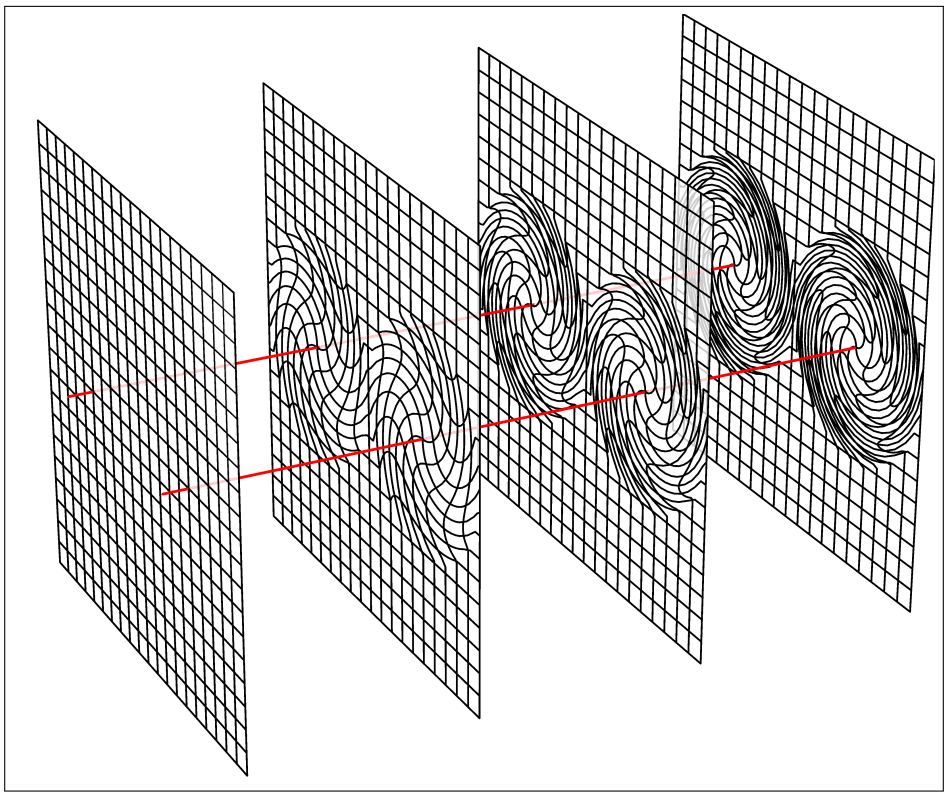

**Figure 4.1**: Polarization rotations cannot be represented by a coordinate transformation. Local field rotations are not globally compatible; they cannot be connected by a global coordinate transformation.

found that a special form of torsion tensor, when added to the Riemannian Levi-Civita connection, yields a new connection that preserves the geodesics of the associated metric but induces a rotation of the normal planes to those geodesics (relative to the parallel transport of framings for those planes that one obtains using the Levi-Civita connection). An equivalent statement, from the viewpoint of optical materials, is that one can add isotropic chirality to a given isotropic refractive index profile without affecting geometric ray paths. In this article, we first define a scalar torsion function (directly related to this special torsion tensor) —*a geometric attribute*—and show that it can be functionally equated to isotropic chirality, *a material property*. This is in exact analogy to the functional equivalence (in traditional transformation electromagnetics) of a coordinate transformation—*a geometric attribute*—and the permittivity and permeability tensors, which are the relevant *material properties*. To use the scalar torsion as an engineering design tool for polarization controlling devices, we need to understand the evolution of polarization in the geometrical limit in the absence of torsion, and the effect of an added scalar torsion on this evolution. This primary geometric result is embodied in (4.34), which equates the rotation or twisting of linear polarization per unit length, to the scalar torsion function. We then supply the basic relationship of torsion optics in (4.38), relating the scalar torsion to isotropic chirality. (This is a reformulation of the results of Horsley.)

Subsequently, the engineering case for the usefulness of torsion optics is made. We find a general formulation for the desired scalar torsion that will eliminate skew aberration (a form of polarization aberration) [31] in gradient index devices, (4.44). As a specific example, we find the required chirality profile for elimination of skew aberration in the Luneburg lens. We test this design with full wave simulations, showing that skew polarization is substantially reduced, increasingly so at larger lens diameters, relative to wavelength (i.e approaching the geometric limit). Finally we turn the design tool to the task of designing devices for creating complex beam polarizations, such as vortex beams. These are also validated with full wave simulations.

A note on style and notation. As some of the content of sections 4.3 and 4.4 pertains to connections, parallel transport, and Riemannian geometry, and is fairly technical from a mathematics point of view, we adopt the style and notation of the associated mathematical literature, including the use of formal theorems and proofs, as well as allowing the rank

of objects to be inferred by context, and not highlighted by type face. In other contexts, such as discussions of electromagnetics, we follow style and notation of the engineering literature. However, we strive to make the material of all sections accessible to readers with either a mathematical or engineering background.

## 4.3 Geometric Optics, Metric Compatible Connections and Torsion

In the usual formulation of geometrical optics for time-independent media, light follows (geodesic) paths $\gamma$ which are stationary and locally minimizing for the total time integral [32]

$$t(\gamma) = \frac{1}{c}\int_{\gamma} n ds. \tag{4.1}$$

Here $c$ is the speed of light in a vacuum, $ds$ is Euclidean arclength, the "index of refraction" $n$ at $\gamma(s)$ is the ratio of $c$ to the speed of light at the point $\gamma(s)$ in the direction $\gamma'(s)$, i.e. $n\,ds = c\,dt$ relates the elements of Euclidean arclength and time.

In a nonisotropic material it is assumed that the refractive index can depend on direction as well as location, via a (positive definite symmetric) Riemannian metric 2-tensor g, so that for $\gamma$ parameterized by Euclidean arclength $s$,

$$n_{\gamma(s)} = ||\gamma'(s)||_g = \sqrt{g_{\gamma(s)}(\gamma'(s), \gamma'(s))}$$

And for general parameterization $\gamma(r)$, the element of optical path length $d\sigma$ is given by,

$$d\sigma = n(\gamma(r))ds = \sqrt{g_{\gamma(r)}(\gamma'(r), \gamma'(r))}dr \tag{4.2}$$

In the geometrical optics limit of Maxwell's equations the electric and magnetic field directions are parallel-transported along geodesic (light) paths $\gamma$ via the Levi-Civita connection $\nabla$ associated with the metric g, so for $\gamma$ parameterized by optical path length, $\sigma$, the Riemannian unit tangent vector $\mathbf{t} = \mathbf{fl}'(\mathbf{œ})$, and the Riemannian unit directions $\mathbf{e}$, $\mathbf{h}$ of the electric and magnetic fields,

$$\nabla_{\mathbf{t}}\mathbf{t} = 0, \nabla_{\mathbf{t}}\mathbf{e} = 0, \nabla_{\mathbf{t}}\mathbf{h} = 0 \tag{4.3}$$

Because $\nabla$ is metric compatible, Riemannian angles and lengths are preserved under parallel transport, so $\mathbf{t}, \mathbf{e}, \mathbf{h}$ are transported as a positively-oriented ortho-normal frame along the light path $\gamma$, as measured by the metric $g$.

As shown in [30], it is possible to specify chiral material properties so that a modified geometrical optics limit of Maxwell's equations will hold: The refractive index $n$ and geodesic light paths $\gamma(\sigma)$ are not changed, but the electric and magnetic fields rotate differently along the curves $\gamma$, relative to how they are parallel transported via $\nabla$. This new parallel transport of the electric and magnetic field directions $\widetilde{\mathbf{e}}, \widetilde{\mathbf{h}}$ is governed by a different metric compatible connection $\widetilde{\nabla}$. Its torsion tensor controls the relative rotation rate between the two normal space framings $\mathbf{e}, \mathbf{h}$ and $\widetilde{\mathbf{e}}, \widetilde{\mathbf{h}}$.

Precisely, in this section we elucidate the following: If $\widetilde{\nabla}$ is another connection that is also metric compatible with $g$, and with the further property that the geodesic equation $\nabla_{\mathbf{t}}\mathbf{t} = 0$ holds for curves $\gamma(\sigma)$ if and only if $\widetilde{\nabla}_{\mathbf{t}}\mathbf{t} = 0$ also holds, then $\nabla$ and $\widetilde{\nabla}$ differ by one half the torsion tensor of $\widetilde{\nabla}$. In this setting the torsion tensor is determined by a single scalar torsion function, $\widetilde{\tau}(\mathbf{x})$. The function $\widetilde{\tau}(\gamma(\sigma))$ determines the relative rotation rate $\widetilde{\varphi}'(\sigma)$ of the angle $\widetilde{\varphi}(\sigma)$ between the $\mathbf{e}, \mathbf{h}$ frame parallel transported along $\gamma$ by $\nabla$, and the $\widetilde{\mathbf{e}}, \widetilde{\mathbf{h}}$ frame parallel transported by $\widetilde{\nabla}$. Thus, once one understands the parallel transport determined by the Riemannian connection $\nabla$, the scalar torsion function $\widetilde{\tau}$ can be specified as desired to control the rotation of the electric and magnetic field directions along specified families of non-intersecting light paths.

### 4.3.1 Levi-Civita Connections

Let $\nabla$ be the Levi-Civita connection for the metric g [33]. This means that

1. $\nabla$ is a connection: For all smooth vector fields X, Y, Z, W and smooth functions f, g $\nabla_X Y$ is also a smooth vector field, thought of at each point as a directional derivative of Y in the direction of X. Furthermore $\nabla$ is linear in the lower argument with respect to vector field addition and function scalar multiplication:

$$\nabla_{X+Y} Z = \nabla_X Z + \nabla_Y Z$$

$$\nabla_{fX} Y = f \nabla_X Y$$

As well, $\nabla$ is linear with respect to vector field addition in the upper argument, but satisfies a Leibniz rule with respect to function multiplication in that argument (so $\nabla_X Y$ is not a tensor with respect to the vector fields (X, Y)):

$$\nabla_X (Y + Z) = \nabla_X Y + \nabla_X Z$$

$$\nabla_X f Y = X(f) Y + f \nabla_X Y$$

2. $\nabla$ is metric compatible: Formally, this means that the tensor covariant derivative of $g$ is zero, i.e., for all smooth vector fields $X, Y, Z$,

$$\begin{aligned}(\nabla_X g)(Y,Z) &:= X(g(Y,Z)) - g(\nabla_X Y, Z) \\ &\quad - g(Y, \nabla_X Z) = 0\end{aligned}$$

Metric compatibility is most usefully thought of as a product rule for differentiating the $g$ inner products of vector fields. Adopting the usual notation $g(X,Y) = \langle X, Y\rangle$, metric compatibility can be rewritten as

$$X\langle Y,Z\rangle = \langle \nabla_X Y, Z\rangle + \langle Y, \nabla_X Z\rangle \tag{4.4}$$

3. $\nabla$ is torsion free: In other words, the torsion tensor

$$\mathcal{T}(X,Y) := \nabla_X Y - \nabla_Y X - [X,Y] \tag{4.5}$$

satisfies $\mathcal{T}(X,Y) \equiv 0$ for all vector fields $X, Y$. (The commutator vector field $[X,Y]$ above is defined to be the directional derivative operator $[X,Y](f) := X(Y(f)) - Y(X(f))$.)

Each Riemannian metric g has a unique Levi-Civita connection, as can be shown using properties (1-3). In fact, in local coordinates $((x^1, x^2 \ldots x^n))$ and corresponding tangent vector (directional derivatives) basis $(\partial/\partial x^1, \partial/\partial x^2, \ldots \partial/\partial x^n) = (\partial_1, \partial_2, \ldots \partial_n)$, one has

$$\nabla_{\partial_i} \partial_j = \Gamma_{ij}^k \partial_k$$

Here we have used the summation convention on the index $k$, namely that repeated indiced are summed over the index values and the $\Gamma_{ij}^k$ are the Christoffel symbols. They are uniquely determined from g via properties (1-3):

$$\Gamma_{ij}^k = \frac{1}{2} g^{kl} \left(\partial_j g_{il} + \partial_i g_{jl} - \partial_l g_{ij}\right) \tag{4.6}$$

Using the linearity and Leibniz rules (and the summation convention), for $X = X^k \partial_k$, $Y + Y^l \partial_l$ one can then compute all covariant derivatives:

$$\begin{aligned}\nabla_X Y &= X^k \left(\left(\partial_k Y^l\right) \partial_l + Y^l \nabla_{\partial_k} \partial_l\right) \\ &= X\left(Y^l\right) \partial_l + X^k Y^l \nabla_{\partial_k} \partial_l\end{aligned} \tag{4.7}$$

Notice that $\nabla_X Y$ can be computed at a point as soon as the vector field $Y$ is known along any curve passing through the point which has tangent vector $X$ there, since if $\phi(t_0) = p$, $\phi'(t_0) = X(p)$ then the directional derivative $X(f)$ can be computed via

$$X(f) = \frac{d}{dt} f(\gamma(t))|_{t=t_0} \tag{4.8}$$

This is relevant to the geodesic equation (4.10).

### 4.3.2 Geodesics

Stationary curves $\gamma$ with fixed endpoints, parameterized over an interval $I$, and for the total length functional, $L$,

$$\begin{aligned} L(\gamma) &= \int_I g\left(\gamma'(r), \gamma'(r)\right)^{1/2} dr \\ &= \int_I ||\gamma'(r)||_g dr \end{aligned} \tag{4.9}$$

are called geodesics. One can always parametrize $\gamma$ by metric arclength, i.e., so that $||\gamma'(\sigma)||_g = 1$. In this case and if $\sigma$ is set to zero at the initial point, then the Riemannian length of the curve image $\gamma([0,\sigma])$ is exactly $\sigma$. In our application to geometrical optics, $\frac{1}{c} L(\gamma)$ is the total travel time for light rays following $\gamma$.

Assuming a candidate geodesic is parametrized by arclength $\sigma$, one may write $\gamma'(\sigma) = \mathbf{t}(\sigma)$ for the unit tangent vector. Computing the first variation of the length integral, using properties (1-3) of the Levi-Civita connection (or alternately, a local coordinate chart and Christoffel symbol computations), one sees that the second order geodesic differential equation for $\gamma(\sigma)$,

$$\nabla_{\mathbf{t}} \mathbf{t} = 0 \tag{4.10}$$

is equivalent to stationarity of (4.9). Note that in local coordinates (4.7), (4.8), and (4.10) reads as

$$(\gamma^l)''(\sigma) + (\gamma^k)'(\sigma)(\gamma^j)'(\sigma)\Gamma^l_{jk} = 0 \tag{4.11}$$

This differential equation has unique solutions $\gamma(\sigma)$ for specified initial point and tangent vector. Such solutions are always parametrized by a multiple of arclength, where this multiple is given by the length of the initial tangent vector, since by metric compatibility (4.4),

$$\frac{d}{d\sigma}\langle \mathbf{t}, \mathbf{t}\rangle = \mathbf{t}\langle \mathbf{t}, \mathbf{t}\rangle = 2\langle \nabla_{\mathbf{t}} \mathbf{t}, \mathbf{t}\rangle \equiv 0$$

### 4.3.3 Metric Compatible Connections with Torsion

Following the ideas of Horsley [30], we now consider another connection $\widetilde{\nabla}$ which is also metric compatible to g but which has nonzero torsion tensor $\widetilde{\mathcal{T}}$, (4.5). In addition, we require that whenever $\gamma$ is a geodesic parametrized by a multiple of arclength, i.e., with constant length tangent vector $\mathbf{t} = \gamma'(\sigma)$, and so $\nabla_{\mathbf{t}}\mathbf{t} = 0$ holds, then also $\widetilde{\nabla}_{\mathbf{t}}\mathbf{t} = 0$ holds. In other words, we require that geodesics for the metric g are also geodesics ("autoparallels") for the connection $\widetilde{\nabla}$. This condition is used in section 4.4.3 to verify that the geometrical optics limit of Maxwell's equations holds for certain chiral media, with metric unit electric and magnetic field directions $\widetilde{\mathbf{e}}, \widetilde{\mathbf{h}}$ parallel translated along the (same) geodesic light paths, but by $\widetilde{\nabla}$ instead of by $\nabla$. In [30] this geometrical optics limit follows from an ansatz in section 5.B restricting the form of $\widetilde{\nabla}$. Here we show the converse, namely that Horsley's ansatz is forced by the metric compatibility and preservation of geodesics requirements.

**Proposition 1.** *Let $\widetilde{\nabla}$ be compatible to the Riemannian metric g in* (4.4)*, let $\nabla$ be the Levi-Civita connection for g, and assume that for any curve $\gamma(\sigma)$ parameterized by a multiple of arclength and for $\mathbf{t} := \mathbf{fl}'(\mathbf{\alpha})$,*

$$\nabla_{\mathbf{t}}\mathbf{t} = 0 \iff \widetilde{\nabla}_{\mathbf{t}}\mathbf{t} = 0 \tag{4.12}$$

*Then*

$$\widetilde{\nabla}_X Y = \nabla_X Y + \frac{1}{2}\widetilde{\mathcal{T}}(X, Y) \tag{4.13}$$

*where $\widetilde{\mathcal{T}}$ is the torsion tensor for $\widetilde{\nabla}$,* (4.5)*. Furthermore, the scalar-valued 3-tensor*

$$(X, Y, Z) \to \langle \widetilde{\nabla}_X Y - \nabla_X Y, Z \rangle \tag{4.14}$$

*is completely anti-symmetric, i.e., alternating.*

*Proof:* It is always true that the difference of two connections is a tensor, although connections themselves are not tensors. Indeed, consider the difference

$$\delta(X, Y) := \widetilde{\nabla}_X Y - \nabla_X Y$$

Note that $\delta$ is sum and function-multiplication linear in the $X$ argument, since each connection is. It is sum linear in the $Y$ argument for the same reason. To show $\delta$ is a tensor it

therefore suffices to verify that it is scalar function multiplication linear in the $Y$ argument. Using the Leibniz rule for each connection verifies this last property,

$$\begin{aligned}\delta(X, fY) &= \widetilde{\nabla}_X fY - \nabla_X fY \\ &= X(f)Y + f\widetilde{\nabla}_X Y - (X(f)Y + f\nabla_X Y) \\ &= f\delta(X, Y)\end{aligned}$$

Thus, since we have shown $\delta$ is a tensor, its value at a point only depends on the values of the corresponding vector fields at that point and not on how they are extended smoothly away from the point. So to compute $\delta(X, X)$ we may assume that $X$ is (any smooth extension of) the tangent field along a geodesic parametrized by a multiple of arclength, i.e., for which both $\widetilde{\nabla}_X X = \nabla_X X = 0$, from (4.11), at the point under consideration. By the tensor nature of $\delta$ We deduce that $\delta(X, X) = 0$ for all vectors $X$, or equivalently that $\delta$ is antisymmetric,

$$\delta(X, Y) = -\delta(Y, X) \tag{4.15}$$

since,

$$\begin{aligned}0 &= \delta(X + Y, X + Y) \\ &= \delta(X, X) + \delta(X, Y) + \delta(Y, X) + \delta(Y, Y) \\ &= \delta(X, Y) + \delta(Y, X)\end{aligned}$$

Thus,

$$\begin{aligned}2\delta(X, Y) &= \delta(X, Y) - \delta(Y, X) \\ &= \widetilde{\nabla}_X Y - \nabla_X Y - (\widetilde{\nabla}_Y X - \nabla_Y X) \\ &= \widetilde{\nabla}_X Y - \widetilde{\nabla}_Y X - [X, Y] - (\nabla_X Y - \nabla_Y X - [X, Y]) \\ &= \widetilde{\mathcal{T}}(X, Y) - 0 = \widetilde{\mathcal{T}}(X, Y)\end{aligned}$$

since the torsion of the Levi-Civita connection is zero. This shows (4.13). Now consider the scalar covarient three tensor defined in (4.14). Since we have shown antisymmetry with respect to $(X, Y)$ in (4.15) it suffices to show anti-symmetry as well with respect to $(Y, Z)$, since antisymmetry with respect to $(X, Z)$ follows from the first two. Via multilinearity, as in the argument for (4.15), it suffices to show

$$\langle \widetilde{\nabla}_X Y - \nabla_X Y, Y \rangle = 0$$

But by metric compatibility for each connection (4.4)

$$\begin{aligned} X\langle Y,Y\rangle &= 2\langle \widetilde{\nabla}_X Y, Y\rangle = 2\langle \nabla_X Y, Y\rangle \\ \Rightarrow \langle \widetilde{\nabla}_X Y, Y\rangle &= \langle \nabla_X Y, Y\rangle \\ \Rightarrow \langle \widetilde{\nabla}_X Y, Y\rangle - \langle \nabla_X Y, Y\rangle &= 0 \end{aligned}$$

□

The following theorem quantifies how the torsion of $\widetilde{\nabla}$ causes the normal spaces to geodesics to be rotated differently when parallel transported by $\widetilde{\nabla}$ rather than by $\nabla$.

**Theorem 2.** *Let $g$ be a Riemannian metric in a $3-$dimensional space. Let $\nabla$ be the associated Levi-Civita connection, and let $\widetilde{\nabla}$ be another metric compatible connection* (4.4) *satisfying* (4.12). *Then $\widetilde{\nabla}$ is determined by a scalar function $\widetilde{\tau}$ via the identity,*

$$\widetilde{\nabla}_X Y = \nabla_X Y + \widetilde{\tau}\, X \times Y \tag{4.16}$$

*(Here $X \times Y$ is computed in the Riemannian tangent space at any point by expressing $X, Y$ as linear combinations of any positively oriented orthonormal basis there, computing the usual cross product of these linear combination coordinates, and definining $X \times Y$ to be the vector with those resulting coordinates.)*

*Furthermore, let $\gamma(\sigma)$ be a geodesic parametrized by arclength for $g$, so that its unit tangent vector $\mathbf{t}(\sigma)$ satisfies* (4.10) *and* (4.12). *Let $\mathbf{e}, \mathbf{h}$ be unit vectors along $\gamma$ which are parallel transported by $\nabla$, i.e.,*

$$\nabla_{\mathbf{t}}\mathbf{e} = \nabla_{\mathbf{t}}\mathbf{h} = 0$$

*and so that $(\mathbf{t}, \mathbf{e}, \mathbf{h})$ are initially and therefore everywhere an orthonormal frame along $\gamma$, with respect to $g$. Analogously, let $\widetilde{\mathbf{e}}, \widetilde{\mathbf{h}}$ be unit vectors along $\gamma$ which are parallel transported by $\widetilde{\nabla}$, i.e.,*

$$\widetilde{\nabla}_{\mathbf{t}}\widetilde{\mathbf{e}} = \widetilde{\nabla}_{\mathbf{t}}\widetilde{\mathbf{h}} = 0$$

*so that $(\mathbf{t}, \widetilde{\mathbf{e}}, \widetilde{\mathbf{h}})$ are also a positively oriented framing along $\gamma$. Let $\widetilde{\varphi}(\sigma)$ describe the angle from the framing $(\mathbf{e}(\sigma), \mathbf{h}(\sigma))$ to the framing $(\widetilde{\mathbf{e}}(\sigma), \widetilde{\mathbf{h}}(\sigma))$ in the normal planes to $\mathbf{t}(\sigma)$. In other words,*

$$\begin{aligned} \widetilde{\mathbf{e}} &= \cos\widetilde{\varphi}\,\mathbf{e} + \sin\widetilde{\varphi}\,\mathbf{h} \\ \widetilde{\mathbf{h}} &= -\sin\widetilde{\varphi}\,\mathbf{e} + \cos\widetilde{\varphi}\,\mathbf{h} \end{aligned} \tag{4.17}$$

*Then,*

$$\widetilde{\varphi}\,'(\sigma) = -\widetilde{\tau}(\gamma(\sigma)) \tag{4.18}$$

*where $\widetilde{\tau}$ is the scalar function defined in* (4.16)*.*

*Proof:* Up to a constant multiple, the only alternating $3-$tensor in the vector space $\mathbb{R}^3$ is the determinant, e.g., as a function of its three columns. Thus in this dimension and at the tangent space to any point of our $3-$dimensional space, the alternating form in (4.14) is a multiple of the determinant. (We define determinant of $X, Y, Z$ at the tangent space to any point to be the determinant of the coordinates of $X, Y, Z$ with respect to any positively oriented orthonormal basis of the tangent space.) Thus

$$\langle \widetilde{\nabla}_X Y - \nabla_X Y, Z\rangle = \widetilde{\tau}\, det(X, Y, Z)$$

for some scalar function $\widetilde{\tau}$, and therefore $\widetilde{\nabla}_X Y - \nabla_X Y$ must be $\widetilde{\tau}\, X \times Y$, as a consequence. Thus (4.16) holds. To check (4.18) we note that $\langle \widetilde{\mathbf{e}}, \mathbf{e}\rangle = \cos\widetilde{\varphi}$ from (4.17), so

$$\begin{aligned}
\frac{d}{d\sigma}\cos\widetilde{\varphi}(\sigma) &= \frac{d}{d\sigma}\langle \widetilde{\mathbf{e}}, \mathbf{e}\rangle = \mathbf{t}\langle \widetilde{\mathbf{e}}, \mathbf{e}\rangle \\
&= \langle \widetilde{\nabla}_{\mathbf{t}}\widetilde{\mathbf{e}}, \mathbf{e}\rangle + \langle \widetilde{\mathbf{e}}, \widetilde{\nabla}_{\mathbf{t}}\mathbf{e}\rangle = 0 + \langle \widetilde{\mathbf{e}}, \widetilde{\nabla}_{\mathbf{t}}\mathbf{e}\rangle \\
&= \langle \widetilde{\mathbf{e}}, \nabla_{\mathbf{t}}\mathbf{e} + \widetilde{\tau}\,\mathbf{t}\times\mathbf{e}\rangle = \langle \widetilde{\mathbf{e}}, \widetilde{\tau}\,\mathbf{t}\times\mathbf{e}\rangle \\
&= \langle \cos\widetilde{\varphi}\,\mathbf{e} + \sin\widetilde{\varphi}\,\mathbf{h}, \widetilde{\tau}\,\mathbf{t}\times\mathbf{e}\rangle = \widetilde{\tau}\,\sin\widetilde{\varphi}
\end{aligned}$$

But we may alternately compute,

$$\frac{d}{d\sigma}\cos\widetilde{\varphi}(\sigma) = -\sin\widetilde{\varphi}(\sigma)\widetilde{\varphi}'(\sigma)$$

so we deduce $\widetilde{\tau}(\gamma(\sigma)) = -\widetilde{\varphi}'(\sigma)$. □

**Remark 1:** Applying this to geometrical optics, the Riemannian arclength parameter $\sigma$ is related to time $t$ by $c\,dt = d\sigma$, so we also have

$$\frac{d}{dt}\cos(\widetilde{\varphi}(\sigma(t)) = -c\,\widetilde{\tau}(\widetilde{\varphi}(\sigma(t))$$

**Remark 2:** An analogous result to the theorem above holds in higher dimensions, i.e. one can consider how orthogonal framings of the normal spaces along the geodesic $\gamma$ are parallel transported with respect to $\nabla$ and $\widetilde{\nabla}$, in the setting of Proposition 1. The torsion tensor of $\widetilde{\nabla}$ measures how the rotation matrix relating the two frames is changing with respect to arclength.

## 4.4 Light Paths and Polarization Control for Isotropic Index of Refraction

In the special case of geometrical optics for isotropic time-independent media, the description of geodesic light paths simplifies, as we review below. This description can be combined with the results of the previous section to give an explicit way to control the twisting of the electric and magnetic field directions along light paths.

### 4.4.1 Light Paths in Isotropic Media

By isotropic index of refraction we mean that the index of refraction $n$ in the total time integral in (4.1) depends on location but not on light direction. In other words, for a curve $\gamma(r)$ we have

$$n\, d\sigma = n(\gamma(r))||\gamma'(r)||dr$$

with

$$||\gamma'(r)|| = (\gamma'(r) \cdot \gamma'(r))^{\frac{1}{2}}$$

being the usual Euclidean norm, expressible in terms of the Euclidean dot product. In the study of conformal geometry one would say that the light paths for the isotropic index $n$ are geodesics for the conformally Euclidean metric

$$g(X, Y) = n^2 X \cdot Y \tag{4.19}$$

The geometry of the geodesic curves and parallel transport for conformally Euclidean metrics in $\mathbb{R}^3$ can be studied by using the relationship between the Euclidean connection $D$, which is just the usual directional derivative of vector fields

$$D_X Y = X(Y^k)\partial_k$$

and the Levi-Civita connection $\nabla$ for the conformal metric with conformal factor $n$. The two connections are related by

$$\nabla_X Y = D_X Y + \frac{X(n)}{n} Y + \frac{Y(n)}{n} X - (X \cdot Y)\frac{\text{grad}(n)}{n} \tag{4.20}$$

where $\text{grad}(n)$ is the Euclidean gradient of $n$. This expression for the difference tensor $\nabla_X Y - D_X Y$ is a special case of a general formula [34] for the Levi-Civita connections of

conformal metrics, and can be checked in local coordinates by comparing their respective Christoffel symbols in (4.6), which are closely related because the metrics are scalar function multiples of each other.

Let $\gamma(s)$ be a geodesic for $g$, but parameterized by Euclidean arclength, $||\gamma'(s)|| = 1$. Write $\mathbf{T}(s) = \gamma'(s)$ for the Euclidean tangent vector, so that $\mathbf{t} = \frac{1}{n}\mathbf{T}$ is the unit tangent vector with respect to $g$. As before, the geodesic equation for the metric $g$ is

$$\nabla_{\mathbf{t}}\mathbf{t} = 0$$

Thus, since $\mathbf{T} = n\,\mathbf{t}$,

$$\begin{aligned} \nabla_{\mathbf{T}}\mathbf{T} &= \nabla_{n\mathbf{t}} n\mathbf{t} = n^2\,\nabla_{\mathbf{t}}\mathbf{t} + n\,\mathbf{t}(n)\,\mathbf{t} \\ &= 0 + n\,\mathbf{t}(n)\,\mathbf{t} = \mathbf{T}(n)\,\mathbf{t} = \frac{\mathbf{T}(n)}{n}\mathbf{T} \end{aligned} \tag{4.21}$$

Note that e.g., $\mathbf{T}(n)$ in the formula above is shorthand for the directional derivative of $n$, at the point $\gamma(s)$, in the direction $\mathbf{T}(s)$, i.e., $\mathrm{grad}(n)\cdot\mathbf{T}$. Compare to $\nabla_{\mathbf{T}}\mathbf{T}$ computed with (4.20):

$$\nabla_{\mathbf{T}}\mathbf{T} = D_{\mathbf{T}}\mathbf{T} + 2\frac{\mathbf{T}(n)}{n}\mathbf{T} - (\mathbf{T}\cdot\mathbf{T})\frac{\mathrm{grad}(n)}{n} \tag{4.22}$$

Since $D_{\mathbf{T}}\mathbf{T}$ is the directional derivative of $\gamma'(s)$ in the direction of $\gamma'(s)$ it is nothing more than $\gamma''(s)$, (4.11). Equating the two expressions for $\nabla_{\mathbf{T}}\mathbf{T}$, using $\mathbf{T}\cdot\mathbf{T} = 1$ and solving for $\gamma''(s)$ yields

$$\begin{aligned} \gamma''(s) &= \frac{\mathrm{grad}(n)}{n} - \frac{\mathbf{T}(n)}{n}\,\mathbf{T} \\ = \frac{\mathrm{grad}(n)}{n} - (\mathbf{T}\cdot\frac{\mathrm{grad}(n)}{n})\mathbf{T} &= \frac{1}{n}\mathrm{grad}(n)^{\perp} \end{aligned} \tag{4.23}$$

where $\mathrm{grad}(n)^{\perp}$ is the part of $\mathrm{grad}(n)$ perpendicular to $\gamma'$. Written in the equivalent form,

$$\frac{d}{ds}(n\,\gamma'(s)) = \mathrm{grad}(n)$$

This equation is known in geometrical optics as the ray equation associated to the Eikonal equation for isotropic media [32]. We summarize the above discussion with,

**Proposition 3.** *Geodesic (light) rays for the isotropic refractive index function $n$, parameterized by Euclidean arclength, may be found by solving initial value problems for first order systems of six differential equations:*

$$\begin{aligned}\gamma'(s) &= \mathbf{T}(s)\\ \mathbf{T}'(s) &= \frac{1}{n}\text{grad}(n)^{\perp}\\ \gamma(0) &= x_0\\ \mathbf{T}(0) &= \mathbf{T}_0, \text{ with } ||\mathbf{T}_0|| = 1\end{aligned} \tag{4.24}$$

The system (4.24) can be solved easily by numerical methods, but closed form solutions are unlikely. For our purposes (4.24) provides a geometric understanding of the shape of geodesic light rays in $\mathbb{R}^3$, which from a Euclidean point of view are seen to bend around regions of larger refractive index in a precise way.

**Example 1**: If there is an open subset of a plane $\pi$ having the property that $\text{grad}(n) \in \pi$ for all points in this subset, then any geodesic with $\gamma(0) \in \pi$, $\gamma'(0) \in \pi$ satisfies $\gamma(s) \in \pi$ as long as $\text{grad}(n(\gamma(s)) \in \pi$ holds. In terms of (4.24), that is because the system can already be solved uniquely in $\pi$, and so this will be the unique solution in $\mathbb{R}^3$ as well. A consequence of this fact is that any light ray hitting a generalized Luneburg lens with radial symmetry will remain in the plane containing the initial point of incidence, initial direction vector there, the focal point and the center point of the lens.

**Example 2**: For the Luneburg lens [35] normalized to the unit ball, and then restricted to a cross-sectional unit disk, and with index of refraction

$$n(r) = \sqrt{2 - r^2}$$

the portions of the ellipses with implicit equations

$$\frac{x^2}{a^2} + \frac{y^2}{b^2} = 1$$

inside the unit disc are geodesic arcs, if and only if $a^2 + b^2 = 2$. We verify this fact as follows: Parameterize the ellipses by $\theta$,

$$\begin{bmatrix} x(\theta) \\ y(\theta) \end{bmatrix} = \begin{bmatrix} b\ \cos\theta \\ a\ \sin\theta \end{bmatrix} \tag{4.25}$$

This is not a parameterization by arclength so in order to verify (4.23) we use the acceleration decomposition formula for arbitrary parameterizations $\phi(t)$, with $s(t)$ the arclength function, $\frac{ds}{dt} = ||\phi'(t)|| := v$:

$$\begin{aligned}\mathbf{T}(s) = \frac{1}{v}\phi'(t) \implies \phi'(t) = v\mathbf{T}(s)\\ \implies \phi''(t) = v'(t)\mathbf{T}(s) + (v(t))^2\,\mathbf{T}'(s)\end{aligned} \tag{4.26}$$

Note $\mathbf{T}'(s)$ points in a normal direction, $0 = \frac{d}{ds}(\mathbf{T} \cdot \mathbf{T}) = 2\mathbf{T}' \cdot \mathbf{T}$.
In fact, for nonzero $\mathbf{T}'$ one defines the curvature and the unit normal $\mathbf{N}$ by

$$k(s) := ||\mathbf{T}'(s)||, \quad \mathbf{N}(s) := \frac{1}{k(s)}\mathbf{T}'(s)$$

So, using $\mathbf{T}' = \frac{1}{n}\text{grad}(n)^{\perp}$ we check that the normal components of the $\phi''$ equation agree, i.e., after dividing by $v^2$:

$$\frac{1}{v^2}\phi''(t) \cdot \mathbf{N} = \frac{1}{n}\text{grad}(n(\phi(t)) \cdot \mathbf{N}$$

From the parameterization in (4.25) we have,

$$\phi'(\theta) = \begin{bmatrix} -a\,\sin\theta \\ b\,\cos\theta \end{bmatrix}, \phi''(\theta) = \begin{bmatrix} -a\,\cos\theta \\ -b\,\sin\theta \end{bmatrix}$$

and $\mathbf{N}$ is parallel to $[b\cos\theta, a\sin\theta]^T$. So it suffices to check,

$$\frac{1}{a^2\sin\theta^2 + b^2\cos\theta^2}\phi''(\theta) \cdot \begin{bmatrix} b\,\cos\theta \\ a\,\sin\theta \end{bmatrix}$$
$$= \frac{1}{n}\text{grad}(n(\phi(\theta))) \cdot \begin{bmatrix} b\,\cos\theta \\ a\,\sin\theta \end{bmatrix}$$

Since

$$\frac{1}{n}\text{grad}(n(\mathbf{x})) = -\frac{\mathbf{x}}{\mathbf{2} - |\mathbf{x}|^{\mathbf{2}}}$$

this reduces to checking whether,

$$\frac{-ab}{a^2\sin\theta^2 + b^2\cos\theta^2} = \frac{-ab}{2 - a^2\cos\theta^2 - b^2\sin\theta^2}$$

which holds if and only if the denominators agree, i.e., $a^2 + b^2 = 2$.

**Remark:** The discussion and example above is not the usual way in which generalized Luneburg lens geodesics are studied for radial indices of refraction. Since rotation about the origin is an isometry in that case, there is an associated conserved quantity along geodesic curves, which lets one reduce the geodesic problem to a single first order differential equation, which is separable in the $(r, \theta)$ coordinate system [35].

### 4.4.2 Measuring the Twisting of Light for Isotropic Index of Refraction

For isotropic index of refraction $n$, Rytov's field vector rotation law [36–38] quantifies the rotation rate between the Euclidean Frenet framing of a geometrical optics light path,

and a framing $(\mathbf{e}, \mathbf{h})$ parallel transported by the Levi-Civita connection $\nabla$. We review Rytov's law and then combine it with Theorem 2, to yield a formula for how the framing $(\widetilde{\mathbf{e}}, \widetilde{\mathbf{h}})$, parallel transported by $\widetilde{\nabla}$, rotates relative to the Frenet framing. This relationship is a step in choosing an appropriate scalar torsion function $\widetilde{\tau}$ (4.18) in order to control polarization along a geodesic flow, in the case of isotropic media, (4.44).

Recall the Frenet system for a curve $\gamma(s)$ parameterized by Euclidean arclength $s$ in $\mathbb{R}^3$ [39]: For the unit vectors $\mathbf{T}(s) := \gamma'(s), \mathbf{N}(s) := \dfrac{\mathbf{T}'(s)}{||\mathbf{T}'(s)||}, \mathbf{B} := \mathbf{T} \times \mathbf{N}$, curvature function $k := ||\mathbf{T}'|| \neq 0$, and Frenet torsion function $\tau := \mathbf{N}' \cdot \mathbf{B}$,

$$\begin{aligned} \mathbf{T}' &= k\,\mathbf{N} \\ \mathbf{N}' &= -k\,\mathbf{T} + \tau\,\mathbf{B} \\ \mathbf{B}' &= -\tau\,\mathbf{N} \end{aligned} \tag{4.27}$$

**Theorem 4.** *(Rytov's field vector rotation law [36–38]) Let $\gamma(s)$ be a geodesic curve for the conformally Euclidean metric, $g(X, Y) = n^2 X \cdot Y$,* (4.23)*, parameterized by Euclidean arclength and having nonzero curvature $k$. Consider $\varphi'(s)$, where $\varphi(s)$ is the angle from the Frenet framing $(\mathbf{N}, \mathbf{B})$ of the normal spaces to $T$ along $\gamma$, to a $g-$orthonormal framing $(\mathbf{e}, \mathbf{h})$ parallel transported by the Levi-Civita connection $\nabla$ for $g$. Then*

$$\varphi'(s) = -\tau(s) \tag{4.28}$$

*where $\tau$ is the Frenet torsion of $\gamma$. In particular, if $\gamma$ is a planar curve as in Example 1 after Proposition 3 then the normalized Frenet framing $\left(\dfrac{1}{n}\mathbf{N}, \dfrac{1}{n}\mathbf{B}\right)$ is parallel transported by $\nabla$.*

*Proof:* After normalizing our two framings to have unit length with respect to $g$, they are related by

$$\begin{aligned} \mathbf{e} &= \cos\varphi\,\frac{1}{n}\mathbf{N} + \sin\varphi\,\frac{1}{n}\mathbf{B} \\ \mathbf{h} &= -\sin\varphi\,\frac{1}{n}\mathbf{N} + \cos\varphi\,\frac{1}{n}\mathbf{B} \end{aligned} \tag{4.29}$$

Thus

$$\begin{aligned} \langle \mathbf{e}, \frac{1}{n}\mathbf{B}\rangle &= \sin\ \varphi(s) \\ \Rightarrow \mathbf{T}\langle \mathbf{e}, \frac{1}{n}\mathbf{B}\rangle &= \cos\ \varphi(s)\,\varphi'(s) \end{aligned} \tag{4.30}$$

By metric compatibility for $\nabla$ (Eqs. (4.4), (4.20)) we can also compute

$$\begin{aligned}
\mathbf{T}\langle \mathbf{e}, \frac{1}{n}\mathbf{B}\rangle &= \langle \nabla_{\mathbf{T}}\, \mathbf{e}, \frac{1}{n}\mathbf{B}\rangle + \langle \mathbf{e}, \nabla_{\mathbf{T}} \frac{1}{n}\mathbf{B}\rangle \\
&= 0 + \langle \mathbf{e}, \mathbf{T}\left(\frac{1}{n}\right)\mathbf{B} + \frac{1}{n}(D_{\mathbf{T}}\mathbf{B} + \frac{\mathbf{T}(n)}{n}\mathbf{B} + \frac{\mathbf{B}(n)}{n}\mathbf{T})\rangle \\
&= \langle \mathbf{e}, -\frac{\mathbf{T}(n)}{n^2}\mathbf{B} + \frac{1}{n}(D_{\mathbf{T}}\mathbf{B} + \frac{\mathbf{T}(n)}{n}\mathbf{B} + \frac{\mathbf{B}(n)}{n}\mathbf{T})\rangle \\
&= \langle \mathbf{e}, \frac{1}{n}(D_{\mathbf{T}}\mathbf{B})\rangle = \langle \mathbf{e}, \frac{1}{n}(-\tau\,\mathbf{N})\rangle \\
&= -\cos\varphi(s)\,\tau
\end{aligned} \tag{4.31}$$

Comparing (4.30) and (4.31), and noting that the Levi-Civita parallel transported frame can always be adjusted by a constant rotation along all of $\gamma$ so as to make $\cos\varphi$ nonzero at any desired value of $s$, proves (4.28). If $\gamma$ is a planar curve then the binormal $\mathbf{B}$ is a (constant) plane normal, (i.e., $\tau = 0$) so the normalized Frenet framing is parallel transported by $\nabla$. (This last result is well known: Using (4.20) one immediately sees that $\nabla_{\mathbf{T}}\left(\frac{1}{n}\mathbf{B}\right) = 0$ in that case.) □

We demonstrate Theorem 4 in a cylindrical graded index optical fiber, using the Ray Optics Module of COMSOL Multiphysics. The graded index fiber has a parabolic refractive index profile given by,

$$n(\rho) = n_1\left(1 - 2\Delta\left(\frac{\rho}{a}\right)^2\right) \tag{4.32}$$

where

$$\Delta = \frac{n_1 - n_2}{2n_1^2} \tag{4.33}$$

$a$ is the radius of cylindrical fiber, $n_1$ and $n_2$ are the core and cladding refractive indices respectively. A skew ray incident on such a fiber creates an elliptical helix trajectory with nonzero curvature, $k(s)$ and curve torsion, $\tau(s)$. The core and cladding refractive indices were chosen to be $n_1 = 1.5$ and $n_2 = 1.4$ respectively. Figure 4.2 shows a particular skew ray and its elliptical helix trajectory. The incident polarization was chosen to be $\hat{\mathbf{y}}$ polarized. We plot the evolution of this polarization vector with respect to the Frenet-Serret frame. The parallel transport of this vector indeed obeys Rytov's rotation law, (4.28). The ray curvature $k(s)$, curve torsion $\tau(s)$, and the derivative of Rytov's rotation angle $\varphi'(s)$ are shown in Fig. 4.2 (e).

Combining Theorems 2, 4 yields:

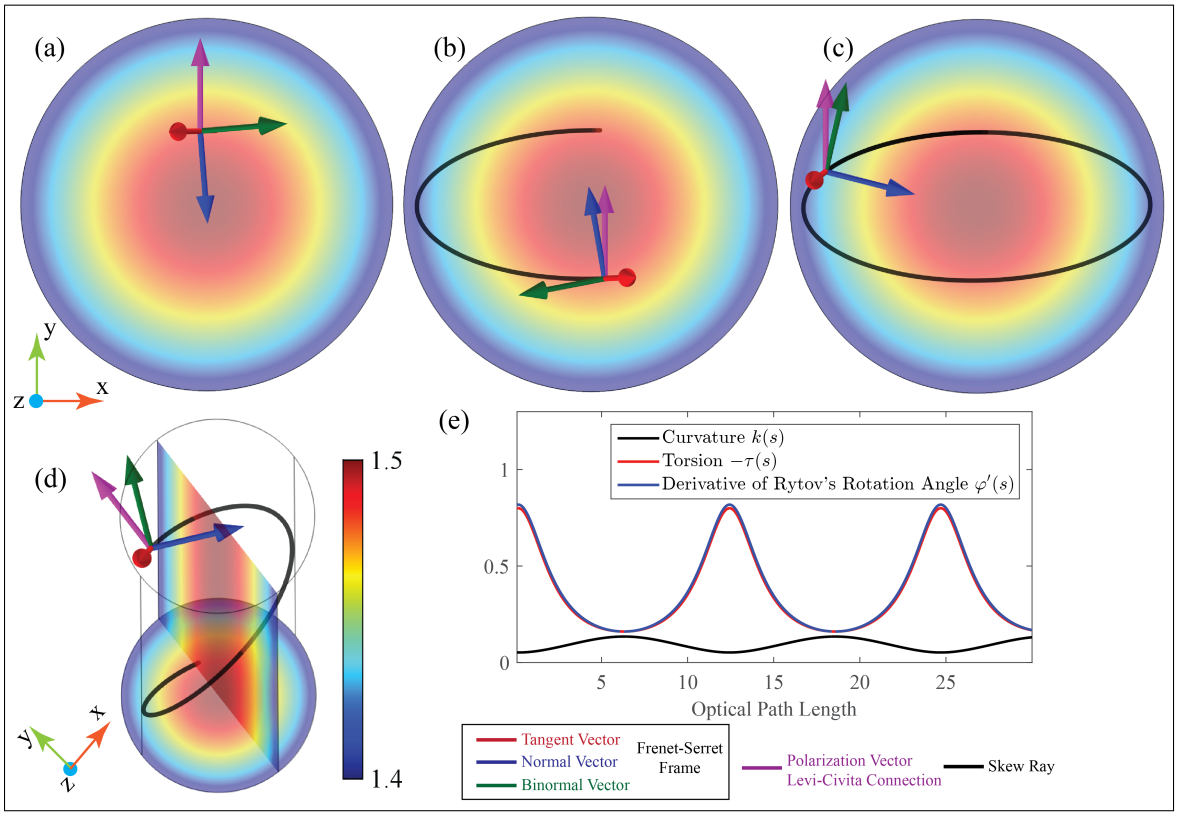


**Figure 4.2**: The parallel transport of polarization vector for a particular skew ray in a cylindrical gradient index optical fiber. The ray trajectory has nonzero curvature and curve torsion. (a)-(c) show the ray trajectory at different instances along with the instantaneous Frenet-Serret frame. (d) shows the perspective view of the nonplanar ray. (e) shows the curvature, $k(s)$ and curve torsion, $\tau(s)$ of the ray. The polarization vector parallel transport obeys Rytov's field vector rotation law. The derivative of Rytov's rotation angle, $\varphi'(s)$ and negative of curve torsion, $-\tau(s)$ are plotted and they satisfy (4.28).

**Proposition 5.** *Let $\gamma(s)$ be a geodesic curve for the conformally Euclidean metric, $g(X,Y) = n^2 X \cdot Y$, (4.23), with $\gamma$ parameterized by Euclidean arclength, having non-zero Frenet curvature $k$, and with Frenet torsion $\tau$. Consider the angles $\varphi(s)$: the angle from the Frenet framing $(\mathbf{N},\mathbf{B})$ along $\gamma$ to a $g-$orthonormal framing $(\mathbf{e},\mathbf{h})$ parallel transported by the Levi-Civita connection $\nabla$; and $\widetilde{\varphi}(s)$: the angle from the $(\mathbf{e},\mathbf{h})$ framing to the $(\widetilde{\mathbf{e}},\widetilde{\mathbf{h}})$ framing parallel transported by the connection $\widetilde{\nabla}$ defined by*

$$\widetilde{\nabla}(X,Y) := \nabla(X,Y) + \widetilde{\tau}\, X \times Y$$

*(so with torsion tensor $\widetilde{\mathcal{T}}(X,Y) = 2\,\widetilde{\tau}\, X \times Y$). Then the angle from the Frenet framing $(\mathbf{N},\mathbf{B})$ to $(\widetilde{\mathbf{e}},\widetilde{\mathbf{h}})$, given by $\varphi + \widetilde{\varphi}$, changes along $\gamma$ according to*

$$n\frac{d}{d\sigma}(\varphi+\widetilde{\varphi}) = \frac{d}{ds}(\varphi+\widetilde{\varphi}) = -\tau - \widetilde{\tau}\, n \tag{4.34}$$

*where $\sigma$ is the optical path length parameter with respect to $g$.*

*Proof.* : This result follows immediately from (4.28) and (4.18) and from the chain rule

$$\frac{d}{ds} = \frac{d\sigma}{ds}\frac{d}{d\sigma} = n\,\frac{d}{d\sigma}$$

□

### 4.4.3 Equation of Torsion Optics

Now that we have established the evolution of polarization along a light path, in terms of well defined geometric quantities, the Frenet curve torsion $\tau$ and the the scalar torsion $\widetilde{\tau}$, we can describe the materials means of controlling polarization. This control leverages the inherent connection between geometry and material properties in Maxwell's equations. First, we provide the constitutive relations for our medium to establish the conventions we employ for the material properties. The constitutive relations for a general bi-isotropic medium are given by,

$$\begin{aligned} \mathbf{D} &= \epsilon\mathbf{E} + \xi\mathbf{H} \\ \mathbf{B} &= \mu\mathbf{H} + \zeta\mathbf{E} \end{aligned} \tag{4.35}$$

where, **D**, **B**, **E**, **H**, $\epsilon$, and $\mu$ are the usual electromagnetic quantities. $\xi$ and $\zeta$ are the magneto-electric coupling coefficients which are intrinsic properties of the medium. $\xi$ and $\zeta$ can be related to the reciprocity $\chi$ and chirality $\kappa$ parameters as

$$\begin{aligned} \xi &= \sqrt{\epsilon_0\mu_0}\,(\chi + i\kappa) \\ \zeta &= \sqrt{\epsilon_0\mu_0}\,(\chi - i\kappa) \end{aligned} \tag{4.36}$$

where we use $\exp(-i\omega t)$, as our convention for the harmonic time dependence. For a reciprocal medium (Pasteur medium), $\chi = 0$, $\kappa \neq 0$, which is the medium of interest for torsion optics. The constitutive relationship then reduces to,

$$\begin{aligned} \mathbf{D} &= \epsilon\mathbf{E} + i\frac{\kappa}{c}\mathbf{H} \\ \mathbf{B} &= \mu\mathbf{H} - i\frac{\kappa}{c}\mathbf{E} \end{aligned} \tag{4.37}$$

where, $1/\sqrt{\epsilon_0\mu_0} = c$ is the speed of light in free space. The equation of torsion optics for this medium is given by

$$\kappa = -\frac{1}{\mathsf{k}_0}\frac{d\widetilde{\varphi}}{ds} = \frac{1}{\mathsf{k}_0}\widetilde{\tau}\,n \tag{4.38}$$

where $\mathsf{k}_0$ is the free-space wave vector,

$$\mathsf{k}_0 = \frac{\omega}{c} \tag{4.39}$$

and not to be confused with the Frenet curvature. We note that the scalar torsion induced by a given chirality will depend on frequency. Also, the chirality itself is likely to depend on frequency, especially if resonant metamaterials are employed to implement it. Thus, the bandwidth of polarization control may be limited, unless some control over the frequency dependence of the chirality can be engineered.

### 4.4.4 Elimination of Skew Aberration: General Form

Consider an incident plane wave propagating in the $\hat{\mathbf{z}}$ direction, with electric field polarized to the $\hat{\mathbf{y}}$ direction (so magnetic field is polarized to the $-\hat{\mathbf{x}}$ direction). We construct a scalar torsion function $\widetilde{\tau}$ to constrain the electric field to that it remains perpendicular to the $\hat{\mathbf{x}}$ direction as follows: Following (4.34) we require:

$$n\,\widetilde{\mathbf{e}} = \cos(\varphi + \widetilde{\varphi})\mathbf{N} + \sin(\varphi + \widetilde{\varphi})\mathbf{T} = \frac{\mathbf{T} \times \hat{\mathbf{x}}}{|\mathbf{T} \times \hat{\mathbf{x}}|} \tag{4.40}$$

Taking dot products with $\mathbf{N}, \mathbf{B}$ and clearing the denominators yields the two equations

$$\begin{aligned} |\mathbf{T} \times \hat{\mathbf{x}}|\ \cos(\varphi + \widetilde{\varphi}) &= (\mathbf{T} \times \hat{\mathbf{x}}) \cdot \mathbf{N} \\ |\mathbf{T} \times \hat{\mathbf{x}}|\ \sin(\varphi + \widetilde{\varphi}) &= (\mathbf{T} \times \hat{\mathbf{x}}) \cdot \mathbf{B} \end{aligned} \tag{4.41}$$

Note that the triple products on the right are Euclidean determinants of the three vectors as, e.g., columns of a matrix. So, expanding $\hat{\mathbf{x}}$ in terms of the Frenet frame, using determinant multilinearity and antisymmetry and the positive orientation of the Frenet frame, we have

$$\begin{aligned} (\mathbf{T} \times \hat{\mathbf{x}}) \cdot \mathbf{N} &= -\hat{\mathbf{x}} \cdot \mathbf{B} \\ (\mathbf{T} \times \hat{\mathbf{x}}) \cdot \mathbf{B} &= \hat{\mathbf{x}} \cdot \mathbf{N} \end{aligned} \tag{4.42}$$

Taking the quotient of the two equations in (4.41), using (4.42) and then clearing the denominator yields

$$(\hat{\mathbf{x}} \cdot \mathbf{B})\ \tan(\varphi + \widetilde{\varphi}) = -\hat{\mathbf{x}} \cdot \mathbf{N}$$

We may differentiate this identity with respect to Euclidean arclength $s$ and use the Frenet equations (4.27) to expand derivatives of the Frenet frame vectors, obtaining

$$\begin{aligned} -\tau(\hat{\mathbf{x}} \cdot \mathbf{N})\ \tan(\varphi + \widetilde{\varphi}) + (\hat{\mathbf{x}} \cdot \mathbf{B})(\sec^2(\varphi + \widetilde{\varphi}))(\varphi + \widetilde{\varphi})' \\ = -\hat{\mathbf{x}} \cdot (\tau\,\mathbf{B} - k\,\mathbf{T}) \end{aligned}$$

Using (4.41) and (4.29) to substitute for the trig functions above, as well as (4.34) to express $(\varphi + \widetilde{\varphi})'$, and clearing the common denominator $\hat{\mathbf{x}} \cdot \mathbf{B}$ yields

$$\begin{aligned} &\tau\,(\hat{\mathbf{x}} \cdot \mathbf{N})^2 + |\mathbf{T} \times \hat{\mathbf{x}}|^2(-\tau - n\,\widetilde{\tau}) \\ &= -\tau(\hat{\mathbf{x}} \cdot \mathbf{B})^2 + k\,(\hat{\mathbf{x}} \cdot \mathbf{T})(\hat{\mathbf{x}} \cdot \mathbf{B}) \end{aligned} \tag{4.43}$$

Since,

$$|\mathbf{T} \times \hat{\mathbf{x}}|^2 = (\hat{\mathbf{x}} \cdot \mathbf{N})^2 + (\hat{\mathbf{x}} \cdot \mathbf{B})^2 = 1 - (\hat{\mathbf{x}} \cdot \mathbf{T})^2$$

we see that the Frenet torsion $\tau$ terms in (4.43) cancel, and we may solve for the scalar torsion function $\widetilde{\tau}$

$$\widetilde{\tau} = -\frac{k}{n}\,\frac{(\hat{\mathbf{x}} \cdot \mathbf{T})(\hat{\mathbf{x}} \cdot \mathbf{B})}{1 - (\hat{\mathbf{x}} \cdot \mathbf{T})^2} \tag{4.44}$$

Then from (4.38), the associated chirality is

$$\kappa = -\frac{k}{\mathsf{k}_0}\,\frac{(\hat{\mathbf{x}} \cdot \mathbf{T})(\hat{\mathbf{x}} \cdot \mathbf{B})}{1 - (\hat{\mathbf{x}} \cdot \mathbf{T})^2} \tag{4.45}$$

$\mathbf{B}$ and $k$ are easily computed in terms of the index function $n$ and its derivatives using (4.24), once you know the unit tangent direction $\mathbf{T}$:

$$\begin{aligned} k &= \frac{1}{n}|\mathrm{grad}(n)^{\perp}| \\ \mathbf{N} &= \frac{\mathrm{grad}(n)^{\perp}}{|\mathrm{grad}(n)^{\perp}|} \\ \mathbf{B} &= \mathbf{T} \times \mathbf{N} \end{aligned} \tag{4.46}$$

## 4.5 Full Wave Verification

Full wave simulations were carried out using COMSOL Multiphysics software. The constitutive relationships relating $\mathbf{D}, \mathbf{E}, \mathbf{B}, \mathbf{H}$ fields in the software were modified appropriately to match (4.37).

### 4.5.1 Skew Aberration Elimination: Luneburg Lens

Using (4.45) and (4.46), one can design a Luneburg lens with chiral material properties that correct for the inherent skew aberration. These equations are especially useful and handy when they are parametrized as a function of positional vector, $\mathbf{r}$ and polar angle, $\theta$. This requires parameterizing the tangent vector $\mathbf{T}$, binormal vector $\mathbf{B}$, and frenet curvature $k$ inside the lens in terms of $(\mathbf{r}, \theta, \boldsymbol{\phi})$.

A ray in the Luneburg lens is shown in Fig. 4.3. The ray initially intersects the lens at polar and azimuthal angle, $\theta_0$ and $\phi$. The ray path lies in a plane with fixed polar angle. The ray follows an elliptical path (also proved in (4.25)) [40], with ellipse's principle axes and ellipse tilt angle are given by

$$A = \sqrt{2}\,\sin\frac{\theta_0}{2} \quad B = \sqrt{2}\,\cos\frac{\theta_0}{2}$$
$$\alpha = \frac{\pi - \theta_0}{2} \tag{4.47}$$

The ray path in the Luneburg lens can be parametrized by the polar angle $\theta$ [40]

$$(r,\theta,\phi) = (r(\theta,\theta_0),\theta,\phi) \quad \text{where,}$$
$$r(\theta,\theta_0) = \frac{\sin\theta_0}{\sqrt{1-\cos(2\theta-\theta_0)\cos\theta_0}} \tag{4.48}$$

It is convenient to specify the position vector using the cylindrical unit basis vectors, since they do not depend on $\theta$,

$$\mathbf{r} = r(\theta,\theta_0)(\sin\theta\,\hat{\boldsymbol{\rho}} + \cos\theta\,\hat{\mathbf{z}}) \tag{4.49}$$

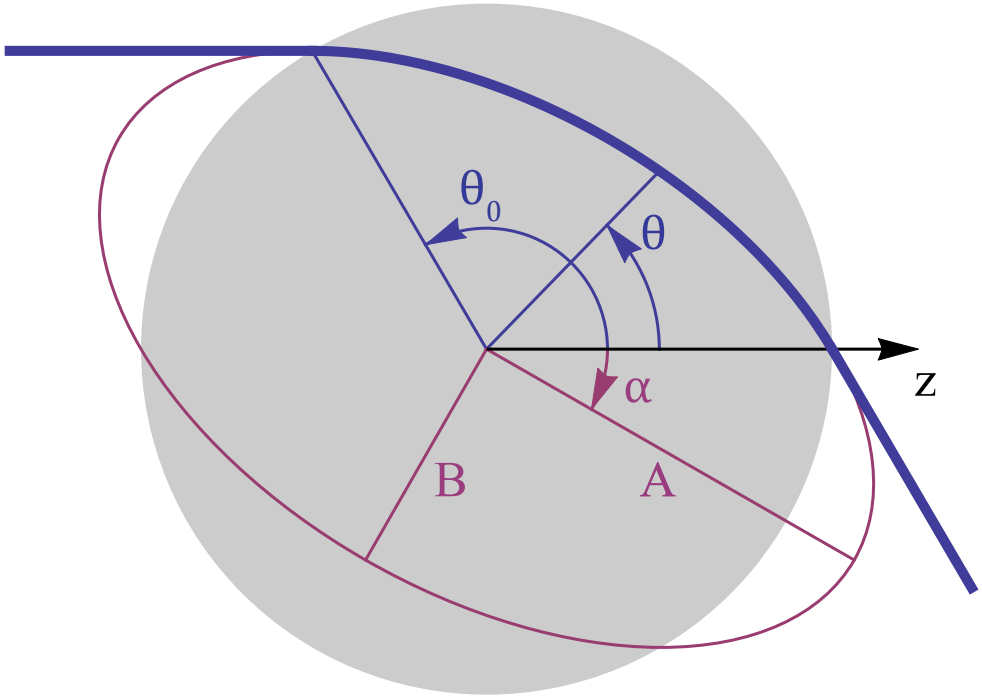


**Figure 4.3**: The cross-section of a Luneburg lens with a particular skew ray (in blue) following an elliptical path (ellipse shown in magenta).

The tangent vector, $\mathbf{T}$, is proportional to the $\theta$ derivative,

$$\mathbf{T} \propto \frac{d\mathbf{r}}{d\theta} = -\,2\,\sin(\theta_0-\theta)\sin\theta_0\,\hat{\boldsymbol{\rho}} + [3\,\sin\theta - \sin(2\,\theta_0-\theta)]\,\hat{\mathbf{z}} \tag{4.50}$$

Since the azimuthal angle, $\phi$, is constant on the curve, the binormal vector is known to be the azimuthal angle unit basis vector.

$$\mathbf{B} = -\hat{\boldsymbol{\phi}} \tag{4.51}$$

The normal vector, N, is found from cross product,

$$\mathbf{N} = \mathbf{B}\times\mathbf{T} \propto -\,[3\,\sin\theta - \sin(2\,\theta_0-\theta)]\,\hat{\boldsymbol{\rho}} - 2\,\sin(\theta_0-\theta)\sin\theta_0\,\hat{\mathbf{z}} \tag{4.52}$$

The sign of the binormal was chosen so that normal, $\mathbf{N}$, will follow convention and point toward the center of curvature.

The Euclidean vector gradient of the refractive index profile,

$$n = \sqrt{2 - r(\theta,\theta_0)^2}$$

is given by,

$$\mathrm{grad}(n) = -\frac{r(\theta,\theta_0)}{n}\,(\sin\theta\,\hat{\boldsymbol{\rho}} + \cos\theta\,\hat{\mathbf{z}}). \tag{4.53}$$

Frenet curvature, $k$, inside the lens can be found by using Eqs. (4.50) and (4.53) as follows,

$$\begin{aligned} k &= \frac{1}{n}|\mathrm{grad}(n)^{\perp}| \\ &= \left|\frac{\mathrm{grad}(n)}{n} - \mathbf{T}\left(\mathbf{T}\cdot\frac{\mathrm{grad}(n)}{n}\right)\right| \\ &= \frac{1}{n^2}\frac{r\,(2-\cos(2[\theta-\theta_0])-\cos 2\theta)}{\sqrt{2\,(3+\cos 2\theta_0 - 2\cos(2[\theta-\theta_0]) - 2\cos 2\theta)}} \end{aligned} \tag{4.54}$$

Plugging (4.50), (4.51), and (4.54) in (4.45), the required chiral properties to achieve the skew aberration correction can be calculated and are shown in Fig. 4.4. (The expression for $\theta_0$ is provided in the supplementary material, [41].) The above procedure can also be applied to other gradient index lenses to correct for skew aberrations.

The simulated lens diameter was up to $30\lambda_0$, for incident plane-wave wavelength $\lambda_0$. The incident plane wave was $\hat{\mathbf{y}}$-polarized, with propagation vector $\mathbf{k}$ pointing in the +z direction. We also performed similar full wave lens simulation without the chiral gradient

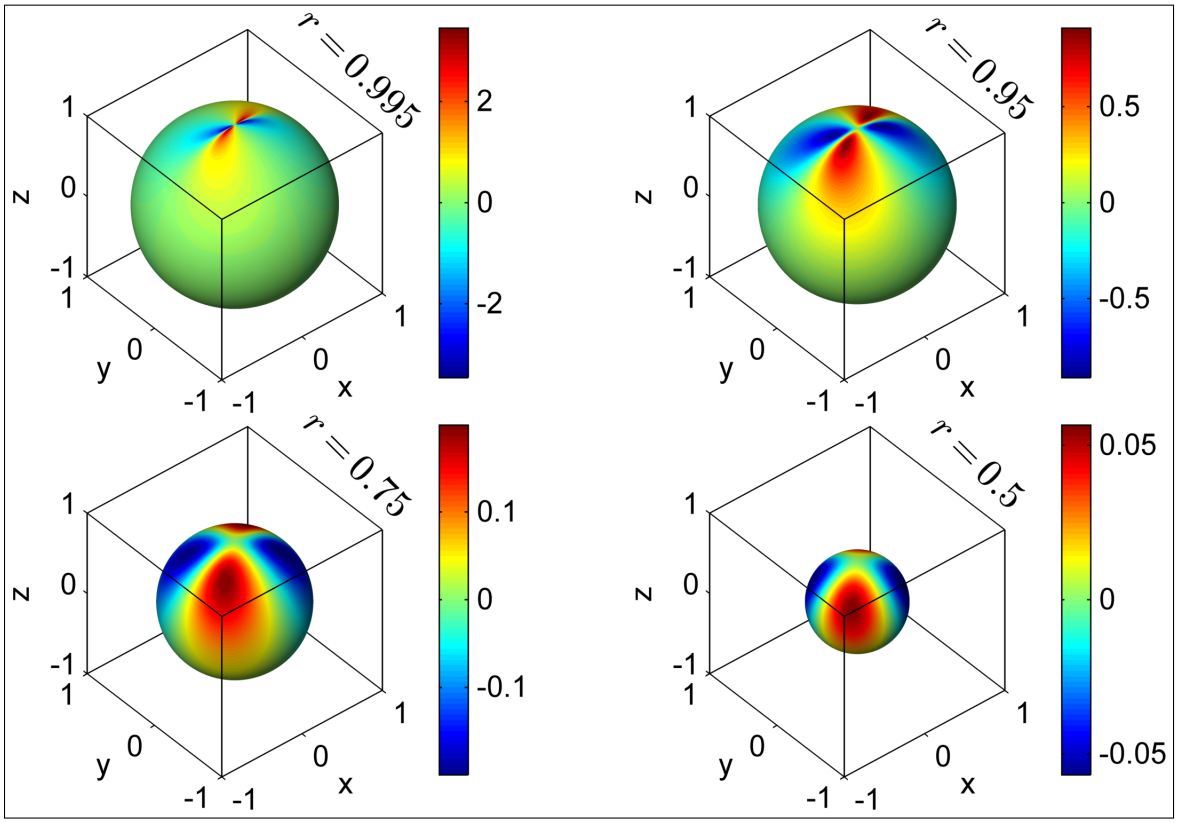


**Figure 4.4**: Chirality volume distribution for a skew aberration reducing Luneburg lens in the geometric limit. Four constant-radius surfaces from the volume distribution are shown. Though the chirality pattern is universal, the chirality parameter shown is for a lens outer radius and $k_0$ equal to unity.

in order to compare the results. The comparison results are shown in Fig. 4.5 which shows the magnitude of perpendicular electric field ($\hat{\mathbf{x}}$ polarized undesired cross polarization) for both without and with chiral correction. The results show the Ex fields at a xy plane with z = $+15\lambda_0$ (at the lens focus). However, the parallel electric field component ($\hat{\mathbf{y}}$ polarized) remains intact in both the cases.

The reduction factor in undesired polarization, RF is defined as,

$$\mathrm{RF} = \frac{\max(\mathbf{E}_{\perp}\text{with chiral correction})}{\max(\mathbf{E}_{\perp}\text{without chiral correction})}. \tag{4.55}$$

This factor is dependent on the size of the lens compared to the free space wavelength $\lambda_0$. This factor approaches to 0 under geometrical optics limit. Figure 4.5(d) shows the effect on reduction factor due to the lens diameter size. Due to the computational resource constraint, we settled for a maximum lens diameter of $30\lambda_0$. (Two symmetry planes were also exploited to reduce the computational resource needed for simulations.)

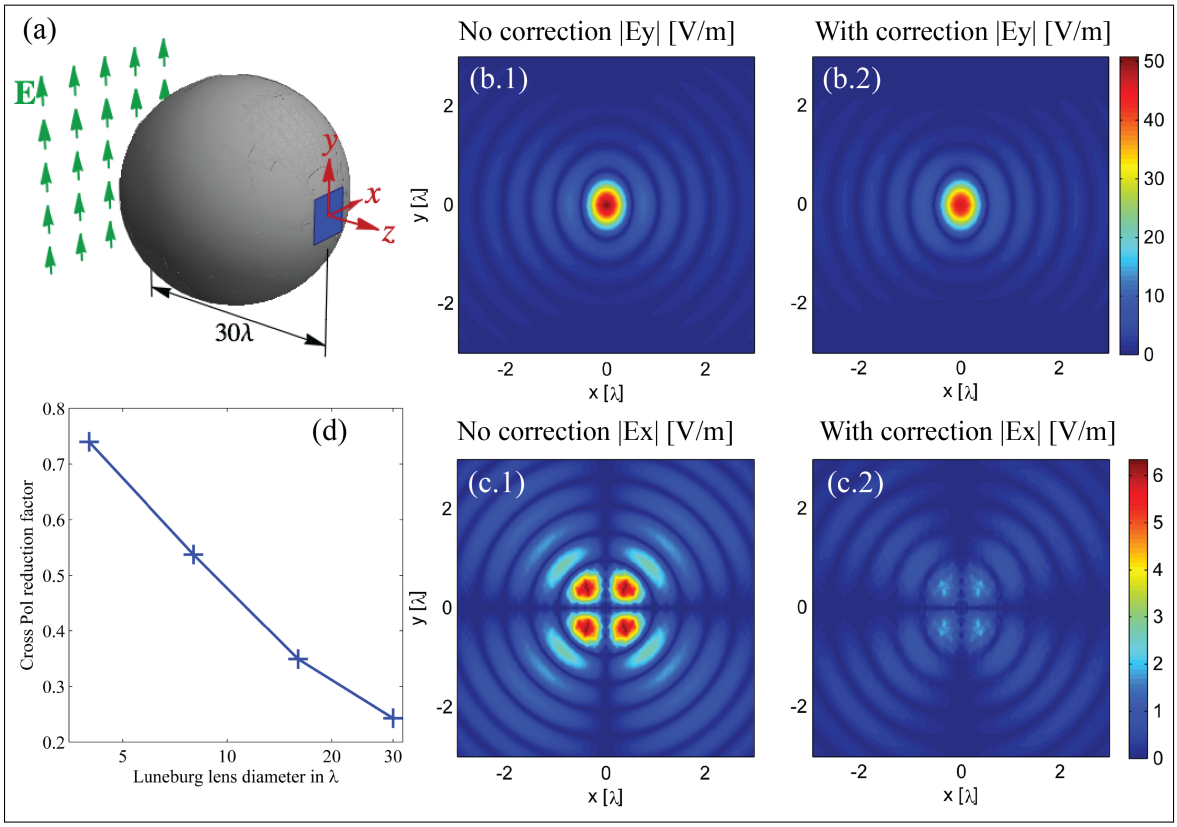


**Figure 4.5**: The effect of skew aberration correction (a) shows the full-wave simulation setup. The incident plane wave to the $30\lambda$ diameter Luneburg lens is **y** polarized. Blue patch denotes the focal plane of the Luneburg lens at which the electric fields are probed. (b) 1 & 2 show the magnitude of Ey component of the electric field ($\mathbf{E}_{\parallel}$) at the focal plane without and with chiral correction respectively. (c) 1 & 2 show the magnitude of Ex component of the electric field ($\mathbf{E}_{\perp}$) at the focal plane without and with chiral correction respectively. (d) shows the cross polarization reduction factor, RF as a function of Luneburg lens diameter.

We also present the ray tracing of a particular $\hat{\mathbf{y}}$ polarized skew ray inside a Luneburg lens. The polarization vector evolution with respect to the local Frenet-Serret frame is shown in Fig. 4.6. The parallel transport of the polarization vector with respect to Levi-Civita connection, **e** is shown in magenta. The parallel transport of the polarization vector with respect to a connection with chirality, $\widetilde{\mathbf{e}}$ is shown in gray. In the latter case, the polarization vector $\widetilde{\mathbf{e}}$ stays in the yz-plane without inducing any undesired cross-polarization. In both the cases, the geodesic path remains unchanged. (Such ray tracing simulations were also performed for other well-known gradient index lenses namely: Maxwell's fish-eye, Eaton, and Invisible sphere lens. See supplementary material [41].) Other brute force methods have been proposed for polarization correction inside spherical GRIN lenses [42],

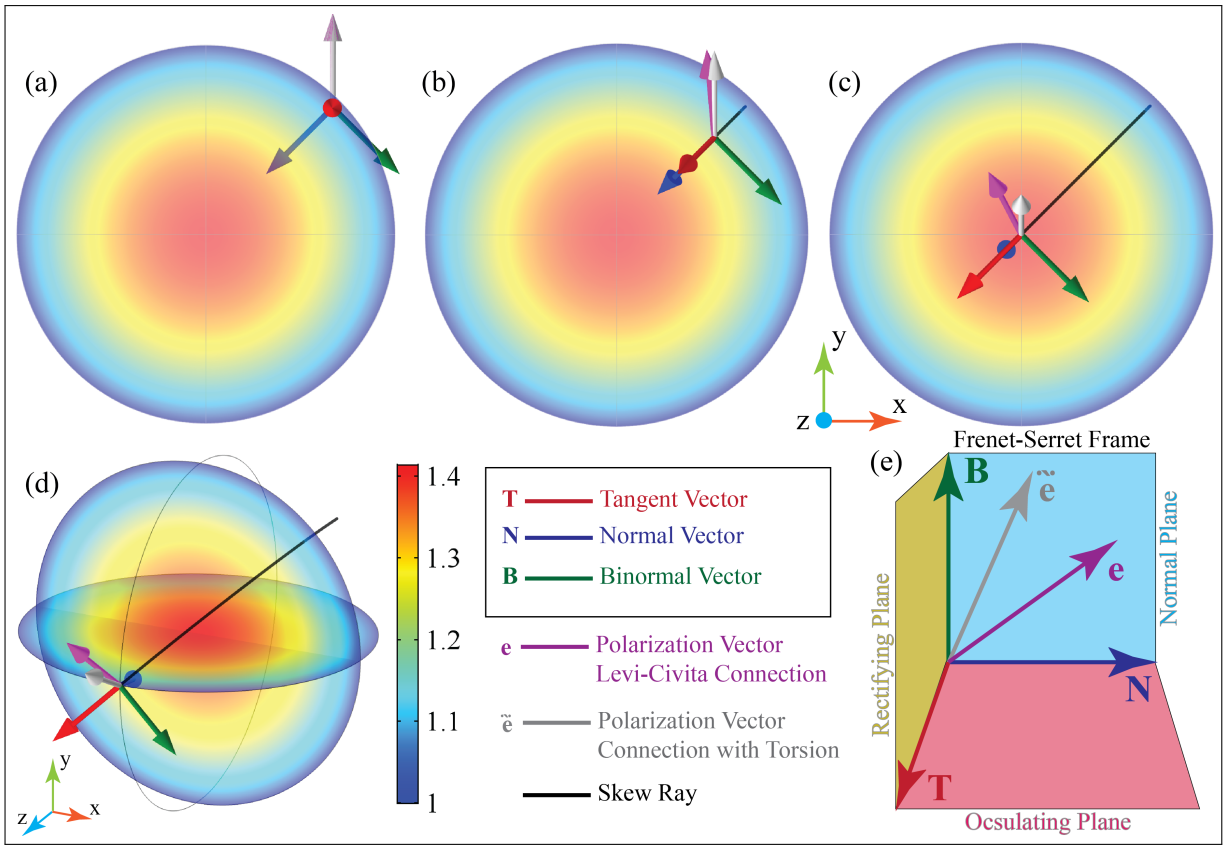


**Figure 4.6**: Parallel transport of a skew ray inside Luneburg lens. (a)-(c) show the parallel transport of polarization vectors based on Levi-Civita connection and a connection with torsion with respect to the Frenet-Serret frame in a Luneburg lens at different arclengths of the skewed ray. The incident polarization is $\hat{\mathbf{y}}$ polarized. (d) shows the perspective view of the vectors at the focus of the lens. Colorbar indicates the gradient refractive index of Luneburg lens. As the skew ray progresses along $\hat{\mathbf{z}}$ direction, the polarization vector $\mathbf{e}$ acquires cross polarization components whereas in the chiral-corrected case, $\tilde{\mathbf{e}}$ stays in the yz-plane. (e) shows the reference Frenet-Serret frame with $\mathbf{T}, \mathbf{N}, \mathbf{B}$ orthonormal vectors. The polarization vectors $\mathbf{e}$ and $\tilde{\mathbf{e}}$ always stay in the normal plane (hence they are always orthogonal to $\mathbf{T}$). The normal vector always points to the center of curvature.

however, our approach is from a Riemannian geometry perspective.

### 4.5.2 Vortex Beams

Apart from polarization aberration (skew aberration) correcting applications, torsion optics as a design tool can also be applied to generate complex beam polarizations or polarization manipulating devices. In this section, we design a chiral gradient slab which converts a uniformly $\hat{\mathbf{y}}$-polarized input Gaussian beam to a spiral vortex beam (with $\mathbf{z}$ being the direction of propagation of the beams). In order to achieve such a functionality, the transverse chiral gradient, $\kappa(x, y)$, inside a slab of thickness, d is defined as,

$$\kappa(x, y) = \frac{1}{d\,\mathrm{k}_0}\,\mathrm{atan2}(y, -x) \tag{4.56}$$

The full-wave simulation setup is shown in Fig. 4.7. The transverse plane chirality gradient map is shown in Fig. 4.8(a). The resulting output vortex beam for an input $\hat{\mathbf{y}}$-polarized Gaussian beam is shown in Fig. 4.8(c) and (b) respectively. Such vortex beams have found useful applications in communications, classical and quantum optics, design of optical tweezers, and recently in astronomical imaging. Design and fabrication of strong chiral gradients using metamaterials could still be very challenging but nevertheless promising.

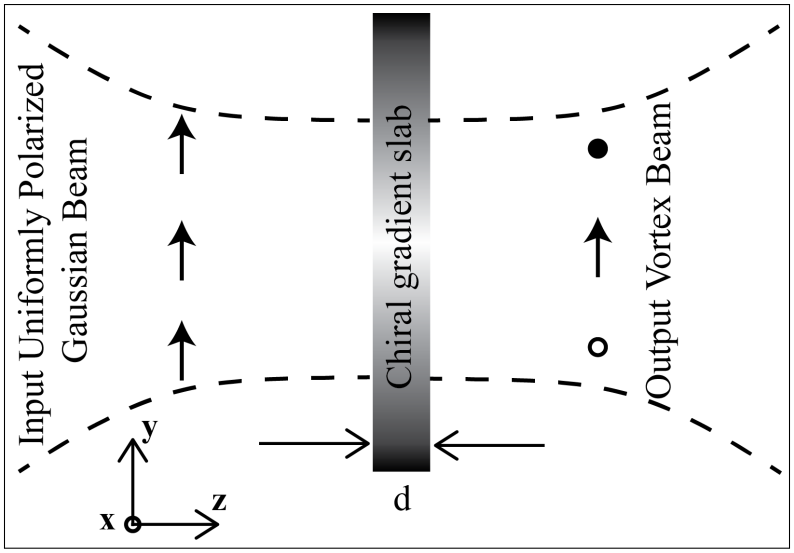


**Figure 4.7**: The full-wave simulation setup to generate vortex beam using torsion optics design.

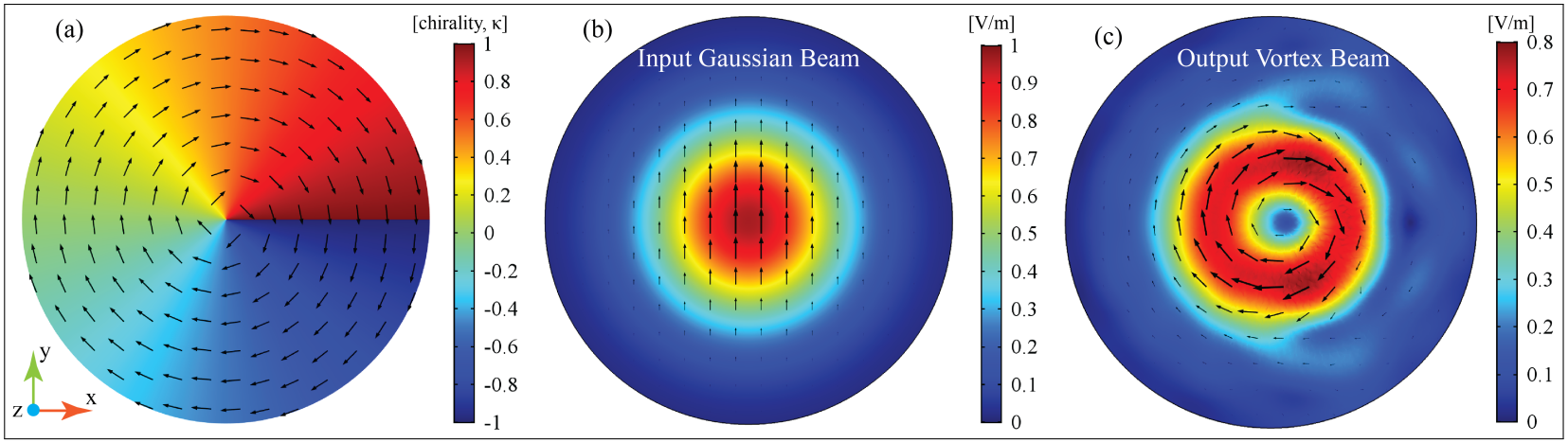


**Figure 4.8**: Vortex beam generation using torsion optics design principles. (a) the slice plot shows the chirality gradient, $\kappa$ inside the chiral slab of thickness d. Overlaid is a vector plot of intended polarization map. (b) shows the electric field norm of the input $\hat{\mathbf{y}}$-polarized Gaussian beam on xy-plane. (c) shows the electric field norm of the output vortex beam on xy-plane along with the vector plot of $E_x$ and $E_y$ components.

## 4.6 Conclusion

We have further developed the formal mathematical basis for a geometric optical design method for controlling polarization—torsion optics. In an analogy to transformation optics, the method exploits an equivalence between geometry and material properties inherent in the physics. The addition of polarization control to optical devices has numerous optical engineering applications. We apply the design method to the reduction of skew aberration in a Luneburg lens and the creation of vortex beams, and validate with full-wave simulations. We believe this intuitive method may facilitate the design of other useful and interesting polarization controlling devices that are not obvious by other approaches.

## 4.7 Supplementary Material

### 4.7.1 Geometrical Optics Limit and Eikonal Equation

- **Isotropic Medium**

Consider a general time harmonic field of the form,

$$\mathbf{E}(\mathbf{r},t) = \mathbf{E}_0(\mathbf{r})\, e^{-i\omega t} \tag{4.57a}$$

$$\mathbf{H}(\mathbf{r},t) = \mathbf{H}_0(\mathbf{r})\, e^{-i\omega t} \tag{4.57b}$$

where $\omega$ is the angular frequency of the electromagnetic wave and $\mathbf{E}_0$, $\mathbf{H}_0$ are the complex vector functions of positions.

Substituting the above solution in source-free Maxwell's equations (time-free form) for isotropic media (non-chiral) we get,

$$\nabla \times \mathbf{H}_0 + ik_0\epsilon\mathbf{E}_0 = 0 \tag{4.58a}$$

$$\nabla \times \mathbf{E}_0 - ik_0\mu\mathbf{H}_0 = 0 \tag{4.58b}$$

$$\nabla \cdot \epsilon\mathbf{E}_0 = 0 \tag{4.59a}$$

$$\nabla \cdot \mu\mathbf{H}_0 = 0 \tag{4.59b}$$

where $k_0 = \omega/c$. For example, a plane wave propagating in a specific direction $\mathbf{s}$ in a medium with refractive index $n = \sqrt{\epsilon\mu}$, can be written as,

$$\mathbf{E}_0 = \mathbf{e}\, e^{ik_0 n(\mathbf{s}\cdot\mathbf{r})} \tag{4.60a}$$

$$\mathbf{H}_0 = \mathbf{h}\, e^{ik_0 n(\mathbf{s}\cdot\mathbf{r})} \tag{4.60b}$$

where $\mathbf{e}, \mathbf{h}$ are some constant vectors.

Representing $\mathbf{E}_0$ and $\mathbf{H}_0$ with more general types of fields,

$$\mathbf{E}_0 = \mathbf{e}(\mathbf{r})\, e^{ik_0\mathcal{S}(\mathbf{r})} \tag{4.61a}$$

$$\mathbf{H}_0 = \mathbf{h}(\mathbf{r})\, e^{ik_0\mathcal{S}(\mathbf{r})} \tag{4.61b}$$

where $\mathcal{S}(\mathbf{r})$ is a scalar function also called as *'the optical path.'* Here again, $\mathbf{e}(\mathbf{r})$ and $\mathbf{h}(\mathbf{r})$ are complex vector functions of position. (Complex $\mathbf{e}$, $\mathbf{h}$ represent all possible polarization states, while real $\mathbf{e}$, $\mathbf{h}$ represent linear polarization states of the fields. Also, $\mathbf{e}(\mathbf{r})$, $\mathbf{h}(\mathbf{r})$, and $\mathcal{S}(\mathbf{r})$ are understood to be functions of position vector, $\mathbf{r}$, and will be dropped.) From (4.61b), we can write,

$$\nabla \times \mathbf{H}_0 = (\nabla \times \mathbf{h} + ik_0 \nabla\mathcal{S} \times \mathbf{h})\, e^{ik_0\mathcal{S}} \tag{4.62}$$

$$\nabla \cdot \mu\mathbf{H}_0 = (\mu\nabla \cdot \mathbf{h} + \mathbf{h} \cdot \nabla\mu + ik_0\mu\mathbf{h} \cdot \nabla\mathcal{S})\, e^{ik_0\mathcal{S}} \tag{4.63}$$

Similar equations can be written for $\nabla \times \mathbf{E}_0$ and $\nabla \cdot \epsilon\mathbf{E}_0$. Using the above equations and letting $k_0 \to \infty$, (4.58) can be rewritten as,

$$\nabla\mathcal{S} \times \mathbf{h} + \epsilon\mathbf{e} = -\frac{1}{ik_0}\nabla \times \mathbf{h} = 0 \tag{4.64a}$$

$$\nabla\mathcal{S} \times \mathbf{e} - \mu\mathbf{h} = -\frac{1}{ik_0}\nabla \times \mathbf{e} = 0. \tag{4.64b}$$

Similarly, (4.59) can be rewritten as,

$$\mathbf{e} \cdot \nabla\mathcal{S} = -\frac{1}{ik_0}(\mathbf{e} \cdot \nabla ln\, \epsilon + \nabla \cdot \mathbf{e}) = 0 \tag{4.65a}$$

$$\mathbf{h} \cdot \nabla\mathcal{S} = -\frac{1}{ik_0}(\mathbf{h} \cdot \nabla ln\, \mu + \nabla \cdot \mathbf{h}) = 0. \tag{4.65b}$$

Assuming that (4.64) has a nontrivial solution (i.e., consistency condition is satisfied) and substituting for $\mathbf{h}$ in (4.64) and (4.64), we get

$$\frac{1}{\mu}\left[(\mathbf{e} \cdot \nabla\mathcal{S})\nabla\mathcal{S} - \mathbf{e}\,(\nabla\mathcal{S})^2\right] + \epsilon\mathbf{e} = 0 \tag{4.66}$$

The first term vanishes because of (4.65) and the above equation becomes,

$$(|\nabla\mathcal{S}|)^2 = \epsilon\mu = n^2 \tag{4.67}$$

where $n = \sqrt{\epsilon\mu}$ is the refractive index of the medium. This is the *Eikonal equation* [32]. In Cartesian coordinates, the above equation can be written as,

$$\left(\frac{\partial\mathcal{S}}{\partial x}\right)^2 + \left(\frac{\partial\mathcal{S}}{\partial y}\right)^2 + \left(\frac{\partial\mathcal{S}}{\partial z}\right)^2 = n^2(x, y, z) \tag{4.68}$$

- **Eikonal Equation in Matrix Form for an Isotropic Medium**

The curl equations in (4.64) can be rewritten in matrix form as (in Cartesian coordinates),

$$\mathbf{M}_{iso} \cdot \mathbf{f} = 0 \tag{4.69}$$

where the matrix $\mathbf{M}_{iso}$ given by;

$$\mathbf{M}_{iso} = \begin{bmatrix} -\epsilon & 0 & 0 & 0 & \mathcal{S}_z & -\mathcal{S}_y \\ 0 & -\epsilon & 0 & -\mathcal{S}_z & 0 & \mathcal{S}_x \\ 0 & 0 & -\epsilon & \mathcal{S}_y & -\mathcal{S}_x & 0 \\ 0 & \mathcal{S}_z & -\mathcal{S}_y & \mu & 0 & 0 \\ -\mathcal{S}_z & 0 & \mathcal{S}_x & 0 & \mu & 0 \\ \mathcal{S}_y & -\mathcal{S}_x & 0 & 0 & 0 & \mu \end{bmatrix} \tag{4.70}$$

$$\mathbf{f} = \begin{bmatrix} e_x \\ e_y \\ e_z \\ h_x \\ h_y \\ h_z \end{bmatrix} \tag{4.71}$$

where $\mathcal{S}_x = \dfrac{\partial \mathcal{S}}{\partial x}$, $\mathcal{S}_y = \dfrac{\partial \mathcal{S}}{\partial y}$, $\mathcal{S}_z = \dfrac{\partial \mathcal{S}}{\partial z}$.

If the (4.64) has a nontrivial solution then the determinant of $\mathbf{M}_{iso}$ should vanish. Eikonal equation from the matrix form is found by equating the determinant of $\mathbf{M}_{iso}$ to zero,

$$\begin{aligned} det(\mathbf{M}_{iso}) = -\epsilon\mu \left(\mathcal{S}_x^2 + \mathcal{S}_y^2 + \mathcal{S}_z^2 - \epsilon\mu\right)^2 = 0 \\ \Rightarrow \mathcal{S}_x^2 + \mathcal{S}_y^2 + \mathcal{S}_z^2 = n^2(x,y,z) \end{aligned} \tag{4.72}$$

The above equations are similar to (4.68).

- **Eikonal Equation in Matrix Form for an Isotropic Chiral Medium**

From the constitutive relationships in (4.37), one can rewrite the curl equations in (4.64). Again, rewriting the matrix in similar fashion as (4.70) for an isotropic chiral medium,

$$\mathbf{M}_{chiral} = \begin{bmatrix} -\epsilon & 0 & 0 & -i\kappa/c & \mathcal{S}_z & -\mathcal{S}_y \\ 0 & -\epsilon & 0 & -\mathcal{S}_z & -i\kappa/c & \mathcal{S}_x \\ 0 & 0 & -\epsilon & \mathcal{S}_y & -\mathcal{S}_x & -i\kappa/c \\ -i\kappa/c & \mathcal{S}_z & -\mathcal{S}_y & \mu & 0 & 0 \\ -\mathcal{S}_z & -i\kappa/c & \mathcal{S}_x & 0 & \mu & 0 \\ \mathcal{S}_y & -\mathcal{S}_x & -i\kappa/c & 0 & 0 & \mu \end{bmatrix} \tag{4.73}$$

Eikonal equation for an isotropic chiral medium can arrived at by equating the $det(\mathbf{M}_{chiral})$ to zero,

$$\begin{aligned} det(\mathbf{M}_{chiral}) = -\left[\epsilon\mu + \Bbbk^2\right]\left[\left(\mathcal{S}_x^2 + \mathcal{S}_y^2 + \mathcal{S}_z^2 - \epsilon\mu\right)^2 + 2\left(\mathcal{S}_x^2 + \mathcal{S}_y^2 + \mathcal{S}_z^2 + \epsilon\mu\right)\Bbbk^2 + \Bbbk^4\right] = 0 \\ \Rightarrow \left[\left(\mathcal{S}_x^2 + \mathcal{S}_y^2 + \mathcal{S}_z^2 - \epsilon\mu\right)^2 + 2\left(\mathcal{S}_x^2 + \mathcal{S}_y^2 + \mathcal{S}_z^2 + \epsilon\mu\right)\Bbbk^2 + \Bbbk^4\right] = 0 \end{aligned} \tag{4.74}$$

where, $\Bbbk = i\kappa/c$. Under the geometrical optics limit, as the wavenumber, $k_0 \to 0$, the required rate of counter-rotation of the polarization vector per unit arclength also approaches 0. This means that the chirality, $\kappa$, required also approaches 0. Hence, under this limit the eikonal equation of an isotropic chiral medium becomes equal to that of isotropic medium. Hence, the geodesics in a chiral corrected lens under the geometrical optics limit are indeed preserved.

### 4.7.2 Luneburg Lens: Ray Arclength

The ray in a Luneburg Lens (unit sphere a = 1) follows follows an elliptical path, with ellipse's principle axes and ellipse tilt angle are given by

$$\begin{gathered} A = \sqrt{2}\,\sin\frac{\theta_0}{2} \quad B = \sqrt{2}\,\cos\frac{\theta_0}{2} \\ \alpha = \frac{\pi - \theta_0}{2} \end{gathered} \tag{4.75}$$

The arclength of an ellipse of the form,

$$\frac{x^2}{A^2} + \frac{y^2}{B^2} = 1 \tag{4.76}$$

can be parametrized with $\theta_0$ as,

$$\begin{aligned} s &= \int_0^{\sin(\theta_0/2)} \sqrt{1 + \left(\frac{dy}{dx}\right)^2}\,dx \\ &= 2\,A\,E\left(\pi/4, \vartheta\right) \\ \text{where,}\quad \vartheta = \vartheta(\theta_0) &= \frac{A^2 - B^2}{A^2} = 1 - \tan^2\left(\frac{\pi - \theta_0}{2}\right), \end{aligned} \tag{4.77}$$

$E(\varepsilon, \vartheta)$ is the elliptic integral of second kind.

Every point in the lens lies on one, and only one ray path. The angle of incidence $\theta_0$ (useful in solving (4.48)) can be parametrized in terms of $(r, \theta)$ as,

$$\theta_0 = \arccos\left(-\frac{1}{2}\sqrt{\frac{4 - 8r^2\cos^2(\theta) - 4\sqrt{2}\cos(\theta)\sqrt{r^6(4 - 3r^2 + r^2\cos(2\theta))\sin^4(\theta)} + 2r^4(2\cos(2\theta) + \sin^2(2\theta)}{r^4 - 2r^2\cos(2\theta) + 1}}\right) \tag{4.78}$$

### 4.7.3 Full Wave Chiral Medium Simulations

To validate the chiral medium simulation setup, we first performed full wave EM simulation of a 2D Luneburg lens which acts both as a lens and a $90^0$ polarizer. These simulations were performed using COMSOL Multiphysics RF module. The controlled twisting of incident in plane electric polarization to out of plane polarization is achieved by keeping the torsion angle per unit arclength inside the medium constant equal to $\pi/2$. For a Luneburg lens, the arclength s as a function of $(r, \theta)$ can be analytically calculated. Using (4.45), we calculate the chirality gradient $\kappa$ inside the Luneburg lens needed to achieve this effect. The constitutive relationship in COMSOL was appropriately changed to match (4.37). It is important to note that COMSOL follows the time harmonic convention of the form $\exp(j\omega t)$. The simulation results are shown in Fig. 4.9. The dashed circle shows the region of 2D Luneburg lens. The arrows in both the plots show the gradual change in polarization along the lens. The normalized chirality gradient $\kappa\, k_0\, a$ required to achieve this polarization conversion is shown in Fig. 4.9(e), where $k_0$ is the wave number and $a$ is the radius of the Luneburg lens.

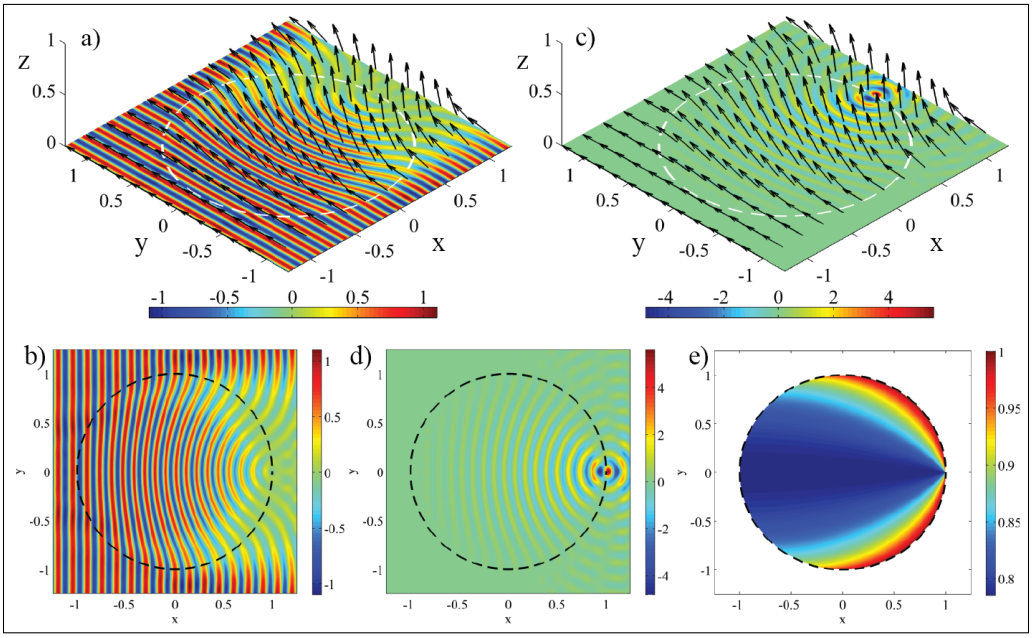


**Figure 4.9**: The rotation of polarization vector from $\hat{\mathbf{y}}$ to $\hat{\mathbf{z}}$ for a modified chiral Luneburg Lens excited with TE polarized plane wave. (a) and (b) show the Ey component and (c) and (d) show the Ez component of the electric field distributions. Dashed circle shows the region of modified chiral Luneburg lens. (e) normalized chirality gradient inside Luneburg lens: $\kappa\, k_0\, a$.

### 4.7.4 GRIN Lenses and Their Polarization Vector Parallel Transport

Parallel transport of polarization vectors based on Levi-Civita connection and "a connection with torsion" are shown for different GRIN lens in Figs. 4.10, 4.11, 4.12, and 4.13.

- **Invisible Sphere Lens**

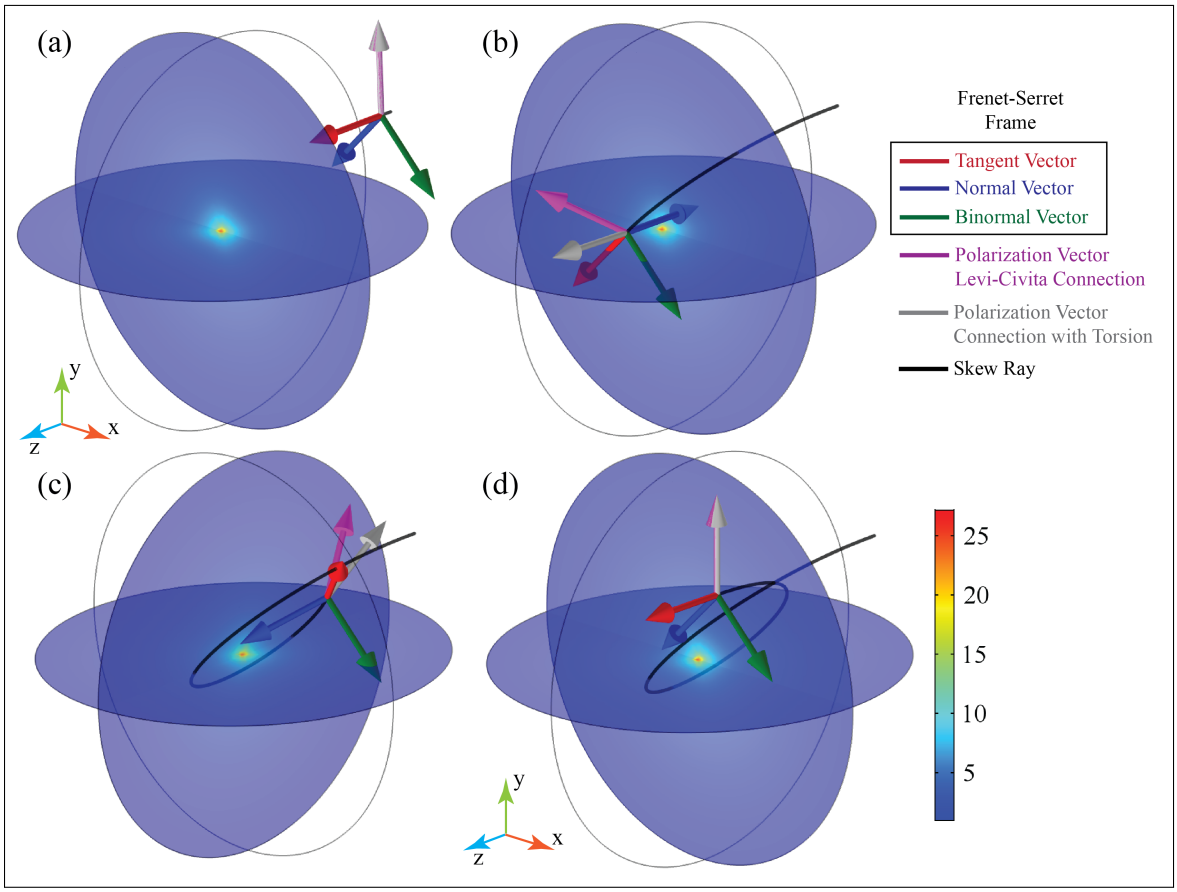


**Figure 4.10**: The parallel transport of polarization vectors **e** (magenta) and $\widetilde{\mathbf{e}}$ (gray) based on Levi-Civita connection and a connection with torsion respectively for a particular skew ray inside invisible sphere lens.

Refractive Index profile: $n(r) = \left( Q(r) - \frac{1}{3Q(r)} \right)^2$

where, $Q(r) = \sqrt[3]{\frac{a}{r}\sqrt{1 + \frac{r^2}{27a^2}} - \frac{a}{r}}$

- **Luneburg Lens**

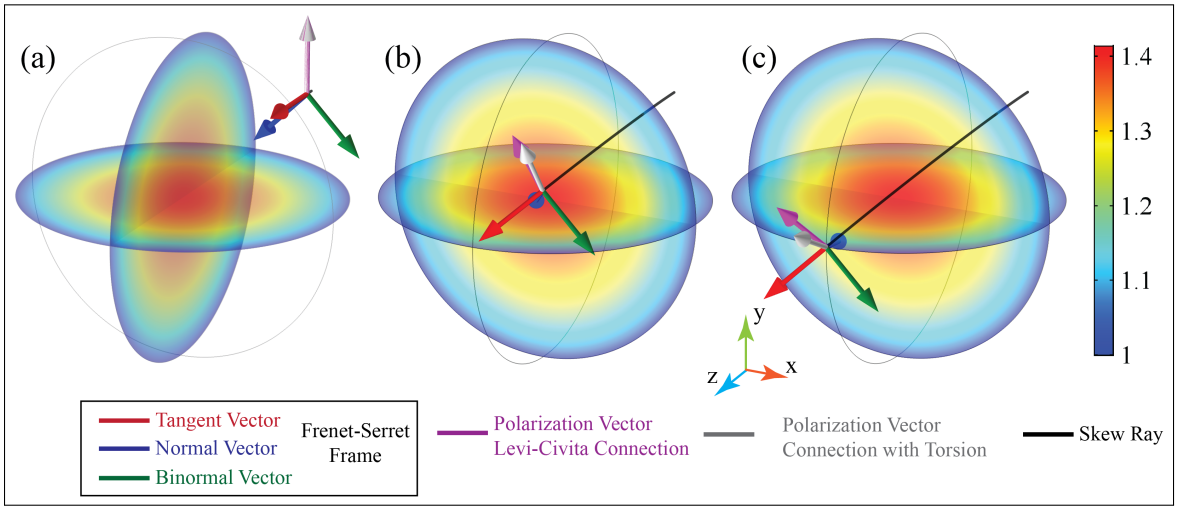


**Figure 4.11**: The parallel transport of polarization vectors **e** (magenta) and $\widetilde{\mathbf{e}}$ (gray) based on Levi-Civita connection and a connection with torsion respectively for a particular skew ray inside Luneburg lens.

Refractive Index profile: $n(r) = \sqrt{2 - (r/a)^2}$

- **Maxwell's Fish-eye Lens**

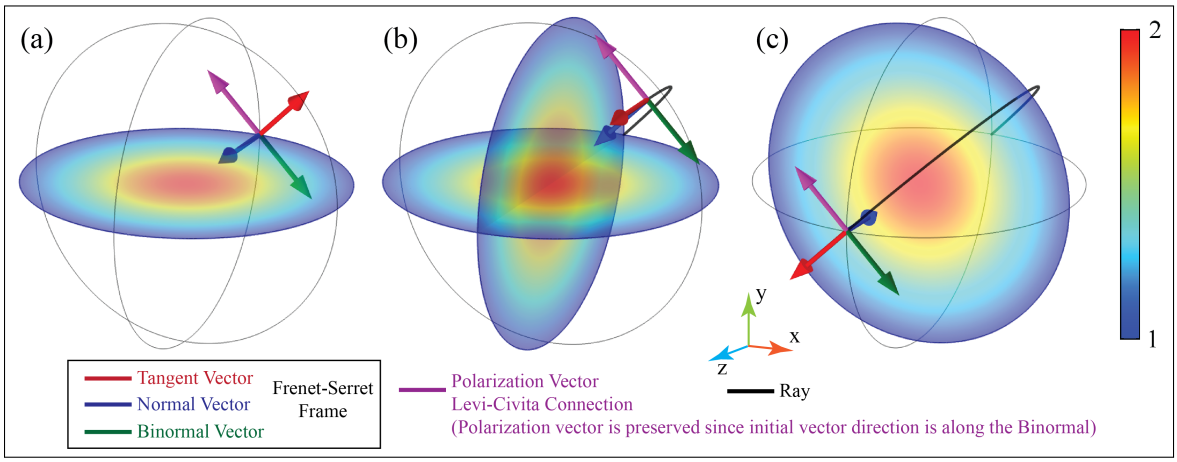


**Figure 4.12**: The parallel transport of polarization vector **e** (magenta) based on Levi-Civita connection for a particular skew ray inside Maxwell's fish-eye lens. Polarization vector $\widetilde{\mathbf{e}}$ overlaps with **e** since the initial angle between **e** and **B** is equal to $\pi$, see (4.92).

Refractive Index profile: $n(r) = \dfrac{2}{1 + (r/a)^2}$

- **Eaton Lens (180° bend)**

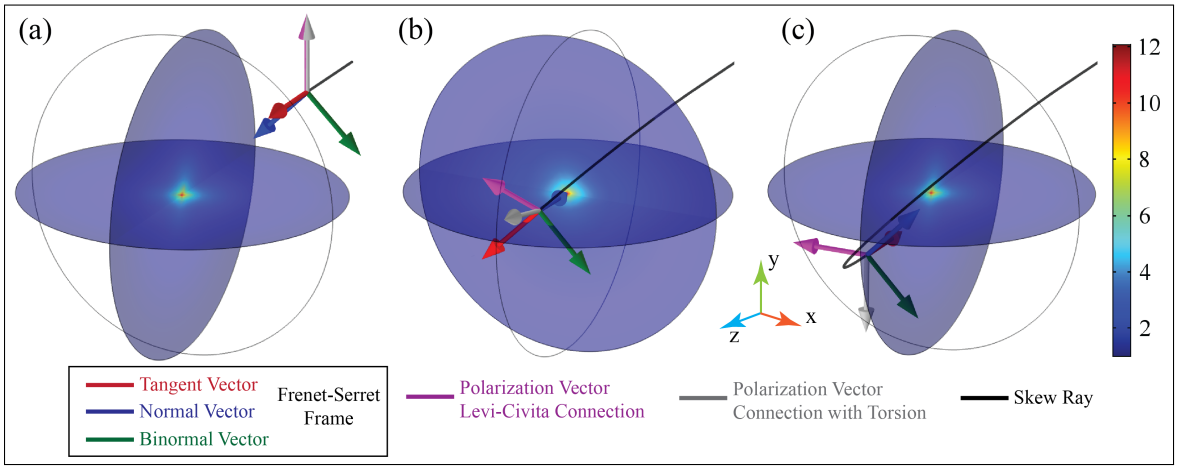


**Figure 4.13**: The parallel transport of polarization vectors **e** (magenta) and $\widetilde{\mathbf{e}}$ (gray) based on Levi-Civita connection and a connection with torsion respectively for a particular skew ray inside 180° Eaton lens.

Refractive Index profile: $n(r) = \sqrt{\dfrac{2}{(r/a)} - 1}$

### 4.7.5 Formulas to Calculate Curvature and Torsion of Rays

The curvature $k$ and torsion $\tau$ of a ray in an inhomogeneous medium with refractive index $n$ is defined as follows [38]. Let $s$ be the arclength parameter used to parameterize the ray. Invoking the Frenet-Serret reference frame associated with the ray, one can define a tangent unit vector $\mathbf{T}$, normal unit vector $\mathbf{N}$, and binormal unit vector $\mathbf{B} = \mathbf{T} \times \mathbf{N}$, at every point on the ray such that following equations are satisfied (see Fig. 4.14).

$$\frac{d\mathbf{T}}{ds} = k\mathbf{N} \tag{4.79}$$

$$\frac{d\mathbf{N}}{ds} = -k\mathbf{T} + \tau\mathbf{B} \tag{4.80}$$

$$\frac{d\mathbf{B}}{ds} = -\tau\mathbf{N} \tag{4.81}$$

The normal vector $\mathbf{N}$ is always parallel to $\text{grad}(n)^{\perp}/n$ where, $\text{grad}(n)^{\perp} = \text{grad}(n) - \mathbf{T}(\mathbf{T} \cdot \text{grad}(n))$. Equation. 4.79 can now be rewritten as,

$$k\mathbf{N} = \frac{\text{grad}(n)^{\perp}}{n} = \frac{\text{grad}(n)}{n} - \mathbf{T}\left(\mathbf{T} \cdot \frac{\text{grad}(n)}{n}\right)$$

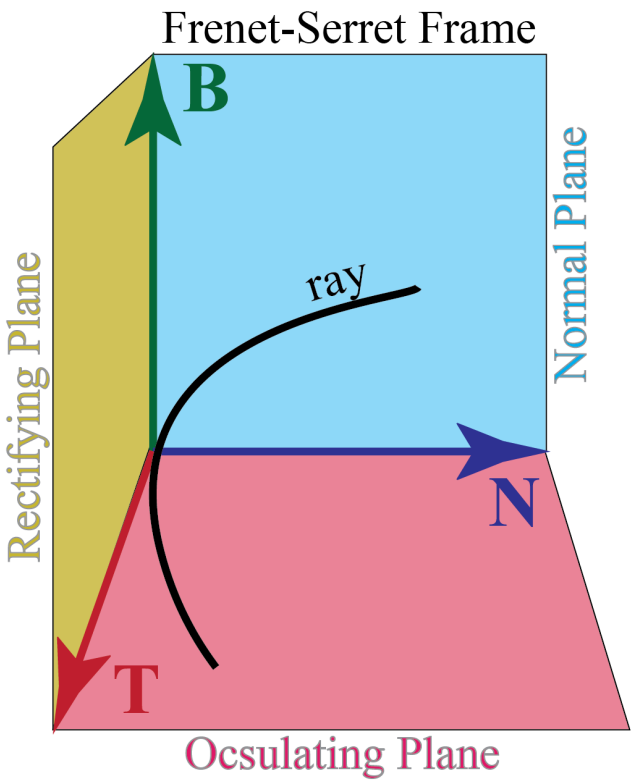


**Figure 4.14**: Frenet-Serret frame (convention right handed screw rule).

The curvature $k$, can be written as,

$$k = \left| \frac{\text{grad}(n)}{n} - \mathbf{T}\left(\mathbf{T} \cdot \frac{\text{grad}(n)}{n}\right) \right| \tag{4.82}$$

Curvature of a spatial curve is always positive and the normal vector $\mathbf{N}$ always points to the center of curvature. Now the normal $\mathbf{N}$ and binormal $\mathbf{B}$ can be expressed solely in terms of $\mathbf{T}$, $n$, and $\text{grad}(n)$ as follows,

$$\mathbf{N} = \frac{\text{grad}(n)^{\perp}}{n\,k} \tag{4.83}$$

$$\mathbf{B} = \mathbf{T} \times \mathbf{B} = \frac{1}{k}\mathbf{T} \times \frac{\text{grad}(n)}{n} \tag{4.84}$$

The torsion of the ray, $\tau$, can be written from (4.81) and (4.80) as,

$$\tau = -\mathbf{N} \cdot \frac{d\mathbf{B}}{ds} = -\mathbf{N} \cdot (\mathbf{T} \cdot \text{grad})\mathbf{B} = \mathbf{B} \cdot \frac{d\mathbf{N}}{ds} = \mathbf{B} \cdot (\mathbf{T} \cdot \text{grad})\mathbf{N}$$

Substituting for $(\mathbf{T} \cdot \text{grad})\mathbf{B}$ and $(\mathbf{T} \cdot \text{grad})\mathbf{N}$ and rewriting the above equation we get,

$$\tau = -\frac{1}{2}\left(\mathbf{N} \cdot \text{curl}(\mathbf{N}) + \mathbf{B} \cdot \text{curl}(\mathbf{B})\right) \tag{4.85}$$

The above equation can again be written solely in terms of $\mathbf{T}$, $n$ and grad$(n)$ using (4.83) and (4.84). For planar rays, torsion, $\tau$, vanishes.

### 4.7.6 Stokes Parameter Analysis of 30$\lambda$ Diameter Luneburg Lens Without and With Chiral Correction

The polarization state of the light on a plane just outside the lens (z = $+15\lambda_0$) can be described in terms of Stokes parameters [43]. The Stokes parameters we used were,

$$\begin{aligned} S0 &= |\mathrm{Ex}|^2 + |\mathrm{Ey}|^2 \\ S1 &= |\mathrm{Ex}|^2 - |\mathrm{Ey}|^2 \\ S2 &= 2\,\mathrm{Re}[\mathrm{Ex}^*\mathrm{Ey}] \\ S3 &= 2\,\mathrm{Im}[\mathrm{Ex}^*\mathrm{Ey}] \end{aligned} \tag{4.86}$$

The normalized Stokes parameters ($S1$, $S1$, $S3$) are shown for both polarization uncorrected and corrected cases in Fig. 4.15. $S1$ represents the tendency of the light to be in a horizontal ($S1 > 0$, x) or vertical state ($S1 < 0$, y). In both the cases the primary y-polarization is the

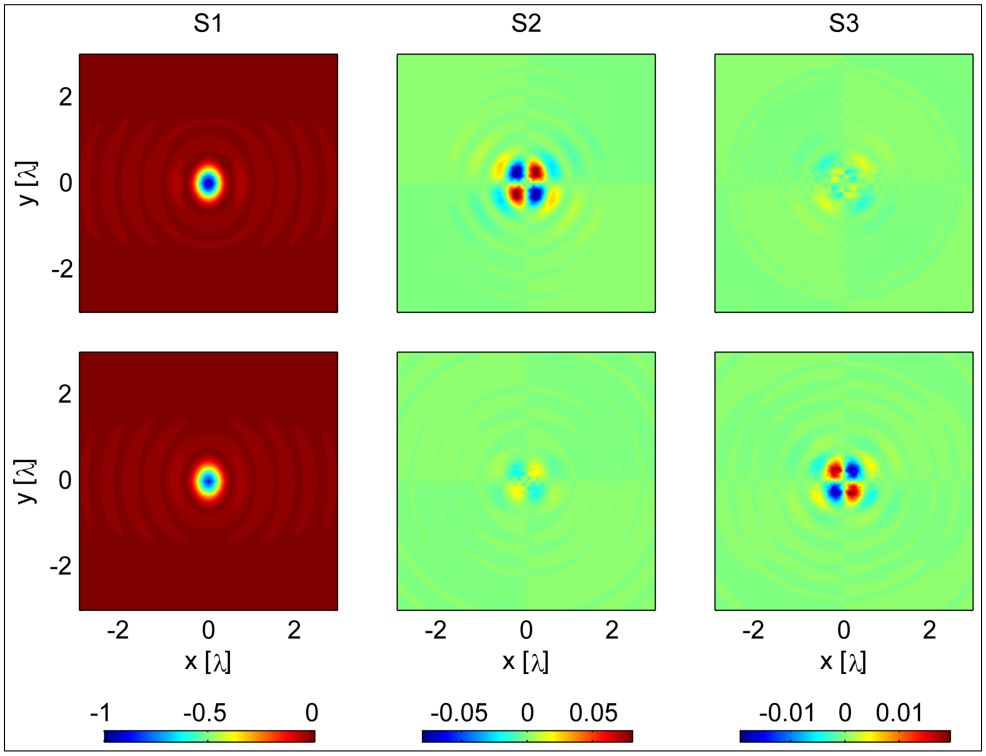


**Figure 4.15**: The extracted normalized Stokes parameters from the transverse plane fields at $z = +15\lambda_0$ (xy-plane containing the focal point) for without (top row) and with (bottom row) chiral correction. In both the full-wave simulations, a $\hat{\mathbf{y}}$ polarized plane wave propagating in +z direction is incident on the lens.

dominant polarization. $S2$ represents the tendency of light to be oriented in $+\pi/4$ ($S2 > 0$), $-\pi/4$ ($S2 < 0$), or neither ($S2 = 0$). In the case of no correction, since the Ex component is significant, $S2$ parameter is dominant near the focus. This parameter almost vanishes in the corrected case due to the reduction in Ex component. $S3$ represents the tendency of the light to be right ($S3 > 0$) or left circularly polarized ($S3 < 0$). The chirality gradient is calculated under the constraints of geometrical optics limit. Due the finite size of the lens compared to its operating wavelength, the prescribed chirality gradient induces some minute amount of circular polarization as compared to the uncorrected case.

## 4.8 Curvature and Local Cross Polarization

In this section we show the effect of geodesic curvature on local polarization vector. Without loss of generality we first align the Frenet-Serret frame with fixed Cartesian coordinates,

$$\mathbf{T}(0) = \hat{\mathbf{z}} \quad \mathbf{N}(0) = \hat{\mathbf{x}} \quad \mathbf{B}(0) = \hat{\mathbf{y}}. \tag{4.87}$$

Assume an arbitrary polarization vector to be parallel transported and compared with initial co- and cross-polarization vectors.

$$\mathbf{e}_{\parallel}(s) = \cos\phi\,\mathbf{N}(s) + \sin\phi\,\mathbf{B}(s)$$
$$\mathbf{e}_{\perp}(s) = \sin\phi\,\mathbf{N}(s) - \cos\phi\,\mathbf{B}(s)$$

Rewriting in Cartesian co-ordinates at $s = 0$,

$$\mathbf{e}_{\parallel}(0) = \cos\phi\,\hat{\mathbf{x}} + \sin\phi\,\hat{\mathbf{y}}$$
$$\mathbf{e}_{\perp}(0) = \sin\phi\,\hat{\mathbf{x}} - \cos\phi\,\hat{\mathbf{y}}.$$

The Taylor series expansion of the co-polarization vector to the second order is,

$$\mathbf{e}_{\parallel}(s) \approx \mathbf{e}_{\parallel}(0) + s\,\frac{d\mathbf{e}_{\parallel}}{ds} + \frac{1}{2}s^2\frac{d^2\mathbf{e}_{\parallel}}{ds^2}. \tag{4.88}$$

The normal plane coefficients are constant for parallel transport (with conformal metric). Also assuming that the planar geodesic has finite curvature, $k$ (and zero curve torsion, $\tau$),

$$\frac{d\mathbf{e}_{\parallel}}{ds} = \cos\phi\frac{d\mathbf{N}}{ds} + \sin\phi\frac{d\mathbf{B}}{ds} = -\cos\phi\,k\,\mathbf{T} \tag{4.89}$$
$$\frac{d^2\mathbf{e}_{\parallel}}{ds^2} = -\cos\phi\,k\,\frac{d\mathbf{T}}{ds} = -\cos\phi\,k^2\mathbf{N}. \tag{4.90}$$

Plugging the above equations in (4.88),

$$\begin{aligned}\mathbf{e}_{\parallel}(s) &\approx \mathbf{e}_{\parallel}(0) - s\cos\phi\, k\, \mathbf{T} - \frac{1}{2}s^2\cos\phi\, k^2\mathbf{N} \\ &\approx \mathbf{e}_{\parallel}(0) - s\cos\phi\, k\, \hat{\mathbf{z}} - \frac{1}{2}s^2\cos\phi\, k^2\hat{\mathbf{x}}. \end{aligned} \tag{4.91}$$

Taking the dot product of the above equation with the initial cross-polarization vector, we find that nonzero cross polarization is introduced at second order in path length and curvature, and it's a maximum for $\phi = \pi/4$ and minimum when $\phi = 0$ or $\phi = \pi/2$.

$$\mathbf{e}_{\parallel}(s) \cdot \mathbf{e}_{\perp}(0) = -\frac{1}{2}\sin\phi\, \cos\phi\, s^2\, k^2 \tag{4.92}$$

## 4.9 Acknowledgments

This work was supported by a Multidisciplinary University Research Initiative, sponsored by the US Army Research Office (Grant No. W911NF-09-1-0539). The support and resources from the Center for High Performance Computing at the University of Utah are gratefully acknowledged.

## 4.10 References

[1] J. B. Pendry, D. Schurig, and D. R. Smith, "Controlling electromagnetic fields," *Science*, vol. 312, no. 5781, pp. 1780–1782, 2006.

[2] D. Schurig, et al., "Metamaterial electromagnetic cloak at microwave frequencies," *Science*, vol. 314, no. 5801, pp. 977–980, 2006.

[3] G. W. Milton, M. Briane, and J. R. Willis, "On cloaking for elasticity and physical equations with a transformation invariant form," *New Journal of Physics*, vol. 8, no. 10, p. 248, 2006.

[4] J. Li and J. Pendry, "Hiding under the carpet: A new strategy for cloaking," *Physical Review Letters*, vol. 101, no. 20, p. 203901, 2008.

[5] M. Rahm, D. Schurig, D. A. Roberts, S. A. Cummer, D. R. Smith, and J. B. Pendry, "Design of electromagnetic cloaks and concentrators using form-invariant coordinate transformations of Maxwell's equations," *Photonics and Nanostructures - Fundamentals and Applications*, vol. 6, no. 1, pp. 87–95, 2008.

[6] W. Cai, U. K. Chettiar, A. V. Kildishev, V. M. Shalaev, and G. W. Milton, "Nonmagnetic cloak with minimized scattering," *Applied Physics Letters*, vol. 91, no. 11, p. 111105, 2007.

[7] U. Leonhardt and T. Tyc, "Broadband invisibility by non-euclidean cloaking," *Science*, vol. 323, no. 5910, pp. 110–112, 2009.

[8] H. Chen and C. Chan, "Transformation media that rotate electromagnetic fields," *Applied Physics Letters*, vol. 90, no. 24, p. 241105, 2007.

[9] D.-H. Kwon and D. H. Werner, "Polarization splitter and polarization rotator designs based on transformation optics," *Optics Express*, vol. 16, no. 23, pp. 18 731–18 738, 2008.

[10] U. Leonhardt and T. G. Philbin, "General relativity in electrical engineering," *New Journal of Physics*, vol. 8, no. 10, p. 247, 2006.

[11] D. A. Genov, S. Zhang, and X. Zhang, "Mimicking celestial mechanics in metamaterials," *Nature Physics*, vol. 5, no. 9, pp. 687–692, 2009.

[12] A. Greenleaf, Y. Kurylev, M. Lassas, and G. Uhlmann, "Electromagnetic wormholes and virtual magnetic monopoles from metamaterials," *Physical Review Letters*, vol. 99, no. 18, p. 183901, 2007.

[13] W. X. Jiang, et al., "Design of arbitrarily shaped concentrators based on conformally optical transformation of nonuniform rational b-spline surfaces," *Applied Physics Letters*, vol. 92, no. 26, p. 264101, 2008.

[14] J. Pendry, A. Aubry, D. Smith, and S. Maier, "Transformation optics and subwavelength control of light," *Science*, vol. 337, no. 6094, pp. 549–552, 2012.

[15] J. Yang, M. Huang, C. Yang, Z. Xiao, and J. Peng, "Metamaterial electromagnetic concentrators with arbitrary geometries," *Optics Express*, vol. 17, no. 22, pp. 19 656–19 661, 2009.

[16] D. Roberts, M. Rahm, J. Pendry, and D. Smith, "Transformation-optical design of sharp waveguide bends and corners," *Applied Physics Letters*, vol. 93, no. 25, p. 251111, 2008.

[17] F. Kong, B.-I. Wu, J. A. Kong, J. Huangfu, S. Xi, and H. Chen, "Planar focusing antenna design by using coordinate transformation technology," *Applied Physics Letters*, vol. 91, no. 25, p. 253509, 2007.

[18] A. V. Kildishev and E. E. Narimanov, "Impedance-matched hyperlens," *Optics letters*, vol. 32, no. 23, pp. 3432–3434, 2007.

[19] D. Lu and Z. Liu, "Hyperlenses and metalenses for far-field super-resolution imaging," *Nature Communications*, vol. 3, 2012.

[20] D. Schurig, J. B. Pendry, and D. R. Smith, "Transformation-designed optical elements," *Optics Express*, vol. 15, no. 22, pp. 14 772–14 782, 2007.

[21] M. Tsang and D. Psaltis, "Magnifying perfect lens and superlens design by coordinate transformation," *Physical Review B*, vol. 77, no. 3, p. 035122, 2008.

[22] M. Yan, W. Yan, and M. Qiu, "Cylindrical superlens by a coordinate transformation," *Physical Review B*, vol. 78, no. 12, p. 125113, 2008.

[23] W. X. Jiang, T. J. Cui, H. F. Ma, X. Y. Zhou, and Q. Cheng, "Cylindrical-to-plane-wave conversion via embedded optical transformation," *Applied Physics Letters*, vol. 92, no. 26, p. 261903, 2008.

[24] D.-H. Kwon and D. H. Werner, "Transformation optical designs for wave collimators, flat lenses and right-angle bends," *New Journal of Physics*, vol. 10, no. 11, p. 115023, 2008.

[25] Y. Lai, et al., "Illusion optics: the optical transformation of an object into another object," *Physical Review Letters*, vol. 102, no. 25, p. 253902, 2009.

[26] Y. G. Ma, C. Ong, T. Tyc, and U. Leonhardt, "An omnidirectional retroreflector based on the transmutation of dielectric singularities," *Nature Materials*, vol. 8, no. 8, pp. 639–642, 2009.

[27] M. Rahm, S. A. Cummer, D. Schurig, J. B. Pendry, and D. R. Smith, "Optical design of reflectionless complex media by finite embedded coordinate transformations," *Physical Review Letters*, vol. 100, no. 6, 2008.

[28] M. Rahm, D. Roberts, J. Pendry, and D. Smith, "Transformation-optical design of adaptive beam bends and beam expanders," *Optics Express*, vol. 16, no. 15, pp. 11 555–11 567, 2008.

[29] D. Schurig, "An aberration-free lens with zero f-number," *New Journal of Physics*, vol. 10, 2008.

[30] S. A. R. Horsley, "Transformation optics, isotropic chiral media and non-Riemannian geometry," *New Journal of Physics*, vol. 13, no. 5, pp. 053 053+, May 2011.

[31] G. Yun, K. Crabtree, and R. A. Chipman, "Skew aberration: A form of polarization aberration," *Optics Letters*, vol. 36, no. 20, pp. 4062–4064, 2011.

[32] M. Born and E. Wolf, *Principles of Optics*, 7th ed. Cambridge University Press, 1999.

[33] http://en.wikipedia.org/wiki/Levi-Civita_connection.

[34] http://en.wikipedia.org/wiki/List_of_formulas_in_Riemannian_geometry#Under_a_conformal_change.

[35] R. K. Luneburg and M. Herzberger, *Mathematical Theory of Optics*. University of California Press, 1964.

[36] S. M. Rytov, "On the transition from wave to geometrical optics," in *Dokl. Akad. Nauk SSSR*, vol. 18, no. 2, 1938, pp. 263–267.

[37] S. I. Vinitskii, V. L. Derbov, V. M. Dubovik, B. L. Markovski, and Y. P. Stepanovskii, "Topological phases in quantum mechanics and polarization optics," *Soviet Physics Uspekhi*, vol. 33, no. 6, p. 403, 1990.

[38] I. U. A. Kravtsov, *Geometrical Optics in Engineering Physics*. Alpha Science, 2005.

[39] http://en.wikipedia.org/wiki/FrenetSerret_formulas.

[40] J. A. Lock, "Scattering of an electromagnetic plane wave by a Luneburg lens. I. Ray theory," *J. Opt. Soc. Am. A*, vol. 25, no. 12, pp. 2971–2979, Dec. 2008.

[41] See Supplementary Material for description on chiral media, full wave simulations with and without chiral gradient, animations of ray tracing for different GRIN lenses and Frenet-Serret Frame.

[42] A. J. Viitanen, I. V. Lindell, and A. H. Sihvola, "Polarization correction of luneburg lens with chiral medium," *Microwave and Optical Technology Letters*, vol. 3, no. 2, pp. 62–66, 1990.

[43] E. Hecht, *Optics*, 4th ed. Addison-wesley, Aug. 2002.

# CHAPTER 5

# W-BAND SPARSE SYNTHETIC APERTURE FOR COMPUTATIONAL IMAGING

This chapter, in full, has been published in Optics Express, **24**, 8317-8331 (2016), with authors Suresh Venkatesh, Naren Viswanathan, and David Schurig. (reprinted with permission)

## 5.1 Abstract

We present a sparse, synthetic-aperture, active imaging system at W-band (75 - 110 GHz) which uses sub-harmonic mixer modules. The system employs mechanical scanning of the receiver module position, and a fixed transmitter module. A vector network analyzer provides the back end detection. A full-wave forward model allows accurate construction of the image transfer matrix. We solve the inverse problem to reconstruct scenes using the least squares technique. We demonstrate far-field, diffraction limited imaging of 2D and 3D objects and achieve a cross-range resolution of 3 mm and a depth-range resolution of 4 mm, respectively. Furthermore, we develop an information-based metric to evaluate the performance of a given image transfer matrix for noise-limited, computational imaging systems. We use this metric to find the optimal gain of the radiating element for a given range, both theoretically and experimentally in our system.

## 5.2 Introduction

Millimeter waves (30 - 300 GHz) occupy a strategic part of the electromagnetic spectrum because they can penetrate many non-metallic barriers including things like walls, clothing, smoke and fog, while at the same time allow probing of objects with superior resolution to microwaves. Hence, millimeter wave imaging systems have found applications in the fields of radio astronomy [1], remote sensing [2], biomedical imaging [3] and security surveillance [4].

The current state of the art in advanced millimeter wave imaging systems used in airports and security checkpoints employ a wideband, cylindrically scanning, 3D imaging system [5, 6]. Specifically, the L3 ProVision ATD body scanner deployed in United States airports consist of two vertical linear antenna arrays (with 384 antenna elements in each array) operating at Ka-band (24.5 - 30 GHz) [6]. The arrays are mounted on a cylindrical mechanical scanning stage, and employ 3D near-field holographic image reconstruction techniques, which are computationally very intensive [4]. In contrast, a more ideal imaging system for security screening applications, might incorporate a planar form factor with fixed (or electrically tuned or switched) elements and operate at greater stand-off. Employing fewer elements could mitigate analog hardware costs, as well as computational requirements, if a suitable compressed image reconstruction algorithm were to enable comparable imaging performance.

In recent years, advances in CMOS and SiGe BiCMOS devices have significantly reduced the per channel cost of operating in this band, enabling more wide spread use of millimeter waves for both communications, and imaging [7–9]. However, over the same period, computational resources have advanced at an even greater pace, so that the optimal trade-off position strongly favors using more computational resources and less analog, source and acquisition hardware. The techniques of computational imaging make such trade-off possible [10]. Not to be confused with image processing, computational imagers use hardware specific algorithms, and generally do not produce useful or recognizable images before the data is processed.

The unique constraints and capabilities of millimeter-waves and the associated source and acquisition hardware lead quite naturally to unconventional imaging systems. The specific system we investigate here is: active and phase sensitive, employs a sparse, undersampled, mechanically-scanned, planar, array aperture, encodes spatial diversity over a swept frequency range, and reconstructs images from acquired data sets that are underdetermined (i.e. compressed imaging).

With the notable exception of astronomy, most millimeter-wave imaging is active, since ambient, terrestrial, millimeter-wave radiation is quite weak [11]. Also, since phase-sensitive measurements are readily supported by the hardware up through millimeter wave frequencies, active imagers are usually also holographic, and do not require focusing optics

[4]. Though less common, active imagers also offer the opportunity to encode distinct spatial patterns (modes) on the sensor *and* source fields. We opted for dominant spatial encoding on the sensor side, the usual case.

Our source is composed of a single-element radiator at a fixed position, co-planar with and adjacent to our sensor array, which is mechanical-scanned and synthetic. Mechanical scanning precludes real-time imaging of dynamic objects, but the performance of a hypothetical parallel-acquisition, multi-static imager can be evaluated from the results obtained with this prototype system. For this purpose, our synthetic aperture is both sparse and under-sampled, to keep the number of channels to a more realist number.

Our objects of interest are at most weakly dispersive over the millimeter wave spectrum. Hyperspectral information is thus fairly limited and not pursued. Instead we take advantage of the option to use data acquired at different frequencies to reconstruct a single, monochromatic image. The multi-frequency measurements can be acquired either in series (with a frequency ramp) or in parallel (frequency multiplexed). We used a frequency ramp, but again some aspects of parallel-acquisition performance may be evaluated using our simpler system. (In any case, available frequency ramp repetition rates allow for real-time use in many circumstances.) For the multi-frequency measurements to provide useful, independent information, they must encode independent spatial information. Frequency encoded spatial diversity can be supplied by an aperture with intrinsic frequency dispersion [12,13] or by the frequency dispersion of the propagation of complex field patterns between the measurement aperture and the object. We rely on the latter, since our aperture elements are either open-ended waveguides or horn radiators that have fixed field patterns versus frequency thus leading to a simpler aperture design. The approach of leveraging frequency encoded spatial diversity allows for additional target spatial information to be acquired with the simple addition of a swept oscillator to the measurement hardware. These frequency encoding approaches are in contrast to the well known single-pixel camera which typically uses a switched (temporal encoded) approach to spatial diversity [14,15]. These temporally encoded spatial diversity approaches rely on creating complex dynamically programmable spatially encoding apertures which could potentially allow for use of a targeted and possibly orthogonal spatial basis. Of course, hybrid systems can employ both temporal and frequency encoding.

Finally, to maximize the utilization of hypothetically-channel-constrained parallel acquisition hardware, we reconstruct images with more voxels than the number of measurements, i.e we perform under-determined reconstructions or compressive imaging [16, 17]. We reconstruct 2D and 3D images and demonstrate diffraction-limited resolution with our experimental system, in agreement with our simulated results. Additionally, we develop a figure of merit for noise-limited computational imaging systems based on the Singular Value Decomposition (SVD) and the Shannon-Hartley theorem, and verify its usefulness experimentally.

## 5.3 W-band Imaging System Setup

Our imaging system consists of a W-band transmitter (Tx) and receiver (Rx) which are sub-harmonic mixer extensions of a vector network analyzer (VNA). The Tx is stationary mounted and the Rx is mounted on a x-y scanning stage to create a synthetic receiver array. Interfaced to an Agilent PNA 5227A VNA through an N5260A millimeter-wave head module, the extensions are provided with a local oscillator (9.375 - 13.75 GHz) to mix between an intermediate-frequency (5 - 300 MHz) and the W-band (75 - 110 GHz). The W-band signal ports are WR-10 wave-guide. Both the bare wave-guide flange and a standard-gain horn were used as radiation elements. The Tx is connected to port1 of the VNA and the Rx to port2. The VNA's frequency offset option is used in measuring and recording the transmission coefficients (S21). These coefficients comprise the measurement set from which images were reconstructed. The setup is shown in Fig. 5.1.

## 5.4 Forward Model and Reconstruction

Using the first-order Born approximation [18], we assume our objects can be represented by a regularly spaced grid of point scatterers in the imaging domain. There is a linear relationship between the cross-sections of this grid of scatterers, represented by the complex-valued vector, $\mathbf{f}$, and our set of measurements, represented by the complex-valued vector, $\mathbf{g}$. This linear relationship is referred to as the image transfer matrix (or H-matrix) and it comprises our forward model,

$$\mathbf{g}_{[M\times 1]} = \mathbf{H}_{[M\times N]}\mathbf{f}_{[N\times 1]} \tag{5.1}$$

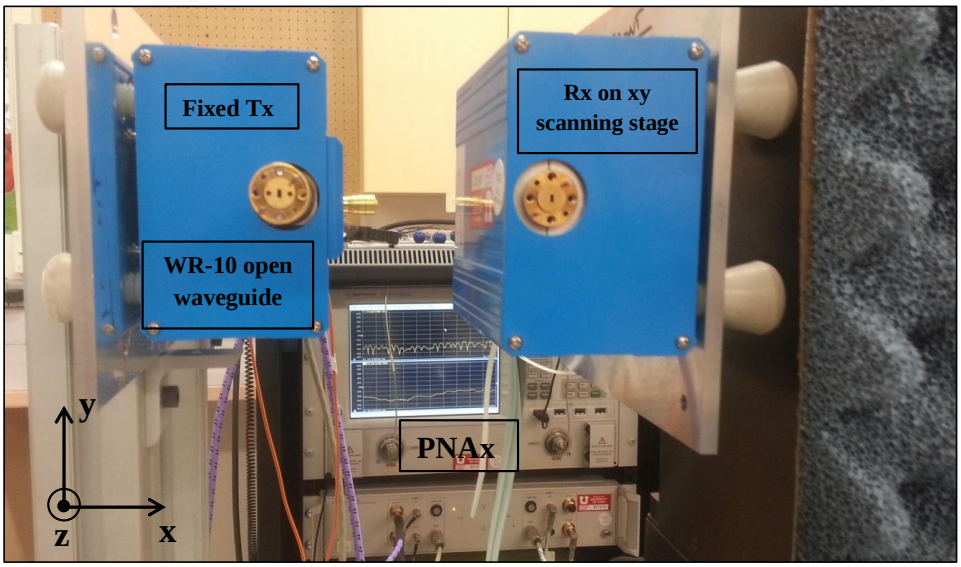


**Figure 5.1**: W-band setup showing Tx and Rx modules. Tx is at a fixed location and Rx is on a x-y scanning stage.

where we have $M$ measurements and $N$ scattering grid points (or voxels) in the imaging space (also called the scene). The forward model, $\mathbf{H}$, is generally fairly straightforward to compute, as will be shown below. However, reconstruction of an image from measurements is the inverse problem, the solutions of which are often under-determined and not unique. To aid in the solution of this often ill-posed problem, prior information, such as scene sparsity, scattering cross-section bounds, or object location, can be used. In this work, we use the regularized least squares approach to reconstruct a scene estimate $\mathbf{f}_e$,

$$\mathbf{f}_e = \min_{\mathbf{f}} ||\mathbf{Hf} - \mathbf{g}||_2^2 + \Upsilon||\mathbf{f}||_1^1 \tag{5.2}$$

where $||\cdot||_2$ is the $L^2$ norm, $\Upsilon > 0$ is a regularization parameter and $||\cdot||_1$ is the $L^1$ norm. For most of the large under-determined systems minimal $L^1$ norm regularization is sufficient [19, 20]. The regularization favors images with smaller combined cross-section. The first-order Born approximation assumes that the grid of point scatterers (representing the object) are weakly interacting. However, strong interactions that are relatively local will only result in a re-scaling of local scattering strength which may not significantly affect the reconstructed image geometry. (Strong interactions that are substantially nonlocal are likely to create image artifacts.) For example, a convex reflective surface with radius of curvature large compared to the wavelength should be reasonably well represented (and

imaged) using this model. Conceptually, an element of the image transfer matrix quantifies (with magnitude and phase) the signal path from source to scattering point to detector - for a unit scattering point. The row index of the transfer matrix element specifies the location of the transmitter and receiver, and the frequency. The column index specifies the location of the scattering point. The signal path includes: the propagation of fields from the transmitting element to a point scatterer, and the propagation of scattered fields from that point to the receiving element and the partial acceptance of the field energy by the receiving aperture. Invoking reciprocity, the back scatter propagation and receiver acceptance can be replaced by a forward propagation of the receiving aperture mode. This representation of the transfer matrix is more symmetric and reduces the complexity of the calculation.

$$H\left(\left\{\mathbf{r}_T, \mathbf{r}_R, \omega\right\}, \left\{\mathbf{r}_S\right\}\right) = \alpha\left(\omega\right) \mathbf{E}\left(\mathbf{r}_S; \mathbf{r}_T, \omega\right) \cdot \mathbf{E}\left(\mathbf{r}_S; \mathbf{r}_R, \omega\right) \tag{5.3}$$

where $\mathbf{E}\left(\mathbf{r}_S; \mathbf{r}_R \text{ or } \mathbf{r}_T, \omega\right)$ is the electric field propagated from either the receiving or transmitting element, to the location of the scattering point, $\mathbf{r}_S$. The factor $\alpha\left(\omega\right)$, includes any non-free-space parts of the signal path, which may be accounted for either through a hardware calibration (that de-embeds the measurement to the element aperture planes) or by inclusion in the transfer matrix. The arguments of $H$ are grouped into sets that comprise the row and column indices. For example the column index, $m$, labels all possible combinations of Tx position, Rx position and frequency.

$$H_{mn} = H\left(\left\{\mathbf{r}_T, \mathbf{r}_R, \omega\right\}_m, \left\{\mathbf{r}_S\right\}_n\right) \tag{5.4}$$

We perform the necessary field-propagations and construct the image transfer matrix by numerical computation. In our system, we use the bare flange of a WR-10 wave-guide or a standard-gain pyramidal horn as the transmitting and receiving element apertures. Both of these have known field patterns, and the former has a simple analytical expression (i.e. the TE10 mode). The electric field pattern at the mouth of a WR-10 open-ended waveguide is given by,

$$\mathbf{E} = E_0 \cos\left(\frac{\pi y}{a}\right) \hat{\mathbf{x}} \tag{5.5}$$

where a=2.54 mm and b=1.27 mm (see inset in Fig. 5.2) are the dimensions of the WR-10

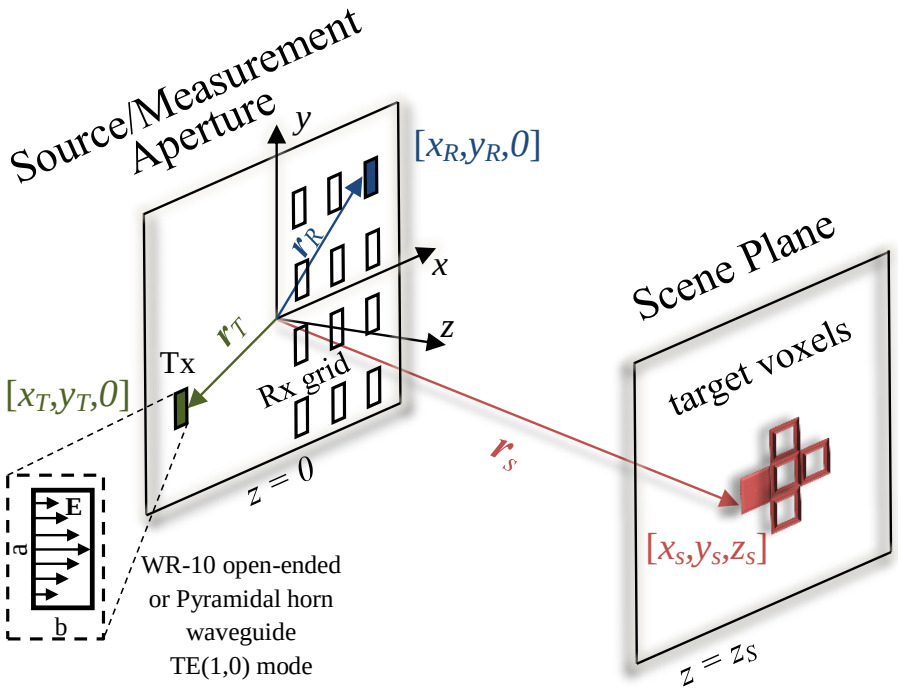


**Figure 5.2**: Forward Model setup showing the stationary Tx and scanned Rx grid on the source/measurement aperture along with target voxels on the scene plane.

rectangular waveguide. Similarly for a standard gain pyramidal horn the near field electric pattern is given by,

$$\mathbf{E} = E_0 \cos\left(\frac{\pi y}{a}\right) \exp\left[-j\frac{\omega}{2}\left(\frac{x^2}{R_1} + \frac{y^2}{R_2}\right)\right] \hat{\mathbf{x}} \tag{5.6}$$

where a=26.2 mm and b=20.3 mm (see inset in Fig. 5.2) are the dimensions of the WR-10 standard gain pyramidal horn and $R_1$ and $R_2$ are the E and H plane phase center distances. The aperture fields from the open-ended waveguide or the horn shown in (5.5) and (5.6) can be converted to magnetic surface currents using surface equivalence theorem [21],

$$\mathbf{M_s} = -2\hat{\mathbf{n}} \times \mathbf{E} \tag{5.7}$$

where $\hat{\mathbf{n}} = \hat{\mathbf{z}}$ is the surface normal. The magnetic surface current in the aperture plane can be converted to a set of magnetic dipoles,

$$\mathbf{m}_p = \left(\frac{j\Delta x \Delta y}{\omega \mu_0}\right) \mathbf{M_s} \tag{5.8}$$

where $\Delta x$ and $\Delta y$ are the near field pixel dimensions used for discretization. These individual dipoles can be propagated to the scene plane of interest using Green's function and

summed to get the overall response of Tx/Rx at a given scene voxel.

$$\mathbf{E}(\mathbf{r}_S;\mathbf{r}_R \text{ or } \mathbf{r}_T,\omega) = \frac{-j\omega\mu_0}{4\pi}\sum_p \left[\left(\frac{\mathbf{m}_p \times \mathbf{r}_S}{|\mathbf{r}_S|}\right)\left(\frac{-jk}{R_p} - \frac{1}{R_p^2}\right)\exp(-jkR_p)\right] \tag{5.9}$$

where k=$2\pi/\lambda$ is the wavenumber, $R_p = |\mathbf{r}_S - \mathbf{r}_R|$ for Rx or $R_p = |\mathbf{r}_S - \mathbf{r}_T|$ for Tx, is the distance of a $p^{th}$ magnetic dipole to the scene voxel. The above equation needs to computed for each Tx/Rx position in the aperture plane in order to construct the H matrix shown in (5.3).

We explored two propagation algorithms. The first approach propagates the element aperture electric field to a distance $z_S$ using fast Fourier angular spectrum method (ASM). The other approach converts the waveguide fields at the aperture to magnetic dipole moments using the surface equivalence theorem, then sums all the dipole fields at a given scene voxel using the dipole Green's function. The periodicity of discrete Fourier transforms and the divergence of the source fields lead to substantial required scaling of the Fourier domain versus propagation distance $z_S$. For this reason we found the Green's function method to be more efficient in our desired configurations. In (5.9), each dipole response at a given voxel can be independently calculated with respect to the other dipoles. This operation can be easily parallelized and hence the Green's function method was implemented on a GPU.

## 5.5 Experimental Imaging

As explained in the previous section, the H matrix is constructed computationally. However, this H matrix is incomplete without knowing the relative amplitude and phase of the Tx and Rx aperture fields as a function of frequency. This requires one calibration measurement between every Tx and Rx pair (in our case one pair). The calibration measurement is configured with the Tx aperture connected directly to the Rx. In this configuration, S21 provides the required *through* measurement. The resulting complex spectrum is used as a scaling factor for calculating the H matrix. The imaging capabilities of this setup were characterized by reconstructing resolution targets at different stand-off distances. The resolution target consists of copper strips glued on to a wooden board. The target consisting of 3mm wide copper strips was placed 15 cm away from the Tx/Rx aperture plane. The Rx was positioned on $11\times11$ sparse rectangular grid with a spacing of

1.2 cm. The distance between the farthest Rx position and the stationary Tx position was $\sim$ 12 cm. This largest baseline D determines the effective size of the synthetic aperture which in turn governs the cross range resolution. The cross range resolution is given by [22],

$$\Delta_{cr} = \frac{\lambda R}{2D} \tag{5.10}$$

where $\lambda$ is the wavelength and $R$ is the distance between aperture plane and target (i.e. stand-off distance). At each Rx position, complex S21 data for 101 frequency points (0.35 GHz frequency spacing) were recorded. This corresponds to a total number of measurements $M = 121 \times 1 \times 101 = 12221$. For the 3mm resolution target, 3D reconstruction was performed for a total number of scene voxels, $N = 60000$. Figure 5.3 shows the reconstruction of a 2D target performed using (5.2) at a stand-off distance of 15 cm. The image reconstructions in both simulation and measurement clearly resolve the 3mm strips. Similarly, a target consisting of 5mm copper strips was placed 30 cm away from the Tx/Rx aperture plane. The cross range resolution worsens with the increase in stand-off distance $R$. For the 5mm resolution target, 3D reconstruction was performed for a total number of scene voxels, $N = 208000$. The image reconstruction of this target is shown in Fig. 5.4. The 5mm wide strips are clearly resolved. We perform reconstruction using 3D scene volumes, even for the 2D planar targets, thus using only rough prior knowledge of the the plane of the scatterer. The depth/range resolution is given by [22],

$$\Delta_{dr} = \frac{c}{2B} \tag{5.11}$$

where $c$ is the speed of light in the medium and $B$ is the bandwidth. To quantify the depth resolution of our system, we used a target consisting of three 5 mm wide copper strips. One of the strips was raised 4mm above the other two strips. For this target, 3D reconstruction was performed for a total number of scene voxels, $N = 180000$. The image reconstructions from both simulation and measurement are shown in Fig. 5.5. The effect of measurement bandwidth on such frequency diverse computational imaging system was also studied (see Appendix A). The reduction of measurement bandwidth decreases the target spatial information that can be acquired from the imaging system.

Some differences between the simulation and experimental image reconstruction results are observed. We believe these differences are primarily due to differences between

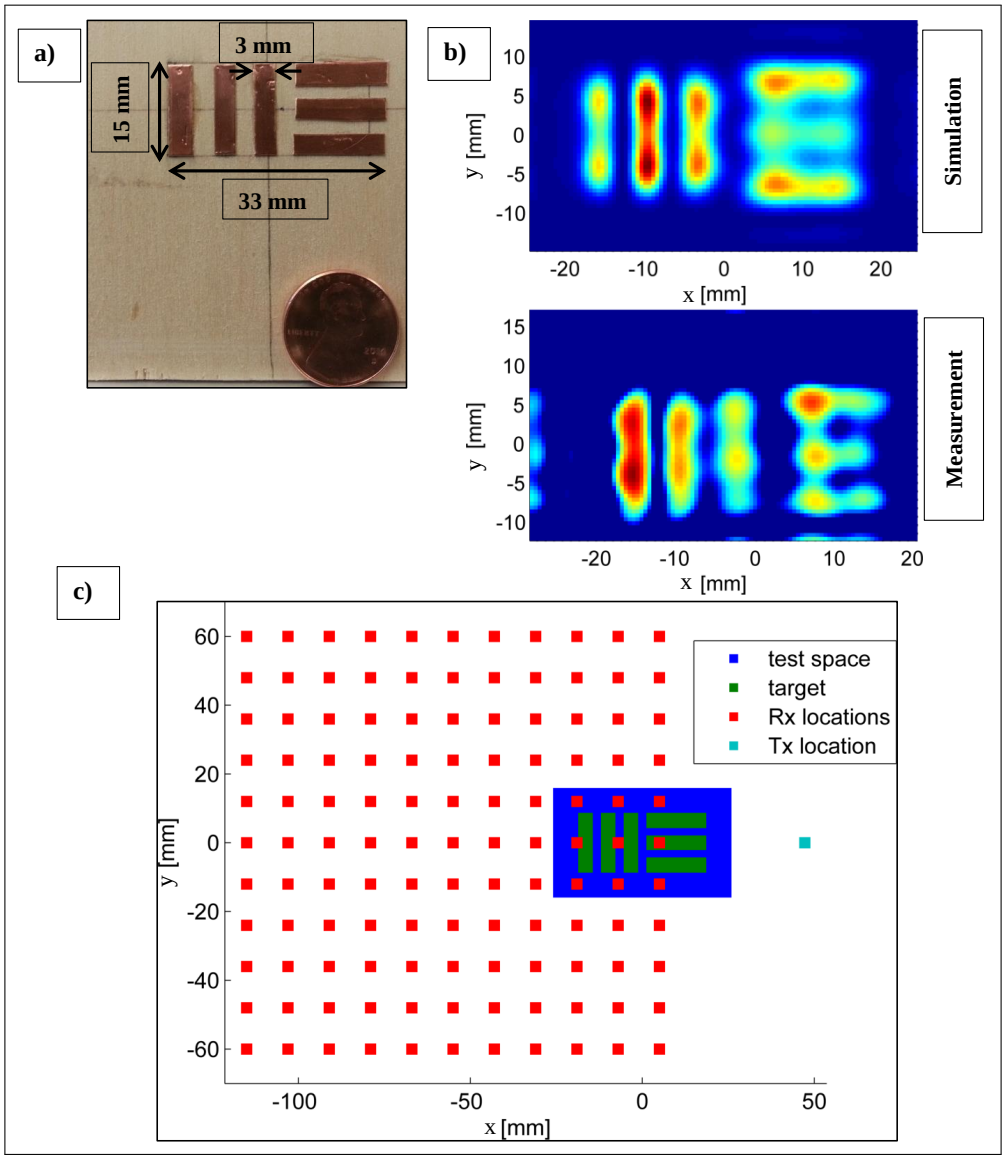


**Figure 5.3**: a). Shows the optical image of 3mm resolution target made of copper strips. b). Shows the W-band reconstructed image of the target from both simulation and measurement at a standoff distance of 15 cm. c). Shows the Rx grid and Tx locations relative to the target.

the configuration geometry used for the propagation model (incorporated in the the construction of the forward model **H** matrix) and the actual positions and orientations of the Tx and Rx modules used in the experiment. Additionally, analytic expressions were used for the waveguide and horn aperture fields in the forward model, which may have differed somewhat from the actual experimentally realized fields. We do not believe, however, that deviations of the experimental noise characteristics from the assumed noise

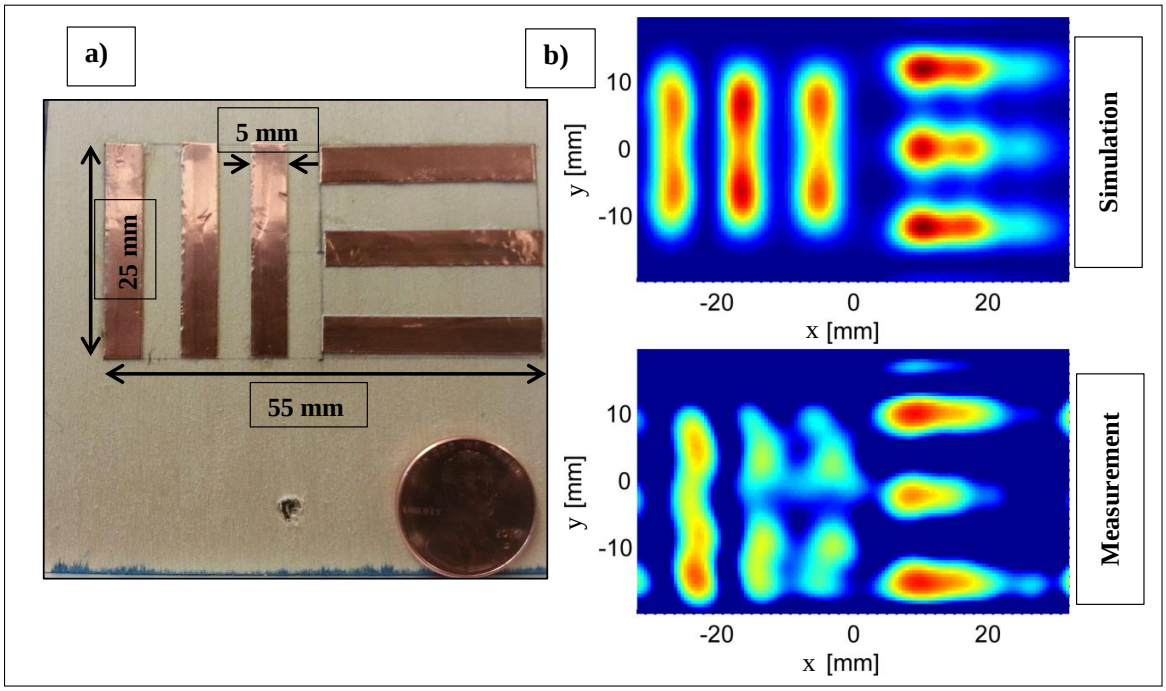


**Figure 5.4**: a). Shows the optical image of 5mm resolution target made of copper strips. b). Shows the W-band reconstructed image of the target from both simulation and measurement at a standoff distance of 30 cm.

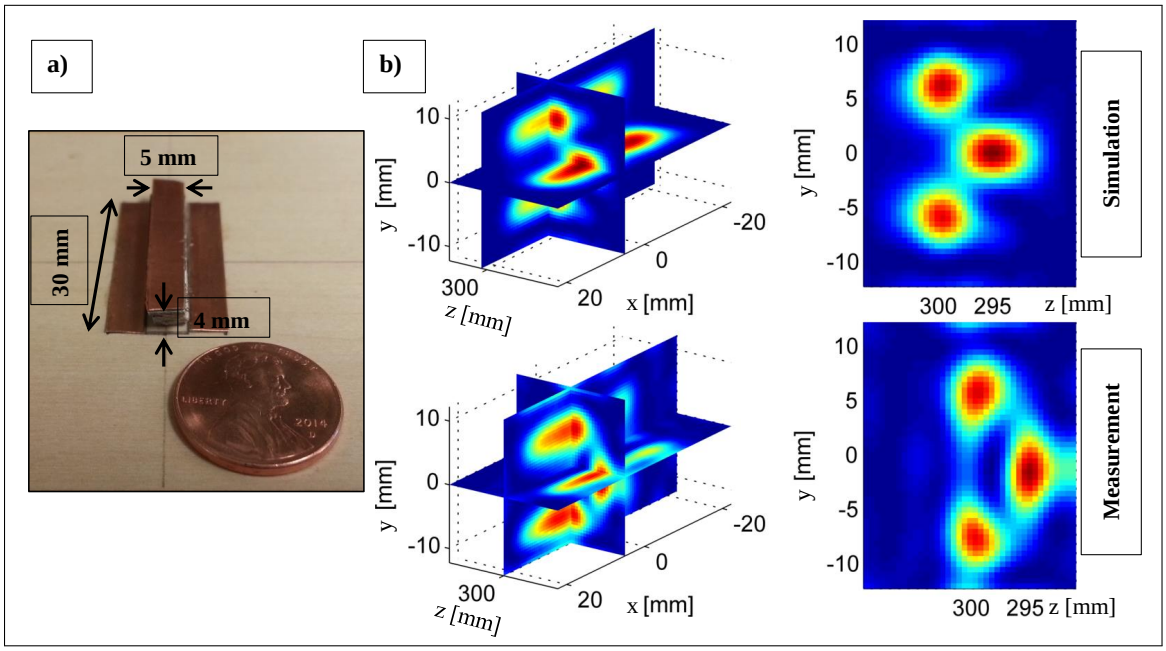


**Figure 5.5**: a). Shows the optical image of 4mm depth resolution target made of copper strips. b). Shows the W-band reconstructed image (perspective and side view) of the target from both simulation and measurement at a standoff distance of 30 cm.

model were significant factors, since the signal-to-noise levels were generally high. Despite these potential sources of error, we found the computed forward model, embodied by the **H** matrix, and used in solving the inverse problem, effective for diffraction-limited experimental image reconstructions.

This method qualifies as a sparse imaging technique because the scene is spatial sampled below the Nyquist limit (unlike a conventional synthetic aperture radar) and the total number of voxels reconstructed is substantially greater than the number of measurements ($N > M$). This overall approach can be easily scaled to multiple Txs and Rxs, to form a multi-static imaging system without requiring mechanical scanning for data acquisition. In our single fixed Tx system, the aperture size, $D$, is constrained by measurement signal-to-noise ratio. This limits the achievable cross range resolution and field of view. Our setup being active and planar Tx/Rx aperture, specularity can also be an issue [23]. Target specular areas with surface normals that point away from the Tx/Rx pair do not contribute significant signal and hence such areas do not appear (appear weaker) in the reconstructions. This can be mitigated by having larger or partially (or totally) curved enclosing apertures. This problem can also be overcome by exploiting polarization information [24]. Our measurements were not optimized to highlight this difficulty. With multiple Txs and Rxs, one could create a larger aperture leading to better cross range resolutions at greater standoff distances and at the same time reduce specularity effects.

## 5.6 Information Metric for Computational Imaging

The image transfer matrix, **H**, is one of the key factors that affects the quality of image reconstructions in a noise limited computational imaging system. Hence, it is useful to develop a strategy to quantify the performance of a system described by the this matrix. Starting with (5.1), $\mathbf{g} = \mathbf{H}\,\mathbf{f}$, we can find an information metric (or figure of merit) for characterizing a given **H** matrix. Consider an ensemble of possible scene vectors, $\{\mathbf{f}\}$. If the scattering of scene voxels is uncorrelated and the spread of scattering amplitudes is equal in all voxels, then the covariance of the ensemble is given by

$$\mathbf{\Sigma}_f = \Delta f^2 \mathbf{I} \tag{5.12}$$

where **I** is the identity matrix, and $\Delta f$ is the spread of scattering amplitudes over the ensemble $\{\mathbf{f}\}$. Equation (5.12) could potentially include correlations of the scene voxels

leading to off-diagonal elements in the covariance matrix and this prior can also be exploited in the image reconstructions. Since we do not leverage this prior in our image reconstructions, the assumption of uncorrelated scene voxels in the calculation of information metric is valid. We can find the related covariance in the measurement space of $\mathbf{g}$, with the standard uncertainty propagation formula, applied to (5.1)

$$\mathbf{\Sigma}_g = \mathbf{H}\mathbf{\Sigma}_f\mathbf{H}^\dagger \tag{5.13}$$

This matrix describes the a priori known range of possible values of the measurements and their correlations. If we have both the a priori measurement ranges and the measurement uncertainty, we can find the added information of the measurements, using the Shannon-Hartley theorem. If we find a basis in which the range and uncertainty covariances are mutually diagonal, the total added information of the measurement set can be easily computed. To find a suitable mutual diagonalizing basis we perform the singular value decomposition $\mathbf{H} = \mathbf{U}\mathbf{S}\mathbf{V}^\dagger$, then the $\mathbf{g}$-covariance matrix becomes,

$$\mathbf{\Sigma}_g = \mathbf{H}\mathbf{\Sigma}_f\mathbf{H}^\dagger = \mathbf{U}\mathbf{S}\mathbf{V}^\dagger\Delta f^2\mathbf{I}(\mathbf{U}\mathbf{S}\mathbf{V}^\dagger)^\dagger = \Delta f^2\mathbf{U}\mathbf{S}\mathbf{S}^\dagger\mathbf{U}^\dagger \tag{5.14}$$

where we have used the unitarity of $\mathbf{V}$. Next, we find the measurement uncertainty of $\mathbf{g}$. If we assume the measurement noise is uncorrelated and equal for all measurement components, the measurement noise covariance matrix is,

$$\sigma_g = \delta g^2\mathbf{I} \tag{5.15}$$

where $\delta$g is the measurement noise magnitude, and $\mathbf{I}$ is the identity matrix. Note that we will use $\mathbf{\Sigma}$ to denote the covariance associated with the ensemble of different possible scenes (i.e the range) and $\sigma$ to denote covariance associated with the measurement noise (i.e. the uncertainty), though the latter is nonstandard. Though $\sigma_g$ is diagonal, $\mathbf{\Sigma}_g$ is not. The singular value decomposition of $\mathbf{H}$ provides a mutually diagonalizing basis through the unitary matrix, $\mathbf{U}$. Define a new "measurement" vector

$$\gamma = \mathbf{U}^\dagger\mathbf{g} \tag{5.16}$$

Now error propagate the range- and uncertainty-covariance matrices to this basis

$$\sigma_\gamma = \mathbf{U}^\dagger\sigma_g(\mathbf{U}^\dagger)^\dagger = \mathbf{U}^\dagger\delta g^2\mathbf{I}(\mathbf{U}^\dagger)^\dagger = \delta g^2\mathbf{I} \tag{5.17}$$

$$\mathbf{\Sigma}_\gamma = \mathbf{U}^\dagger\mathbf{\Sigma}_g(\mathbf{U}^\dagger)^\dagger = \mathbf{U}^\dagger\Delta f^2\mathbf{U}\mathbf{S}\mathbf{S}^\dagger\mathbf{U}^\dagger(\mathbf{U}^\dagger)^\dagger = \Delta f^2\mathbf{S}\mathbf{S}^\dagger \tag{5.18}$$

The covariances in this basis are mutually diagonal and their components represent independent measurements both in terms of range and uncertainty. Employing the Shannon–Hartley theorem, the added information of one such measurement component is

$$Q_m = \Delta t B \log_2 \left[ \frac{\Sigma_{\gamma mm}}{\sigma_{\gamma mm}} + 1 \right] = \Delta t B \log_2 \left[ \left( \frac{\Delta f}{\delta g} S_{mm} \right)^2 + 1 \right] \tag{5.19}$$

where $\Delta t B$ is the measurement time–bandwidth product. The total measurement–added information is just the sum of these independent pieces of information

$$Q = \sum_{m=1}^{M} Q_m \tag{5.20}$$

where $M$ is the total number of measurements.

To use this metric we require the singular values of the image transfer matrix, $S_{mm}$, the measurement noise level, $\delta g$, and the scattering variance, $\Delta f$. The singular values come from the **H** matrix, which is determined as described above. The measurement noise level, $\delta g$, can be found from the variance of multiple measurements of the same configuration. (The multiple measurements should be net measurements, including any calibration procedures. We used a Rx-position and frequency dependent calibration.) Since we assume a constant noise level in the metric analysis, we assign a typical value for the noise level based on measurements of different configurations. The scattering variance, $\Delta f$, should scale with the maximum scattering cross-section that will be observed for the ensemble of measurements being considered. In particular, it will be dependent on the size of the scene voxels. One could find the maximum scattering cross-section analytically from fundamental electromagnetic scattering calculations and scale the result appropriately to the desired **H** matrix. Alternatively, one could perform a reconstruction from measured data, **g**, using an arbitrarily scaled **H** matrix and a strong scattering target. Then the largest magnitudes in the reconstructed scene vector, **f**, provide a maximum scattering cross-section appropriately scaled to the **H** matrix used. Based on this maximum scattering cross-section, the scattering variance, $\Delta f$, can be assigned.

## 5.7 Gain and Stand-off Distance Trade-off

We use information metric analysis described in the previous section to evaluate the trade-off between Tx/Rx aperture gain and standoff distance of the target. This approach

is particularly useful while designing computational imaging systems. We construct different H matrices corresponding to every combination of gain and stand-off values. For each H matrix, we evaluate the total information Q for an uncorrelated scene ensemble given by (5.19). We assume a measurement time bandwidth product, $\Delta tB = 1$, and a $\delta g$ and $\Delta f$ from measurement (as described in the previous section). Figure 5.6(b) shows the normalized information metric Q as a function of gain and range. Heuristically arguing, a lower gain element (eg. an open ended WR10 waveguide) for the Tx and Rx, leads to a beam with wider divergence that illuminates the target more broadly as compared to the highly directive beam provided by a high gain element (eg. standard gain WR10 pyramidal horn). The higher-gain element can fail to significantly illuminate the target at wider Tx/Rx baselines and miss some of the available information. However, at larger stand-off distance, the highly directive beam *will* illuminate the target sufficiently broadly, and provide greater signal to noise (and thus greater information) as compared to the broader beam.

We experimentally demonstrate this effect by choosing a 1 mm thick wire scatterer as the target and reconstructing this same target in different scenarios. The image reconstructions were performed at three different stand-off distances and two element gain values. The two gain values corresponded to a WR10 open-ended waveguide ($\sim$6 dB gain at 92.5 GHz) and a WR10 standard pyramidal horn ($\sim$22 dB gain at 92.5 GHz). The white ovals on Fig. 5.6(b) mark these six scenarios on the normalized information metric plot. At a stand-off range of 4 cm, the open-ended waveguide setup resolves the wire target better than the horn setup and the corresponding reconstructions for both cases are shown in Fig. 5.7. At a target distance of 20 cm, the open-ended waveguide and horn elemental apertures perform about equally well, in qualitative agreement with the information metric shown in Fig. 5.6(b). The image reconstructions are shown in Fig. 5.8. At 50 cm, the reconstruction from open-ended waveguide setup completely fails, but the imaging system with horn still reconstructs the target effectively. This is shown in Fig. 5.9. In all the above cases, the effective synthetic aperture size was kept constant. A single thin-wire target (with constant scattering cross section at all stand-off distances) was chosen for this demonstration as one can also easily visualize the change in resolution and field of view as gain and stand-off distance varies.

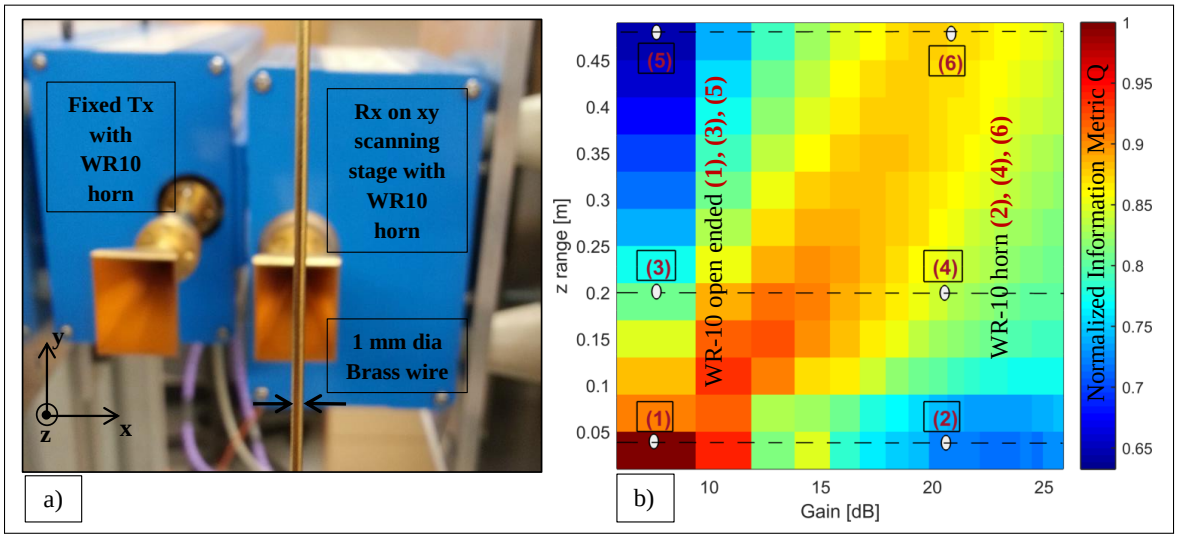


**Figure 5.6**: a). Shows the Tx and Rx modules with brass wire as the target. b) Shows the plot of normalized total information metric, $Q$, as a function of Tx/Rx aperture gain and stand-off range distance. Points (1), (3) and (5) correspond to WR10 open ended waveguide element-apertures (low gain) for both Tx and Rx. Points (2), (4) and (6) correspond to WR10 standard pyramidal horn element-apertures (high gain) for both Tx and Rx.

## 5.8 Conclusion

We have demonstrated diffraction limited imaging in the W-band with a system that is both under-sampled and under-determined. Specifically, the synthetic aperture of transmitter locations is spaced at intervals greater than that prescribed by the Shannon-Nyquist sampling theorem, and the number of voxels in the reconstruction space exceed the total number of measurements. Though this system employs a mechanically-scanned synthetic receiver aperture with periodic locations, the methods of analysis and image reconstruction could easily be applied to a system with any combination of mechanically-scanned or parallel receivers and/or transmitters, at aperiodic locations. In particular, the information metric described here, applies to any noise limited imaging system where a forward model determination allows the construction of the image transfer matrix. This metric provided the answer to the simple, yet fundamental, question of optimal element gain for a given target range. Such questions can be difficult to answer for a complex computational imaging system.

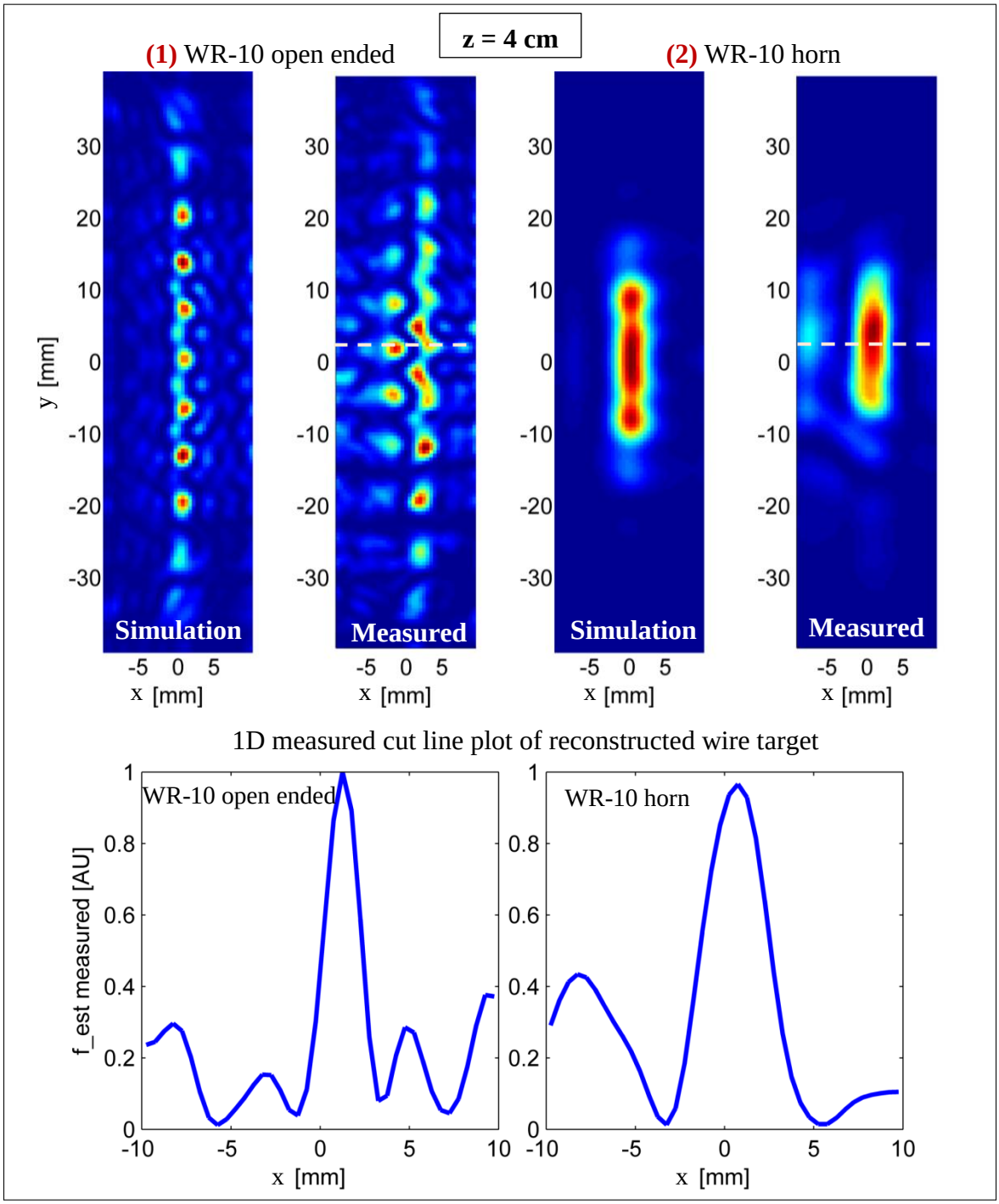


**Figure 5.7**: Image reconstructions of a 1 mm wire target at a stand-off distance of 4 cm with WR10 open-ended waveguide and standard gain pyramidal horn on Tx/Rx. The line plots correspond to the dashed line region in the 2D measured plots. The corresponding information metric Q for these two cases corresponds to marked points (1) and (2) in Fig. 5.6.

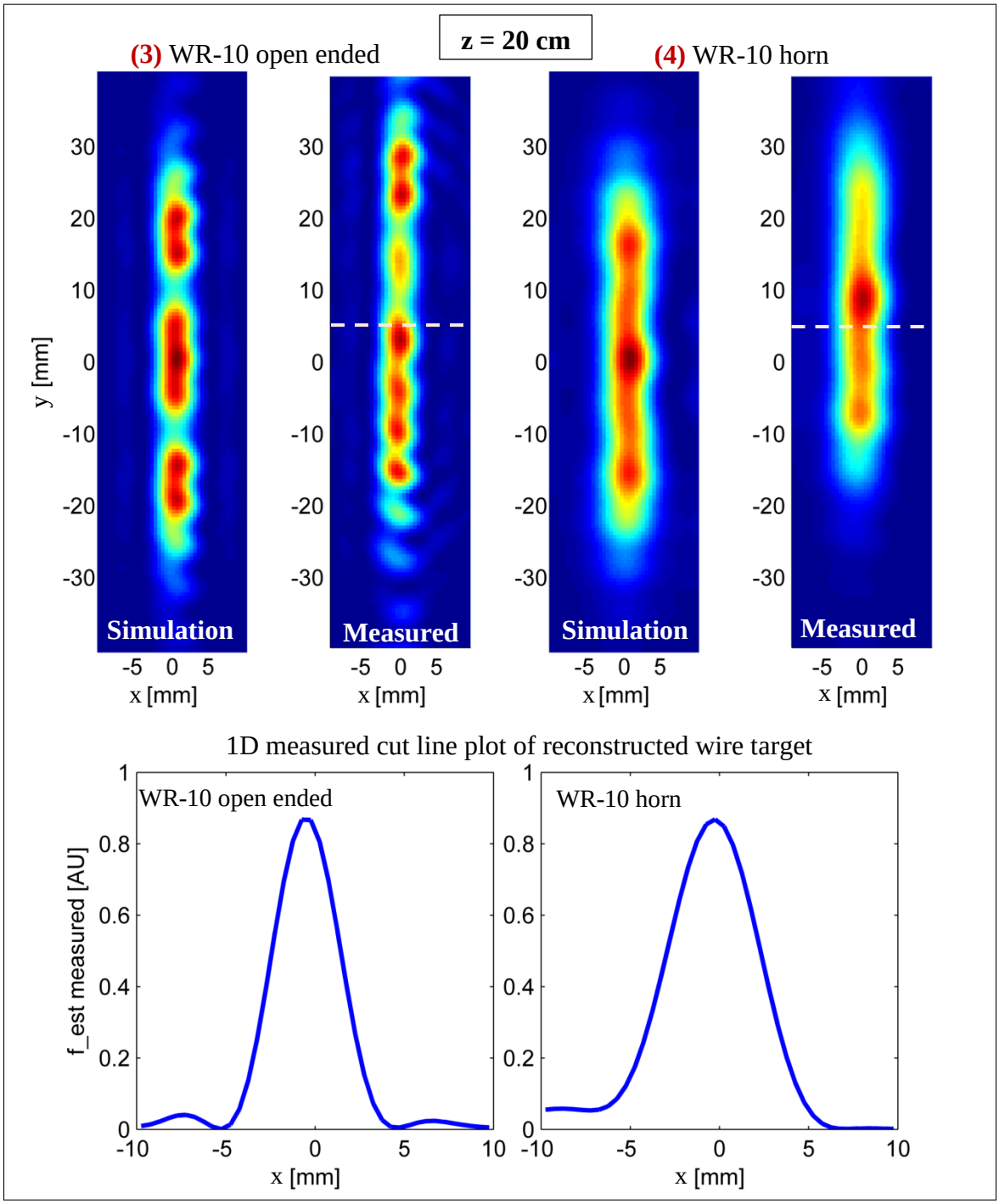


**Figure 5.8**: Image reconstructions of a 1 mm wire target at a stand-off distance of 20 cm with WR10 open-ended waveguide and standard gain pyramidal horn on Tx/Rx. The line plots correspond to the dashed line region in the 2D measured plots. The corresponding information metric Q for these two cases corresponds to marked points (3) and (4) in Fig. 5.6.

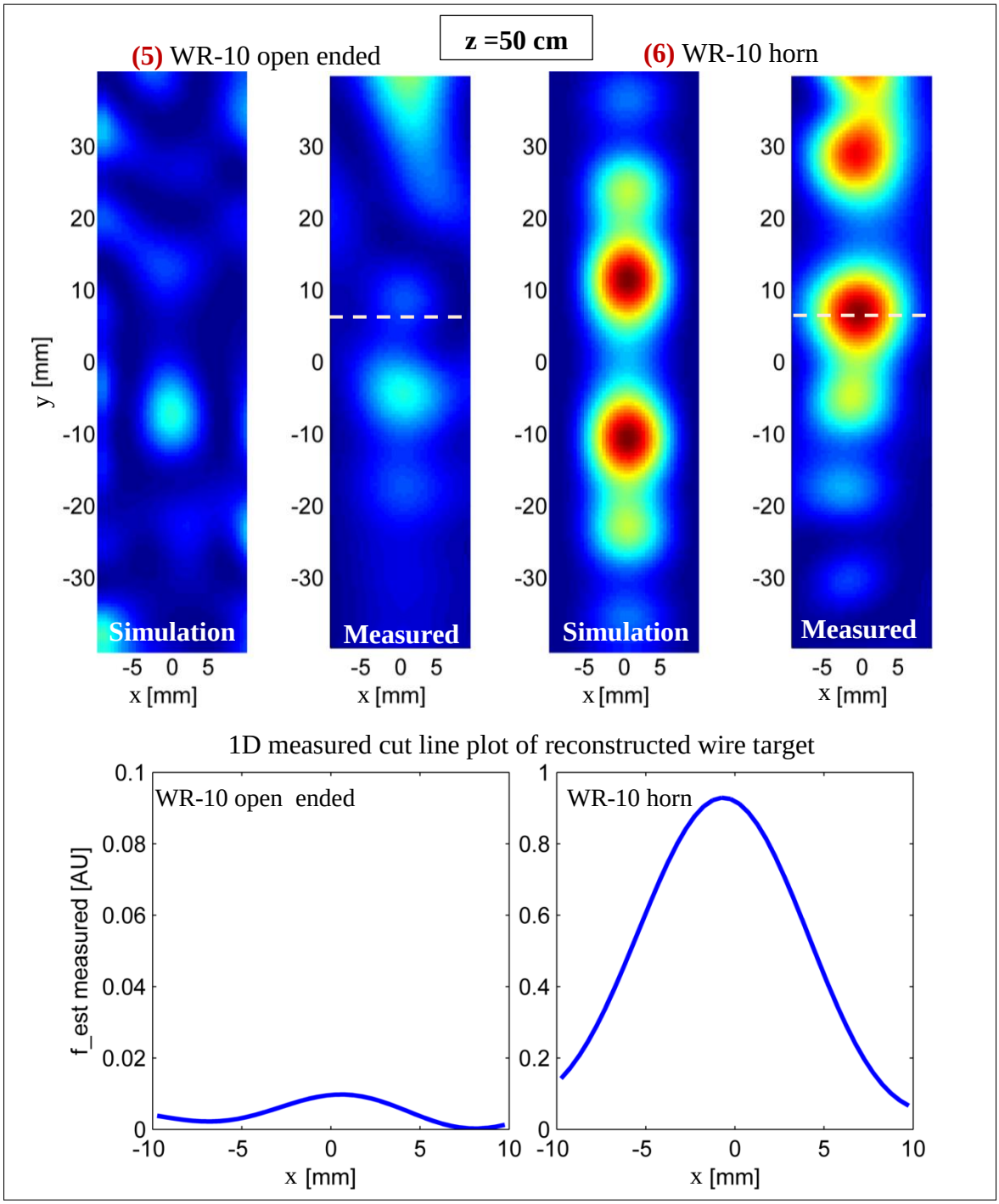


**Figure 5.9**: Image reconstructions of a 1 mm wire target at a stand-off distance of 50 cm with WR10 open-ended waveguide and standard gain pyramidal horn on Tx/Rx. The line plots correspond to the dashed line region in the 2D measured plots. The corresponding information metric Q for these two cases corresponds to marked points (5) and (6) in Fig. 5.6.

## 5.9 Supplementary Material: Effect of Measurement Bandwidth on Image Reconstructions

Figure 5.10 shows the effect of reducing the bandwidth on frequency diverse computational imaging system. Figure 5.10a) corresponds to the image reconstruction of 3 mm resolution target using complete 100% bandwidth (75 -110 GHz) measured data. All the features corresponding to the original target are effectively resolved. Upon reducing the measurement bandwidth to 70% (75 -100 GHz), 25% (88 -97 GHz) and 10% (90.75 - 94.25 GHz) the experimental image reconstructions degrade with the bandwidth reduction (corresponding to Fig. 5.10 b), c) and d) respectively). The reduction of measurement bandwidth also has an adverse effect on depth resolution.

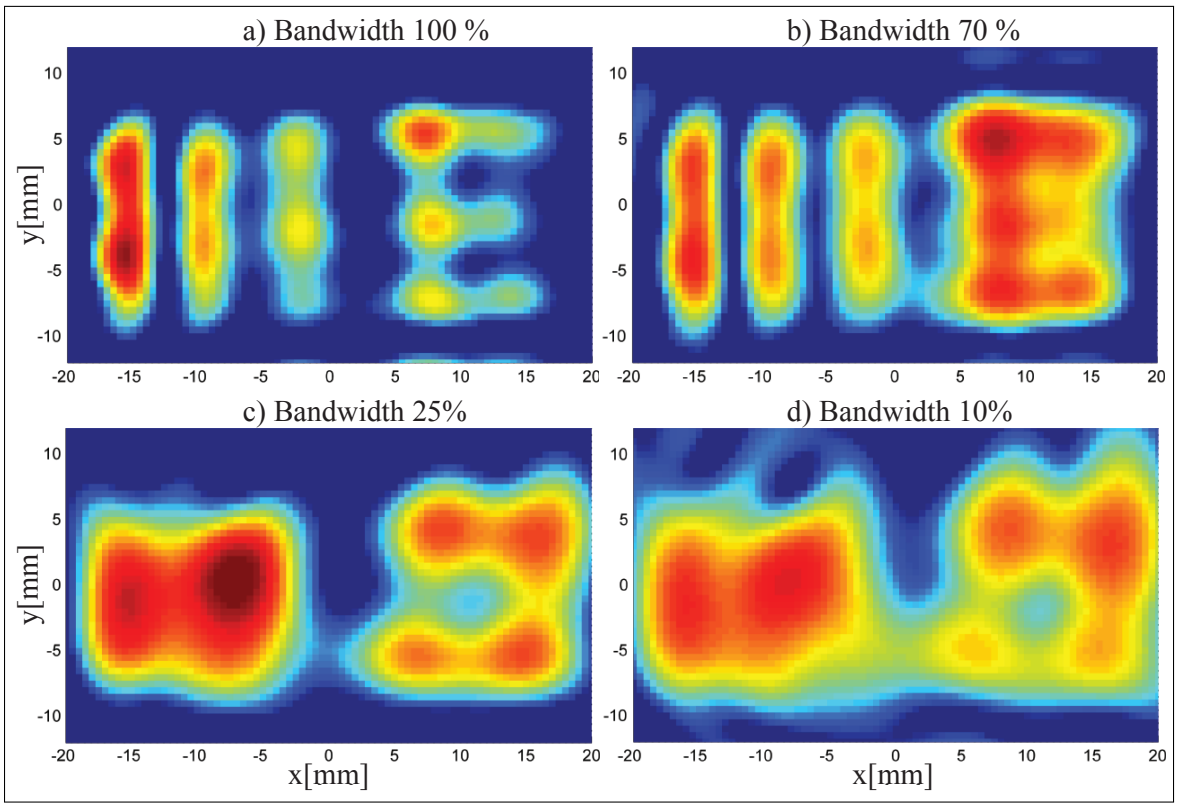


**Figure 5.10**: Shows the effect of reducing the bandwidth on our frequency diverse computational imaging system. Shown are the experimental image reconstructions for the 3 mm resolution target.

## 5.10 Acknowledgments

This work was supported by the Department of Homeland Security, Science and Technology Directorate (Contract No. HSHQDC-12-C-00049). The published material represents the position of the authors and not necessarily that of the DHS or S&T. We would like to acknowledge Prof. David Smith (Duke University) and Dr. Alec Rose (Evolv Technology) for their help with the simulations.

## 5.11 References

[1] A. Wootten and A. R. Thompson, "The Atacama large millimeter/submillimeter array," *Proceedings of the IEEE*, vol. 97, no. 8, pp. 1463–1471, Aug 2009.

[2] G. M. Rebeiz, D. P. Kasilingam, Y. Guo, P. A. Stimson, and D. B. Rutledge, "Monolithic millimeter-wave two-dimensional horn imaging arrays," *IEEE Transactions on Antennas and Propagation*, vol. 38, no. 9, pp. 1473–1482, Sep 1990.

[3] Z. Q. Zhang and Q. H. Liu, "Three-dimensional nonlinear image reconstruction for microwave biomedical imaging," *IEEE Transactions on Biomedical Engineering*, vol. 51, no. 3, pp. 544–548, March 2004.

[4] D. M. Sheen, D. L. McMakin, and T. E. Hall, "Three-dimensional millimeter-wave imaging for concealed weapon detection," *IEEE Transactions on Microwave Theory and Techniques*, vol. 49, no. 9, pp. 1581–1592, Sep 2001.

[5] R. Appleby and C. Cameron, "Seeing hidden objects with millimetre waves," *Physics World*, vol. 25, no. 01, p. 35, 2012.

[6] D. Sheen, D. McMakin, and T. Hall, "Near-field three-dimensional radar imaging techniques and applications," *Appl. Opt.*, vol. 49, no. 19, pp. E83–E93, Jul 2010.

[7] E. Ojefors, B. Heinemann, and U. R. Pfeiffer, "Active 220- and 325-ghz frequency multiplier chains in an sige hbt technology," *IEEE Transactions on Microwave Theory and Techniques*, vol. 59, no. 5, pp. 1311–1318, May 2011.

[8] B. A. Floyd, S. K. Reynolds, U. R. Pfeiffer, T. Zwick, T. Beukema, and B. Gaucher, "Sige bipolar transceiver circuits operating at 60 ghz," *IEEE Journal of Solid-State Circuits*, vol. 40, no. 1, pp. 156–167, Jan 2005.

[9] E. Ojefors and U. R. Pfeiffer, "A 650ghz sige receiver front-end for terahertz imaging arrays," in *2010 IEEE International Solid-State Circuits Conference-(ISSCC)*, 2010.

[10] B. Gonzalez-Valdes, G. Allan, Y. Rodriguez-Vaqueiro, Y. lvarez, S. Mantzavinos, M. Nickerson, B. Berkowitz, J. A. Martnez-Lorenzo, F. Las-Heras, and C. M. Rappaport, "Sparse array optimization using simulated annealing and compressed sensing for near-field millimeter wave imaging," *IEEE Transactions on Antennas and Propagation*, vol. 62, no. 4, pp. 1716–1722, April 2014.

[11] S. Stanko, F. Klppel, J. Huck, D. Ntel, M. Hgelen, G. Briese, A. Gregor, S. Erukulla, H.-H. Fuchs, H. Essen, and A. Pagels, "Remote concealed weapon detection in millimeter-wave region: active and passive," pp. 639 606–639 606–6, 2006.

[12] J. Hunt, J. Gollub, T. Driscoll, G. Lipworth, A. Mrozack, M. S. Reynolds, D. J. Brady, and D. R. Smith, "Metamaterial microwave holographic imaging system," *J. Opt. Soc. Am. A*, vol. 31, no. 10, pp. 2109–2119, Oct 2014.

[13] G. Lipworth, A. Mrozack, J. Hunt, D. L. Marks, T. Driscoll, D. Brady, and D. R. Smith, "Metamaterial apertures for coherent computational imaging on the physical layer," *J. Opt. Soc. Am. A*, vol. 30, no. 8, pp. 1603–1612, Aug 2013.

[14] P. Llull, X. Liao, X. Yuan, J. Yang, D. Kittle, L. Carin, G. Sapiro, and D. J. Brady, "Coded aperture compressive temporal imaging," *Opt. Express*, vol. 21, no. 9, pp. 10 526–10 545, May 2013.

[15] C. M. Watts, D. Shrekenhamer, J. Montoya, G. Lipworth, J. Hunt, T. Sleasman, S. Krishna, D. R. Smith, and W. J. Padilla, "Terahertz compressive imaging with metamaterial spatial light modulators," *Nature Photonics*, vol. 8, no. 8, pp. 605–609, 2014.

[16] E. J. Candes, J. Romberg, and T. Tao, "Robust uncertainty principles: exact signal reconstruction from highly incomplete frequency information," *IEEE Transactions on Information Theory*, vol. 52, no. 2, pp. 489–509, Feb 2006.

[17] C. F. Cull, D. A. Wikner, J. N. Mait, M. Mattheiss, and D. J. Brady, "Millimeter-wave compressive holography," *Appl. Opt.*, vol. 49, no. 19, pp. E67–E82, Jul 2010.

[18] M. Born and E. Wolf, *Principles of optics: Electromagnetic theory of propagation, interference and diffraction of light*. CUP Archive, 2000.

[19] D. L. Donoho, "For most large underdetermined systems of linear equations the minimal 1-norm solution is also the sparsest solution," *Communications on Pure and Applied Mathematics*, vol. 59, no. 6, pp. 797–829, 2006.

[20] L. C. Potter, E. Ertin, J. T. Parker, and M. Cetin, "Sparsity and compressed sensing in radar imaging," *Proceedings of the IEEE*, vol. 98, no. 6, pp. 1006–1020, June 2010.

[21] C. A. Balanis, *Advanced Engineering Electromagnetics*. John Wiley & Sons, 1989.

[22] M. I. Skolnik, *Introduction to Radar*, 1962, vol. 2.

[23] G. Charvat, A. Temme, M. Feigin, and R. Raskar, "Time-of-flight microwave camera," *Scientific Reports*, vol. 5, 2015.

[24] S. Rahmann and N. Canterakis, "Reconstruction of specular surfaces using polarization imaging," in *Computer Vision and Pattern Recognition, 2001. CVPR 2001. Proceedings of the 2001 IEEE Computer Society Conference on*, vol. 1. IEEE, 2001, pp. 149–155.

# CHAPTER 6

# COMPUTATIONALLY EFFICIENT VECTOR EM-WAVE PROPAGATION THROUGH AXI-SYMMETRIC MEDIA USING CYLINDRICAL HARMONIC DECOMPOSITION

This chapter, in full, has been published in Optics Express, **24**, 29246-29268 (2016), with authors Suresh Venkatesh and David Schurig. (adapted with permission)

## 6.1 Abstract

We describe and provide a systematic procedure for computationally fast propagation of arbitrary vector electromagnetic (EM) fields through an axially symmetric medium. A cylindrical harmonic field propagator is chosen for this purpose and in most cases, this is the best and obvious choice. Firstly, we describe the cylindrical harmonic decomposition technique in terms of both scalar and vector basis for a given input excitation field. Then we formulate a generalized discrete Fourier-Hankel transform to achieve efficient vector basis decomposition. We allow a slower, precomputation step, that finds a representation of the axi-symmetric medium as a transfer matrix in a discrete, cylindrical-harmonic basis. We find this matrix from a series of axi-symmetric (2D) finite element simulations (also known as the 2.5D technique). This transfer matrix approach significantly reduces the computational load when the transverse size or range exceeds about 30 wavelengths. This matrix is independent of the input excitation field for a given space-bandwidth product and hence makes it reusable for different excitation fields. We numerically validate the above approaches for different axi-symmetric EM scattering media which include a hemispherical gradient-index Maxwell's fish-eye lens, a transformation optics designed spherical invisibility cloak, a thin aspheric lens, and a cylindrical perfect lens.

## 6.2 Introduction

Large scale computational electromagnetic problems involving propagation through inhomogeneous media are often computationally expensive. One of the major challenges is to reduce the computational cost of using methods like finite element or finite difference, in electrically large problems, without sacrificing the accuracy of the result. One approach to reducing the computational complexity is to downgrade the optics abstraction level from a vector EM model to a scalar optics (wave optics) model or even further down to a ray tracing model. However, in some cases these approaches are unacceptable. The problem difficulty increases when complete 3D vector field results are required in real-time. Some of the motivating applications are: forward model calculation in computational imaging systems with an array of axi-symmetric lenses [1–3], radome design and distortion mitigation for radio telescopes and airborne vehicular antennas [4, 5], specialized coaxial waveguide or conical feed antenna design [6, 7], magnetic coil design or Fresnel plate design for wireless power transfer or super-lensing applications [8, 9], and recently in plasmonic applications such as excitonic laser [10, 11] and metallic nanosphere design for plasmonic enhancement at optical frequencies [12–14]. The above mentioned electromagnetic problems are computationally hard due to the fact that the scattering structures involved are large compared to the operating wavelength ($> 100\lambda$), or a design optimization process requires repeated calculation of the scattering fields. However, in some cases the scattering structures might possess mirror/reflection, translational, or rotational symmetry which can be exploited to reduce the computational cost [15]. For example, a simple circular cross-section waveguide possesses all of the above symmetries.

In this article, we focus on exploiting rotational/axial symmetry in scattering structures (which are bodies of revolution), as this symmetry reduces the dimensionality of the problem. In such structures the solutions (modes) can be represented by products of separate functions of radial, azimuthal, and longitudinal variables. This in turn helps to reduce a 3D problem $(\rho, \phi, z)$ to a 2D problem $(\rho, z)$ and thereby reduces the computational effort [16]. (The excitation source need not be axi-symmetric to exploit this symmetry.) This happens due to the fact that each cylindrical harmonic propagates independently. Often, the fields of the arbitrary source are decomposed into a series of plane wave components using Fourier transform. The response from each of the obliquely incident (w.r.t $z$) plane

wave is simulated in 2D $(\rho, z)$ and these responses are revolved and summed to get the complete 3D solution (2.5D technique). The spectral decomposition happens in a plane wave basis (Cartesian) and the evaluation of scattered fields happens in a cylindrical basis.

Instead of performing spectral decomposition of the excitation source in a plane wave basis, we wish to perform the decomposition in cylindrical harmonic basis (also a complete basis). The choice of cylindrical basis avoids the unnecessary coordinate transformation (which, in some cases, requires regridding or interpolation) that might be needed if a plane-wave basis is used. We consider both a scalar and vector cylindrical-harmonic basis decomposition to accommodate the cases when either: the normal components of the electric and magnetic fields are known, or the transverse components of the electric field are known. We also formulate a discrete cylindrical harmonic decomposition using generalized discrete Fourier-Hankel transforms. This decomposition approach also provides a significant computational advantage in terms of constructing the overall response transfer matrix for the scattering structure involved. This sparse block diagonal transfer matrix is independent of the arbitrary source of excitation, provided one precalculates the scattering response for all possible propagating modes with unit mode coefficients for a given space-bandwidth product.

In this article, we first formalize cylindrical harmonic decomposition of arbitrary fields (including both $\mathrm{TM}^z$ and $\mathrm{TE}^z$ polarizations, which are in further sections referred to as TM and TE respectively) by deriving the continuous integral equations for mode coefficients using appropriate orthogonality conditions. In Section 6.3, we discretize these continuous integrals using discrete Fourier-Hankel transforms (DFHT). For the discrete vector basis we formulate generalized DFHT. We also develop a composite indexing approach which facilitates the expression of these transforms in matrix form, contributing to the efficiency of the cylindrical decomposition process. In Section 6.4, we describe the 2.5D cylindrical harmonic simulations using the COMSOL RF module, whose scattered field results are used to compute the transfer matrix for a given scattering medium. We show four numerical validation results involving axi-symmetric scattering media namely: (a) gradient refractive index (GRIN) hemispherical Maxwell's fish-eye lens, (b) Coordinate transformed spherical invisibility cloak with anisotropic material properties illuminated with offset vector Gaussian beam, (c) A simple $\sim 40\lambda$ diameter thin-aspheric-plano-convex

lens illuminated with Gaussian vector beam, and (d) An isotropic negative index perfect lens with arbitrary excitation field. In each case, we performed a series of axi-symmetric 2D finite element simulations for all possible propagating modes to construct a transfer matrix of the scattering medium. Then this transfer matrix is multiplied by the cylindrical harmonic coefficients of the excitation field to derive the output mode coefficients at a prescribed plane. The results of this method are compared and agree well with analytical results. For the GRIN lens (case (a)) we also perform complete conventional 3D finite element simulations to test accuracy and compare the computational resource requirements. For the other numerical validation cases there exist straightforward analytical results for comparison. The choice of using a cylindrical harmonic propagator in such problems is also well justified, and we compare the computational requirement of this method with an another approach, namely, the plane wave propagator. Even though we restrict our discussions to EM problems, some of the techniques and methods described in this article can also be extended to other areas of computational physics problems such as: acoustics, thermodynamics, and fluid dynamics.

## 6.3 Cylindrical Harmonic Decomposition

Cylindrical harmonic decomposition (CHD) is the process of decomposing an arbitrary function into basic patterns/harmonics that have simple radial and angular structures. Cylindrical harmonics, just like plane waves or spherical harmonics, form a complete orthonormal basis set. Any arbitrary field that is a solution to Helmholtz's equation can be represented as an infinite weighted sum of these cylindrical harmonics. Often, for most of the real world signals of interest, the cylindrical harmonic expansion converges rapidly leading to good representation accuracy using a finite and relatively small number of cylindrical harmonic modes. Any arbitrary vector field can be decomposed into cylindrical harmonics as follows. Consider an arbitrary electromagnetic vector field including both TM and TE polarizations propagating in $+z$ direction. We decompose either the z-components of both the electric and magnetic fields, or the transverse component of electric field, into cylindrical harmonic modes. We formulate the expansions so that both types use the same set of expansion coefficients. These expansion coefficients can then be propagated (from a plane $z = z_0$ to another plane $z = z_1$) by a transfer matrix and

recomposed into the spatial field representation as follows.

$$\begin{array}{c}\mathbf{E}_t\left(\rho,\phi,z_0\right)\\ \text{or}\\ E_z\left(\rho,\phi,z_0\right),H_z\left(\rho,\phi,z_0\right)\end{array}\Rightarrow\ a_{lmn}\ \Rightarrow\ \mathbf{T}\ \Rightarrow\ \begin{array}{c}\mathbf{E}_t\left(\rho,\phi,z_1\right)\\ \text{or}\\ E_z\left(\rho,\phi,z_1\right),H_z\left(\rho,\phi,z_1\right)\end{array}\Rightarrow\ b_{lmn} \tag{6.1}$$

where sub-index $l$ refers to the mode type, $l = 1 \rightarrow$ TM mode and $l = 2 \rightarrow$ TE mode; $m$ and $n$ are the azimuthal and radial mode numbers respectively; $a_{lmn}$ and $b_{lmn}$ are the input and output plane cylindrical harmonic mode coefficients related through the transfer matrix $\mathbf{T}$. Field components are derived by expanding and summing all their respective basis functions.

For decomposing the field z-components, we use the usual scalar basis functions employed in the analysis of cylindrical wave-guides, but the transverse electric field decomposition requires a less well-known set of vector basis functions. Below we show both the continuous and discretized versions of this change of basis. For the discrete case of the change to the scalar basis we use a Discrete Fourier-Hankel Transform (DFHT). For the discrete case of the change to the vector basis we use a generalization of the DFHT.

In what follows we assume a maximum radius over which the fields are nonnegligible is given by $R$, and a maximum radial phase constant (or maximum radial spatial bandwidth) is given by $B$. The latter might be, for example, the maximum radial phase constant which permits propagating fields, i.e. the plane wave propagation constant in the medium.

### 6.3.1 Scalar Basis

The expansion of arbitrary z-components of the fields at $z = z_0$ is given by,

$$E_z\left(\rho,\phi,z_0\right) = \sum_{m,n} a_{1mn}\psi_{1mn}\left(\rho,\phi\right) \tag{6.2a}$$

$$\eta_0 H_z\left(\rho,\phi,z_0\right) = \sum_{m,n} a_{2mn}\psi_{2mn}\left(\rho,\phi\right) \tag{6.2b}$$

and at $z = z_1$ is given by,

$$E_z\left(\rho,\phi,z_1\right) = \sum_{m,n} b_{1mn}\psi_{1mn}\left(\rho,\phi\right) \tag{6.3a}$$

$$\eta_0 H_z\left(\rho,\phi,z_1\right) = \sum_{m,n} b_{2mn}\psi_{2mn}\left(\rho,\phi\right) \tag{6.3b}$$

The equations (6.2a, 6.3a) represents the TM modes and (6.2b, 6.3b) represents the TE modes. $\psi_{lmn}$, $a_{lmn}$, and $b_{lmn}$ are the basis functions, input mode coefficients, and output

mode coefficients, respectively, with mode type, $l$, azimuthal mode number, $m$, and radial mode number, $n$. The normalized basis functions are given by,

$$\psi_{lmn}(\rho,\phi) = C_{lmn}\, J_m(\beta_{lmn}\rho)\; e^{-jm\phi} \tag{6.4}$$

The radial phase constants $\beta_{1mn}$ and $\beta_{2mn}$ are found from the roots of the first kind Bessel functions and their derivatives respectively.

$$J_m(\beta_{1mn}\, R) = 0 \text{ and } J'_m(\beta_{2mn}\, R) = 0 \tag{6.5}$$

The roots are frequently defined with respect to unit radius as,

$$J_m(\chi_{1mn}) = 0 \text{ and } J'_m(\chi_{2mn}) = 0 \tag{6.6}$$

The normalizing constants are given by,

$$C_{1mn}^{-1} = \sqrt{\pi} R J_{m+1}(\chi_{1mn}) \tag{6.7a}$$

$$C_{2mn}^{-1} = \sqrt{\pi} R \left[J_m^2(\chi_{2mn}) - J_{m-1}(\chi_{2mn})\, J_{m+1}(\chi_{2mn})\right]^{1/2} \tag{6.7b}$$

The basis functions and the normalizing coefficients are defined separately for convenience in representing the discrete transforms below. Within each mode type (TM or TE) the basis functions are ortho-normal,

$$\begin{aligned}\left\langle \psi_{lmn} | \psi_{lm'n'} \right\rangle &= \int_0^R \int_{-\pi}^{\pi} \psi^*_{lmn}(\rho,\phi)\; \psi_{lm'n'}(\rho,\phi)\; \mathrm{d}\phi\, \rho \mathrm{d}\rho \\ &= \delta_{mm'}\delta_{nn'}\end{aligned} \tag{6.8}$$

where $\delta_{ij}$ is the Kronecker delta function. Using (6.15) below, and the fact that $E_z$ is zero for TE modes, one can see that, for the full *vector* electric field, TM and TE fields are orthogonal. However, the scalar basis functions of different mode types are not necessarily orthogonal to each other. Having access to $E_z$ and $H_z$ means that the TM and TE fields are already separated, and need not be decomposed. $l = 1$ basis functions need only, and should only, be used with $E_z$, and the $l = 2$ basis functions need only, and should only, be used with $H_z$.

Using the orthogonality condition and the expansions above, we find the expressions for the cylindrical harmonic mode coefficients,

$$\begin{aligned} a_{lmn} &= \left\langle \psi_{lmn} \left| \begin{array}{cc} E_z & l=1 \\ \eta_0 H_z & l=2 \end{array} \right. \right\rangle \\ &= \int_0^R \int_{-\pi}^{\pi} \psi^*_{lmn}(\rho,\phi) \left\{ \begin{array}{cc} E_z(\rho,\phi,z_0) & l=1 \\ \eta_0 H_z(\rho,\phi,z_0) & l=2 \end{array} \right\} d\phi\, \rho d\rho \end{aligned} \tag{6.9}$$

### 6.3.2 Vector Basis

We expand the transverse electric field,

$$\mathbf{E}_t = \mathbf{E} - E_z \hat{\mathbf{z}} \tag{6.10}$$

in terms of a vector basis set at $z = z_0$

$$\mathbf{E}_t(\rho,\phi,z_0) = \sum_{l,m,n} a_{lmn}\, \Upsilon_{lmn}\, \boldsymbol{\Psi}_{lmn}(\rho,\phi) \tag{6.11}$$

and at $z = z_1$,

$$\mathbf{E}_t(\rho,\phi,z_1) = \sum_{l,m,n} b_{lmn}\, \Upsilon_{lmn}\, \boldsymbol{\Psi}_{lmn}(\rho,\phi) \tag{6.12}$$

where we can use the same expansion coefficients as the scalar basis and the customary normalization of these vector basis functions, if we include an additional factor,

$$\Upsilon_{lmn} = j\sqrt{\frac{\omega^2 \epsilon_0 \mu_0}{\beta^2_{lmn}} - \delta_{l1}} \tag{6.13}$$

The normalized vector basis functions are given by,

$$\boldsymbol{\Psi}_{1mn}(\rho,\phi) = C_{1mn}\left[ -J'_m(\beta_{1mn}\rho)\hat{\boldsymbol{\rho}} + jm\frac{J_m(\beta_{1mn}\rho)}{\beta_{1mn}\rho}\hat{\boldsymbol{\phi}} \right] e^{-jm\phi} \tag{6.14a}$$

$$\boldsymbol{\Psi}_{2mn}(\rho,\phi) = C_{2mn}\left[ jm\frac{J_m(\beta_{2mn}\rho)}{\beta_{2mn}\rho}\hat{\boldsymbol{\rho}} + J'_m(\beta_{2mn}\rho)\hat{\boldsymbol{\phi}} \right] e^{-jm\phi} \tag{6.14b}$$

using the same radial phase constants $\beta_{lmn}$ from (6.5) and normalizing constants $C_{lmn}$ from (6.7) as were found for the scalar basis functions above. The orthogonality condition (including cross-mode-type) is given by,

$$\begin{aligned} \left\langle \boldsymbol{\Psi}_{lmn} | \boldsymbol{\Psi}_{l'm'n'} \right\rangle &= \int_0^R \int_{-\pi}^{\pi} \boldsymbol{\Psi}^*_{lmn}(\rho,\phi) \cdot \boldsymbol{\Psi}_{l'm'n'}(\rho,\phi)\ \mathrm{d}\phi\, \rho \mathrm{d}\rho \\ &= \delta_{ll'}\delta_{mm'}\delta_{nn'} \end{aligned} \tag{6.15}$$

where the primed superscript indices $(l', m', n')$ just refer to independent indices of same type as $(l, m, n)$.

Using this condition and the field expansion above, we find the expression for the expansion coefficients as,

$$\begin{aligned} a_{lmn}\,\Upsilon_{lmn} &= \left\langle \boldsymbol{\Psi}_{lmn} | \mathbf{E}_t \right\rangle \\ &= \int_0^R \int_{-\pi}^{\pi} \boldsymbol{\Psi}^*_{lmn}\left(\rho,\phi\right) \cdot \mathbf{E}_t\left(\rho,\phi,z_0\right)\, \mathrm{d}\phi\, \rho \mathrm{d}\rho \end{aligned} \tag{6.16}$$

One could use scalar or vector basis expansions depending on the type of fields specified. For both expansions, the $z = z_1$ plane coefficients are related to $z = z_0$ plane coefficients through the transfer matrix, $\mathbf{T}$, as:

$$b_{l'm'n'} = \sum_{l,m,n} T_{l'm'n'lmn}\, a_{lmn} \tag{6.17}$$

For example, the transfer function of a uniform medium is,

$$\begin{aligned} T_{l'm'n'lmn} &= \delta_{l'l}\delta_{m'm}\delta_{n'n}\, e^{j\beta_{zlmn}(z_1 - z_0)} \\ \text{where, } \beta_{zlmn} &= \sqrt{\omega^2\epsilon\mu - \beta^2_{lmn}} \end{aligned} \tag{6.18}$$

since all the modes propagate independently. The construction of the transfer matrix is discussed in detail in Section 6.5.

## 6.4 Discrete Fourier-Hankel Transform

The discretized form of transforming to the cylindrical harmonic basis from the position basis requires a combined discrete Fourier transform of the angle, $\phi$, and a discrete Hankel transform of the radial variable, $\rho$. This is seldom done because, on the surface, the Discrete Fourier-Hankel Transform (DFHT) appears to be more complex and confusing than applying the Discrete Fourier Transform (DFT) in the Cartesian basis. A relatively simple, but useful, scheme for understanding and implementing the DFHT incorporates three composite indices: one for the cylindrical harmonic components, $\mathbf{l}$, one for the input samples, $\mathbf{i}$, and one for the output samples, $\boldsymbol{\alpha}$. Here we use bold face to denote these composite indices.

We wish to compute a set of cylindrical harmonic coefficients that span a specified range of in-plane spatial bandwidth, $B$. For a given domain radius, $R$, this implies a specific space-bandwidth product, $BR$. Our composite index should include all modes that lie in this space-bandwidth product, and thus satisfy $\beta_{lmn}R = \chi_{lmn} \leq BR$.

We can start from an initial set of azimuthal and radial mode indices, $m$ and $n$, with maximum values given by,

$$\begin{aligned} M &= \max\{m|\chi_{1m1} \leq BR \text{ or } \chi_{2m1} \leq BR\} \\ N &= \max\{n|\chi_{10n} \leq BR \text{ or } \chi_{21n} \leq BR\} \end{aligned} \tag{6.19}$$

and choose the index triples, $lmn$, that represent modes in the specified space-bandwidth product range,

$$\begin{aligned} \{\mathbf{1}\} &= \{l, m, n|\chi_{lmn} \leq BR\} \\ &\subset \{l = 1, 2\} \otimes \{-M \leq m \leq M-1\} \otimes \{1 \leq n \leq N\} \end{aligned} \tag{6.20}$$

Such a composite index is determined solely by the space-bandwidth product and can be computed and stored once for repeated use with different field patterns (bound by the space-bandwidth product).

The best accuracy for cylindrical harmonic coefficients results by using the roots of the radial basis functions (i.e., the first-kind Bessel functions) for selecting the radial sample points. These samples are not uniformly spaced and their values depend on both the mode type, $l$, and azimuthal mode number, $m$, of the cylindrical harmonic coefficient being computed, that is to say that the computation of each cylindrical harmonic coefficient has its own unique set of radial sample points. The density of the sample points in the spatial domain is controlled by the desired spatial bandwidth. Just as with the DFT, a certain amount of over-sampling provides better accuracy. We define the sampling bandwidth, $B_s$, to be larger than the spatial bandwidth of the desired cylindrical harmonics, $B_s > B$.

The index ranges for the azimuthal angle and radial samples are controlled by this sampling bandwidth,

$$\begin{aligned} J &= \max\left\{j|\chi_{1j1} \leq B_s R \text{ or } \chi_{2j1} \leq B_s R\right\} \approx \frac{B_s}{B} M \\ K &= \max\left\{k|\chi_{10k} \leq B_s R \text{ or } \chi_{21k} \leq B_s R\right\} \approx \frac{B_s}{B} N. \end{aligned} \tag{6.21}$$

The azimuthal angle is transformed using a standard DFT that uses uniform sampling. The sample points are given by,

$$\rho_{lmk} = \frac{\chi_{lmk}}{B_s} \quad \text{and} \quad \phi_j = j\frac{\pi}{J}. \tag{6.22}$$

The composite index should include the full range of azimuthal angle samples for each radial coordinate sample as required for a DFT. Finally, the composite input sample index

should include a subindex that specifies whether the field component is sampled. For the scalar basis decomposition, this subindex specifies either the electric or magnetic field z-component. For the vector basis decomposition, this subindex specifies either the $\rho$ or $\phi$ component of the electric field. The complete composite index is thus given by,

$$\begin{aligned} \{\mathbf{i}\} &= \{i,j,k\} \\ &= \{i=1,2\} \otimes \{-J \leq j \leq J-1\} \otimes \{1 \leq k \leq K\} \end{aligned} \tag{6.23}$$

To form a proper inverse, the output sample coordinates, that result from the inverse DFHT, should be the same as the input sample coordinates. However, this leads to distinct sets of sample coordinates for each cylindrical harmonic mode. Typically, one wants the total field, due to all modes, on some convenient grid of points. One could perform the inverse DFHT and then interpolate the fields from the different modes onto a single grid, or one could accomplish both operations together, by choosing a set of output sample coordinates that are mode independent, and in effect using the basis functions for the interpolation. Though any suitable grid can be used, here we show a Cartesian grid,

$$x_\alpha = \alpha\delta \text{ and } y_\gamma = \gamma\delta \tag{6.24}$$

with grid indices $\alpha$ and $\gamma$, and uniform grid spacing, $\delta$. The corresponding cylindrical coordinates are,

$$\rho_{\alpha\gamma} = \delta\sqrt{\alpha^2+\gamma^2} \text{ and } \phi_{\alpha\gamma} = \text{atan2}(\gamma,\alpha) \tag{6.25}$$

and the composite index with points selected to lie within the domain radius, $R$, is given by,

$$\begin{aligned} \{\boldsymbol{\alpha}\} &= \{i,\alpha,\gamma | \rho_{\alpha\gamma} \leq R\} \\ &\subset \{i=1,2\} \otimes \{-A \leq \alpha \leq A\} \otimes \{-A \leq \gamma \leq A\} \end{aligned} \tag{6.26}$$

where

$$A = \text{floor}\left(\frac{R}{\delta}\right). \tag{6.27}$$

An example of such composite indices are shown in Table 6.1, with unit domain radius, spatial bandwidth of $B = 2\pi$, sampling bandwidth of $B_s = 1.1B$, and grid spacing of $\delta = 0.5$. The representative form of the transfer matrix $\mathbf{T}$ for this example is shown in (6.49)

**Table 6.1**: Composite indices **l**, **i**, and $\boldsymbol{\alpha}$ constructed for an example case: $R = 1$, $B = 2\pi$, $B_s = 1.1B$, and $\delta = 0.5$. Highlighted (grey colored rows) in **l** index indicate that the harmonics have space-bandwidth product less than or equal to $RB$. Highlighted (grey colored rows) in $\boldsymbol{\alpha}$ index indicate that the spatial coordinate is within the domain radius $R$.

| **l** | l | m | n | $\chi_{lmn}$ |
|---|---|---|---|---|
| | 1 | -4 | 1 | 7.588 |
| | 1 | -4 | 2 | 11.065 |
| 1 | 2 | -4 | 1 | 5.318 |
| | 2 | -4 | 2 | 9.282 |
| | 1 | -3 | 1 | 6.38 |
| | 1 | -3 | 2 | 9.761 |
| 2 | 2 | -3 | 1 | 4.201 |
| | 2 | -3 | 2 | 8.015 |
| 3 | 1 | -2 | 1 | 5.136 |
| | 1 | -2 | 2 | 8.417 |
| 4 | 2 | -2 | 1 | 3.054 |
| | 2 | -2 | 2 | 6.706 |
| 5 | 1 | -1 | 1 | 3.832 |
| | 1 | -1 | 2 | 7.016 |
| 6 | 2 | -1 | 1 | 1.841 |
| 7 | 2 | -1 | 2 | 5.331 |
| 8 | 1 | 0 | 1 | 2.405 |
| 9 | 1 | 0 | 2 | 5.52 |
| 10 | 2 | 0 | 1 | 0. |
| 11 | 2 | 0 | 2 | 3.832 |
| 12 | 1 | 1 | 1 | 3.832 |
| | 1 | 1 | 2 | 7.016 |
| 13 | 2 | 1 | 1 | 1.841 |
| 14 | 2 | 1 | 2 | 5.331 |
| 15 | 1 | 2 | 1 | 5.136 |
| | 1 | 2 | 2 | 8.417 |
| 16 | 2 | 2 | 1 | 3.054 |
| | 2 | 2 | 2 | 6.706 |
| | 1 | 3 | 1 | 6.38 |
| | 1 | 3 | 2 | 9.761 |
| 17 | 2 | 3 | 1 | 4.201 |
| | 2 | 3 | 2 | 8.015 |

| **i** | i | j | k | $\chi_{ijk}$ |
|---|---|---|---|---|
| 1 | 1 | -5 | 1 | 8.771 |
| 2 | 1 | -5 | 2 | 12.339 |
| 3 | 1 | -4 | 1 | 7.588 |
| 4 | 1 | -4 | 2 | 11.065 |
| 5 | 1 | -3 | 1 | 6.38 |
| 6 | 1 | -3 | 2 | 9.761 |
| 7 | 1 | -2 | 1 | 5.136 |
| 8 | 1 | -2 | 2 | 8.417 |
| 9 | 1 | -1 | 1 | 3.832 |
| 10 | 1 | -1 | 2 | 7.016 |
| 11 | 1 | 0 | 1 | 2.405 |
| 12 | 1 | 0 | 2 | 5.52 |
| 13 | 1 | 1 | 1 | 3.832 |
| 14 | 1 | 1 | 2 | 7.016 |
| 15 | 1 | 2 | 1 | 5.136 |
| 16 | 1 | 2 | 2 | 8.417 |
| 17 | 1 | 3 | 1 | 6.38 |
| 18 | 1 | 3 | 2 | 9.761 |
| 19 | 1 | 4 | 1 | 7.588 |
| 20 | 1 | 4 | 2 | 11.065 |
| 21 | 2 | -5 | 1 | 6.416 |
| 22 | 2 | -5 | 2 | 10.52 |
| 23 | 2 | -4 | 1 | 5.318 |
| 24 | 2 | -4 | 2 | 9.282 |
| 25 | 2 | -3 | 1 | 4.201 |
| 26 | 2 | -3 | 2 | 8.015 |
| 27 | 2 | -2 | 1 | 3.054 |
| 28 | 2 | -2 | 2 | 6.706 |
| 29 | 2 | -1 | 1 | 1.841 |
| 30 | 2 | -1 | 2 | 5.331 |
| 31 | 2 | 0 | 1 | 0. |
| 32 | 2 | 0 | 2 | 3.832 |
| 33 | 2 | 1 | 1 | 1.841 |
| 34 | 2 | 1 | 2 | 5.331 |
| 35 | 2 | 2 | 1 | 3.054 |
| 36 | 2 | 2 | 2 | 6.706 |
| 37 | 2 | 3 | 1 | 4.201 |
| 38 | 2 | 3 | 2 | 8.015 |
| 39 | 2 | 4 | 1 | 5.318 |
| 40 | 2 | 4 | 2 | 9.282 |

| $\boldsymbol{\alpha}$ | i | $\alpha$ | $\gamma$ | $\rho_{\alpha\gamma}$ | $\phi_{\alpha\gamma}$ |
|---|---|---|---|---|---|
| | 1 | -2 | -2 | 1.414 | -2.356 |
| | 1 | -2 | -1 | 1.118 | -2.678 |
| 1 | 1 | -2 | 0 | 1. | 3.142 |
| | 1 | -2 | 1 | 1.118 | 2.678 |
| | 1 | -2 | 2 | 1.414 | 2.356 |
| | 1 | -1 | -2 | 1.118 | -2.034 |
| 2 | 1 | -1 | -1 | 0.707 | -2.356 |
| 3 | 1 | -1 | 0 | 0.5 | 3.142 |
| 4 | 1 | -1 | 1 | 0.707 | 2.356 |
| | 1 | -1 | 2 | 1.118 | 2.034 |
| 5 | 1 | 0 | -2 | 1. | -1.571 |
| 6 | 1 | 0 | -1 | 0.5 | -1.571 |
| 7 | 1 | 0 | 0 | 0. | 0. |
| 8 | 1 | 0 | 1 | 0.5 | 1.571 |
| 9 | 1 | 0 | 2 | 1. | 1.571 |
| | 1 | 1 | -2 | 1.118 | -1.107 |
| 10 | 1 | 1 | -1 | 0.707 | -0.785 |
| 11 | 1 | 1 | 0 | 0.5 | 0. |
| 12 | 1 | 1 | 1 | 0.707 | 0.785 |
| | 1 | 1 | 2 | 1.118 | 1.107 |
| | 1 | 2 | -2 | 1.414 | -0.785 |
| | 1 | 2 | -1 | 1.118 | -0.464 |
| 13 | 1 | 2 | 0 | 1. | 0. |
| | 1 | 2 | 1 | 1.118 | 0.464 |
| | 1 | 2 | 2 | 1.414 | 0.785 |
| | 2 | -2 | -2 | 1.414 | -2.356 |
| | 2 | -2 | -1 | 1.118 | -2.678 |
| 14 | 2 | -2 | 0 | 1. | 3.142 |
| | 2 | -2 | 1 | 1.118 | 2.678 |
| | 2 | -2 | 2 | 1.414 | 2.356 |
| | 2 | -1 | -2 | 1.118 | -2.034 |
| 15 | 2 | -1 | -1 | 0.707 | -2.356 |
| 16 | 2 | -1 | 0 | 0.5 | 3.142 |
| 17 | 2 | -1 | 1 | 0.707 | 2.356 |
| | 2 | -1 | 2 | 1.118 | 2.034 |
| 18 | 2 | 0 | -2 | 1. | -1.571 |
| 19 | 2 | 0 | -1 | 0.5 | -1.571 |
| 20 | 2 | 0 | 0 | 0. | 0. |
| 21 | 2 | 0 | 1 | 0.5 | 1.571 |
| 22 | 2 | 0 | 2 | 1. | 1.571 |
| | 2 | 1 | -2 | 1.118 | -1.107 |
| 23 | 2 | 1 | -1 | 0.707 | -0.785 |
| 24 | 2 | 1 | 0 | 0.500 | 0. |
| 25 | 2 | 1 | 1 | 0.707 | 0.785 |
| | 2 | 1 | 2 | 1.118 | 1.107 |
| | 2 | 2 | -2 | 1.414 | -0.785 |
| | 2 | 2 | -1 | 1.118 | -0.464 |
| 26 | 2 | 2 | 0 | 1. | 0. |
| | 2 | 2 | 1 | 1.118 | 0.464 |
| | 2 | 2 | 2 | 1.414 | 0.785 |

in Section 6.8.4. We also present a pseudoalgorithm for one of the composite indicies, $\mathbf{l}$, in Section 6.8.4.

We can use these composite indices to form matrices for efficient computation of DFHT as;

$$\mathbf{a} = \text{diag}(\mathbf{H}\mathbf{E}^0) \tag{6.28}$$

the transfer function operation,

$$\mathbf{b} = \mathbf{T}\mathbf{a} \tag{6.29}$$

and the inverse DFHT,

$$\mathbf{E}^1 = \overline{\mathbf{H}}\mathbf{b}. \tag{6.30}$$

The above operations can be composed together and written compactly as,

$$\mathbf{E}^1 = \overline{\mathbf{H}}\mathbf{T}\text{diag}(\mathbf{H}\mathbf{E}^0). \tag{6.31}$$

Note that the diag operation returns a vector. The correspondence between matrix elements indexed by the original indices and the composite indices are as follows:

$$\begin{array}{lll} \mathbf{E}^0 = E^0_{\mathbf{il}} = E^0_{ijklmn} & & \mathbf{b} = b_{\mathbf{l}'} = b_{l'm'n'} \\ \mathbf{H} = H_{\mathbf{li}} = H_{lmnijk} & \Longrightarrow \mathbf{T} = T_{\mathbf{l}'\mathbf{l}} = T_{l'm'n'lmn} \Longrightarrow & \overline{\mathbf{H}} = \overline{H}_{\boldsymbol{\alpha}\mathbf{l}'} = \overline{H}_{i\alpha\gamma\, l'm'n'} \\ \mathbf{a} = a_{\mathbf{l}} = a_{lmn} & & \mathbf{E}^1 = E^1_{\boldsymbol{\alpha}} = E^1_{i\alpha\gamma}. \end{array} \tag{6.32}$$

### 6.4.1 Scalar Basis DFHT

For the case of the scalar basis decomposition, the matrix elements for: the input samples, the forward DFHT, the inverse DFHT, and the output samples are given by,

| Input Samples & Forward DFHT | Inverse DFHT & Output Samples |
|---|---|
| $E^0_{ijklmn} = \delta_{il} \begin{cases} E_z\left(\rho_{1mk}, \phi_j, z_0\right) & l = 1 \\ \eta\, H_z\left(\rho_{2mk}, \phi_j, z_0\right) & l = 2 \end{cases}$ | $\overline{H}_{i\alpha\gamma\, l'm'n'} = \delta_{il'}\, \psi_{l'm'n'}\left(\rho_{\alpha\gamma}, \phi_{\alpha\gamma}\right)$ |
| $H_{lmnijk} = \delta_{il} \dfrac{2\pi^2\, R^2}{J\, B_s^2} C^2_{lmk}\, \psi^*_{lmn}\left(\rho_{lmk}, \phi_j\right)$ | $E^1_{i\alpha\gamma} = \begin{cases} E_z\left(\rho_{\alpha\gamma}, \phi_{\alpha\gamma}, z_1\right) & i = 1 \\ \eta\, H_z\left(\rho_{\alpha\gamma}, \phi_{\alpha\gamma}, z_1\right) & i = 2 \end{cases}$ |

(6.33)

### 6.4.2 Vector Basis DFHT

For the case of the vector basis decomposition, the matrix elements for: the input samples, the forward DFHT, the inverse DFHT, and the output samples are given by,

| Input Samples & Forward DFHT | Inverse DFHT & Output Samples |
|---|---|
| $E^0_{ijklmn} = \mathbf{E}_t\left(\rho_{lmk}, \phi_j, z_0\right) \cdot \hat{\mathbf{e}}_i$ | $\overline{H}_{i\alpha\gamma\, l'm'n'} = \mathbf{\Psi}_{l'm'n'}\left(\rho_{\alpha\gamma}, \phi_{\alpha\gamma}\right) \cdot \hat{\mathbf{e}}_i$ |
| $H_{lmnijk} = \dfrac{2\pi^2 R^2}{J B_s^2} C^2_{lmk}\, \mathbf{\Psi}^*_{lmn}\left(\rho_{lmk}, \phi_j\right) \cdot \hat{\mathbf{e}}_i$ | $E^1_{i\alpha\gamma} = \mathbf{E}_t\left(\rho_{\alpha\gamma}, \phi_{\alpha\gamma}, z_1\right) \cdot \hat{\mathbf{e}}_i$ |

(6.34)

where $\hat{\mathbf{e}}_1 = \hat{\boldsymbol{\rho}}$, and $\hat{\mathbf{e}}_2 = \hat{\boldsymbol{\phi}}$. The fields and basis functions are assumed to be zero when the radius is greater than the domain radius, $R$. If the functions used to compute the matrix elements are defined otherwise, the radius should be tested and the element set to zero appropriately. This can be done for either the $E^0$ or $H^0$ elements. It is not required for both, since when computing the diagonal of the matrix product, the element product pairs always have the same radius.

One might assume, that since the $l = 2$ scalar basis functions are nonzero (but with zero radial derivative) at the the domain boundary, $\rho = R$, that one can accurately find cylindrical harmonic coefficients for $H_z$ fields that are finite at $\rho = R$. In fact, the accuracy will be poor in this case. Only when fields are near zero at the boundary can the DFHT provide accurate coefficients. The usual derivation of the discrete Hankel transform involves approximating a finite radial integration by an infinite one. This approximation is only accurate when the functions being transformed are zero outside the specified domain radius. Due to the intrinsic periodicity, an analogous problem exists for functions with nonzero amplitude at the boundary of a Fast Fourier Transform (FFT).

## 6.5 Cylindrical Harmonic Mode Propagation (2.5D) and Construction of Transfer Matrix T

The vector wave propagation of electromagnetic fields through an inhomogeneous medium is a well known problem and is often solved using finite difference time domain (FDTD) or finite element methods (FEM). However, this problem becomes computationally challenging when the size of this inhomogeneous structure is fairly large compared to wavelength. This forces one to exploit symmetries in the structure in order to reduce the computational load [17]. In this section we describe a technique to model axially symmetric structures using quasi-two-dimensional modeling method (2.5D modeling).

This approach exploits the rotational symmetry of the structure (about the z axis) without imposing any restrictions on the source excitation field.

In section 6.3 and 6.4 we described the decomposition of arbitrary fields in terms of cylindrical harmonics. The TM and TE coefficients determined by this method can be used to completely describe the source excitation field. Similarly, the scattered fields due to the test object can again be decomposed into TM and TE cylindrical harmonic modes and their respective coefficients can be found. These scattered field coefficients form the transfer matrix **T** shown in (6.1). By combining the excitation and the scattered field coefficients appropriately with their respective basis functions one can determine the total fields due to the scattering test object. When the inhomogeneous scattering structure is rotationally symmetric ($\phi$ independent), a cylindrical harmonic mode of a given azimuthal mode number, m, couples only to modes of the same mode number, m. In such a structure, the electric field in cylindrical coordinate varies with the azimuthal mode m as:

$$\mathbf{E}(\rho, \phi, z) = \widetilde{\mathbf{E}}(\rho, z)\, e^{-jm\phi} \tag{6.35}$$

Using (6.35), the wave equation can be written in the form [18],

$$\left[\nabla - j\frac{m}{\rho}\hat{\boldsymbol{\phi}}\right] \times \left[\frac{1}{\boldsymbol{\mu}}\left(\nabla - j\frac{m}{\rho}\hat{\boldsymbol{\phi}}\right) \times \widetilde{\mathbf{E}}\right] - \beta^2 \boldsymbol{\epsilon}\widetilde{\mathbf{E}} = 0 \tag{6.36}$$

where $\boldsymbol{\epsilon}$ and $\boldsymbol{\mu}$ are the relative electric permittivity and magnetic permeability second-order tensors of the medium. For each m, the above (6.36) can be solved on a two dimensional $(\rho, \phi = 0, z)$ plane for any arbitrary excitation field provided the scattering medium under test is axially symmetric. For a given domain with maximum radius R having a maximum radial spatial bandwidth B, there exists approximately S number of modes, S $\approx 2MN$. So, one needs to perform S number of independent 2D simulations (easily parallelizable), and hence the name 2.5 D. Also, there exists a parity relation between the propagating modes with positive and negative azimuthal mode numbers and this fact can be exploited to further reduce the number of 2D simulations by a factor of 2 (see Section 6.8.3). Such an axi-symmetric medium can be solved numerically using finite element methods which are available in commercial software like COMSOL Multiphysics [18]. The scattered electric field formulation in COMSOL axi-symmetric solver (RF module) is used

to specify a single cylindrical harmonic (with unit mode harmonic coefficient), whose the background input electric fields $\mathbf{E}^{\text{bg}}$ are given based on equations in Section 6.3,

$$\mathbf{E}^{\text{bg}}_{lmn}(\rho,z) = [\Upsilon_{lmn}\boldsymbol{\Psi}_{lmn}(\rho,0) + \delta_{l1}\,\psi_{lmn}(\rho,0)\,\hat{\mathbf{z}}]\;\; e^{-j\,\beta_{zlmn}(z-z_0)} \tag{6.37}$$

where $\psi_{lmn}$, $\Upsilon_{lmn}$, and $\boldsymbol{\Psi}_{lmn}$ are given from (6.4, 6.13, 6.14), respectively.

The output of each such cylindrical harmonic 2D axi-symmetric simulation is a 1D function $f_{l'lmn}$ at $z = z_1$, where $z_1$ is output plane at which net response from an axi-symmetric scatterer is reconstructed. This 1D function at $z = z_1$ can again be decomposed with 1D Hankel transforms (as the fields are independent of $\phi$) to compute the output coefficients and inturn the transfer matrix $\mathbf{T}$. The output coefficients and transfer matrix (for unity input harmonic coefficient) are given by,

$$\begin{aligned} T_{l'm'n'lmn} &= b_{l'm'n'lmn} \\ &= \int_0^R \int_{-\pi}^{\pi} \psi^*_{l'm'n'}(\rho,\phi)\;\exp(-j\,m\,\phi)\,f_{l'lmn}\,d\phi\rho d\rho \\ &= 2\pi\delta_{mm'}\,C_{l'mn'}\int_0^R J_m(\beta_{l'mn'}\rho) f_{l'lmn}\,\rho d\rho \end{aligned} \tag{6.38}$$

where the function $f_{l'lmn}$ is given by the sum of background field and the calculated scattered field $E^{\text{sc}}_z$ or $H^{\text{sc}}_z$,

$$f_{l'lmn}(\rho) = \delta_{l'l}\psi_{lmn}(\rho,0)e^{-j\beta_{zlmn}(z_1-z_0)} + \;\begin{cases} E^{\text{sc}}_z(\rho,z_1) & l'=1 \\ \eta H^{\text{sc}}_z(\rho,z_1) & l'=2. \end{cases} \tag{6.39}$$

Since the azimuthal mode number is preserved in the axi-symmetric simulation, in the above equation, $m$ is used in the basis function instead of $m'$. The transfer function can also be given in terms of a discrete Hankel transform,

$$\begin{aligned} T_{l'm'n'lmn} &= \sum_{k=1}^{K} H_{l'm'n'mk}F_{kl'lmn} \\ H_{l'm'n'mk} &= \delta_{m'm}4\pi^2\frac{R^2}{B_s^2}C_{l'm'n'}C^2_{l'm'k}J_{m'}(\beta_{l'm'n'}\rho_{l'm'k}) \\ F_{kl'lmn} &= f_{l'lmn}(\rho_{l'mk}) \end{aligned} \tag{6.40}$$

The transfer matrix $\mathbf{T}$, constructed using the scattered fields from all S simulations (negative azimuthal modes need not be simulated) can be written in a lexicographical order to form a sparse block diagonal matrix as shown in Fig. 6.1. In Fig. 6.1, $\mathbf{T}$ is a

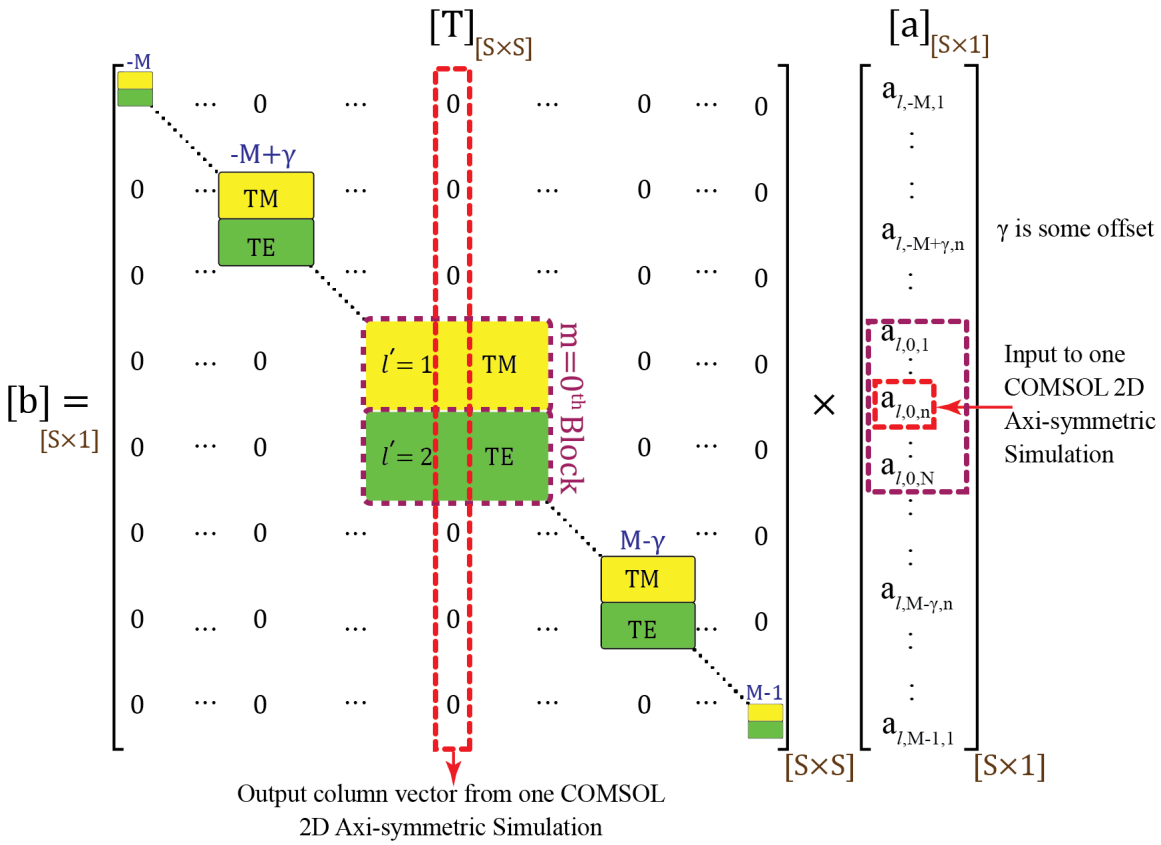


**Figure 6.1**: Transfer Matrix **T** in its sparse, block-diagonal form. The $m = 0^{th}$ block is highlighted in magenta.

sparse, block-diagonal transfer matrix of size [S×S] constructed from the COMSOL 1D scattered fields. Each input mode generates a column vector in **T** matrix. It is important to note that in a linear axially symmetric scattering medium excited with a particular cylindrical harmonic mode with a specific mode type $l$, always preserves the azimuthal mode number m, but need not necessarily preserve the mode type (TM mode can partially or fully get converted to TE mode or vice versa). Hence the scattered fields have to be decomposed again into TM and TE modes for each background field mode type to construct a complete transfer matrix. There exist $2M$ number of blocks. This matrix **T** can be precomputed for a given spatial bandwidth $B$ and later reused for different excitations by appropriately changing the right hand side column vector **a**, i.e., the input cylindrical harmonic coefficients.

The computational complexity of this numerical technique is mainly dependent on the total number of band-limited modes; S in a given space-bandwidth product; $R \times B$. The

total number of modes increases quadratically with space-bandwidth product and this is shown in the Fig. 6.2. The number of 2D cylindrical harmonic simulations and in turn the size of the transfer matrix **T** are directly dependent on total number of modes, S as shown in Fig. 6.1. An important advantage of this approach is that the 2D cylindrical harmonic simulations are independent of one another and can be completely parallelized. The computational complexity of this method can now be written as $O(\mathrm{S})$.

## 6.6 Numerical Validation

The following examples are considered to numerically verify the techniques described in the previous sections.

### 6.6.1 Gradient Index Hemispherical Maxwell's Fish-eye Lens

Maxwell's fish-eye lens is a radially symmetric GRIN lens whose refractive index profile n is of the form, $n(r) = \dfrac{2}{1+(r/a)^2}$, where a is the radius of the lens and $r = \sqrt{x^2+y^2+z^2}$ is the radial coordinate. We simulate the hemispherical version of this lens excited by an offset Gaussian vector beam. For this example, we perform a detailed computational performance analysis between complete 3D full wave and 2.5 D cylindrical harmonic

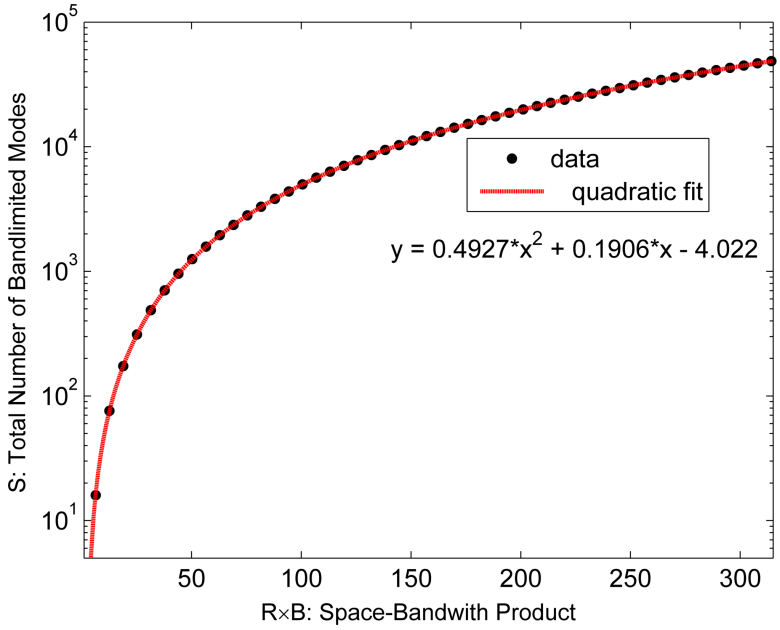


**Figure 6.2**: The total number of band-limited modes; S as a function of space-bandwidth product $R \times B$ along with a quadratic fit.

propagation technique. We also compare the numerical results between the two methods. For this purpose, we chose a nominal lens radius, a = 4$\lambda$ and an incident offset Gaussian full beam-waist of 2$\lambda$ propagating along $+z$ direction. (An offset Gaussian beam ensures a nonsymmetric excitation field with harmonic components that have azimuthal mode numbers m greater than 1). We first simulate the blue region of the lens (one half of the 2D slice of the lens named as 2.5 D COMSOL Simulation Domain) as shown in Fig. 6.3 and construct the transfer matrix **T** based on all possible propagating modes inside this simulation domain (R=8$\lambda$). The input cylindrical harmonic mode coefficients of the source field and the transfer matrix are used to generate output plane mode coefficients. These output modes are then expanded (and also independently further propagated) using their respective basis functions to calculate the full wave vector fields post the lens. This procedure is as explained in Section 6.5. The electric field norm on the xz plane (y = 0) is shown in Fig. 6.4 a. The internal fields of the lens for the 2.5D case are not shown as the transfer matrix was constructed for a plane just outside of the lens ($z = 4\lambda$) and the resulting output modes were propagated. We also simulated the full wave complete 3D structure in COMSOL. These results are shown in Fig. 6.4 b. We plot the transverse plane electric field norm (xy plane) at the focal plane of the lens and at the source plane in Fig. 6.4 c and d respectively. At the focal plane, we subtract the results from cylindrical harmonic propagator technique (2.5D) and 3D full wave simulations and show that the results are indeed accurate within a maximum error $< 1$ %. The normalized absolute error map at the focal plane of the lens is shown in Fig. 6.4 e.

#### 6.6.1.1 3D versus 2.5D Based Transfer Matrix

To compare a complete 3D full-wave simulation with a cylindrical harmonic propagator, using the 2.5D method and a transfer matrix approach, an example with a specific space-bandwidth product was analyzed. Performance analysis comparison between the two methods is presented in Table 6.2. The cylindrical harmonic technique has superior performance in terms of computational burden, simulation time, memory usage, computational scaling, result reusability, and parallelizability.

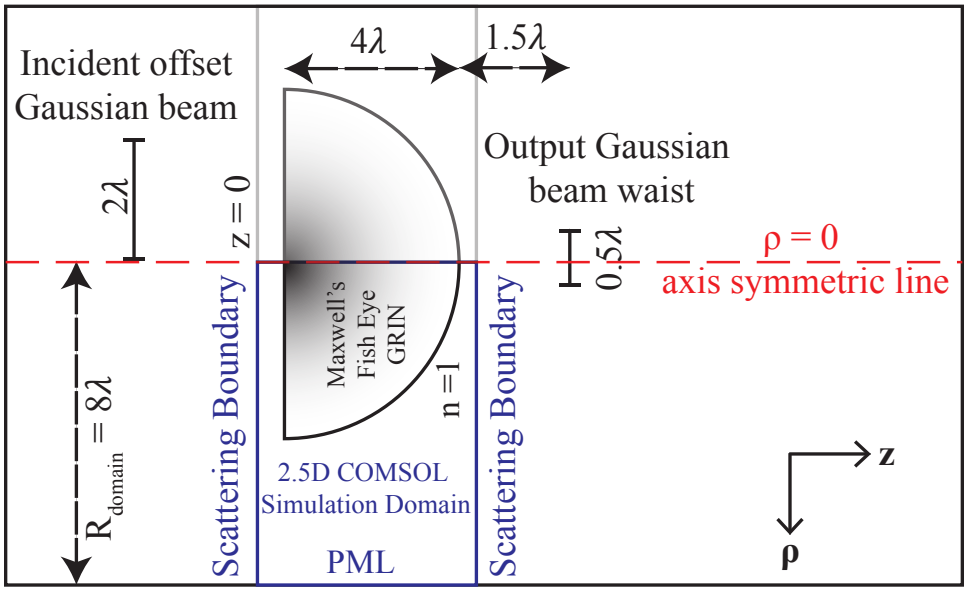


**Figure 6.3**: Hemispherical Maxwell's fish-eye gradient index lens schematic for 2.5 D technique. Blue outline box indicates the simulated domain ($\rho, z, \phi = 0$).

#### 6.6.1.2 Plane Wave versus Cylindrical Harmonic Basis

As stressed in previous sections, construction of a reusable transfer matrix for a given axi-symmetric medium is one of the main goals of this article. The transfer matrix, **T**, for a given medium can be constructed using any complete basis, including plane waves, which comprise the most commonly used basis. Since plane waves cannot be simply represented in cylindrical coordinates, one is at first tempted to use a full-wave 3D solver (rather than an axi-symmetric solver). Such an approach is indeed more straightforward, but does not fully exploit the axial symmetry of the mediums of interest in this article. One can employ one mirror plane symmetry but the solution domains will remain three dimensional, with the associate unfavorable size scaling. Somewhat surprisingly, it is more advantageous to expand a plane wave in a cylindrical-harmonic basis and use the axi-symmetric solver as we now describe. The z-components of a plane wave incident at an arbitrary angle, $\theta_i$ (angle between the wave vector and $\hat{\mathbf{z}}$), can be expanded in cylindrical coordinates using cylindrical harmonics as [17, 19],

$$\begin{matrix} E_z\left(\rho,\phi,z_0\right) \\ \text{or} \\ \eta_0 H_z\left(\rho,\phi,z_0\right) \end{matrix} = E_0 \sin\theta_i \, e^{-j\beta_0 z_0 \cos\theta_i} \sum_{m=-\infty}^{\infty} j^{-m} J_m(\beta_0 \rho \sin\theta_i) \, e^{jm\phi} \tag{6.41}$$

where $\beta_0 = \omega\sqrt{\epsilon_0\mu_0}$ is the free-space wave number. Even though the above equation is an infinite sum of azimuthal mode numbers, for a given finite space-bandwidth product (and

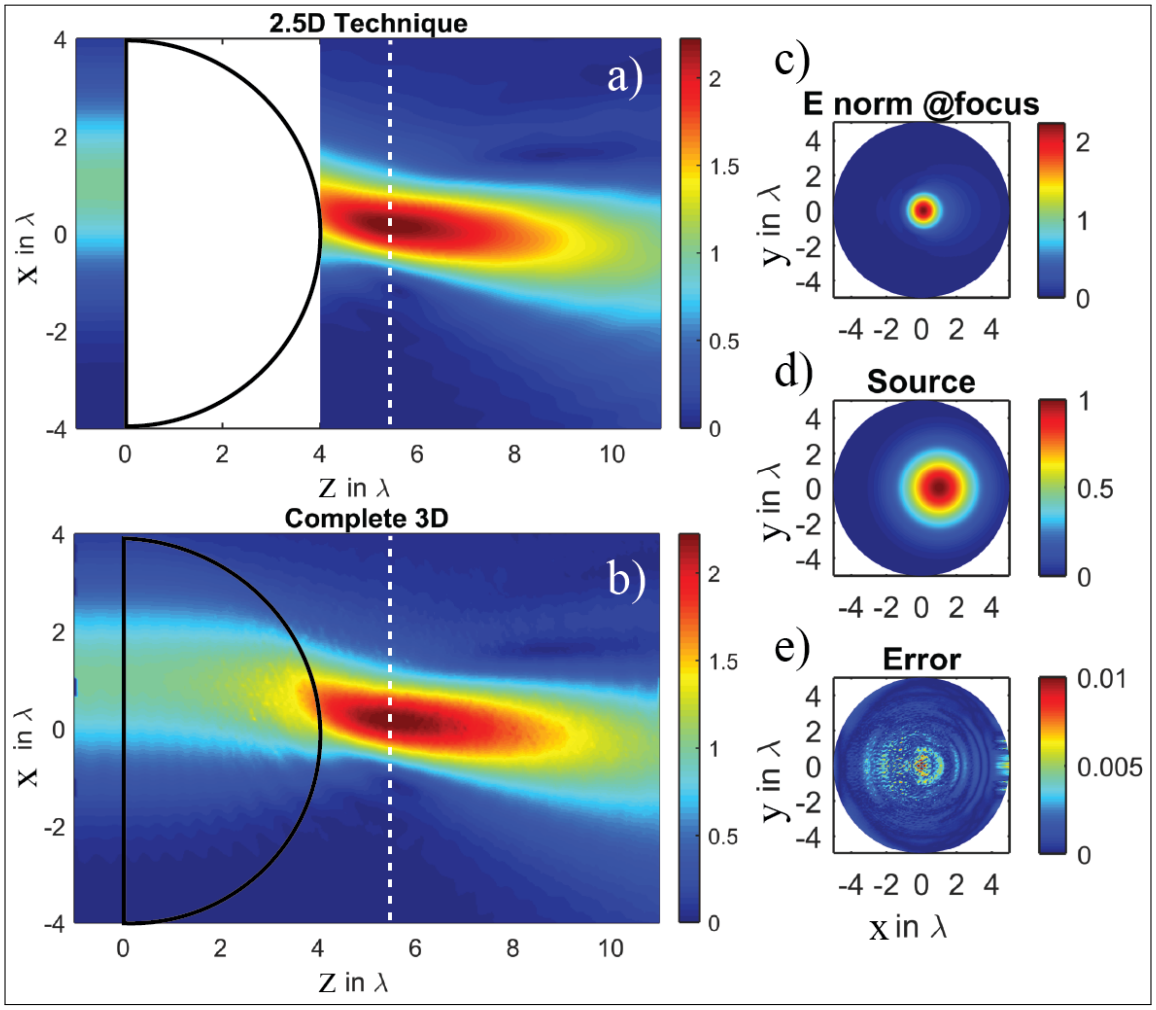


**Figure 6.4**: The comparison between 2.5D technique and complete 3D simulations. (a) electric field norm on xz plane (y = 0) using 2.5 D technique (only fields pre and post the scattering medium are computed using the transfer matrix. Hence the fields inside the lens in (a) are blank). (b) electric field norm on xz plane (y = 0) computed using conventional 3D approach in COMSOL. (c) electric field norm at the focal plane of the lens. The white dashed line indicates the focal line. (d) offset Gaussian beam with a beam waist=$2\lambda$ propagating along $+z$ direction is the source excitation field in both 2.5D and 3D simulations. (e) normalized absolute error between 2.5D technique and 3D simulations at the focal plane.

a reasonable tolerance), the above equation converges quickly for a finite set of azimuthal mode numbers.

In order to construct the transfer matrix **T** for an axi-symmetric medium based on plane wave propagator, each cylindrical harmonic that contributes to a plane wave (every plane wave has a discrete value of $\theta_i$ in the range 0 to $\pi/2$) has to be propagated using an axi-symmetric solver. The 2D scattered fields due to a plane wave at $z = z_1$ plane

**Table 6.2**: Comparison of computational performance between complete 3D simulation and cylindrical harmonic mode propagation technique (2.5D technique) for a domain radius $R = 8\lambda$ .

| Metrics | Complete 3D Simulation [a] | Cylindrical Harmonic Propagator technique (2.5D)[b] Total TM & TE +ve azimuthal modes = 664 | | |
|---|---|---|---|---|
| | | 2D Axi-symmetric Simulation | Source field CHD | Transfer Matrix & 3D Field reconstruction |
| Degrees of freedom (DOFs)[c] | 16260252 | 64612 | - | - |
| Mesh cells Max. element size = $\lambda/7$ | 2706892 | 9163 | - | - |
| Simulation or Post Processing time | $\sim$ 8.5 h | 7 s /mode $\Rightarrow$ $\sim$ 1.2h all modes | $\sim$120 s (+ve & -ve azi-modes) | $\sim$90 s |
| Memory Usage | High (Iterative Solver) | Low (Direct Solver) | Low | Low |
| Computational Scaling | $R^3_{domain}$ | $R^2_{domain}$ | | |
| Result Reusability for different excitations | Requires resimulation for each excitation source | 2D COMSOL scattered fields and inturn Transfer matrix, **T**, is reusable; just requires computing the CHD coefficients for different excitation source. | | |
| Parallelizability | Not easy | Each mode simulation is independent of other; extremely parallelizable | Involves Matrix multiplication and can be implemented on a GPU and parallelizable. (Parity conditions also reduce the computation by factor of 2.) | |

[a] Simulations were performed on an AMD Opteron(tm) Processor 6238 with 12×4 cores with 512 GB RAM.
[b] Simulations and post processing were performed on an AMD Opteron(tm) Processor 4180 with 6x1 cores with 64 GB RAM.
[c] DOFs $\approx$ Number of Mesh nodes $\times$ Number of dependent variables; [18].

is calculated by revolving the 1D fields in $(\phi = 0, z = z_1)$ cut-line (i.e., multiplying by the factor $e^{jm\phi}$, with $\phi$ discretely varying from 0 to $2\pi$) and summing all the 2D field contributions from each cylindrical harmonic. These summed 2D scattered fields due to a single plane wave input need to be regridded and interpolated to transform from $(\rho, \phi)$ cylindrical coordinates to (x,y) Cartesian coordinates. Then, 2D FFT can be applied on these fields to calculate the output harmonic coefficients for a particular input harmonic.

(Parity conditions exist and can be exploited for -ve azimuthal mode numbers). Once the output coefficients are known, inverse FFT can be applied to calculate the vector field results post the medium. In this approach, as one can very evidently note, there is a back and forth change of basis. Hence, this approach to construct **T** may not be the best choice in terms of computational load for a given space-bandwidth product inspite of superior, well known FFT algorithms. Table 6.3 illustrates the case for cylindrical harmonic propagator by comparing the computational load required to construct **T** using the two methods for a specific (Maxwell's Fish-eye with R = $8\lambda$) example.

### 6.6.2 Spherical Invisibility Cloak

A spherical invisibility cloak is a transformation optics designed media whose material properties are anisotropic but yet radially symmetric. This example was chosen to show the versatility of cylindrical harmonic propagator technique in exploiting axial symmetry and in dealing with such sophisticated medium. The second-order electric permittivity tensor, $\epsilon$ (or the magnetic permeability, $\mu$) for a spherical invisibility cloak in spherical coordinates $(r, \theta, \phi)$ is given by [20],

**Table 6.3**: Comparison of computational load between plane wave propagator and cylindrical harmonic propagator using the same 2D axi-symmetric solver (2.5D technique) for a domain radius $R = 8\lambda$.

| Metrics | Plane wave propagator | Cylindrical Harmonic propagator |
|---|---|---|
| No. of 2D simulations (TM & TE +ve azi modes) | 1276[(a)] | 664 |
| Input harmonic | Plane wave $\rightarrow$ sum of individual Cylindrical harmonics to exploit symmetry | Directly a particular Cylindrical harmonic |
| Post processing on scattered fields after each i/p harmonic for **T** construction | Revolve 1D field solution by $\times e^{jm\phi}$ $\rightarrow$ Sum the fields for all possible m's for a given $\theta_i$ $\rightarrow$ Regrid and interpolate from $(\rho, \phi)$ to (x,y) $\rightarrow$ 2D FFT $\rightarrow$ o/p coefficients | 1D Hankel Transform on 1D fields $\rightarrow$ o/p coefficients |
| Transfer Matrix **T** | Dense matrix | Sparse, Block Diagonal Matrix (azimuthal mode number is preserved) |

[(a)] Convergence tolerance error was assumed to be = 1e-3. $\theta_i$ was discretely Nyquist sampled from 0 to $\pi/2$.

$$\epsilon = \mu = \begin{bmatrix} \epsilon_{rr} & \epsilon_{r\theta} & \epsilon_{r\phi} \\ \epsilon_{\theta r} & \epsilon_{\theta\theta} & \epsilon_{\theta\phi} \\ \epsilon_{\phi r} & \epsilon_{\phi\theta} & \epsilon_{\phi\phi} \end{bmatrix} = \begin{bmatrix} \frac{b}{b-a}\frac{(r-a)^2}{r^2} & 0 & 0 \\ 0 & \frac{b}{b-a} & 0 \\ 0 & 0 & \frac{b}{b-a} \end{bmatrix} \tag{6.42}$$

where $a$ is the radius of the sphere to be hidden and the cloaking region is contained in the annulus $a < r < b$. In cylindrical coordinates, $(\rho, \phi, z)$, the tensor in (6.42) transforms to,

$$\begin{bmatrix} \epsilon_{\rho\rho} & \epsilon_{\rho\phi} & \epsilon_{\rho z} \\ \epsilon_{\phi\rho} & \epsilon_{\phi\phi} & \epsilon_{\phi z} \\ \epsilon_{z\rho} & \epsilon_{z\phi} & \epsilon_{zz} \end{bmatrix} = \begin{bmatrix} \frac{1}{2}[\epsilon_{rr} + \epsilon_{\theta\theta} + (\epsilon_{\theta\theta} - \epsilon_{rr})\cos 2\theta] & 0 & (\epsilon_{rr} - \epsilon_{\theta\theta})\cos\theta\sin\theta \\ 0 & \epsilon_{\phi\phi} & 0 \\ (\epsilon_{rr} - \epsilon_{\theta\theta})\cos\theta\sin\theta & 0 & \epsilon_{rr}\cos^2\theta + \epsilon_{\theta\theta}\sin^2\theta \end{bmatrix} \tag{6.43}$$

The 2.5D simulation setup for a spherical cloak is shown in Fig. 6.5. The simulation domain just consists of one half of a 2D slice of the cloak. The inner cloaked region has a radius a=2$\lambda$ and is set to perfect electric boundary condition (PEC). The cloaking region annulus is between the radii a=2$\lambda$ and b=4$\lambda$. The material property tensor components used in the cloaking annulus is shown in Fig. 6.6. The effect of cloaking is also shown in Fig. 6.6. The incident beam is an offset **y**-polarized Gaussian vector beam propagating along $+z$ direction. The electric fields shown in Fig. 6.6 correspond to the real part of y-component on xz-plane (y = 0).

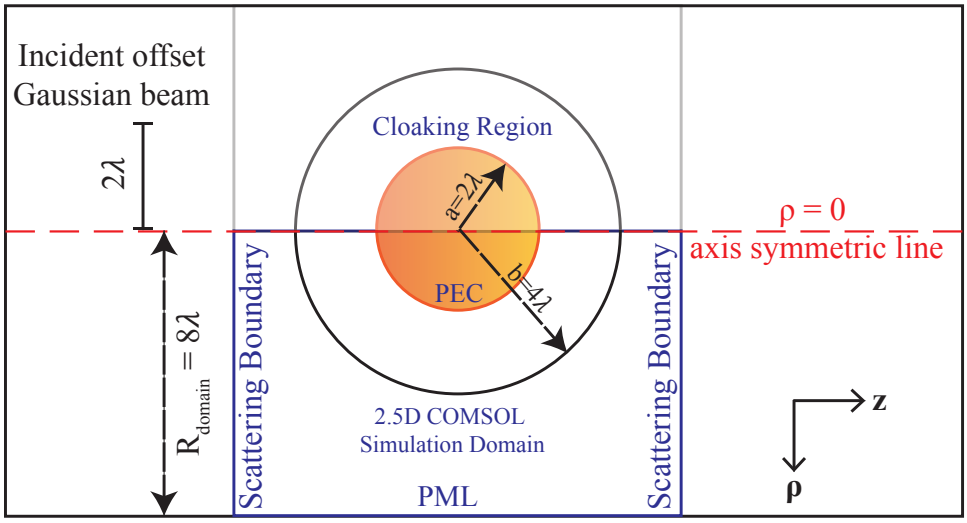


**Figure 6.5**: Spherical invisibility cloak schematic for 2.5 D technique. Blue outline box indicates the simulated domain.

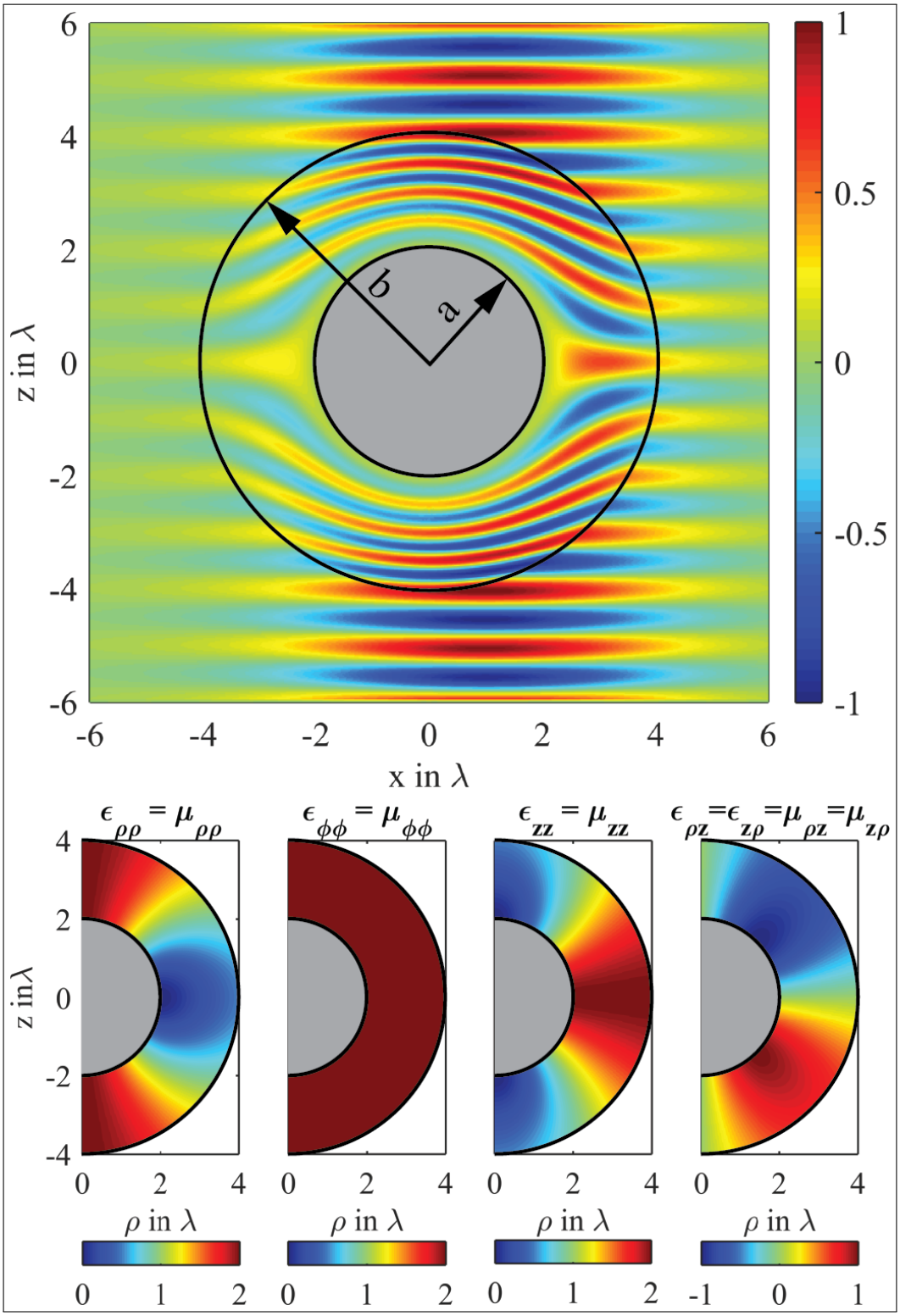


**Figure 6.6**: The real part of the field due to incident offset Gaussian vector beam on xz plane (y = 0) inside and outside the spherical cloak simulated using 2.5D technique. The subfigures below show the individual component of the material property tensors required inside the cloaking region.

### 6.6.3 Free Space Impedance Matched Thin Aspheric Plano-convex Lens

In this case, we consider a simple aspheric, thin plano-convex lens with a focal length f = 15$\lambda$, refractive index of n = 3.58, and relative impedance Z = 1 ($\epsilon_r = \mu_r = n$) as the homogeneous linear scattering medium. The lens is axially symmetric with a maximum thickness of 0.8$\lambda$ and a diameter of 18$\lambda$. The lens is illuminated normally by a $\hat{\mathbf{y}}$-polarized Gaussian beam of waist diameter = 5$\lambda$ at the source plane (40$\lambda$ behind the lens). This example was chosen to demonstrate the versatility of this method when the transverse size and range are large compared to $\lambda$. Figure 6.7 shows the complete schematic diagram of the setup. The blue colored rectangular box in the figure shows the COMSOL 2.5 D simulation domain along with the boundary conditions that were applied. The simulation domain has a transverse radius $R_{domain} = 30\lambda$. Figure 6.8 a shows the numerically computed electric field norm pre- and post-lens. The input Gaussian beam is focused at z = 15$\lambda$ in front of the lens as per the design. Since a reflectionless lens in general converts a normally incident input Gaussian beam to another output Gaussian beam, one can derive the complete analytical solution for this setup using Gaussian beam optics theory [21]. Using the parameters of the considered lens and the excitation Gaussian beam, the waist

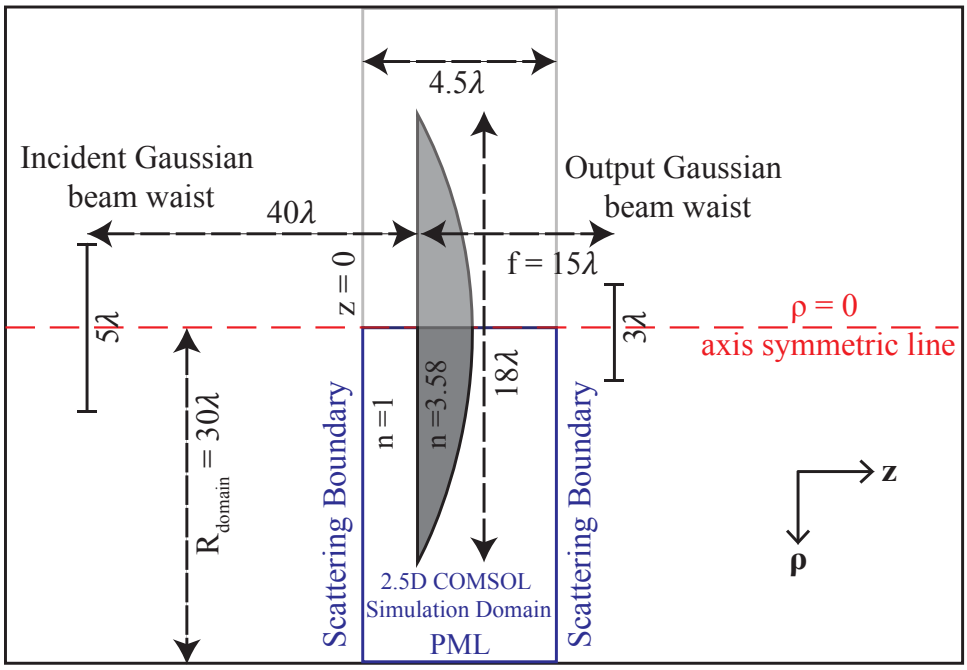


**Figure 6.7**: Aspheric thin plano-convex lens schematic for 2.5 D technique. Blue outline box indicates the simulated domain.

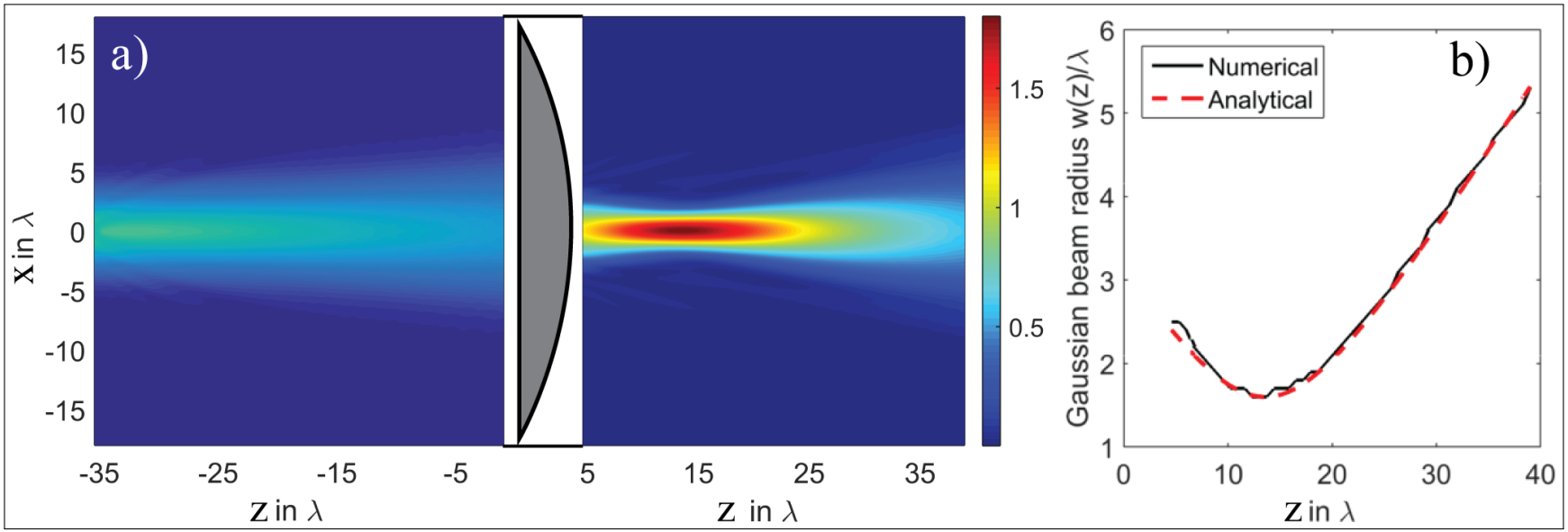


**Figure 6.8**: Aspheric plano-convex lens 2.5D simulation. a) numerically computed fields norm of electric field pre and postlens. b) comparison between the output Gaussian beam radius as a function of z calculated numerically (black solid) and analytically (dashed red).

radius of the output beam as a function of z was analytically calculated. Figure 6.8 b shows the comparison between the numerical technique and the exact analytical result. The numerical and the analytical output beam radius are in good agreement with each other within an RMS error of 3%.

### 6.6.4 Negative Refractive Index Perfect Lens

In this example, we choose a perfect negative index lens excited by a completely arbitrary source excitation field. A perfect lens has a straightforward analytical relationship between the image and source fields. A perfect lens ($\epsilon_r = \mu_r = n = -1$) acts as a focusing slab in which the image is the exact reproduction of the source (when there is no loss) [22]. The perfect lens disk has a thickness $z_2 = 3.6\lambda$ and a radius $R_{domain} = 30\lambda$ . The distances from the edge of the lens slab to the object and image plane are $z_1 = 0.45\lambda$ and $z_3 = 3.15\lambda$, respectively, such that $z_2 = z_1 + z_3$. Figure 6.9 shows the schematic diagram of the setup along with the COMSOL simulation domain and the boundary conditions used. Figure 6.10 a shows the source plane electric field norm of the excitation field. Since the image is the object for a perfect lens with no loss, the fields at the image plane should be

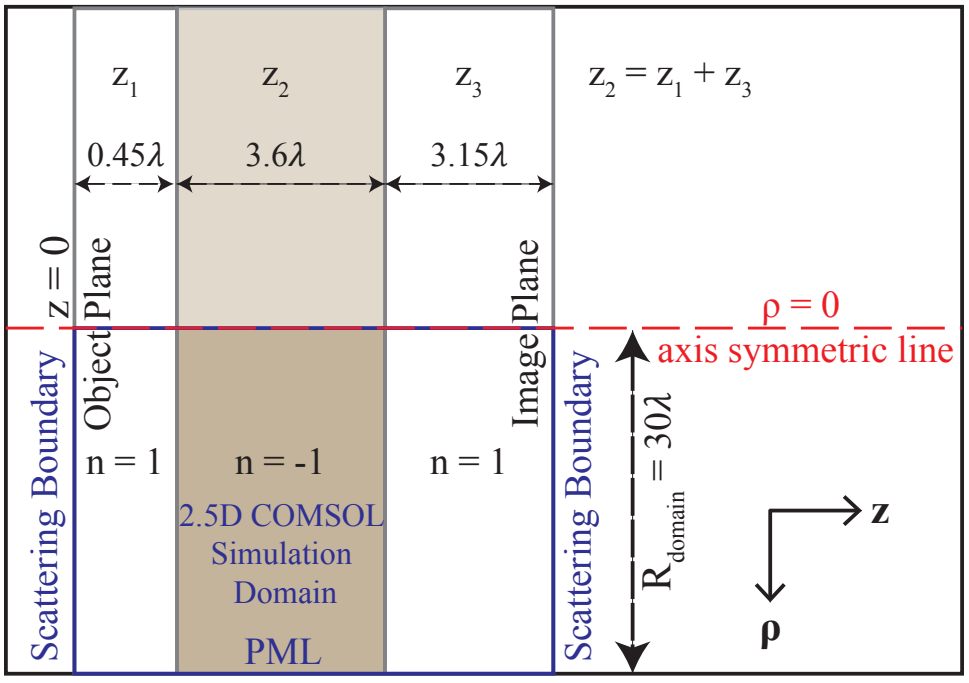


**Figure 6.9**: Perfect Lens schematic for 2.5D technique. Blue outline box shows the simulated domain.

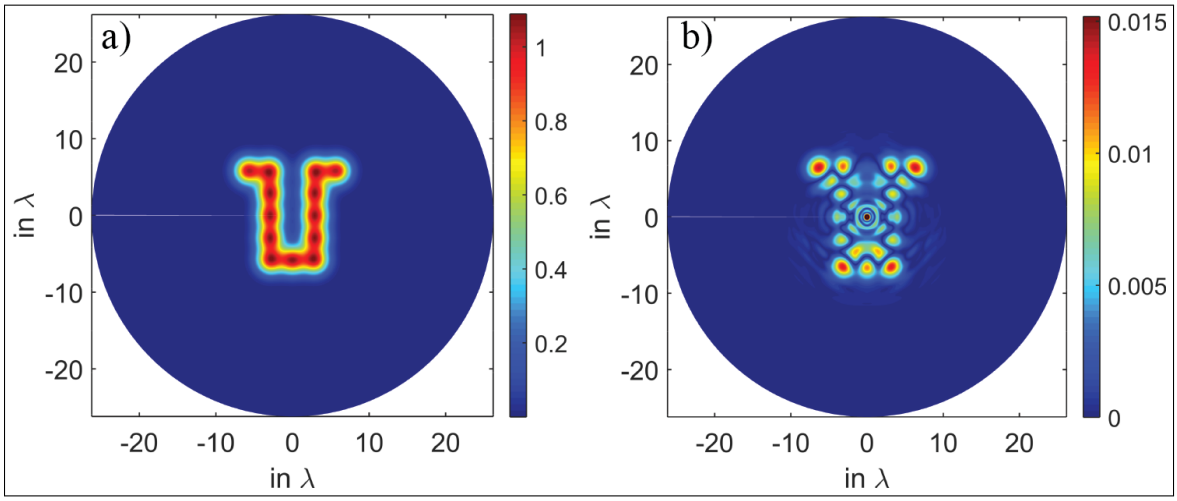


**Figure 6.10**: Negative refractive index perfect lens 2.5D simulation. a) shows the source plane electric field norm of the chosen arbitrary excitation source at z = 0 plane. b) shows the difference map between the image and the object plane electric field norms.

exactly equal to the source fields. Figure 6.10 b shows the difference between the image and source fields and the absolute peak error about 1.5%.

## 6.7 Conclusion

In this article we develop a complete formulation for both continuous and discrete cylindrical harmonic decomposition. We formulate this decomposition method for both scalar and vector basis fields. Such harmonic decomposition methods (like Fourier transforms and spherical harmonics) play a vital role in many computational physics problems. Some future developments regarding the decomposition will include reducing the computational burden further and parallelizing the decomposition technique on a Graphical Processing Unit (GPU). We use this decomposition method to propagate the individual harmonics through an axi-symmetric medium using a 2D axi-symmetric EM solver as a part of a precomputational step (2.5D technique). The fields from this solver are in turn used to construct an efficient, modular, and reuseable transfer matrix, which can be later used to calculate the total scattered fields due to the inhomogeneous axi-symmetric medium for any given arbitrary incident excitation and a finite space-bandwidth product. We also present a composite index ordering strategy to perform the required forward and/or inverse DFHT. This ordering helps to reduce the operations to simple matrix multiplications. This overall approach was numerically verified on well known and relevant

axi-symmetric media. We also compare our method with other possible techniques in terms of computational load. The exploitation of axial symmetry along with transfer matrix approach using CHD help to significantly reduce the computational burden/resources without sacrificing accuracy.

## 6.8 Supplementary Material

### 6.8.1 Orthogonality Properties of Bessel and Exponential Functions

The following orthogonality properties of the Bessel and exponential functions are used in the article,

$$\int_0^R J_m(\chi_{1mn}\,\rho)\, J_m(\chi_{1mn'}\,\rho)\rho d\rho = \frac{R^2}{2} J_{m+1}^2(\chi_{1mn})\,\delta_{nn'} \tag{6.44}$$

$$\int_0^R J_m(\chi'_{2mn}\,\rho)\, J_m(\chi'_{2mn'}\,\rho)\rho d\rho = \frac{R^2}{2}\left[J_m^2(\chi'_{2mn}) - J_{m-1}(\chi'_{2mn})J_{m+1}(\chi'_{2mn})\right]\,\delta_{nn'} \tag{6.45}$$

$$\int_{-\pi}^{\pi} \exp\left(-jm\phi\right)\exp\left(jm'\phi\right) d\phi = 2\pi\delta_{mm'} \tag{6.46}$$

### 6.8.2 Bessel Function Identities Used in the Chapter

$$\text{Recurrence relation:}\quad J_{n+1}(x) + J_{n-1}(x) = \frac{2n}{x} J_n(x) \tag{6.47}$$

$$\text{Derivative of Bessel Function:}\quad J'_n(x) = \frac{1}{2}\left[J_{n-1}(x) - J_{n+1}(x)\right] \tag{6.48}$$

### 6.8.3 Parity Condition between Positive and Negative Azimuthal Mode Numbers

The following Tables (6.4 and 6.5) show the parity condition between positive and negative azimuthal mode numbered basis functions for TM and TE modes.

**Table 6.4**: Parity condition for TM modes.

| TM Modes | Relationship between positive and negative azimuthal mode numbered basis functions. | | |
|---|---|---|---|
| -ve Azi Mode Number m | $E_\rho(\rho,z)$ | $E_\phi(\rho,z)$ | $E_z(\rho,z)$ |
| Odd | $(-1)^{\lvert m\rvert}$ | $(-1)^{(\lvert m\rvert+1)}$ | $(-1)^{\lvert m\rvert}$ |
| Even | $-(-1)^{(\lvert m\rvert+1)}$ | $-(-1)^{\lvert m\rvert}$ | $-(-1)^{(\lvert m\rvert+1)}$ |

**Table 6.5**: Parity condition for TE modes.

| TE Modes | Relationship between positive and negative azimuthal mode numbered basis functions. | | |
|---|---|---|---|
| -ve Azi Mode Number m | $E_\rho(\rho,z)$ | $E_\phi(\rho,z)$ | $H_z(\rho,z)$ |
| Odd | $(-1)^{(\lvert m\rvert+1)}$ | $(-1)^{\lvert m\rvert}$ | $(-1)^{(\lvert m\rvert)}$ |
| Even | $-(-1)^{\lvert m\rvert}$ | $-(-1)^{(\lvert m\rvert+1)}$ | $-(-1)^{\lvert m\rvert+1}$ |

### 6.8.4 Composite Indices for DFHT

Based on the example composite indices shown in Table 6.1, the transfer matrix $\mathbf{T}$ takes the representative form shown in (6.49), where $\bowtie$ and # in $\mathbf{T}$ matrix indicates the TM ($l'=1$) and TE ($l'=2$) mode coefficients, respectively. The rest of the values in the $17\times 17$ transfer matrix are zeros, making it a sparse, block-diagonal matrix.

$$[\mathbf{b}] = \begin{bmatrix} \# & & & & & & & & & & & & & & & & \\ & \# & & & & & & & & & & & & & & & \\ & & \bowtie & \bowtie & & & & & & & & & & & & & \\ & & \# & \# & & & & & & & & & & & & & \\ & & & & \bowtie & \bowtie & \bowtie & & & & & & & & & & \\ & & & & \# & \# & \# & & & & & & & & & & \\ & & & & \# & \# & \# & & & & & & & & & & \\ & & & & & & & \bowtie & \bowtie & \bowtie & \bowtie & & & & & & \\ & & & & & & & \bowtie & \bowtie & \bowtie & \bowtie & & & & & & \\ & & & & & & & \# & \# & \# & \# & & & & & & \\ & & & & & & & \# & \# & \# & \# & & & & & & \\ & & & & & & & & & & & \bowtie & \bowtie & \bowtie & & & \\ & & & & & & & & & & & \# & \# & \# & & & \\ & & & & & & & & & & & \# & \# & \# & & & \\ & & & & & & & & & & & & & & \bowtie & \bowtie & \\ & & & & & & & & & & & & & & \# & \# & \\ & & & & & & & & & & & & & & & & \# \end{bmatrix}_{17\times 17} \times \begin{bmatrix} a_{2,-4,1} \\ a_{2,-3,1} \\ a_{1,-2,1} \\ a_{2,-2,1} \\ a_{1,-1,1} \\ a_{2,-1,1} \\ a_{2,-1,2} \\ a_{1,0,1} \\ a_{1,0,2} \\ a_{2,0,1} \\ a_{2,0,2} \\ a_{1,1,1} \\ a_{2,1,1} \\ a_{2,1,2} \\ a_{1,2,1} \\ a_{2,2,1} \\ a_{2,3,1} \end{bmatrix}_{17\times 1} \tag{6.49}$$

The functional form of the composite indices $[\mathbf{l},\mathbf{i},\boldsymbol{\alpha}]$ mapping are neither illuminating nor easy to specify in mathematical notation. It is best to generate a vector of triplets that store the mapping and use elements of this vector for building up the needed matrices. Some pseudocode for generating this composite index vector $\mathbf{l}$ is shown in Algorithm 1.

## 6.9 Acknowledgements

This work was supported by the Department of Homeland Security, Science and Technology Directorate (Contract No. HSHQDC-12-C-00049). The published material represents the position of the authors and not necessarily that of the DHS or S&T. The support and resources from the Center for High Performance Computing at the University of Utah

**Algorithm 1** Finding Composite Index **l**

**procedure** COMPOSITEINDEX ▷ Composite Index **l** ⇒ (l,m,n)
  $BR \leftarrow 2\pi$ ▷ BR ⇒ Space-Bandwidth Product
  $p \leftarrow 0$ ▷ Find max Azimuthal mode number for l=1 (TM)
  **while** $\chi_{1p1} \leq BR$ **do** ▷ The TM mode is propogating; $J_m(\chi_{1p1}) = 0$
    $p \leftarrow p + 1$
  **end while**
  $M_1 \leftarrow (p - 1)$
  $p \leftarrow 0$ ▷ Find max Azimuthal mode number for l=2 (TE)
  **while** $\chi_{2p1} \leq BR$ **do** ▷ The TE mode is propogating; $J'_m(\chi_{2p1}) = 0$
    $p \leftarrow p + 1$
  **end while**
  $M_2 \leftarrow (p - 1)$
  $\overline{m} \leftarrow min(-M_1, -M_2)$; $M \leftarrow max(M_1 - 1, M_2 - 1)$; $n_1 \leftarrow 2$; $n_2 \leftarrow 2$; $L \leftarrow 0$ ▷ Initialize
  **while** $[(n_1 - 1) > 0 \,||\, (n_2 - 1) > 0]$ **do**
    $n_1 = n_2 \leftarrow 1$
    **while** $\left[\chi_{1,\overline{m},n_1} \leq BR\} \;\&\&\; \{\overline{m} \leq M\}\right]$ **do** ▷ TM modes
      $\mathbf{l} \leftarrow (\mathbf{l} + 1)$; $l \leftarrow 1$; $m \leftarrow \overline{m}$; $n \leftarrow n_1$
      $n_1 \leftarrow (n_1 + 1)$ ▷ Assign l,m,n and increment radial mode
    **end while**
    **while** $[\{\chi_{2,\overline{m},n_2} \leq BR\} \;\&\&\; \{\overline{m} \leq M\}]$ **do** ▷ TE modes
      $\mathbf{l} \leftarrow (\mathbf{l} + 1)$; $l \leftarrow 2$; $m \leftarrow \overline{m}$; $n \leftarrow n_2$
      $n_2 \leftarrow (n_2 + 1)$ ▷ Assign l,m,n and increment radial mode
    **end while**
    $\overline{m} \leftarrow (\overline{m} + 1)$ ▷ Increment azimuthal mode number
  **end while**
**end procedure**

are gratefully acknowledged. Authors would like to acknowledge Richard Edwards for some useful comments on the manuscript.

## 6.10 References

[1] O. Furxhi, D. L. Marks, and D. J. Brady, "Echelle crossed grating millimeter wave beam scanner," *Opt. Express*, vol. 22, no. 13, pp. 16 393–16 407, Jun. 2014.

[2] O. S. Cossairt, D. Miau, and S. K. Nayar, "Scaling law for computational imaging using spherical optics," *J. Opt. Soc. Am. A*, vol. 28, no. 12, pp. 2540–2553, Dec. 2011.

[3] S. Venkatesh, N. Viswanathan, and D. Schurig, "W-band sparse synthetic aperture for computational imaging," *Opt. Express*, vol. 24, no. 8, pp. 8317–8331, 2016.

[4] M. Meeks and J. Ruze, "Evaluation of the haystack antenna and radome," *Antennas and Propagation, IEEE Transactions on*, vol. 19, no. 6, pp. 723–728, Nov. 1971.

[5] G. Crone, A. Rudge, and G. Taylor, "Design and performance of airborne radomes: A review," *Communications, Radar and Signal Processing, IEEE Proceedings F*, vol. 128, no. 7, pp. 451–464, 1981.

[6] M. Ibanescu, Y. Fink, S. Fan, E. L. Thomas, and J. D. Joannopoulos, "An all-dielectric coaxial waveguide," *Science*, vol. 289, no. 5478, pp. 415–419, 2000.

[7] B. Thomas, G. L. James, and K. J. Greene, "Design of wide-band corrugated conical horns for cassegrain antennas," *Antennas and Propagation, IEEE Transactions on*, vol. 34, no. 6, pp. 750–757, 1986.

[8] G. Lipworth, et al., "Magnetic metamaterial superlens for increased range wireless power transfer," *Scientific Reports*, vol. 4, pp. 3642+, Jan. 2014.

[9] R. Merlin, "Radiationless electromagnetic interference: Evanescent-field lenses and perfect focusing," *Science*, vol. 317, no. 5840, pp. 927–929, 2007.

[10] Y. Ye, et al., "Monolayer excitonic laser," *Nat Photon*, Oct. 2015.

[11] Y. Zhao, et al., "Creating and probing electron whispering-gallery modes in graphene," *Science*, vol. 348, no. 6235, pp. 672–675, 2015.

[12] J. B. Pendry, A. Aubry, D. R. Smith, and S. A. Maier, "Transformation optics and subwavelength control of light," *Science*, vol. 337, no. 6094, pp. 549–552, 2012.

[13] C. Ciraci, et al., "Probing the ultimate limits of plasmonic enhancement," *Science*, vol. 337, no. 6098, pp. 1072–1074, 2012.

[14] Y. Ou, D. Pardo, and Y. Chen, "Fourier finite element modeling of light emission in waveguides: 2.5-dimensional fem approach," *Opt. Express*, vol. 23, no. 23, pp. 30 259–30 269, Nov 2015.

[15] C. C. Johnson, *Field and Wave Electrodynamics*. McGraw-Hill, 1965.

[16] A. F. Peterson, S. L. Ray, and R. Mittra, *Computational Methods for Electromagnetics, Volume 4 of IEEE Press Series on Electromagnetic Wave Theory*. Wiley, 1998.

[17] C. Ciraci, Y. Urzhumov, and D. R. Smith, "Far-field analysis of axially symmetric three-dimensional directional cloaks," *Opt. Express*, vol. 21, no. 8, pp. 9397–9406, 2013.

[18] *COMSOL Multiphysics, RF Module User's Guide*. COMSOL, 2012.

[19] C. A. Balanis, *Advanced Engineering Electromagnetics, 2nd Edition*. Wiley, 2012.

[20] J. B. Pendry, D. Schurig, and D. R. Smith, "Controlling electromagnetic fields," *Science*, vol. 312, no. 5781, pp. 1780–1782, 2006.

[21] B. E. A. Saleh and M. C. Teich, *Fundamentals of Photonics*. Wiley, 2007.

[22] J. B. Pendry, "Negative refraction makes a perfect lens," *Physical Review Letters*, vol. 85, no. 18, pp. 3966–3969, Oct. 2000.

# CHAPTER 7

# FUTURE DIRECTIONS: MULTI-FUNCTIONAL RF SYSTEM LEVERAGING Ka-BAND COMMERCIAL OFF-THE-SHELF INTEGRATED CIRCUITS

This chapter, in part, will be submitted for publication, with authors Suresh Venkatesh and David Schurig. This chapter, in part, was also part of an awarded research grant proposal, with proposers David Schurig and Suresh Venkatesh.

## 7.1 Abstract

We propose to explore the multifunctionality of antenna arrays and their associated back-end electronics in the Ka-band (26.5-40 GHz). Current interest in arrays operating in this band is strong and applications can include security imaging, satellite communications, and active denial systems (employing nonlethal force). With sufficient flexibility of the connected electronics (i.e., the back-end transmit and receive chains), providing independent acquisition or control of the phase of each element, these applications are made compelling by including focusing-optic-free computational imaging, satellite links on mobile platforms, and electronic targeting of nonlethal force. We will investigate, in particular, the synergies that result when a single hardware platform can support all of these applications (see Fig. 7.1). For example, if the platform supports both imaging and active denial, energy can be accurately deposited on targets identified in the imaging data without the need for an external target calibration. Similarly, jamming (or even damaging) energy can be directed to hostile broadcasting communications systems identified in communications sweeps, again without the need for external calibration. (External calibration interrupts operations, and can be a time consuming step that requires frequent repetition due to hardware drift.) Technological development of low-cost, highly-efficient hardware

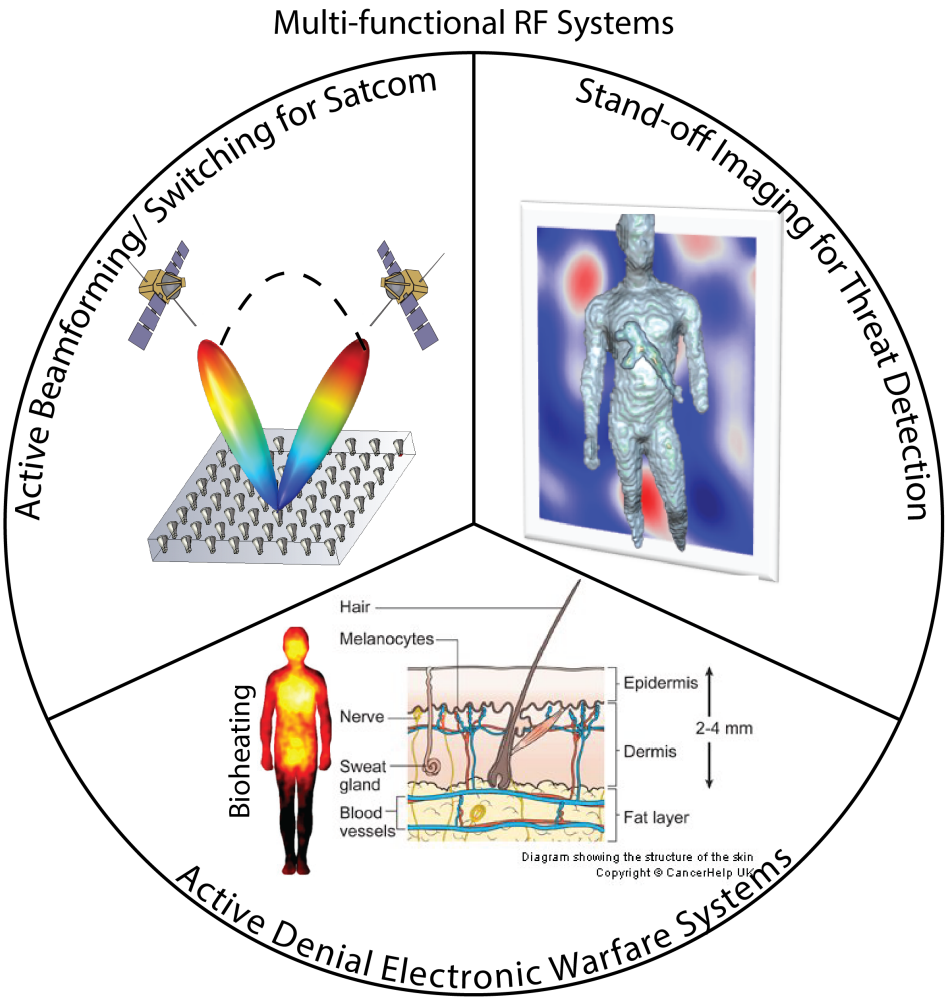


**Figure 7.1**: Conceptual diagram of multifunctional RF system.

components with capability in the Ka-band have only recently become available. Off the shelf packages can now enable a compelling deployed system in the $10k range rather than the $100k range. Accordingly, individual channels, or even moderate channel count systems, can now be investigated on a modest budget.

## 7.2 Background

Millimeter-waves (30-300 GHz) occupy a strategic part of the electromagnetic spectrum because they can penetrate many nonmetallic barriers including things like walls, clothing, smoke, fog, dust/sand, and clouds, while at the same time allow probing of objects with superior resolution to microwaves. Hence mm-wave systems have found applications in the fields of radio astronomy, satellite communication, remote sensing, biomedical imag-

ing, security screening, and surveillance [1–6]. The recent opening up of Ka-band (26.5-40 GHz) spectrum by the US military for satellite communications has led to the rapid commercial development of advanced CMOS/Bi-CMOS based integrated circuits (ICs) at this frequency band. We propose to leverage this technology to demonstrate advanced multifunctional RF systems (MFRF) by integrating Ka-band, low-cost, commercial-off-the-shelf (COTS) ICs. Using these COTS ICs saves a significant amount of time and cost in design/development without sacrificing the performance. This also helps in developing rapid prototypes for desired functionality. We first propose to integrate all the individual COTS surface mount ICs such as power amplifier, up/down mixers, phase shifters, voltage-controlled oscillators, and phase-locked loops on a PCB along with a microstrip antenna to form Ka-band transmitter (Tx) and receiver (Rx) elements. We then plan to develop a prototype baseline configuration that would include about ten such Txs and Rxs, mounted in an aperture size on the order of 1.5 meters. With addressable, coherent control over all the Tx and Rx elements, such an aperture can deliver antenna gain, coding gain, and implementation of parallel, orthogonal channels. This physical layer, combined with reconfigurable computational resources can support not only communication functionality (satcom and terrestrial line-of-sight, and jamming), but also several additional applications. Multifunctional applications include computational imaging (including long range threat detection and motion tracking), Active Denial Systems (ADS), and other Electronic Warfare applications. In particular, our proposed platform, that includes both imaging and ADS capability, could support nonlethal hostile crowd management, perimeter security, and border control objectives, in a human-directed or possibly even autonomous mode. Further, the low cost per Watt and high RF power efficiency of the proposed hardware components allow this functionality to be projected at considerable stand-off distances, and to be packaged into a compact form-factor with modest power requirements, enabling mobile operation or rapid deployment.

The ideas proposed here address ongoing Department of Defense (DoD) programs and objectives. For example, COTS-based MFRF systems are specifically requested by the Defense Advanced Research Projects Agency (DARPA) ADAPTable Sensor System (ADAPT) program [9], "*The ADAPT program seeks novel techniques and processes to rapidly develop low-cost Imaging, Surveillance, Reconnaissance (ISR) sensor systems by adapting com-*

*mercial manufacturing approaches. The primary goal of the ADAPT program is to deliver common hardware and software that can be quickly configured to perform a variety of mission-specific ISR applications."*

## 7.3 Multifunctional RF COTS Hardware

The transmitter and receiver block diagrams along with COTS ICs are shown in Figs. 7.2 and 7.3. Tx and Rx channels are basic heterodyne configurations with tunable phase shifters at the local oscillator (LO) end. This tunable LO frequency synthesis will be reused on Tx and Rx elements. All the identified individual components here in the block diagram are low-cost, packaged, surface mount ICs which will be integrated on a ROGERS printed circuit board. The crucial component in the transmitter is the last power amplifier whose maximum output is ∼4 W (36 dBm) at Ka-Band. The cost per watt for a single completely integrated transmitter is ∼$150/Watt (including PCB process). The cost per single completely integrated Rx channel is ∼$100/channel. We also propose to explore different circuit configurations to achieve polar phased beamforming and DC-DC converters to further improve the power efficiency of Tx power amplifiers.

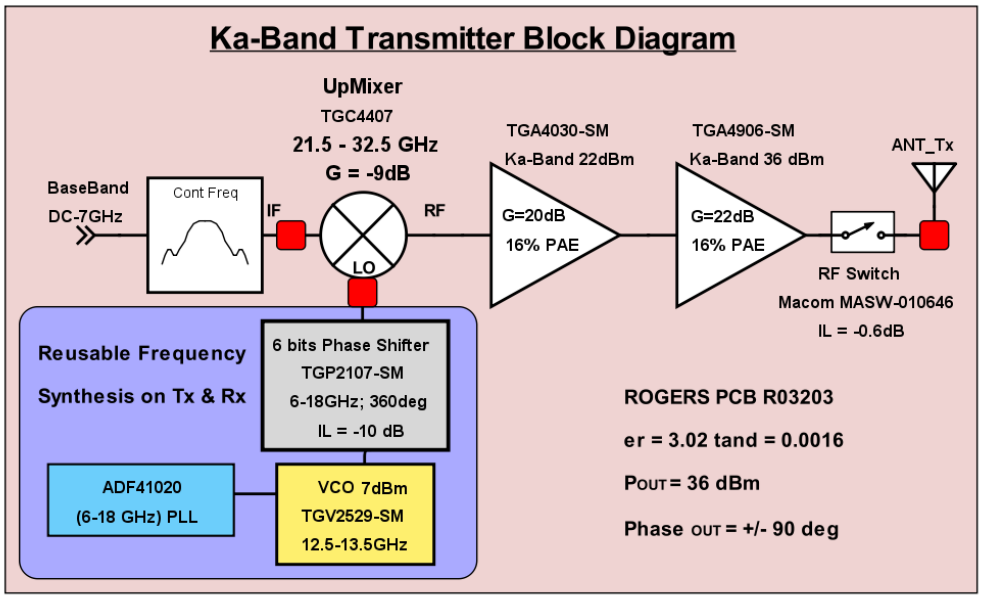


**Figure 7.2**: Ka-band transmitter block diagram with IC part numbers.

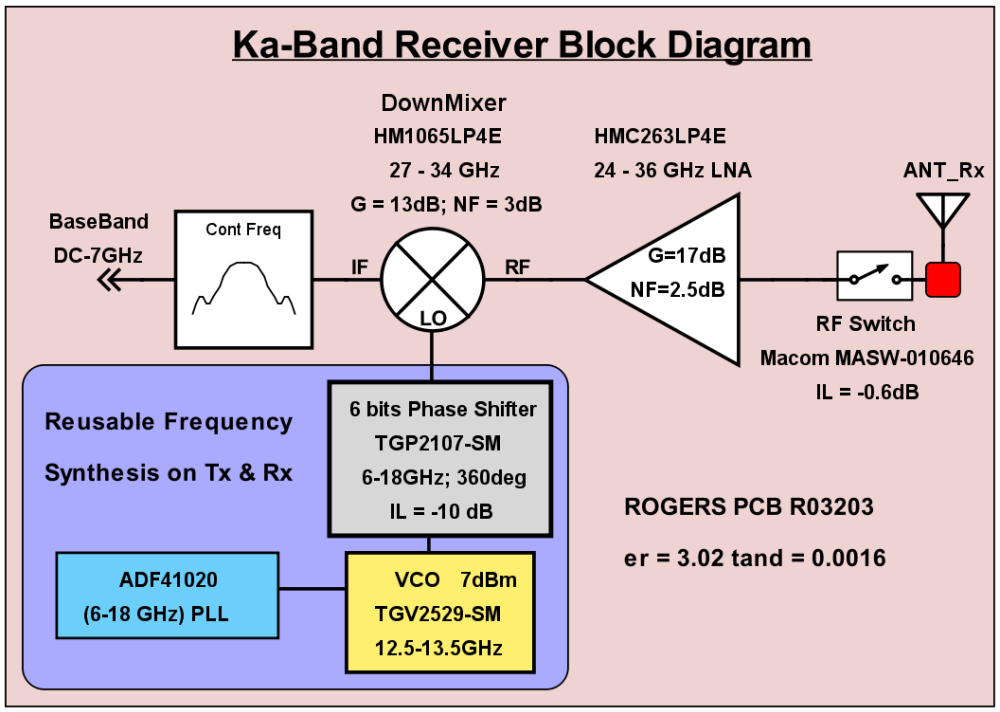


**Figure 7.3**: Ka-band receiver block diagram with IC part numbers.

## 7.4 Multifunctional RF Applications

The main areas in Multi-functional RF applications we wish to explore are:

### 7.4.1 Satellite Communications and Jamming

Satellite communication systems often use large mechanically-scanned, parabolic dishes to achieve high antenna gain and tracking capabilities. Alternatively, one could use multiple, low-cost Tx and Rx elements in a flat, coherent array with electronic beam-steering, facilitating mobile platform satcom with no moving parts [7,8]. Electronic beam steering can be implemented using digitally controlled phase shifters operating at a lower frequency band (6-18 GHz). A 1.5 m x 1.5 m aperture of 25 Txs would have an aperture gain of 55 dB and a total transmit RF power of 100 W. This performance level can support both communications and jamming or hardware damaging applications in hostile environments.

### 7.4.2 Computational Imaging for Security Surveillance

Using the methods of compressed sensing, the same or an even sparser aperture can be used for imaging. An array of 16 Tx and 12 Rx elements can achieve cross- and depth-range

resolutions of 2cm and 5cm, respectively, at a stand-off distance of 10m. This resolution is sufficient for identifying and tracking human forms, and due to high transmit power at Ka-band, such tracking is not impeded by weather or airborne particulates. The achievable cross-range resolution as a function of frequency and aperture area is shown in Fig. 7.4.

### 7.4.3 Active Denial Systems (ADS) for Electronic Warfare

ADS is a nonlethal electronic warfare technology that directs a high-power millimeter wave beam to create an intense heat sensation on the skin without causing permanent damage. An array of 25 Txs, each transmitting at 4 W (with an overall RF transmitted power of 100 W), and distributed over an aperture of 2 m x 2 m, can form a beam with sufficient power density at a stand-off of 25 m to elevate the surface body temperature by ∼40 °C (see Fig. 7.5). This intense heat sensation can be used to deter persons from

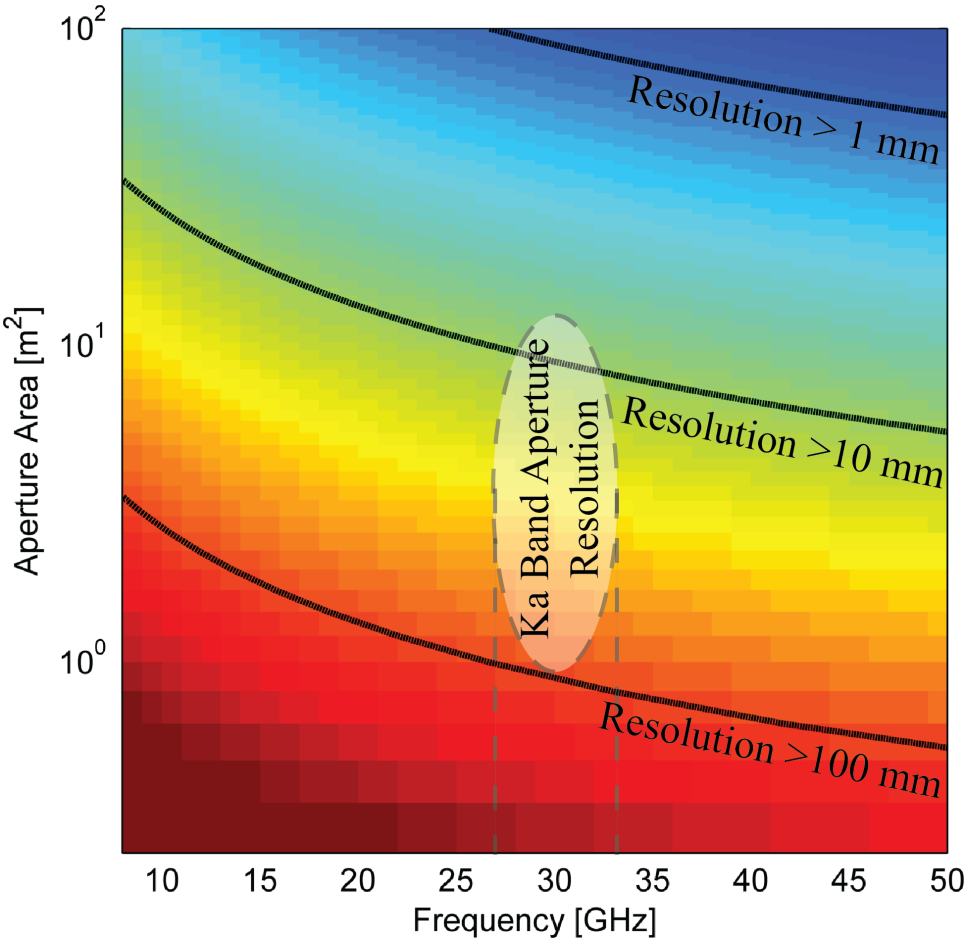


**Figure 7.4**: Cross-range resolution at a stand-off of 10m as a function of aperture area and frequency.

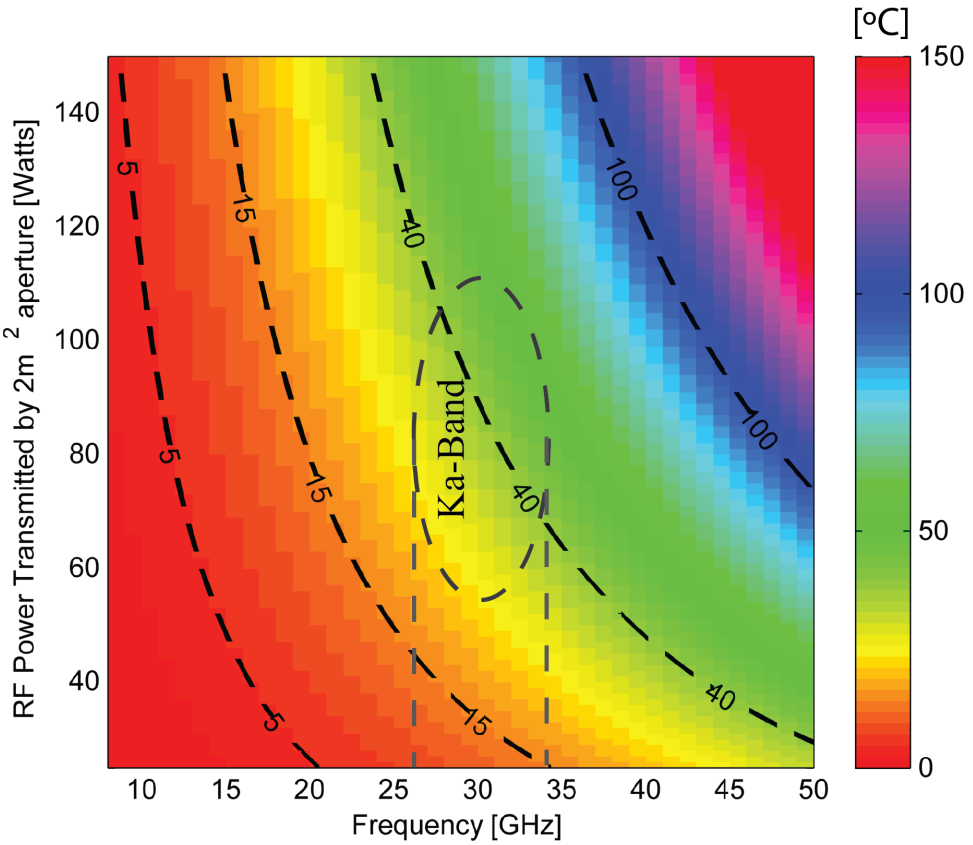


**Figure 7.5**: Temperature elevation in [°C] at the human skin surface due to high power millimeter wave exposure from a 2 $m^2$ aperture.

entering secured areas. The skin penetration depth of Ka-Band radiation is about 1 mm, allowing thermal stimulation in proximity to epidermal nerve fibers. This capability, together with the imaging capabilities and electronic beamforming described above, could enable an autonomous perimeter control system. Using the same platform for imaging and denial functions allows for targeting without requiring external calibration.

The potential multifunctional RF system is light weight, compact, and reconfigurable which makes it ideal to be deployed on mobile, vehicular, and airborne platforms.

## 7.5 References

[1] A. Wootten and A. R. Thompson, "The Atacama large millimeter/submillimeter array," *Proceedings of the IEEE*, vol. 97, no. 8, pp. 1463–1471, 2009.

[2] J. Laskar and C.-H. Lee, *Compact Ku-band Transmitter Design for Satellite Communication Applications: From System Analysis to Hardware Implementation*. Springer Science & Business Media, 2007.

[3] G. M. Rebeiz, D. P. Kasilingam, Y. Guo, P. A. Stimson, and D. B. Rutledge, "Monolithic millimeter-wave two-dimensional horn imaging arrays," *IEEE Transactions on Antennas and Propagation*, vol. 38, no. 9, pp. 1473–1482, 1990.

[4] Z. Q. Zhang and Q. H. Liu, "Three-dimensional nonlinear image reconstruction for microwave biomedical imaging," *IEEE Transactions on Biomedical Engineering*, vol. 51, no. 3, pp. 544–548, 2004.

[5] R. Appleby and C. Cameron, "Seeing hidden objects with millimetre waves," *Physics World*, vol. 25, no. 01, p. 35, 2012.

[6] D. M. Sheen, D. L. McMakin, and T. E. Hall, "Three-dimensional millimeter-wave imaging for concealed weapon detection," *IEEE Transactions on microwave theory and techniques*, vol. 49, no. 9, pp. 1581–1592, 2001.

[7] http://www.kymetacorp.com.

[8] http://echodyne.com.

[9] http://www.darpa.mil/program/adaptable-sensor-system.